N°d'ordre NNT : 2016ISAL0008

THESE de DOCTORAT DE L'UNIVERSITE DE LYON
préparée au sein de
l'INSA LYON

Ecole Doctorale ED34
(Ecole Doctorale Matériaux de Lyon)

Spécialité de doctorat: Science des Matériaux

Soutenue publiquement le 19/01/2016, par :

Inas ISSA

In situ TEM Nanocompression & Mechanical Analysis of Ceramic Nanoparticles

Devant le jury composé de :

LEGROS, Marc	*Directeur de recherche CNRS/Université de Toulouse* III	Rapporteur
TROMAS, Christophe	*Professeur des Universités/Univesité de Poitiers*	Rapporteur
EGGEMAN, Alexander	*Docteur/Université de Cambridge*	Examinateur
MACHON, Denis	*Maitre de Conférence HDR /Université Lyon 1*	Examinateur
CHEVALIER, Jérôme	*Professeur des Universités/INSA de Lyon*	Président
MASENELLI-VARLOT, Karine	*Professeur des Universités/INSA de Lyon*	Directrice de thèse
RETHORE, Julien	Chargé de Recherches HDR /INSA de Lyon	Co-directeur de thèse
JOLY-POTTUZ, Lucile	*Maitre de conférence/INSA de Lyon*	Encadrante de thèse

INSA Direction de la Recherche - Ecoles Doctorales – Quinquennal 2011-2015

SIGLE	ECOLE DOCTORALE	NOM ET COORDONNEES DU RESPONSABLE
CHIMIE	**CHIMIE DE LYON** http://www.edchimie-lyon.fr Sec : Renée EL MELHEM Bat Blaise Pascal 3^{e} etage 04 72 43 80 46 Insa : R. GOURDON secretariat@edchimie-lyon.fr	M. Jean Marc LANCELIN Université de Lyon – Collège Doctoral Bât ESCPE 43 bd du 11 novembre 1918 69622 VILLEURBANNE Cedex Tél : 04.72.43 13 95 directeur@edchimie-lyon.fr
E.E.A.	**ELECTRONIQUE, ELECTROTECHNIQUE, AUTOMATIQUE** http://edeea.ec-lyon.fr Sec : M.C. HAVGOUDOUKIAN Ecole-doctorale.eea@ec-lyon.fr	M. Gérard SCORLETTI Ecole Centrale de Lyon 36 avenue Guy de Collongue 69134 ECULLY Tél : 04.72.18 60.97 Fax : 04 78 43 37 17 Gerard.scorletti@ec-lyon.fr
E2M2	EVOLUTION, ECOSYSTEME, MICROBIOLOGIE, MODELISATION http://e2m2.universite-lyon.fr Sec : Bat Atrium- UCB Lyon 1 04.72.44.83.62 Insa : S. REVERCHON secretariat.e2m2@univ-lyon.fr	M. Fabrice CORDEY Laboratoire de Géologie de Lyon Université Claude Bernard Lyon 1 Bât Géode – Bureau 225 43 bd du 11 novembre 1918 69622 VILLEURBANNE Cédex Tél : 04.72.44.83.74 Sylvie.reverchon-pescheux@insa-lyon.fr fabrice.cordey@univ-lyon1.fr
EDISS	**INTERDISCIPLINAIRE SCIENCES-SANTE** http://www.ediss-lyon.fr Sec : Bat Atrium – UCB Lyon 1 04 72 44 83 62 Insa : secretariat.ediss@univ-lyon1.fr	Mme Emmanuelle CANET-SOULAS INSERM U1060, CarMeN lab, Univ. Lyon 1 Bâtiment IMBL 11 avenue Jean Capelle INSA de Lyon 696621 Villeurbanne Tél : 04.72.11.90.13 Emmanuelle.canet@univ-lyon1.fr
INFOMATHS	INFORMATIQUE ET MATHEMATIQUES http://infomaths.univ-lyon1.fr Sec :Renée EL MELHEM Bat Blaise Pascal 3^{e} etage infomaths@univ-lyon1.fr	Mme Sylvie CALABRETTO LIRIS – INSA de Lyon Bat Blaise Pascal 7 avenue Jean Capelle 69622 VILLEURBANNE Cedex Tél : 04.72. 43. 80. 46 Fax 04 72 43 16 87 Sylvie.calabretto@insa-lyon.fr
Matériaux	MATERIAUX DE LYON http://ed34.universite-lyon.fr Sec : M. LABOUNE-DAHMANI PM : 71.70 –Fax : 87.12 Bat. Direction 1er et. Ed.materiaux@insa-lyon.fr	M. Jean-Yves BUFFIERE INSA de Lyon MATEIS Bâtiment Saint Exupéry 7 avenue Jean Capelle 69621 VILLEURBANNE Cedex Tél : 04.72.43 71.70 Fax 04 72 43 85 28 Ed.materiaux@insa-lyon.fr
MEGA	**MECANIQUE, ENERGETIQUE, GENIE CIVIL, ACOUSTIQUE** http://mega.universite-lyon.fr Sec : M. LABOUNE PM : 71.70 –Fax : 87.12 Bat. Direction 1er et. mega@insa-lyon.fr	M. Philippe BOISSE INSA de Lyon Laboratoire LAMCOS Bâtiment Jacquard 25 bis avenue Jean Capelle 69621 VILLEURBANNE Cedex Tél : 04.72 .43.71.70 Fax : 04 72 43 72 37 Philippe.boisse@insa-lyon.fr
ScSo	**ScSo*** http://recherche.univ-lyon2.fr/scso/ Sec : Viviane POLSINELLI Brigitte DUBOIS Insa : J.Y. TOUSSAINT viviane.polsinelli@univ-lyon2.fr	Mme Isabelle VON BUELTZINGLOEWEN Université Lyon 2 86 rue Pasteur 69365 LYON Cedex 07 Tél : 04.78.77.23.86 Fax : 04.37.28.04.48 isavonb@dbmail.com

*ScSo : Histoire, Géographie, Aménagement, Urbanisme, Archéologie, Science politique, Sociologie, Anthropologie

ACKNOWLEDGMENTS

First, I would like to thank the members of the jury who accepted to exmainate this PhD work. I would like to thank Marc LEGROS and Cristophe TROMAS for reporting this manuscript and Jérôme CHEVALIER, Denis MACHON and Alexander EGGEMAN for examinating it.

I would like to thank my superviors Karine MASENELLI-VARLOT, Julien RETHORE and Lucile JOLY-POTTUZ for their guidance, advices and encouragemet during the three years of this PhD. I would like to thank them for always finding time for their PhD student and for always being there to overpass together all the challenges we had to face during this PhD. I have learnt a lot from them, from their patience and wisdom. It has been a pleasure to work with them.

Second and foremost, I would like to thank Claude ESNOUF, for his guidance that shaped this PhD work. I would like to express my gratitude for him, for long hours of discussions on theoretical and practical principles in Transmission Electron Microcscopy. I have learned a lot from him. I would like to thank him for different methods of analysis of TEM images he taught me (dislcoations analysis, crystallographic indexation among many others using different softwares for such analysis). I had the chance to work with him and it has been a privilige to work with a person like Claude ESNOUF.

I would like to thank Jerôme CHEVALIER for following this PhD work and participating in different meetings and discussions that provided the best continuity of this PhD work.

I would like to thank Jonathan AMODEO for performing Molecular Dynamics simulations in a collaboration work with him and for long discussions on plasticity and dislocations processes in Magnesium Oxide.

These Acknowledgements would not be complete without appreciating persons I worked with in MATEIS laboratory like Thierry DOUIILLARD for thin foils preaprations by FIB and training on the TEM with Annie MALCHERE. I would like to thank both of them. I would like also to thank Vincent GARNIER and Yves JORAND from Ceramic Team in MATEIS

for participating in meetings concerned with work performed on transition Alumina as well as Denis MACHON and Sylvie LEFLOCH (From ILM- University Lyon 1 in a collaboration work). I would like also to thank Julien MORTHOMAS for participating in meetings concerned with works on MD simulations and Magnesium Oxide.

I would like to thank persons I am glad that I have met in MATEIS and encouraged me all over the three years like Sandrine GONNET, Emilie CALVIE, Thierry EPICIER, Lucian ROIBAN, Sophie CAZOTTES, Philippe STEYER, Cyril LANGLOIS, Alexandra PODGOURSKAIA and Bérangère LESAINT. I will never forget the PhD students and friends with whom I have shared offices like Mohamed, Hui, Serjiu, and Sid.

My deepest appreciation belongs to my family. My mother Fadwa, my father Ahmad, my brothers Amine and Ayman, my sister in law Daniella and my best friend Nour. I would like to thank them all, for their motivation, patience and support in everything in my life and especially during these three years of Phd. Their support means a lot and makes always the difference. I would like to thank as well all my friends, especially Jamal and Ali, whose support and encouragments always contribute to the good motivation.

Résumé

Les matériaux micro- et nanométriques comme les fils, les films minces, les piliers et les particules ont suscité un intérêt considérable ces dernières années dû à leurs surprenantes propriétés mécaniques. Ces systèmes montrent une limite d'élasticité bien supérieure à celle des matériaux massifs et une grande déformation plastique. À l'origine de ce comportement, plusieurs mécanismes potentiels sont proposés comme la nucléation de dislocations en surface, la troncation ou encore l'appauvrissement des sources actives. De plus, la nature même des mécanismes peut devenir dépendante de la taille.

La majeure partie des études récentes sur les nano-objets a été dédiée aux métaux cubiques à faces centrées. Ce n'est que dernièrement que davantage de travaux ont visé les métaux cubiques centrés, hexagonaux ou les alliages complexes. Quelques travaux expérimentaux, sur des nanoparticules d'alumine de transition, ont montré que ces céramiques classiques, bien que réputées pour leur caractère fragile sous leur forme massive, présentaient des propriétés mécaniques comparables (notamment en terme de ductilité) à celles des métaux aux petites échelles. Une meilleure appréhension des processus mécaniques, qui agissent aux petites échelles dans ces matériaux, permettrait d'optimiser leur mise en forme et d'adapter leur utilisation.

Dans cette étude, nous proposons d'utiliser la compression *in situ* dans le MET afin de caractériser les propriétés mécaniques de nanoparticules céramiques dont la taille caractéristique est de l'ordre de quelques dizaines de nanomètres. Nous appliquerons cette méthode à des nanocubes monocristallins de MgO, une céramique modèle dont la plasticité est bien connue dans le matériau massif. Les essais de nanocompression montrent que les nanocubes de MgO se déforment de façon homogène jusqu'à de grandes déformations (>50%) sans fissure apparente. L'analyse des résultats est assistée par des méthodes de corrélation d'images numériques et simulations de type dynamique moléculaire. Le mécanisme de déformation est identifié.

En outre, une étude statistique sur des nanocubes compressés *in situ* dans le MET montrent l'effet de taille sur la limite élastique des cubes dans une gamme de taille [62 nm-450 nm]. La limite élastique d'un cube de 62 nm est trouvée 60 fois plus grande que celle du MgO monocristallin massif et correspond à 1/10 de la contrainte de cisaillement résolue théorique.

Le faisceau d'électrons a montré dans des études sur des matériaux cristallins et amorphes un effet sur les propriétés élastiques et plastiques étudié de ces matériaux. Ici nous présentons

également cet effet du faisceau sur la limite élastique des nanocubes de MgO, cristallins et ioniques.

Dans une deuxième partie de la thèse, nous présentons une étude sur des nanoparticules d’alumine de transition compactée en CED (Cellule à Enclumes en Diamant) à température ambiante, sous plusieurs pressions (5 GPa, 15 GPa et 20 GPa). Des lames minces préparées par FIB ont été étudiées en MET. Des images HRTEM montrent une texture cristallographique qui devient plus importante à des pressions plus élevées. Une orientation cristallographique préférentielle est observée, avec les plans {220} de la phase gamma de l’alumine la plupart du temps parallèles à la surface de contact avec une particule voisine. Ce comportement mécanique est cohérent avec un système de glissement <110>{111}, connu pour les structures spinelles. Une corrélation de ce comportement avec les tests *in situ* MET réalisés sur des nanoparticules similaires, par Emilie Calvié lors de sa thèse, est présentée.
Enfin, des clichés de diffraction de type Debye Scherrer sont réalisés sur ces lames minces de nanoparticules d’alumine de transition compactées en CED à différentes pressions. L’analyse quasi-quantitative de ces clichés montre une transformation de phase de ces nanoparticules d’alumine de phase gamma en phase delta*, de manière croissante avec la pression.

Abstract

Nanometer-sized objects, such as micropillars, thin films and nanowires, are attracting large attention nowadays due to their breaking through mechanical properties such as high hardness, crack propagation resistance and high elastic limit in comparison to their bulk counterparts.

Moreover, these nano-objects exhibit large plastic deformation under high load. This was not expected for certain materials and especially for ceramics. A large number of studies nowadays are dedicated on plastic deformation of metals at the nano-scale, and few are reported on ceramics. The origin of this plastic deformation is still not very well defined. The mechanisms proposed are size dependent and correlated to different dislcoations processes as dislocations nucleation at surfaces and slipping on certain planes depending on the crystal orientation with respect to the solicitation direction and others.

In this study, we propose an innovative mechanical observation protocol of ceramics nanoparticles in the 100nm size range. This Protocol consists of *in situ* TEM nano-compression tests of isolated nanoparticles. Load–real displacements curves, obtained by Digital Image Correlation, are analyzed and these analyses are correlated with Molecular Dynamics simulations. By this protocol the deformation mechnaism is identified and the mechanical parameters (Young modulus, Yield stress...) of the studied material at the nano-scaleare obtained.

In situ TEM nano-compression tests on magnesium oxide nanocubes are performed. Magnesium oxide is a model material and its plasticity is very well known at bulk.

The MgO nanocubes show large plastic deformation, more than 50% of plastic strain without any fracture. The TEM results are correlated to MD simulations and the deformation mechanism can be identified. A strong size effect on the yield strength is observed. The smallest MgO nanocube yields at 3.09 GPa which is 60 times higher than the yield stress of bulk single crystal MgO (50 MPa) but only at 1/10 of the theoretical resolved shear strength. The effect of the electron beam on the yield strength is also investigated.

In a second part of the dissertation, we present a study on transition alumina nanoparticles compacted in a Diamond Anvil Cell at different uniaxial pressures. Thin Foils of these compacted nanoparticles are prepared by FIB for HRTEM Observations. Their analysis

reveals the plastic deformation of the nanoparticles. The crystallographic texture observed in these compacted nanoparticles in DAC shows a preferred orientation of the {110} lattice planes, orientated perpendicular to the compression direction. This is compatible with the {111} <110> slip system. This argument was reinforced with a preferred orientation of slip bands observed during *in situ* TEM nano-compression tests.

Moreover, electron diffraction patterns (Debye Scherrer) analysis on these compacted transition alumina nanoparticles reveals the decrease of the presence of gamma-alumina and the increase of delta-alumina with increasing pressure. This reveals the phase transformation with increasing pressure from gamma to delta* alumina.

Table of Contents

CHAPTER3: RESULTS ON IN SITU TEM NANOCOMPRESSION OF MAGNESIUM OXIDE NANOCUBES *113*

General Introduction

Single crystal nanoparticles have a long history and they are not necessarily produced only by using modern elaboration methods, but have obviously existed in nature for a long time.

However, the thorough fundamental works on nanoparticles physical properties go back to the 20th century when they were called ¨Ultrafine particles¨. It is from the 1990's that the name ¨nanoparticles¨ became fashionable and worldwide used.

Their strongly size-dependent properties offer uncountable opportunities for interesting discoveries. The often unexpected behavior and the high efficiency of their physical properties (thermal, electronic, magnetic, optical, mechanical...) with respect to their bulk counterparts, carry great potential for innovative technological applications. They are for example used in a wide range of applications, including Micro and Nano Electro-Mechanical Systems (MEMS, NEMS), catalysts for fuels, energetic materials as well as pharmaceutical drugs and biomedical ceramics with nanometer grain size, etc.… Properties of the nanoparticles can affect their performance either if they are end-products themselves, as in the case of quantum dots, or if they are used as base components, as in the case of polycrystalline ceramics.

Nanocrystalline ceramics (NC) (ceramics with grain size in the 100 nm range) are of a particular interest because of their high mechanical characteristics (high hardness, crack propagation resistance), which are better than their conventional polycrystalline counterparts [*Mayo et al.1993*]-[*Meyers et al. 2006*]. Due to their interesting mechanical properties, they are increasingly used in modern orthopedic surgery where they are employed as femoral heads or acetabular cups, in replacement of metallic alloys, to extend medical prosthesis lifetime. Their use indeed reduces wear rates and ion release, presumed to be responsible for inflammatory reactions [*Narayan et al. 2004*]-[*Chevalier et al. 2009*]. In this context, one way to enhance the mechanical properties of post-processed NC ceramics and thereby optimize their compaction and sintering processes is to improve the global understanding of the mechanics of single ceramic nanoparticle under load in real time.

The most highlighted and interesting mechanical property of materials that appears with downscaling effect is the higher strength that a materials gain when its volume decreases.

In the 20th century, the size effect on the strength of materials and especially on that of metals in the micron and sub-micron scale has become an attracted field for researchers. Hall [*Hall (1951)*] and Petch [*Petch (1953)*] works on thin films are the most famous initiation in this field. It was shown that the strength of pure metal or alloy thin film scales inversely to its thickness or grains size. Tensile experiments carried out by Brenner on iron, copper and silver whiskers, in the late 50's [*Brenner (1956)]*, demonstrated that the whisker strength increases as the whisker diameter decreases, as shown in *Figure 1*-a. It was also found that small whiskers could have a very high strength, comparable to the theoretical strength which is, of course, far higher than the bulk strength of the same material.

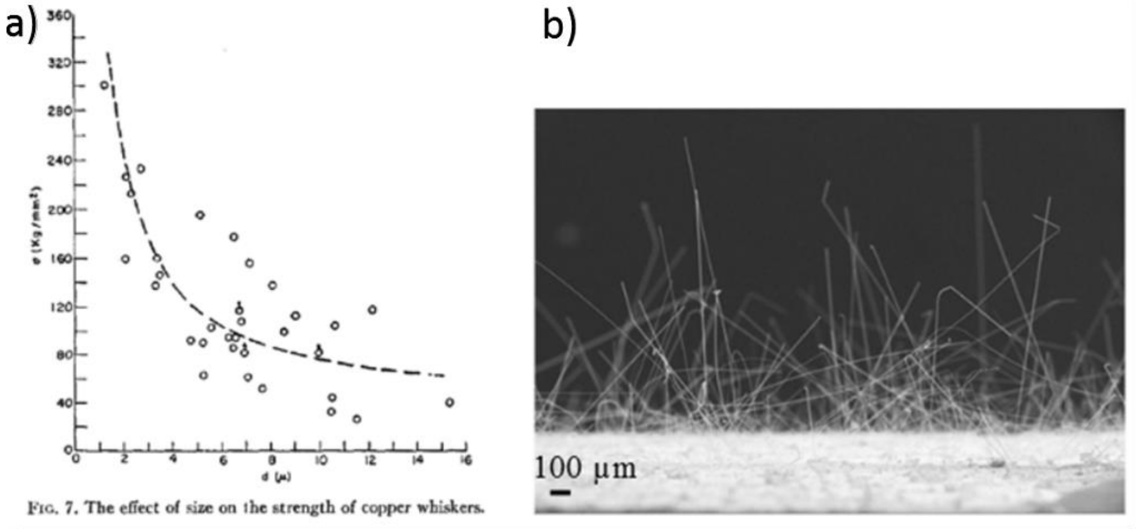

Figure 1: *Brenner works on iron Whiskers [Brenner-1956]. a) Size effect on the yield strength observed in copper whiskers in the micron and sub-microscale b) SEM image of whiskers.*

Beside the higher yield strength the materials exhibit at the micron and sub-micron scale, large plastic behaviors are generally observed before failure or fracture. Since these works, a huge number of papers have been published. The main interest of such research studies lies in the investigation of the origin of plastic deformation that leads to such size effect on strength, and the determination of the deformation mechanisms. The mechanical testing techniques used are numerous and vary from micro/nanoindentation on surfaces or thin films, to tensile, compression and bending tests applied on whiskers, nanowires, micro/nanopillars, and micro/nanoparticles. SEM (Scanning electron microscope) and TEM (Transmission Electron Microscope) studies on post-mortem samples provide also numerous pieces of information, especially when the deformation mechanisms involve dislocations.

An important progress in mechanical testing of materials at the micron and the sub-micron scale was the development of ***in situ* nanoindentation in SEM**: in 1968, Gane and Bowden [*Gane-Bowden 1968]* published indentation experiments on gold, copper and aluminum surfaces *in situ* in SEM, ***Figure 2***.

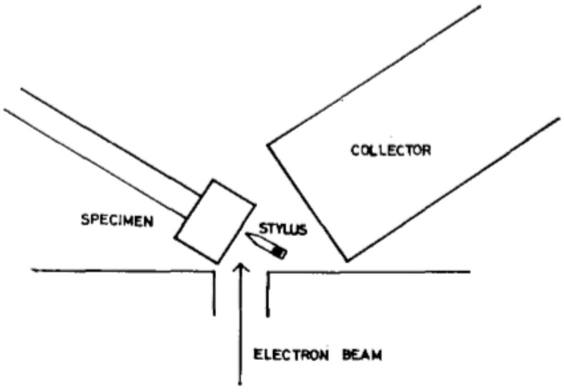

FIG. 1. Schematic arrangement for placing a fine stylus on to a surface in a scanning electron microscope.

Figure 2: *Gane Bowden in situ SEM setup from surfaces nanoindentation [Gane-Bowden 1968]*

With the development of *in situ* nanoindentation inside SEM, direct observations of the materials behavior under deformation could be obtained and measurements of depths and deformed volumes could be corrected and correlated to force-displacements curves.

With developments in the Focused Ion Beam (FIB) field, single crystalline micropillars milled from bulk material could be obtained and the ***ex situ* micro-compression tests** of single crystalline materials arise since works of Uchic et al. [*Uchic et al.2003*][*Uchic et al.2004*]. ***In situ*** mechanical tests in **SEM** arise later with developments made in setups for such experiments.

***In situ* mechanical testing in TEM** was first introduced by Gane [*N. Gane (1970)*] [*N. Gane 1972*]. Later on many works have treated deformation of crystal materials *in situ* in TEM but however developments in the field NEMS/MEMS devices have contributed to the appearance of TEM sample holders dedicated to *in situ* TEM mechanical testing. Qualitative ***In situ* mechanical tests in TEM** [*Wall M.A et al.1998*] was developed in the 1990's. Observation of dislocations processes in material during deformation in real time has been possible since A. Minor and co-authors first published quantitative *in situ* nano-indentation experiments inside a TEM in 2006 [*Minor-et al.2006*]. This technique has since gained interest because it permits a direct observation of the dynamics and dislocation processes controlling the deformation behavior of materials. Many research studies on plasticity mechanisms have been revisited after introducing the *in situ* TEM mechanical tests as an accurate qualitative as well as quantitative tool for studying mechanics of materials at the nanoscale including dislocations processes controlling deformation mechanisms. However this technique can only be used on thin section of bulk materials, nanopillars and nanoparticles. In the latter case, such tests can also be called ¨nanocompression¨ since it consists in loading in compression the particle between two plateaus.

Herein and as ceramic nanoparticles are concerned, one must mention that *In situ* mechanical testing in TEM is one of the most relevant tools to characterize the mechanical properties of such nano-objects and this is due to (i) mechanical parameters can be determined for nanoparticles of different sizes, in the 100 nm range; (ii) deformation mechanisms can be observed in real time, like for instance dislocations processes. Nevertheless, these experiments still have to be developed for different kinds of materials, and especially ceramics since few studies have been performed on ceramics, even though they seem to present a totally different behavior than at the macroscale.

Alumina based Nanocrystalline ceramics are one of the materials used for orthopedic applications. First experiments performed on alumina reveal its interesting properties at the nanoscale [*E. calvié 2012*]. However, the deformation mechanism may not be obvious since spherical alumina nanoparticles exist at the nanometer scale as transition alumina phases. Later phases do not exist at bulk and thus, their mechanical properties are not known. Since *In situ* TEM nanocompression is the most relevant existing tool nowadays to test mechanical properties of such nanoparticles, the mechanical protocol has to be validated in order to validate extracted mechanical parameters of transition alumina [*E. calvié 2014*].

In this context, **this PhD work consists of presenting** a quantitative observation protocol of mechanical properties of ceramics nanoparticles under load in real time. Thereby it is composed of two main parts:

- A first part presents quantitative *in situ* TEM uniaxial nanocompression tests performed on MgO nanocubes (model material and its mechanical properties are widely studied at bulk) and TEM observation analysis where deformation mechanism could be identified. This is coupled with MD molecular dynamics simulations (MD) performed in a collaborative work with Jonathan Amodeo and Julien Morthomas from the Team ¨ Metal¨ in the MATEIS laboratory. Moreover a statistical experimental study, performed on MgO nanocubes of different sizes [62 nm-450 nm] is presented. This study reveals the dependence of dislocations processes, substructure evolution and yield strength on the nanocube size. This is reinforced by observations in different TEM modes: Bright Field (BF), Dark Field (DF), and Weak Beam Dark Field (WBDF) TEM.

- A second part deals with TEM and High Resolution TEM observations on thin foils prepared from transition alumina nanoparticles compacted in a Diamond Anvil Cell (DAC) at room temperature under different pressures (5GPa, 15 GPa and 20GPa). This part is the continuation of *in situ* TEM tests on transition alumina of E. Calvié's PhD work. It will be used to investigate the possible deformation mechanism. Different TEM observations have been performed on these thin foils in order to investigate the presence of a possible crystalline texture induced by plastic deformation. Moreover, Electronic Diffraction patterns (Debye Scherer) are performed on these thin foils in order to quantitatively evaluate the evolution of possible phase transformation with increasing uniaxial pressure in DAC. A coupling of the behavior of these transition alumina nanoparticles compacted in DAC with the behavior of similar isolated nanoparticles tested in nanocompression *in situ* in TEM is also presented.

The dissertation is composed of five chapters:

Chapter1 Presents a bibliographic work on the evolution of nanocompression technique from ex-situ, *in situ* SEM to finally *in Situ* TEM. The size effect on the deformation mechanisms and yield strength of materials in the micron and sub-micron scale is presented. Different parameters (pre-existing dislocation densities, FIB damages...) affecting these two main aspects are discussed. Including Challenges with electron beam effect on the measured strength in *in situ* testing in electron microscopes.

Part A:

Chapter 2 presents the MgO nanocubes studied, and the development of the experiments and data processing made to fully to characterize the deformation mechanisms. MgO nanocubes are synthesized by two different techniques (microwave method or burning MgO in air). A full characterization is then performed by scanning and transmission electron microscopy coupled to EDX analyses to characterize the purity of the nanocubes and the possible presence of defects.

Chapter 3 describes the main results obtained on MgO nanocubes. Results obtained by *in situ* testing in TEM are compared to those obtained by MD simulations.

Moreover the size effect on the yield strength of MgO nanocubes is presented by a statistical experimental study performed on MgO nanocubes *in situ* in TEM of different sizes [62 nm-450 nm]. The electron beam effect on the yield strength of MgO nanocubes is presented.

Part B

Chapter 4 presents the alumina samples, the compaction processes of the powder by using a Diamond Anvil Cell (DAC) and the samples preparation by Focused Ion Beam (FIB).

Chapter 5 describes the main results obtained on the compaction powder (crystallographic texture and phase transformation).

Finally a **general conclusion** and perspectives are presented.

REFERENCES:

- **Brenner**, S. S. « Tensile Strength of Whiskers ». *Journal of Applied Physics* 27, nº 12 (1 décembre **1956**): 1484-91. doi:10.1063/1.1722294.
- **Calvié**, Emilie, Lucile Joly-Pottuz, Claude Esnouf, Philippe Clément, Vincent Garnier, Jérôme Chevalier, Yves Jorand, Annie Malchère, Thierry Epicier, et Karine Masenelli-Varlot. « Real time TEM observation of alumina ceramic nano-particles during compression ». *Journal of the European Ceramic Society* 32, nº 10 (août **2012**): 2067-71. doi:10.1016/j.jeurceramsoc.2012.02.029.
- **Calvié**, E., J. Réthoré, L. Joly-Pottuz, S. Meille, J. Chevalier, V. Garnier, Y. Jorand, et al. « Mechanical behavior law of ceramic nanoparticles from transmission electron microscopy in situ nano-compression tests ». *Materials Letters* 119 (15 mars **2014**): 107-10. doi:10.1016/j.matlet.2014.01.002.
- **Chevalier**, J., et L. Gremillard. « Ceramics for medical applications: A picture for the next 20 years ». *Journal of the European Ceramic Society*, Special Issue on Advanced MaterialsAdvanced Materials and Innovative Glass Melting Technologies, 29, nº 7 (avril **2009**): 1245-55. doi:10.1016/j.jeurceramsoc.2008.08.025.
- **Gane,** N. « Microdeformation of Solids ». *Journal of Applied Physics* 39, nº 3 (**1968**): 1432. doi:10.1063/1.1656376.
- **Gane, N. « The Compressive Strength of Sub-Micrometre Diameter Magnesium Oxide Crystals ». Philosophical Magazine 25, no 1 (janvier 1972): 25 34. doi:10.1080/14786437208229212.**
- **Gane, N. « The Direct Measurement of the Strength of Metals on a Sub-Micrometre Scale ». Proceedings of the Royal Society A: Mathematical, Physical and Engineering Sciences 317, no 1530 (23 juin 1970): 367 91. doi:10.1098/rspa.1970.0122.**
- **Hall,** E. O. « The Deformation and Ageing of Mild Steel: III Discussion of Results ». *Proceedings of the Physical Society. Section B* 64, nº 9 **(1951):** 747. doi:10.1088/0370-1301/64/9/303.
- **Mayo**, M. J., D. C. Hague, et D. -J. Chen. « Processing nanocrystalline ceramics for applications in superplasticity ». *Materials Science and Engineering: A* 166, nº 1-2 (15 juillet **1993**): 145-59. doi:10.1016/0921-5093(93)90318-9.
- **Meyers**, M. A., A. Mishra, et D. J. Benson. « Mechanical properties of nanocrystalline materials ». *Progress in Materials Science* 51, nº 4 (mai **2006**): 427-556. doi:10.1016/j.pmatsci.2005.08.003.
- **Minor**, Andrew M., S. A. Syed Asif, Zhiwei Shan, Eric A. Stach, Edward Cyrankowski, Thomas J. Wyrobek, et Oden L. Warren. « A new view of the onset of plasticity during the nanoindentation of aluminium ». *Nature Materials* 5, nº 9 (septembre **2006**): 697-702. doi:10.1038/nmat1714.
- **Narayan**, Roger J., Prashant N. Kumta, Charles Sfeir, Dong-Hyun Lee, Daiwon Choi, et Dana Olton. « Nanostructured Ceramics in Medical Devices: Applications and Prospects ». *JOM* 56, nº 10 (octobre **2004**): 38-43. doi:10.1007/s11837-004-0289-x.
- **Petch**. N.J « The cleavage strength of polycrystals». Journal of Iron Steel Inst. 174:25–28 (**1953**)
- **Uchic**, M. D. « Sample Dimensions Influence Strength and Crystal Plasticity ». *Science* 305, nº 5686 (13 août **2004**): 986-89. doi:10.1126/science.1098993
- **Uchic**, Michael D., Dennis M. Dimiduk, Jeffrey N. Florando, et William D. Nix. « Exploring specimen size effects in plastic deformation of Ni3(Al, Ta) ». In *Symposium BB – Defect Properties and Related Phenomena in Intermetallic Alloys*, Vol. 753. MRS Online Proceedings Library, **2003**. doi:10.1557/PROC-753-BB1.4.
- **Wall,** M. A., et U. Dahmen. « An in Situ Nanoindentation Specimen Holder for a High Voltage Transmission Electron Microscope ». *Microscopy Research and Technique* 42, nº 4 (15 août **1998**): 248-54. doi:10.1002/(SICI)1097-0029(19980915)42:4<248::AID-JEMT3>3.0.CO;2-M.

Chapter1

Micro/Nano-Compression & Featured Mechanical Properties at Small Scale

Fundamental understanding of plasticity at sub-micron scale is important because it provides useful pieces of information and design guidelines in many fields concerned with nano-objects as base components (electromechanical devices, NC ceramics..) or end components (quantum dots, …). Therefore many mechanical tests at small scale are introduced: nanoindentation techniques, tensile, bending and compression tests.

This PhD work provides first a fundamental understanding of mechanical properties of single crystal ceramic nanoparticles in the 100 nm range. It also presents a quantitative observation protocol for investigation of mechanical properties of ceramic nanoparticles under compressive load in real time (*in situ* in TEM). This can provide a better understanding of their mechanical behavior in order to optimize the compaction and sintering steps and therefore enhance mechanical properties of the final nano-crystalline ceramics.

In this context, this chapter provides at first place, a description restricted to the evolution of **compression techniques** of micron and sub-micron/nanometric **single crystals**. However, a few other mechanical tests developed for polycrystalline samples testing in the micron and sub-micron range may be mentioned, especially at the beginning while presenting the reasons for developing uniaxial micro/nanocompression tests of single crystal samples at small scale. Secondly, **featured mechanical properties** of single crystals at small scale will be presented.

1.1 Development of micro/ nanocompression technique

Many reasons were at the source of the first introduction, of a mechanical testing setup for single crystal samples in the micron and sub-microscale in 2003, by Uchic et al [*Uchic et al. (2003)*]. Tensile tests by Brenner on whiskers (single crystals) exist since the late 50's but not all metals or other materials can grow in whiskers form. Moreover, getting micron and sub-micron single crystals from the melt is impossible and the extraction of single crystal from bulk seemed a hard task before the introduction of the brilliant method by Uchic et al. in 2003.

Uchic et al. [*Uchic et al. (2003) (2004)*] introduced the first methodology: machine single crystal metallic micropillars in the micron scale using FIB (Focused Ion Beam) and perform a uniaxial micro-compression test using a conventional nanoindenter with an outfitted diamond flat tip. This opened the route to the investigation of the size effect in various single crystalline 3-dimentional micro and nano-objects as well as the study of their plastic behavior.

First, since the works from Hall [*Hall (1951)*] and Petch [*Petch (1953)*] on thin films, it has been known that a higher strength is obtained when decreasing the grain size of a polycrystalline materials and decreasing the sample size from bulk, in one dimension at least, to the micron and sub-microscale. One must mention here that micromechanical tests on **polycrystalline** samples have been widely developed. One can cite a few ones, like torsion of polycrystalline Cu wires [*N.A. fleck et al. (1994)*], bending tests on thin polycrystalline Ni foils [*J.S Stoklen et al. (1998)*] and further developed techniques like *in situ* TEM indentation on thin films [*A. Minor 2001*]. Many TEM works on postmortem samples have provided the description of most important dislocations processes controlled by grain size and interfaces. In general, dislocations motion is controlled by obstacles represented by grain boundaries. Thus, decreasing grain sizes means less space for dislocations to pile up and thus larger driving forces are required to move them to other grains in order to accommodate plastic deformation, as shown in ***Figure 3***. Thus larger stress is required before yielding and higher strengths can be achieved.

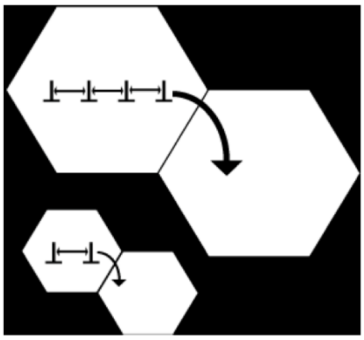

Figure 3: *a smaller grain size means less space for dislocations to pile up, leading to higher driving force required to move them to the next grain in order to accommodate plastic deformation*

According to this, one would not expect a size effect in single crystalline small structures that represents free surfaces. But the experiments from Brenner, on metallic whiskers in the late 50's, demonstrated that small whiskers (Copper, iron, and aluminum) [*Brenner (1956)*] can have very high strengths, comparable to the theoretical strengths. This was attributed to the fact that whiskers are dislocation-free. Therefore the yielding before their plastic deformation is controlled by dislocation nucleation, which occurs at stress higher than that needed to only enable their activation from pre-existing dislocation sources. However, dislocations exist also in microscale samples. But, according to the simple scheme shown in ***Figure 4*****,** smaller samples are expected to contain fewer dislocations for a given dislocation density and therefore higher strengths may be reached.

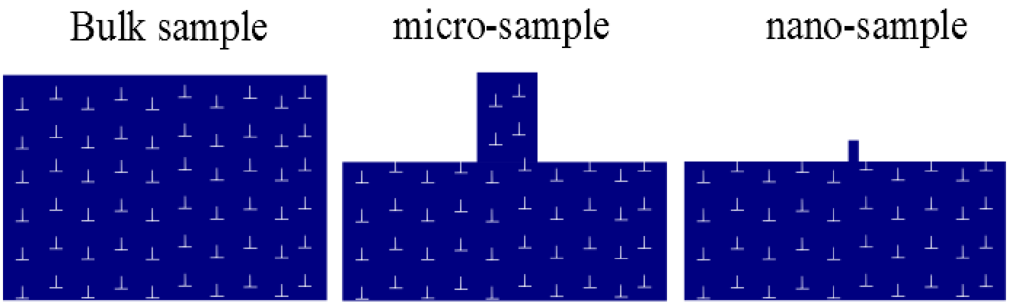

Figure 4: *Sample size versus dislocation population*

Moreover, in FCC (face centered cubic) metals, it is well known that at large plastic deformation, the dislocation substructure length is a few microns [*Uchic et al. (2005)*]. So there is a need to understand the dislocation evolution when the sample size approaches the dislocation substructure size.

Second, a uniaxial compression may offer an advantage over the well-known indentation tests on material surfaces, especially the anisotropic one. It is known that the volume and shape of the deformed material depends on the profile of the indenter tip (for example the Berkovich tip, often used) that causes activation of different sets of slip systems of different critical resolved shear stress. This poses ambiguity on data analysis often encountered in nanoindentation tests [*M Y Khan-(1992)*]-[*Lylod (2002)*] [*bouvier (2006)*]. Therefore the properties of an individual slip system cannot be measured. As a consequence, indentation may not be the most appropriate tool to test a target slip system in anisotropic materials.

Finally, microcompression suppresses fracture when material is made small enough [*Kendal (1978)*] [*Ostlund (2011)*]. It has been known since Kendall (1978), that making particles smaller increases the energy of a fracture nucleation and propagation. This was at the origin of understanding why there is a size limit for comminuting brittle nanoparticles by ball milling and other techniques to decrease nanoparticles sizes. Nowadays, fundamental works on observing and describing the increase of plastic strain before fracture in ceramic nanoparticles are available *[Calvié et al. 2014.][Issa et al. 2015*] (The work of this PhD). Therefore micro/ nanocompression is a powerful tool to study plasticity in brittle material.

Making single crystals and controlling their geometries are the main difficulties first encountered with mechanical testing at small scale. Among other difficulties like how to manipulate samples in such scale and align them correctly. Therefore the aid of microscopes, especially those who provide high resolution (electron microscopes) appears as an unavoidable tool.
Thus at first, fabricating a microcompression sample fixed at one end and applying a load upon it, seems easier than a tensile sample or other mechanical tests which requires more micromanipulation and sophisticated grip holder at such small scale.

As a consequence, the discussion below is restricted to compression of single crystalline three dimensional micron and sub-micron/nanosamples.

1.1.1 *Ex situ* microcompression

As mentioned previously, the first micro-compression experiments on single crystals were introduced by Uchic et al. in 2003 [*Uchic et al. (2003)*]. They developed a methodology to machine single crystal micropillars using Focused Ion Beam (FIB) (Two FIB approaches are used: FIB annulus milling and the ¨ion lathe¨ method [*Uchic et al. (2003)*] adapted for various types of materials. It consists in FIB milling pillars into the surface of a single crystal bulk material (Ni_3Al, in the cited work). The crystallographic orientation of the pillar can be selected and identified using back-reflection Laue x-ray diffraction. Pillars remain attached to the surface at one end which eliminates both the use of a manipulator and the pillar deposition onto a substrate for testing. Then, the pillar can be found with the optical microscope of the commercial outfitted nanoindenter, and the uniaxial compression test is performed. Imaging can be carried out by SEM after testing, as shown in ***Figure 5***-c. The corresponding sample dimensions are measured by SEM imaging before testing. The Berkovich-diamond tip is flatten, by FIB milling also, to fit a compression test on a micro-sample, as shown in ***Figure 5***-a&b.

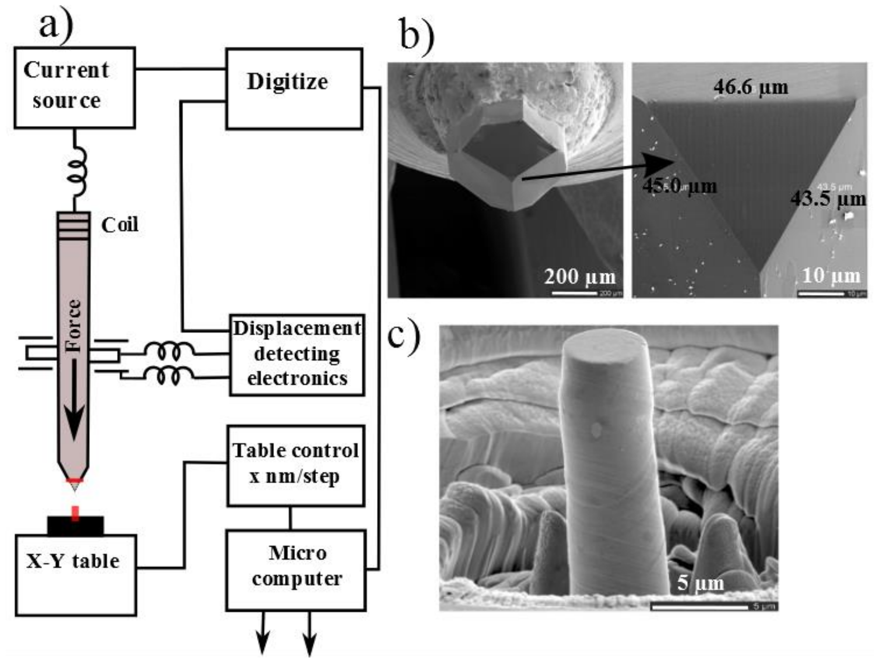

Figure 5: a) *ex situ microcompression setup: Nanoindenter: black-colored-part / (Modifications: red-colored-part for microcompression tests) [Page- 1992].* ***b)*** *Flatten tip by FIB.* ***c)*** *SEM image of a micropillar after testing [Uchic-2003].*

Many other researchers inspired by their work and performed *ex situ* micro-compression tests on different other materials, see for instance [*Greer et al. (2005)*] [*Volkert et al. (2006)*].

The nanoindentation systems used for *ex situ* microcompression tests are usually commercial ones. However, pioneer tests [*Uchic et al. (2003)*] used the conventional nanoindenter, shown in ***Figure 5*** [*Nanoindenter: black-colored-part / (Modifications: red-colored-part for* *microcompression tests)*]. This apparatus was designed to perform low-load depth-sensing microcompression tests and to produce load-displacements curves converted to stress-stain curves with microstrain and submegapascal resolution suited for micro-samples. In this apparatus, the movement of the flat tip is ensured by a coil and magnet assembly. The force (load) is controlled by the current in the coil and its resolution is of sub-micron Newton. Displacements are measured by a capacitive displacement sensor (in which the value of the capacitance is proportional to the distance between the capacitor plates) with a sub-nanometer resolution. The flat diamond tip can be commercial as the one used in [*Volkert et al. (2006)*] or flatten by FIB as in [*Greer et al. (2005)*][*Uchic et al. (2003)(2004)(2005)*]. This apparatus enables micro-compression tests where a maximum load is controlled (voice coil) and displacements are read (capacitive displacements sensor), thus are all load-controlled at constant load-rate, as used in [*Volkert et al. (2006)*]. However, they can be displacement-control by using a feedback loop that imposes a constant displacement rate by actively changing the loading via the voice coil, as used in [*Greer et al. (2005)*] or [*Uchic et al. (2003)(2004)(2005)*]. One must mention that some devices, for *in situ* SEM or TEM tests described below, are based on piezoelectric elements that actuate the tip or sample displacements. Load cells are introduced for force measurements. As a consequence, such devices are real displacement control setups, as the one used in [*Shade et al. (2009)*]. The main difference between both types of control (load or displacement) results in different stress-strain responses especially during plastic deformation events (strain bursts/stress-drops). This will be discussed in **section 1.2.** It also has to be mentioned that even when using a feedback loop, as mentioned above, to provide displacement-control tests from a naturally load-control test, the feedback loop does not control the tip displacements at large strain bursts. As a consequence, no data force is recorded during large strain bursts for given time and thus the associated stress-strain curves are not typical for displacement-control tests as mentioned in [*W.M Mook-2009*].

I. The most important features and advantages of *ex situ* tests

These experiments were at the origin of the notion ¨smaller is stronger¨ in single crystalline metals. For most of the studied single crystal micropillars (Ni_3Al) [*Uchic et al. (2003)*], Ni, Ni_3Al-Ta and Ni supperalloy [*Uchic et al. (2004)*], Ni supperalloy [*Uchic et al. (2005)*], Au micropillars [*Greer et al. (2005)*], Au columns [*Volkert et al. (2006)*]…), the yield stress was measured to be higher than that of their bulk counterparts. Moreover, smaller pillars showed higher strengths than pillars with larger diameters. Since then, the size effect on the yield strength in the micron and sub-microscale has drawn the attention of many researchers. All of them try to describe the size effect using the following power-fit law:

$$\sigma_y \sim A d^{-x} + \sigma_0$$

where σ_y is the yield stress, d is the sample diameter or size, σ_0 is the yield stress of the material at bulk, A is a fitting constant and x is the power-law fit constant. ***Figure 6***-a show an example on gold columns, from Volkert et al. [*Volkert et al. (2006)*].

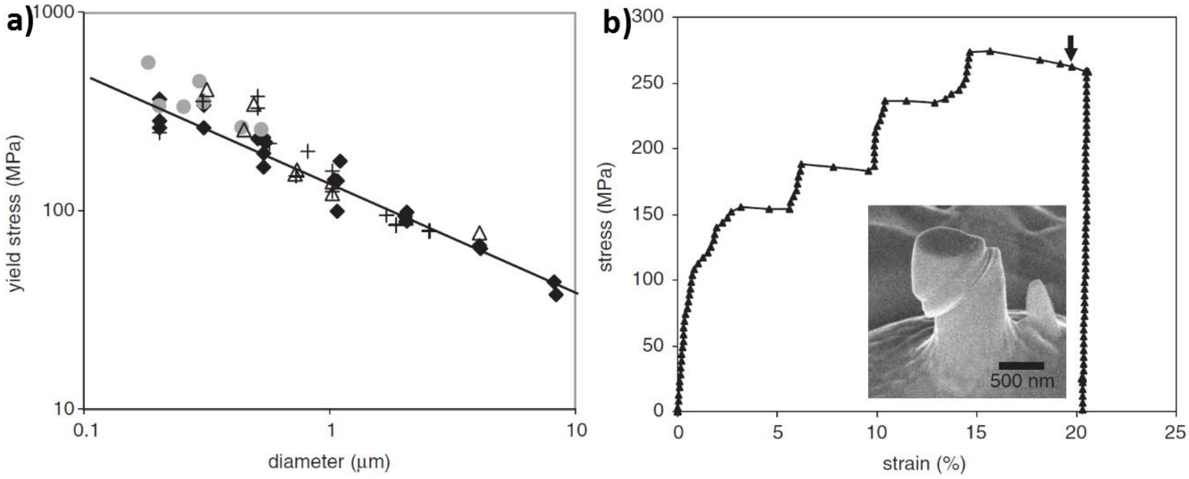

***Figure 6 a)** Volkert et al. results on the effect of the size on the yield strength of gold columns **b)** stress-strain curve in a load-control test. Inset: post-mortem SEM image on a gold column [Volkert et al. (2006)].*

Another important feature is the stress-strain response which shows stress-drops (displacement-control test) or strain bursts (load-control-test) that are not usually observed in stress-strain response of bulk materials. An example is given in ***Figure 6***-b. These stress drops are attributed to dislocations activities. More details will be available in **section 1.2** while discussing the effect of the size on the magnitude of these strain bursts or stress drops.

Traces of dislocation activities, especially possible active slip systems, could be observed by SEM imaging on post-mortem samples. Slip traces could be analyzed with respect to the known pillar orientation, see Figure 7-a&b, especially when pillars are oriented for single slip, as shown in Figure 7-a.

Moreover, due to simple requirements for these ex-situ micro-compression tests, one can machine many micropillars on the surface of the single crystal bulk and locate them easily under the optical microscope of the nanoindenter. For this purpose, large cavities are usually made to easily locate pillars; under the optical microscope of the nanoindenter as shown in ***Figure 7***-c. The large number of pillars facilitates statistical studies.

Many other methods for the fabrication of single crystal micron and sub-micron objects (cubic shape, rectangular cylinders or pillars & others…) are nowadays introduced. One can cite lithography based fabrication method followed by annealing, to produce single crystal gold micropillars shown in ***Figure 7***-d [*Greer et al. (2005)*], solid state dewetting [*Mordehai et al. (2011)*], directional solidification [*Bei et al. (2007)*], physical vapor deposition [*Richter et al. (2009)*], and direct nanoimprinting or embossing [*Buzzi et al. (2009)*]. The existence of other fabrication techniques allows the investigation of the mechanical properties modification due to irradiation damage by FIB.

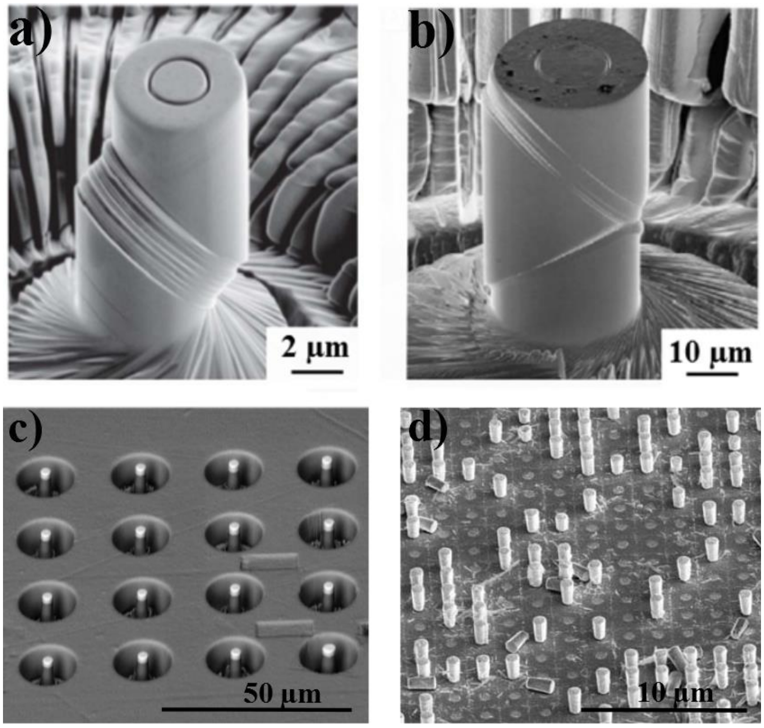

Figure 7: a-b) *slip traces could be observed in SEM images on postmortem samples and analyzed with respect to the known single crystal pillar orientation [Uchic et al. (2004)]-[Uchic et al.(2005)]* ***c)*** *Many micropillars can be machined on the bulk surface, facilitating statistical studies.* ***d)*** *Single crystal gold micropillars fabricated by lithography based method followed by annealing [Greer et al. (2005)].*

II. Main drawbacks of *ex situ* tests

The main drawback encountered with many of these *ex situ* tests lies in the fact that different elastic loading slopes can be obtained, leading to different values of the Young modulus. An example is shown in ***Figure 8***-a&b. However for most of the tests, the unloading curves show often similar elastic slopes.

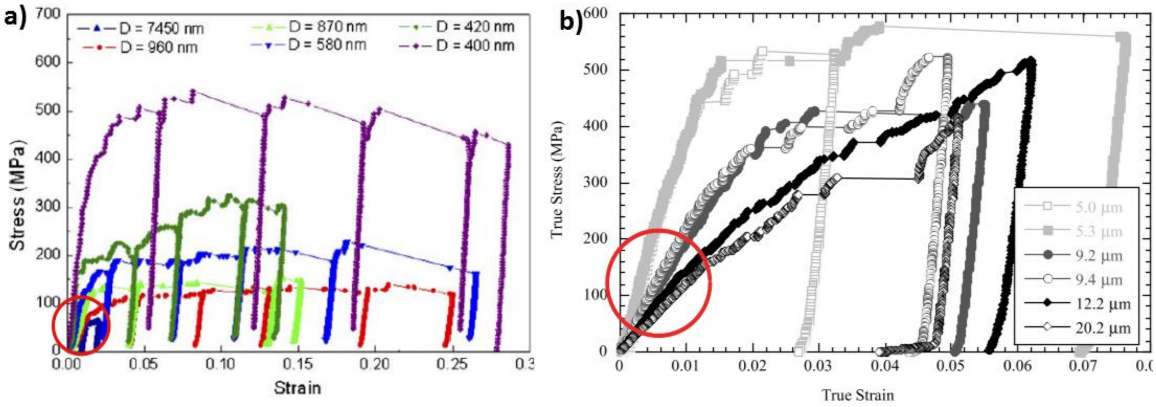

Figure 8:* *a-b) *different elastic loading slope [Greer et al (2005)] [Uchic et al. (2003)]*

This is attributed to a misalignment between the sample surface and the tip surface. This misalignment issue is well discussed in the literature [*Zhang et al. (2006)*]-[*Y.S. Choi et al. 2007*]. It induces a not perfect uniaxial microcompression during initial loading. This induces stress localization, non-uniform plastic deformation and non-accurate measurements when calculating the critical resolved shear stress of a target slip system for example.

Uchic *et al.* [Uchic *et al (2005)*] improved the alignment between the tip and the sample, for such *ex situ* microcompression tests. They used a miniature goniometer that allows small changes in the orientation of the bulk sample to minimize the misalignment between the tip and the micro-sample. However, this still does not always provide a perfect alignment at the nanometer scale.

Moreover, SEM observations on post-mortem deformed samples permits the analysis of slip traces, and the identification of the expected slip systems. However, no direct observation of the sample behavior under load is possible. Thus no possible correlation can be drawn in time and space between the sample behavior at initial plastic deformation and its behavior at strain bursts (or stress drops). Both drawbacks complicate the interpretation of the stress-strain curves and poses ambiguity on the results. Moreover, such tests do not provide accurate information on the deformation mechanism responsible for the observed size effects.

The *in situ* SEM micro-compression appears as a tool that may correct the misalignments problems and correlate more accurately the sample deformation in real time to possible and observable plastic events at stress drops (or strain bursts).

1.1.2 *In situ* SEM micro-compression

In situ SEM micro-compression is possible thanks to the large SEM chamber. However the main challenges include the vacuum environment, electron irradiation during the test. However modifications of the setup have been made, as shown in ***Figure 9***-a&b. These modifications include its configuration, position and inclination (~ 90° from the incident beam). This permits to let the incident electrons reach the surface of interest (flat tip and micro/sub-microsample to compress) and to let secondary electrons (or other signals resulting from electron-matter interactions) coming from these surfaces to reach the secondary electrons detector (or other detectors) in the SEM. One must mention that *in situ* SEM, nanoindentation has been developed since the indentation works of N. Gane et al. *[Gane-Bowden et al. (1968)*]. However, more accurate devices for *in situ* quantitative micromechanical testing (microcompression, tension, bending…) in SEM exist nowadays. Some are built by research groups and some others are custom-built commercial devices [*kiener et al. (2006)*]-[*Michler et al.(2007)*]-[*Mook et al. (2009)*]-[*Gianola et al. (2011)*]-[*Shade et al. (2009)*]-[*Romeis et al.(2012)*].

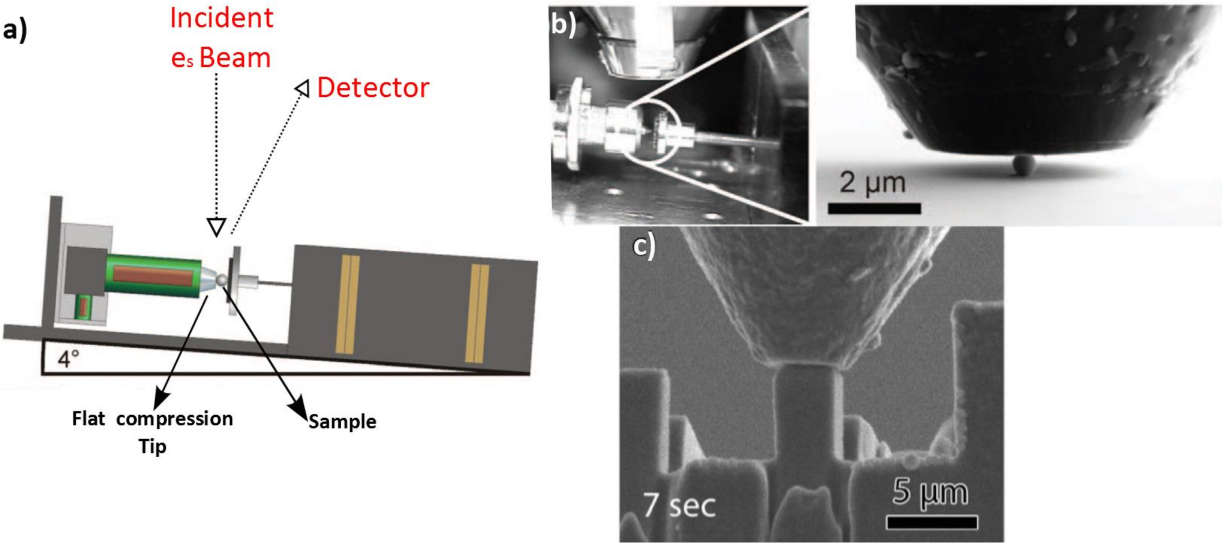

***Figure 9** a) in Situ SEM setup general configuration with respect to the incident electron bean and secondary electron detector [Romeis et al. (2012)] **b)** in situ SEM microcompression of gold nanoparticle [romeis et al. (2012)] **c)** in situ SEM microcompression [Minor et al. (2014)]*

Concerning *in situ* SEM microcompression, some devices are based on parallel-plate transducers for force actuation and capacitive displacement sensing providing a load control, and use a feedback loop [*W.M Mook et al. (2009)*] [*Rzepiejewska et al. (2008)*]. Other devices include piezoelectric actuators for sample or tip displacements and provide subnanometer displacement control. They also include a strain-gauge-based load cell [*Shade et al. (2009)*] or different types of load cells for force measurements. An Attocube piezoelectric is usually used, based on stick-slip motion, x-y-z positioning stage, which enables a precise positioning of the sample under the flat tip and provide their proper alignment. The force resolution depends on each device but it can reach a few tens of nN in some devices [*Romeis et al (2012*)].

I. Main Features and advantages of *in situ* SEM microcompression tests

Due to the fact that a proper alignment of the tip and the sample is feasible by *in situ* SEM at the nanometer scale, as shown in *Figure 9*-b&c, accurate measurements of yield stress and so accurate calculations of critical resolved shear stress on slip systems can be done.

A huge number of studies have been performed *in situ* SEM microcompression tests on various materials structures. The **main feature** is the size effect on the yield strength. This inspired some research groups to investigate if a unique x (the power-law fit constant) exists for each structure group (FCC, or BCC, hard materials…). Different ways of plotting data to show this size effect have been proposed by Uchic et al. [*Uchic et al. (2009)*] and Dou & Derby [*Dou-Derby (2009)*]. This will also be presented in **section 1.2.**

Much geometry and freestanding nanostructures, other than the one-end-attached micropillars, have been tested: one can cite for instance freestanding Ni_3Alcubic nanoparticles [*Maaß et al. Small 2012*] and gold spherical nanoparticles [*Romeis et al. (2012*)], shown in ***Figure 9***.

The main advantage of *in situ* SEM microcompression tests is that different SEM imaging modes can be used during the tests. First, the secondary electron mode enables surface observations in real time, as those shown in ***Figure 9***-b&c. It allows monitoring a proper alignment at the nanometer scale of the tip and the sample. It also allows measurements of the sample lateral and longitudinal dimensions by the use of image analysis methods and so the determination of true stress- true strain curves. Besides, it enables the correlation of the sample behavior at the onset of plasticity and during plastic events that often appear in the stress-strain curve at the micron and sub-microscale.

Other SEM imaging modes enable to detect many problems or challenges that may modify the mechanical behavior of the microsample during compression. For example, Electron

BackScattered Diffraction (EBSD) is often used to monitor the crystal orientation evolution in function of time during microcompression, as in these two works [*Kiener et al. (2008)*]-[*Shade et al. (2009)*]. Similarly, Laue X-ray diffraction has been performed *in situ* in this work [*Maaß et al. (2008)*], especially when studying the effect of ¨friction¨ between the flat tip and the flat surface of micropillars (due to the high stiffness of the compression punch). Such “friction” may indeed induce crystal rotation and hence buckling of pillars at their middle, and prevent possible single slip, as shown in ***Figure 10***-c.

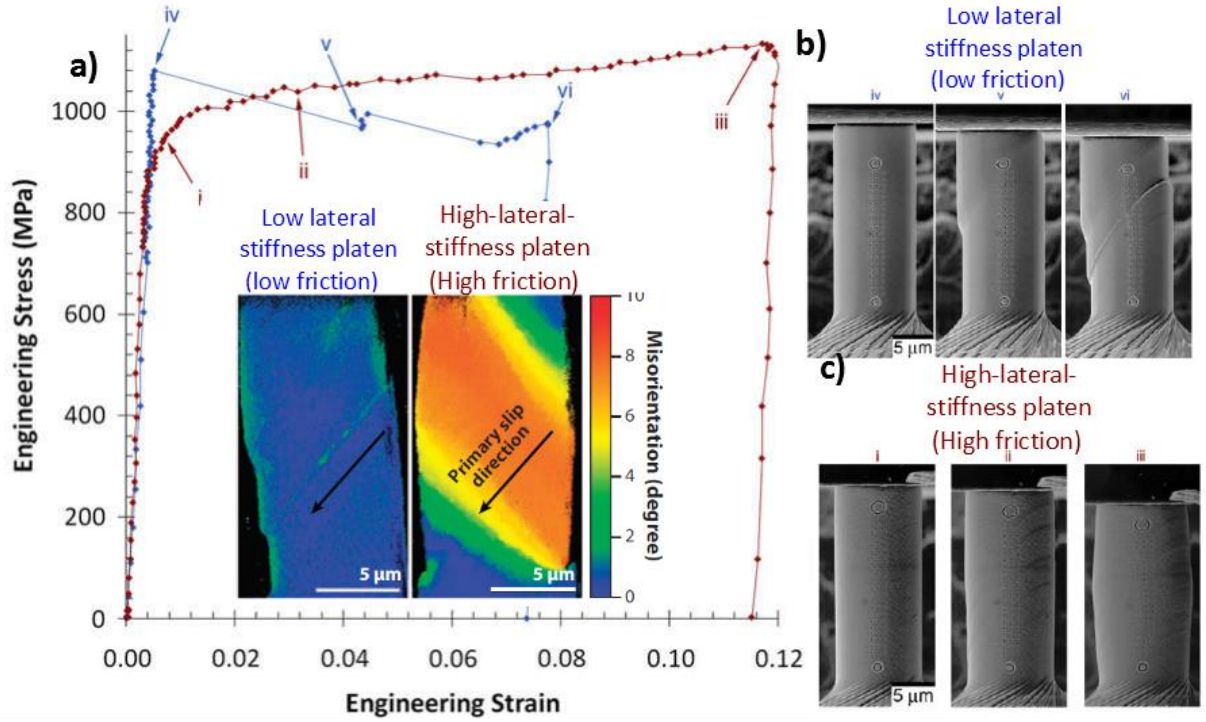

Figure 10:a) *Experimental stress-strain curves for two 10-µm-diameter Ni-based supperalloy microcrystals oriented for single slip, in which the lateral constraint has been varied significantly between the two experiments. This change has a clear effect on the stress-strain response and, for the highly constrained sample, results in significant internal crystal rotations as shown in the electron backscatter diffraction maps (inset).* ***b)*** *Three SEM images at various strain levels while a low lateral stiffness SiC platen.* ***c)*** *Three SEM images at various strain levels while using a high lateral stiffness diamond platen. [Shade et al.2009]*

This problem of high stiffness of the platen load is often encountered when testing micropillars or microsamples that are totally attached at one end to the bulk substrate. Moreover, it is thanks to *in situ* SEM tests that Shade et al. [*Shade et al. (2009*)] could FIB milled micropillars oriented for single slip and with FIB milling they made features lines of three lateral dots and track *in situ* the axial positional change of distinct features of interest as shown in ***Figure 10***-b-c. Also, by performing EBSD they could observe the crystal rotations shown in inset of ***Figure 10***-a when using a platen load of high lateral stiffness. However they could also observe a different behavior of the micropillars when using a platen load of low lateral stiffness, where single slip is observed and buckling is absent, see ***Figure 10***-b and inset in **Figure 10**-a. This different behaviors are also observed in stress-strain curves where strain bursts are observed instantaneously when a single slip is activated when using a low-lateral-stiffness platen, whereas no strain bursts are observed when crystal rotation occurs when using high-lateral-stiffness platen), see **Figure 10**-a.

Finally, *in situ* SEM tests do not demand sophisticated requirements, therefore statistical studies are possible, for example of the size effect, see **Figure 11**.

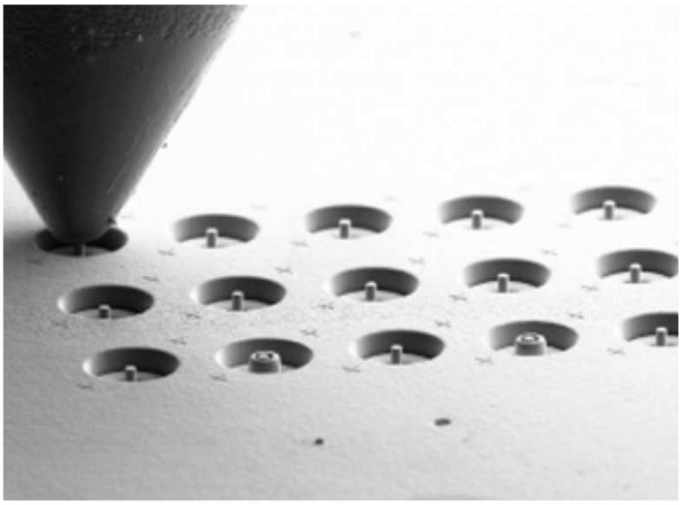

Figure 11: *Group of Micropillars ready to be indented for in situ mechanical testing. Each pillars is ~2 micrometers in diameter [from Experimental Micromechanical Characterization Research website-October-2015]*

II. Main challenges of *in situ* SEM microcompression tests

In SEM, the best imaging resolution can reach few nm. Thus there's possibility to detect dislocations at high magnification and low scanning speed. But in *in situ* tests, magnification is often kept low, especially that the view side must include the sample, the substrate and the tip to ensure their proper alignment and to monitor any buckling or other effects in the sample during the test. Moreover, decreasing the scanning speed too much may not offer an appropriate time resolution to follow the deformation behavior of the sample during the test. However, a dislocation observation has not been reported in *in situ* SEM tests.

Thus, any investigation of substructure evolution of dislocations or the sites of its nucleation and processes in the sample is not possible. The latter is a main issue to accurately describe plasticity and deformation mechanism at small scale.

Many researchers extracted thin sections from pillars by FIB milling, after *in situ* SEM microcompression [*Korte et al. (2011)*]. By TEM, they could analyze slip systems that controlled the plastic deformation, as shown in **Figure 12**-a.

Beside the effect on the mechanical behavior that FIB milling may induce due to Ga+ implantation and damage that adds defects on the surface layers of the sample during pillar fabrication, this technique of thin section extraction after compression may add more defects and may pose ambiguities on the defects analysis in TEM.

However, some studies mention sometimes that they could make the difference between dislocations already present in the sample (long segments of dislocations), small dislocation loops (small dark spots) induced by FIB damage during sample preparation before testing and dislocations that accompanied the deformation (short lines and curves near the slip system), as reported by Sun et al. [*Sun et al. (2011)*] (see ***Figure 12***-b).

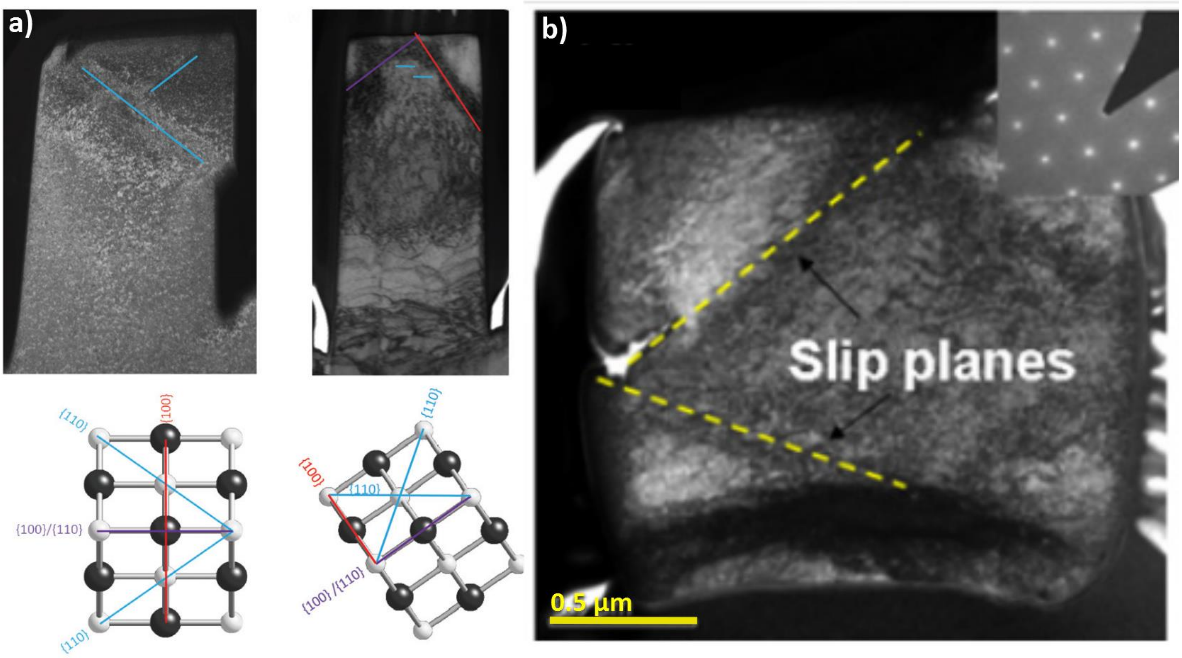

Figure 12: a) *TEM thin section obtained by FIB milling from MgO FIB milled micropillars [Korte et al. (2011)]* ***b)*** *Bright-field TEM image showing multiple dislocations in a 1 micron Titanium micropillar after testing [Sun et al. (2011)]*

These ambiguities disappear when compression tests are performed *in situ* in TEM. Indeed, it is possible to identify and categorize different deformation mechanisms from direct observation and correlation of the sample stress-strain response with spatial-temporal characterizations of dislocations substructure evolution and processes. However, samples smaller than 50 nm can be tested. Due to this smaller scale testing, *in situ* TEM compressions are often named *in situ* TEM nanocompression. They are presented in the following **section.**

1.1.3 *In situ* TEM nano-compression

I. Why TEM?

After what was mentioned previously, one can see that there are several needs that require carrying out nano-mechanical testing with direct observations and sub-nanometer/Angstrom (atomic) resolution characterizations (to enable dislocations observations), especially when deformation mechanisms are questioned.

Briefly, a TEM (operating at ~50 keV-300 keV) consists of a coherent electron beam passing through a thin enough specimen (few nm to few 100s of nm). The interactions between the incident electron beam and the specimen give rise to several signals, as shown in *Figure 13*. Due to the high energy of incident electrons, their wavelength is smaller than the atomic size thus providing their interactions.

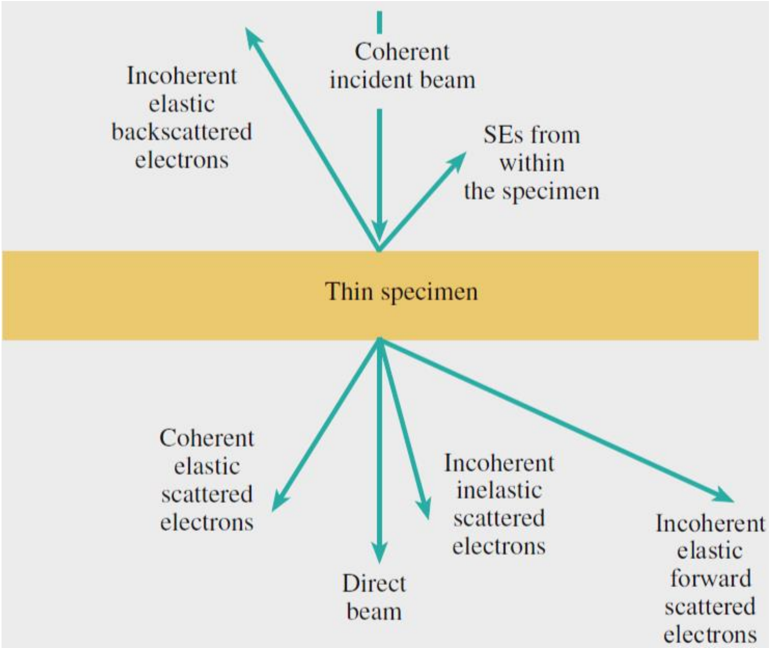

Figure 13: *Different kinds of electrons scattered or emitted by a thin specimen [Williams, David B., & C. Barry Carter. book]*

The electrons from the sample interact with the highly energetic incident electrons, causing their scattering (elastic scattering and inelastic scattering) through the crystal and provide information on the sample crystallographic structure and composition [*Williams, David B., et C. Barry Carter. book: Transmission Electron Microscopy; Chap.2*]. Various modes of observations in TEM that allow elemental and analytical characterizations are based on these scattered electrons. Some of these modes are used in this PhD work and will be presented in **Chapter 2**. The unscattered electrons (direct beam) are those that do not undergo any interaction with the crystal or the sample and thus represents the projection of the sample along the direction of the beam and are used to form Bright Field (BF) images. All these scattered and unscattered electrons pass through a series of EM lenses, and finally the image is formed on the image plane where a CCD (Charge Coupled Device) detector provide a digital image by the electrons at very high rate (it can reach ~ 400 frames/s). This represents a good temporal resolution and is another advantage for the TEM over other scanning microscopes (SEM, STM and AFM). Indeed in those scanning microscopes the resolution is inversely proportional to the scanning speed, which is related to the speed of formation of the digital image.

Thus TEM seems the best choice of microscopes for *in situ* mechanical testing of nanoscale samples, as it enables observations and characterizations of the crystal structure and crystal defects that pre-exist in the sample, and defects nucleated and/or activated during the deformation under load in ¨real time¨ (with a good temporal resolution).

II. Main challenges for setup

The most challenging step to carry out *in situ* mechanical testing in TEM arises first from the setup configuration and the size limitations due to the small volume available for sample holder in TEM.

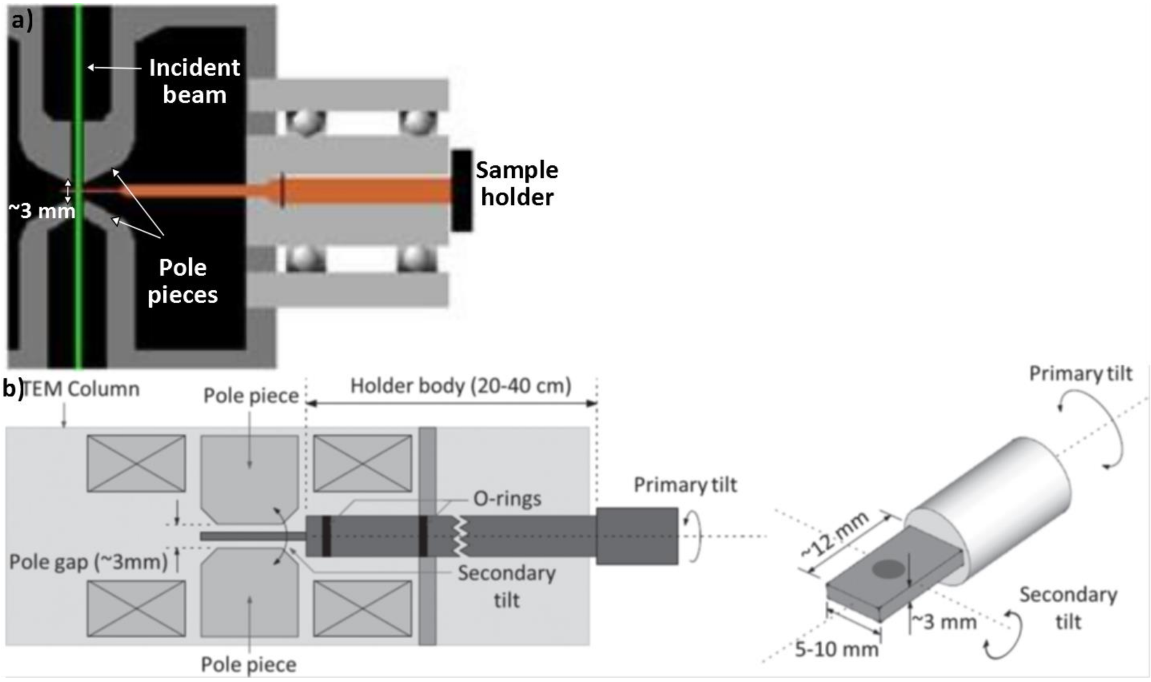

Figure 14 a) *Side view of the sample holder and the pole pieces in the TEM column* ***b)*** *Cross sectional view [H.D ESPINOSA et al. (2012)]*

The thickness of the end of the sample holder (sample or sample substrate, force sensor and transducer or end of a transducer) must fit a space that should not exceed ~3 mm because of the small gap between the pole pieces, as shown in *Figure 14*a-b [*Espinosa et al. (2012)*]. However, this gap between the pole pieces varies from a TEM to another. The two other dimensions of the setup must be less than ~ 15 mm, as shown in *Figure 14*-b. This makes tilting very sensitive and restricted to few degrees and thus makes diffraction conditions (orientation of specific planes in the beam direction), sometimes, impossible especially for sample holders designed for simple tilt. However some sample holders are double-tilt (primary and secondary tilt *Figure 14*-b, providing easier monitoring of the crystal reorientation in diffraction conditions but also the value of the second tilt remains limited also.

This makes *in situ* TEM setups for mechanical testing more complex and sophisticated, because all the setup components (sample, actuator, tip and force sensors) have very small dimensions. They are sometimes called “the lab on the chip”. The miniaturization of the main components of the setup were made possible with the technological advances in micro-actuators and MEMS /NEMS (Micro/Nano Electro-Mechanical-Systems) that provide accurate calibration and quantitative output data of the mechanical test (force-displacements) [*Haque et al. (2010)*]-[*Espinosa et al. (2012)*]-[*Legros et al. (2010)*].

III. Sample Holders for *in situ* TEM

The first setup for mechanical testing in TEM appeared in the 1970’s, when N. Gane, a pioneer in *in situ* SEM nanoindentation [*Gane et al. (1968)*], built a device from his previous works. He performed nanoindentation (loads) in TEM with a tungsten tip on gold surface by using a piezo bimorph actuator [*Gane (1970)*]. This was also used to perform uniaxial compression of single crystal MgO nanocubes [*Gane (1971)*] and sub-micron gold structures [*Gane (1970)*]. However, during these tests no images were recorded, only before and after.

Further developments in sample holders led to the use of piezoelectric elements for controlled motion, image acquisition in real time. However, it was not possible to record quantitative force data and thus the tests remained qualitative [*Stach et al. (2001)*] [*book: in-situ electron microscopy: applications in physics, chemistry & materials science-ch.11]*. Further improvements were made for *in situ* TEM sample holders, when Minor et al [*Minor et al. (2001)*]-[*Minor et al. (2002)*] introduced a piezo-ceramic actuator that controls the displacements of the tip (coarse and fine movements). For a given voltage–force–displacement characteristic of the piezo-ceramic actuator, the latter was also used to measure the force developed as a function of both voltage and displacement. Finally, the displacement was measured by direct observation in bright-field TEM, and the force was computed from the actuator characteristics after tests. As a consequence, this type of force-displacements measurements remains not accurate due to nonlinearities in the piezo responses [*book: in-situ electron microscopy: applications in physics, chemistry & materials science.ch.11*]-[*Minor et al. (2006)*].

Many technological advances in micro-actuators and miniaturization of different types of force sensors for *in situ* TEM holders have been developed and their basics description is available in [*Haque et al. (2010)*]-[*Espinosa et al. (2012)*]-[*Legros et al. (2010)*].

These advances result in TEM holders compatible for quantitative *in situ* nanoindentation tests on thin films, tensile tests, bending tests and nano-compression of nanopillars or nanowires attached to the bulk or on nanoparticles deposited on a substrate with specific characteristics (thickness, surface roughness, and material). Some sample holders are simple tilt and others are double tilt. As mentioned above, the latter is interesting for crystalline materials especially when a specific zone axis is to be brought to diffraction conditions.

Herein, we restrict the discussion to nanocompression tests, where a flat punch (tip), usually diamond, is used in a way that the sample deposited on a substrate or attached to a bulk substrate, sees two parallel plateaus. This enables performing uniaxial compression, as shown in ***Figure 15***-b (ex: compression of gold nanowire).

The Hysitron sample holder has been the first sample holder that enables *in situ* tests in TEM with quantitative acquisition of force-displacements data and images in real time [*Minor et al. (2006)*]. In this setup shown ***Figure 15***-a, a capacitive force sensor is incorporated behind the tip in order to measure forces. A piezo element is used only to impose coarse and fine movements of the tip with a micrometers and sub-Angstrom resolution respectively.

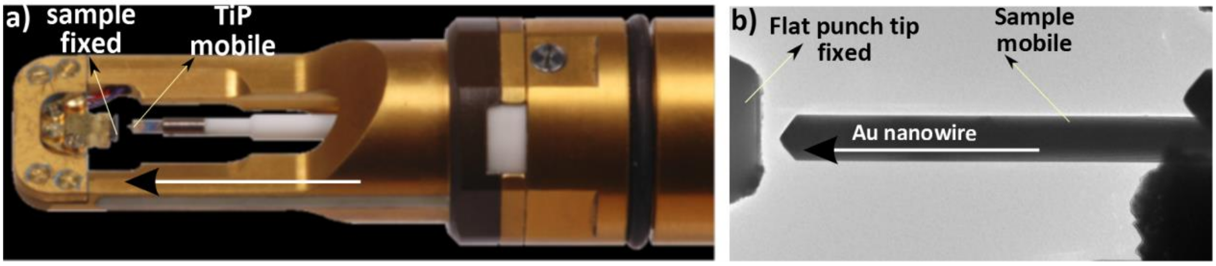

Figure 15 a) *Hysitron sample holder. The sample is fixed and the tip is actuated to move toward the sample. A capacitive force sensor is incorporated behind the tip* ***b)*** *in situ TEM nanocompression of gold nanowire using a sample holder from Nanofactory. The tip is fixed and the sample is moved toward the tip. The force sensor is fixed and incorporated behind the tip [Lee et al. (2014)]*

Another sample holder (from Nanofactory) came onto market. It was based on the <u>same concept</u> but the tip and force sensor are fixed whereas the sample is attached to a piezo that enables its fine and coarse movements in three directions, as displayed in ***Figure 15***-b (compression of gold nanowire). This sample holder is used in this PhD work, and will be presented in **chapter 2**. Unfortunately, Nanofactory went bankrupt in 2013 and Hysitron is up to now the only supplier for this type of sample holder.

IV. Main Features and advantages of *in situ* TEM nanocompression tests

As mentioned previously, during *in situ* TEM nanocompression tests, images (movies) and load-displacement curves can be recorded simultaneously. By DIC (Digital Image Correlation) presented in **chapter 2**, one can correct any possible displacement of the rigid part (indenter) and thus obtain real-displacement of the sample and correlate image to each point in the load-real displacement curve.

1. This is of high interest, due to the **high temporal resolution** of the TEM. Indeed, it is possible to observe fracture in Si nanoparticles (200-250nm) [*Deneen et al. (2006)*]-[*Nowak et al. (2007)*] in real time and to determine the possible mechanism that trigger it [*Mook et al (2007)*].

2. **Different TEM imaging Modes are** available. During *in situ* nanocompression tests it is then possible to observe dislocations in real time and track their movement and their substructure evolution at each stage of deformation (stress-strain response, see ***Figure 16***-a-b-c-d-e-f). Many different deformation mechanisms occurring during compressive loading of single crystal three dimensional nanostructures could be observed directly *in situ*. TEM observations analysis could also be combined with theoretical simulations, thereby giving a complete description of different deformation mechanisms.

One can cite a few featured works investigating deformation mechanisms using different TEM modes:

- The deformation through ¨mechanical annealing¨ of pre-existing dislocations (dislocation annihilation and escape from the surfaces, see ***Figure 16***-c-d) following the emergence of dislocations from dislocations sources surfaces (Frank-Read sources, see ***Figure 16***-b) at the beginning of the compression was observed in BF (Bright field*)* (the most easy mode to perform in situ TEM tests) *in situ* TEM nanocompression of FIB milled Mo nanopillars [*Huang et al (2014)*]. This deformation behavior ends with the collapse of dislocation free-region (see ***Figure 16***-e) due to explosive dislocation self-multiplication, as called in the cited paper. This was correlated to mechanical events observed in the stress-strain curve of the nanopillar (See ***Figure 16***-f).

-

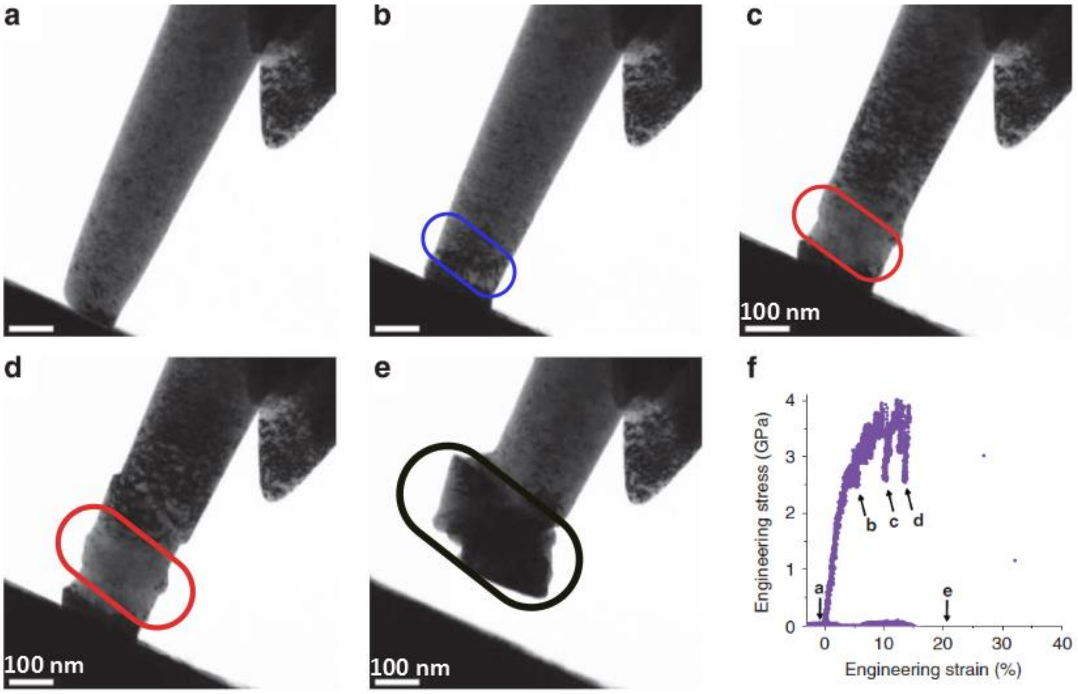

Figure 16: *Mechanical annealing during an in situ nanocompression test of a typical Mo nanopillar. BF TEM images of a pillar exhibiting a diameter D = 142 nm* ***(a)*** *before and* ***(e)*** *after the in situ compression test.* ***(b), (c), (d)*** *and* ***(e)*** *correspond to the points indicated in the engineering stress versus strain curve in* ***(f).*** *[Huang et al (2014)]*

During *In situ* TEM nanocompression of Au [110]-oriented nanowires [*Lee et al. (2014)*], it was possible to observe the emission of prismatic dislocations loops (shown in Figure 17-a) in the Dark Field (DF) mode. It was found that such dislocations slipped down the wire, at the beginning of compression. It was also possible to reveal the transition in the nucleation mechanism from closed loops to open dislocations loops, after less than ten dislocations loops that were punched out under continuous compressive load (shown in ***Figure 17***-b). Their burgers vector could be determined also by applying the **g. b** invisibility criteria to two-beam DF images (method presented **in chapter 2**).

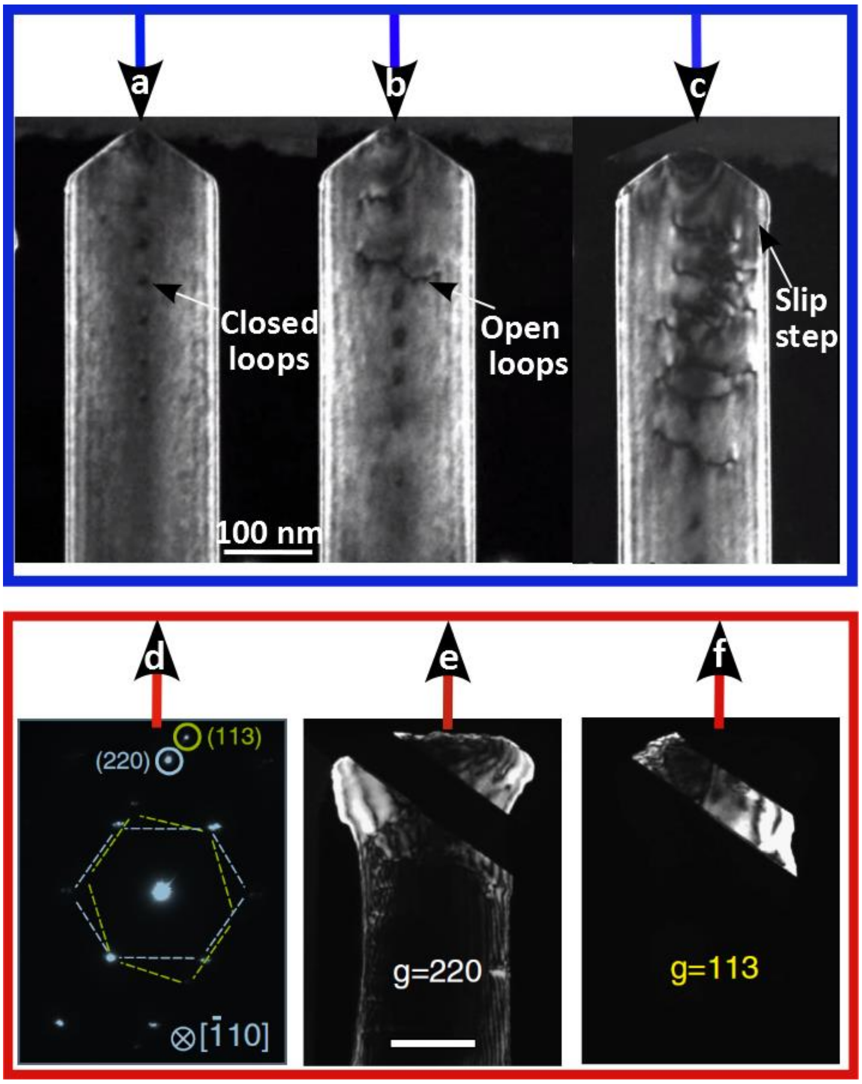

Figure 17: *in situ TEM nanocompression of gold nanowires* ***a)*** *DF TEM image: appearance of closed loops at the beginning of compression.* ***b)*** *DF TEM image: Transition of the nucleation mechanism to open loops.* ***c)*** *DF TEM image: Slip steps appear the nanowire surface revealing ordinary fast dislocation slip and escape.* ***d)*** *Selected area Diffraction pattern of the nanowire****.*** ***e)*** *DF TEM image with the (220) diffracting planes.* ***d)*** *DF TEM image with the (113) diffracting planes. [Lee et al. (2014)]*

Moreover, ordinary dislocation slip was also observed in DF mode. These perfect dislocations nucleate and slip out the nanowire faster than the closed and open loops dislocations. Such high speed prevented to capture their underlying mechanism but the remaining slip steps on surfaces (shown in ***Figure 17***-c) allowed the description of their path mechanism as ¨nucleation-glide-escape¨. A similar behavior was observed during the unloading part of the cycle (described as a tensile test, because of the adhesive contact formed between the nanowire and the punch in this specific test [*Lee et al. (2014)*]. As a consequence, it was possible to observe the twinning deformation mechanism when reversing the loading direction to tensile. In fact, twinning is often observed in tensile tests.

It was possible to observe twinning and describe the planes of occurrence by choosing specific diffracting planes from the selected area electron diffraction pattern, as shown in*Figure 17*-d-e-f. The Second cycle of compression was found to be governed by de-twining rather than by dislocation loops or nucleation-glide-escape of ordinary loops. On the contrary, the tensile part governed by twinning. As a conclusion, the deformation mechanism of Au single crystal nanowires could be well described during *in situ* TEM nanocompression, combined with atomistic simulations [*Lee et al. (2014)*].

- Other types of events could also be evidenced. For example, the deformation through phase transformation of Nitinol (NiTi) from austenite phase to martensite phase at 1 GPa was observed by recording in real time the diffraction patterns of nanopillars [*Jia Ye et al (2009)*]. Moreover, other analytical techniques can be used during *in situ* TEM tests. The Electron Energy Loss Spectroscopy (EELS) is a very useful to follow structures changes also during solicitation. This has been used to monitor an eventual crystallization of amorphous silica during compression [*Zheng K et al. (2010)*]

3. Another advantage of *in situ* TEM nanocompression tests over *in situ* SEM ones is the possibility to test **particles less than 100nm**. For example, it was possible to determine the critical size for brittle-ductile behavior transition in transition alumina nanoparticles (crystallographic phase that does not exist at bulk). Calvié et al. [*Calvié et al (2012)*] observed that particles larger than 100nm underwent failure before or after plastic deformation, whereas smaller particles showed pure plastic deformation without failure. This is of major importance to understand the origin of the limit size when grinding ceramic nanoparticles by ball-milling or other comminuting techniques.

4. One must also mention **the interest of simulations** coupled with these *in situ* TEM tests. Indeed, when specific restrictions make impossible the observation of dislocations during the test, ambiguity remain on the deformation behavior. For example, the identification of elementary mechanisms responsible for plastic deformation in transition alumina nanospheres could not be determined *in situ*. In particular, no dislocation could be observed experimentally. This lack was primarily attributed to the non-fulfilment of the diffraction conditions. Nevertheless Finite Elements (FE) simulations could bring useful pieces of information [*Calvié et al (2014)*].

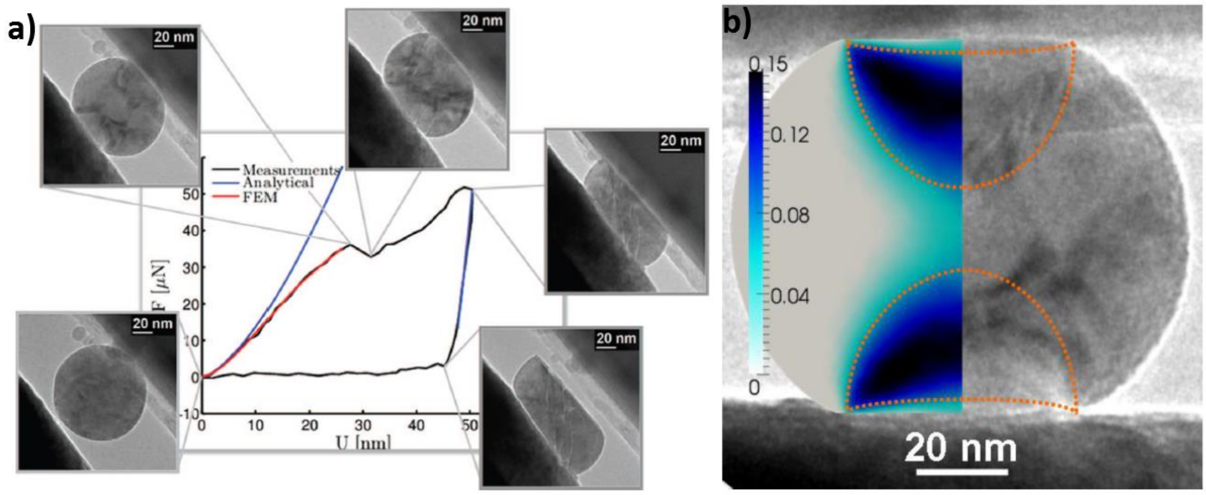

Figure 18-a) *in situ TEM nanocompression force–displacement curve of spherical transition alumina. Images are displayed at key points of the force–displacement curve by using DIC. The result obtained by Finite Elements (FE) simulation is presented by the red curve and the analytical method (Hertz' contact) by the blue curve.* ***b)*** *Superposition of an experimental TEM image with the corresponding map of the total equivalent plastic strain calculated by FE [Calvié et al (2014)].*

FE results indeed confirmed an analytical method in which the elastic part of the loading curve was fitted by a Hertzian model and the unloading curve was fitted by a power-law function through the classical Oliver & Pharr model (see ***Figure 18***-a). Moreover, FE simulations allowed the determination of a constitutive mechanical law and the extraction of a yield stress and Young modulus for transition alumina [*Calvié et al (2014)*]. It was also possible to calculate the map of the total equivalent plastic strain of the nanoparticle using the determined constitutive law (see ***Figure 18***-b). The calculated map matched very well the contrast observed on the TEM image. Thereby, it could be possible to attribute the observed Bragg fringes to plastic deformation.

Similar *in situ* TEM works reveal many important features describing deformation mechanisms of various materials at small scale. These deformations mechanisms will be presented in **section 1.2,** with results obtained from *ex situ* and *in situ* SEM microcompression that performed TEM observations on post-mortem samples.

V. Main challenges for *in situ* TEM nanocompression

All the *in situ* tests in TEM are not an easy task. Indeed, it combines sample preparation with specific geometries (nanopillars, thin sections, thin films or nanoparticle deposition on a specific substrate) the *in situ* mechanical test itself and the possible use of many diffraction modes (BF, DF, WBDF or Diffraction patterns…) during the test. Moreover, the contrasts in the images have to be analyzed and correlated to the events in the force-displacement curve, in order to extract the deformation mechanisms.

Nanopillars and thin sections samples are prepared from a bulk material, often by FIB. During preparation, a specific orientation may be chosen to allow a specific orientation axis.

Nanoparticles are deposited on a specific substrate. The main challenge in these tests is the choice of the substrate material nature, surface roughness and thickness. The substrate hardness must be higher than that of nanoparticles, in order to prevent its deformation during sample solicitation and thus eliminate ambiguity for sample stress-strain analysis. The substrate must be smooth and show no roughness, especially roughness that is smaller than nanoparticles dimensions in order to prevent stress localization in the nanoparticle and non-uniform uniaxial deformation. Moreover the substrate should not be too thick or too thin. In the case of a too thick substrate, a small misalignment between the punch and the substrate, even at the nanoscale, may induce a shadowing effect during the *in situ* test, as shown in *Figure 19*-a. If the sample holder is a simple tilt one, thus only primary tilt is possible (see *Figure 19*-c). The latter does not correct this misalignment, as shown in *Figure 19*-a. This correction is only possible if a sample holder is a double-tilt one, since secondary tilt is possible (see *Figure 19*-c). However, if the sample holder is simple tilt, than the only solution is to remove the sample holder from the TEM and make, under an optical microscope, the optimum possible correction of this misalignment. Thus this is so delicate and may require many trial and error experiments and thus huge experimental time. On, the contrary when the substrate is too thin, an easy sliding of the nanoparticles may occur during compression and lead to the absence of deformation.

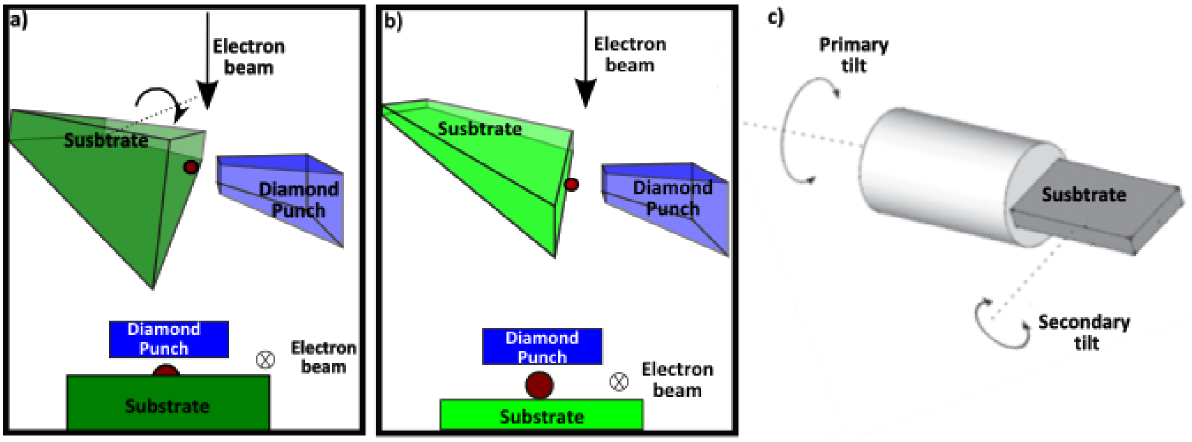

Figure 19a) a thick substrate causing shadowing b) thin substrate avoids the shadowing effect. c) Scheme shows a double tilt-sample holder that provides primary tilt and secondary tilt.

In addition, depositing nanoparticles may be easy by dry route but in some cases they may have to be dispersed in a solvent. In the latter case, solvent residues may remain on the surface of nanoparticles, modify the chemical composition on the surface and thereby affect mechanical properties.

When spherical crystalline nanoparticles are concerned, the identification of the compression axis or their reorientation along a specific crystallographic zone axis may not be an easy task, especially with a simple tilt sample holder. In fact, nanoparticles remain on the substrate due to electrostatic forces, and vibration due to controlling the imaging mode (opening or closing diaphragms of TEM) or interaction with the tip may change the electrostatic interactions and cause their loss. One must mention that Calvié et al. *[Calvié et al. (2012)][Calvié et al. (2014)]* and Carlton & Ferreira [*Carlton et al. (2009)*] could not identify the compression axis with spherical transition alumina nanoparticles and silver nanoparticles, respectively. However, Carlton & Ferreira [*Carlton et al. (2009)*] could successfully observe dislocations but as the compression axis could not be clearly determined from the images and the interpretation remained qualitative.

All these effects made *in situ* TEM nanocompression tests, a sophisticated and not trivial technique, especially on freestanding nanoparticles. As a consequence, a statistical study may be a hard work, especially since reproducible conditions may be almost impossible.

Nevertheless, choosing single crystal nanocubes as objects for in situ TEM nanocompression may be a solution for the identification of the compression axis and the analysis of contrasts with respect to the crystallographic oriented faces.

1.2 Featured Mechanical Properties at Sub-micron/Nano-scale: ¨Smaller is Stronger¨ & ¨ Intermittent Superplasticity¨

In situ TEM mechanical tests and *in situ* SEM, even *ex situ*, combined with TEM observations on post-mortem samples and theoretical computational works, have revealed important information on deformation mechanisms and mechanical properties of various single crystal materials at the small scale.

In general, two distinct featured mechanical properties of single crystalline, especially FCC metals, arise at small scale: the first is "Smaller is stronger", presented in strengthening of materials showing yield stresses or elastic limits higher than those obtained in the bulk, and even showing a size effect in the sub-microscale where yield stress scales inversely to the sample size. The second feature is "superplasticity", presented as large plastic deformation with intermittent stress-strain curves (strain bursts /stress-drops) different than bulk stress-strain response.

1.2.1 "Smaller is Stronger": Size effect in the Sub-micron/Nanoscale and Controlling Deformation Mechanism

I. Size Effect on the Yield Strength

As mentioned briefly in **section 1.1**, since Brenner experiments [*Brenner et al. (1956)*] on single crystal metallic whiskers in the late 50's, it has been demonstrated that small whiskers that are dislocations-free can have a very high strength comparable to the theoretical strength. This was attributed to the absence of dislocations in initial whiskers that lead to a higher stress needed to generate dislocations rather than stress concentrations in pre-existing dislocations that enables only dislocation activation to accommodate plastic deformation, at lower stresses. Even if dislocations pre-exist in specimen, their processes are expected to be different than in the bulk, and higher strength is observed in thin metallic filaments made from bulk in the late 60's [*Smith (1968)*].

With FIB facilities, Uchic *et al.* [Uchic *et al.* (2003)-(2004)] showed first works on compression of single-crystal micropillars produced by FIB milling from bulk. It was shown that the strength of small single-crystals FIB milled micropillars scales inversely to the pillar diameter. Numerous studies on single-crystals produced by FIB have provided similar experiments on FCC (Face Centered Cubic) [*Greer et al. (2005)*]-[*Dimiduk et al. (2005)*]-[*Greer et al. (2006)*] [*Volkert et al. (2006)*]-[*Kiener et al. (2006)*]-[*Frick et al. (2008)*]-[*Ks Ng et al. (2008)*]-[*Lee et al. (2014)*] , BCC (Body Centered Cubic) [*Kim et al. (2012)*]-[*Schneider* *et al. (2009)*]-[*Huang et al.(2011)*], and on HCP (Hexagonal Close-Packed) [*Sun et al. (2011)*] lattices. All the above-cited studies and many others on single-crystals nanoparticles and other geometries [*Kraft et al. (2010)*] demonstrate the presence of an influence of the size on the yield stress and try to describe the scaling effects by using a power-law fit:

$$\sigma_y = Ad^{-x} + \sigma_0$$

Where σ_y is the yield stress, d is the characteristic length scale of the structure or the diameter of the micropillars, σ_0 is the bulk yield stress of the same material, A is a fit constant and x is the power-law exponent.

However, different ways of plotting data, to show this size effect, and to show that all FCC metals, for example, collapse on a linear relationship between pillar diameter and yield stress with an exponent $x \sim 0.6$, were proposed by Uchic et al. [*Uchic et al. (2009)*] and Dou & Derby [*Dou & derby (2009)*].

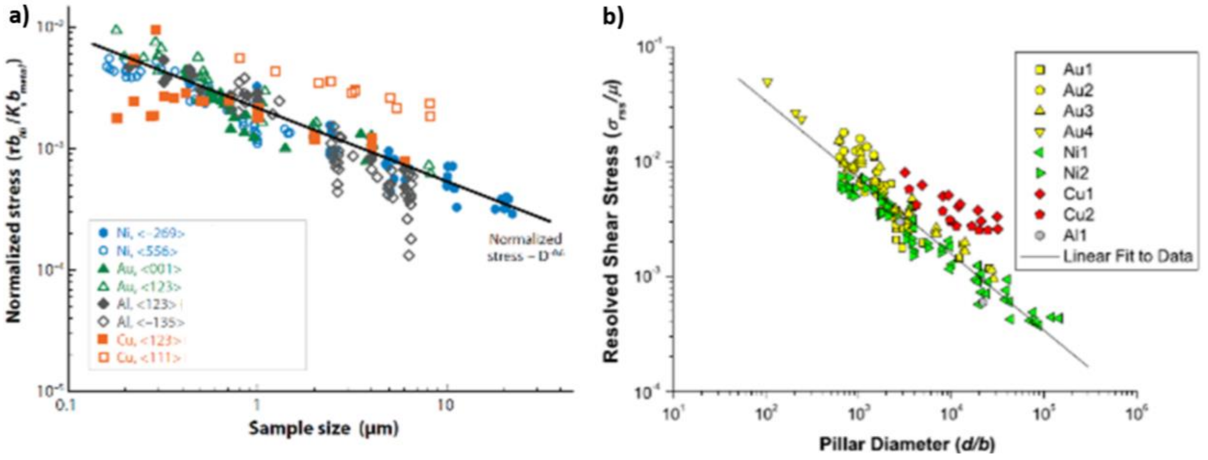

Figure 20: a) *Uchic et al. [Uchic et al. (2009)] proposed to normalize the resolved shear stress* $\boldsymbol{\tau}$ *of FCC metals by their resolved shear modulus* $\boldsymbol{\mu}$ *(or K in the graph) and the relative ratio of the Burgers vector of each metal to the burger's vector of Nickel Burgers vector* $\boldsymbol{b_{metal}/b_{Ni}}$*. b) Dou-derby [Dou-Derby (2009)] proposed to present dimensionless graph axis and to normalize to normalize the resolved shear stress* $\boldsymbol{\tau}$ *of FCC metals by their resolved shear modulus* $\boldsymbol{\mu}$ *and the sample size by the material's Burgers vector.*

It is argued that since the deformation of samples is controlled by dislocation motion and/or nucleation, therefore, strengthening of the specimen is assumed to be governed by interactions of the dislocations with some specimen features (pinning points). Thus the controlling physical property is the dislocation line tension determined by the Burgers vector and the shear modulus of the material [*Dou Derby et al. (2009)*].

Therefore, Uchic et al. [*Uchic et al. (2009)*] proposed to show the size effect represented by $x = 0.6$ for fcc metals by using the fitting law:

$$\boldsymbol{(\tau - \tau_0)\, b_{Ni}/\mu b_{metal}) = Ad^{-x}}$$

Hence, it is proposed to normalize the resolved shear stress $\boldsymbol{\tau}$ of any FCC metal by its resolved shear modulus $\boldsymbol{\mu}$ and by its Burgers vector normalized by the Burgers vector of Nickel. $\boldsymbol{\tau_0}$ is the critical resolved shear stress of its bulk counterpart (negligible for FCC metals) (see ***Figure 20***-a). However*Dou & derby (2009*) argued that this way of plotting was not intuitive since the Burgers vector of the metal is normalized by that of Nickel and proposed to present dimensionless axes (shown in ***Figure 20***-b) by using:

$$\left(\frac{\boldsymbol{\tau}}{\boldsymbol{\mu}}\right) = \boldsymbol{A}\left(\frac{\boldsymbol{d}}{\boldsymbol{b_{metal}}}\right)^{-\boldsymbol{x}}$$

The literature is well documented on the size effect in FCC metals, and in general, one can find that single crystalline nano- and micropillars made from FCC metals show an exponent $\boldsymbol{x}$ going from 0.6 to 0.97 [*D.M. Dimiduk et al. (2005)*] - [*Volkert CA. et al. (2006)*] [*Brinckmann et al. (2008)*] [*Frick CP et al. (2008)*] [*A.T. Jennings et al. (2010)*], whereas it is roughly equal to 0.77 for FCC nanoparticles [*Dan Mordehai et al. 2011*]. This power-law exponent $\boldsymbol{x}$ of FCC metals is obviously higher than those of BCC crystals (W, Mo and Ta…), where the power exponent varies from 0.22 to 0.48 for average sizes ranging from several microns to 200 nm [*J.Y. Kim et al. (2010)*] [*A.S. Schneider et al. (2009)*]. Moreover, *Huang et al*. [*Huang et al. (2011)*] reported two different regimes: FIB milled Mo micropillars of diameter > 200 nm exhibited an exponent $\boldsymbol{x}$=0.3, which is persistent with [*J.Y. Kim et al. (2010)*] [*A.S. Schneider et al. (2009)*]. They also reported a transition critical size (D_C~200nm), below which the size effect is highly pronounced and $\boldsymbol{x}$ becomes equal to ~1, as shown in ***Figure 21***.

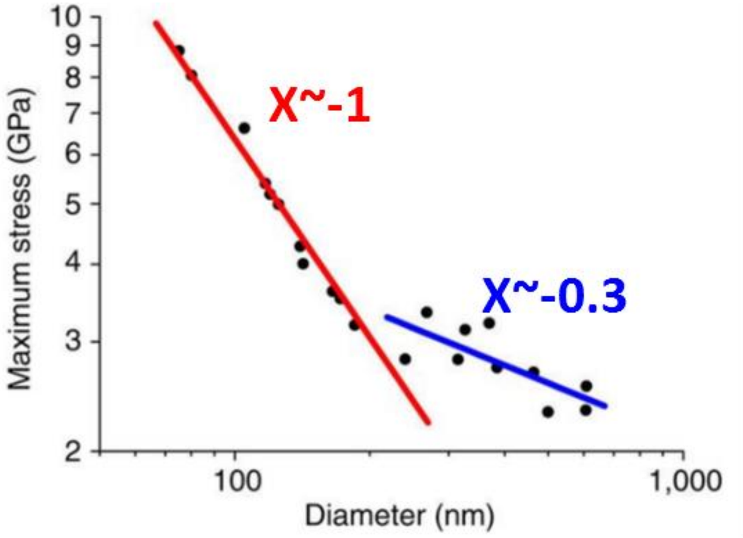

Figure 21: *Two different regimes in the size effect on the yield stress observed in Mo- nanopillars, with a critical size of pillar diameter around 200 nm [Huang et al. (2011)].*

II. FIB Machining Effect on the Yield Strength

One must briefly include a few words about the fabrication methods of micro and nanosamples. These methods of fabrications are categorized in two families: the top-down approach consists in making micro and nanosamples from a bulk material, by decreasing the size of the bulk section and machining a sample with a specific geometry. This can typically be performed by FIB. The bottom-up approach consists in growing samples from chemical reactions (atomic growth or atomic deposition). It can result in dislocation-free samples, whereas the top-down approach techniques may induce defects and damage layer on surfaces of samples due to ions.

Some researchers assumed that FIB machining generates crystals defects (among which Ga^+ implantations, precipitates and damaged amorphous layers) at the surface of micropillars, thus affecting the strength [*Bei et al. (2007)- Effects of focused ion beam milling on the nanomechanical behavior of a molybdenum-alloy single crystal*]. In this work, it was argued that the higher strength reached in smaller FIB milled pillars never reach the theoretical strength of the material, even though some of the pillars are small enough to contain very small dislocation populations or no dislocation, as shown in *Figure 4*. Thus there is a reasonable chance that a specimen with micrometer dimensions would be dislocation free, and yielding would require the nucleation of dislocations at stresses near the theoretical strength. Theoretical strength is often estimated to range from $\frac{\mu}{30}$ to $\frac{\mu}{10}$, where μ is the shear modulus or resolved shear modulus for anisotropic materials [*Brenner (1956)*].

It was argued [*Bei et al (2007)-Compressive strengths of molybdenum alloy micro-pillars prepared using a new technique*] [*Bei. et al (2008)*] first that the low yield strength, lower than the theoretical strength, is due to defects (dislocations) introduced during FIB fabrication. Therefore other methods have been introduced for micro and sub-micrometer samples fabrication such as directional solidification [*Bei et al. (2007) - Compressive strengths of molybdenum alloy micro-pillars prepared using a new technique*], physical vapor deposition [*Richter et al. (2009)*], direct nanoimprinting or embossing [*Buzzi et al. (2009)*] and solid state dewetting [*Mordehai et al. (2011)*]. Some of the latter methods produce samples free of dislocations. For example, experiments on Mo-alloy micropillars (bcc metal) [*Bei et al. –(2007)- Compressive strengths of molybdenum alloy micro-pillars prepared using a new technique*][*Bei. et al. (2008)*], produced via eutectic solidification followed by chemical etching, and believed to be free of dislocations, show yield strengths near the theoretical strength. It is noteworthy that these Mo-alloy micropillars show no size dependence of the yield stress on the micropillars size, as shown in Figure 22-a (0% pre-strain) pillars.

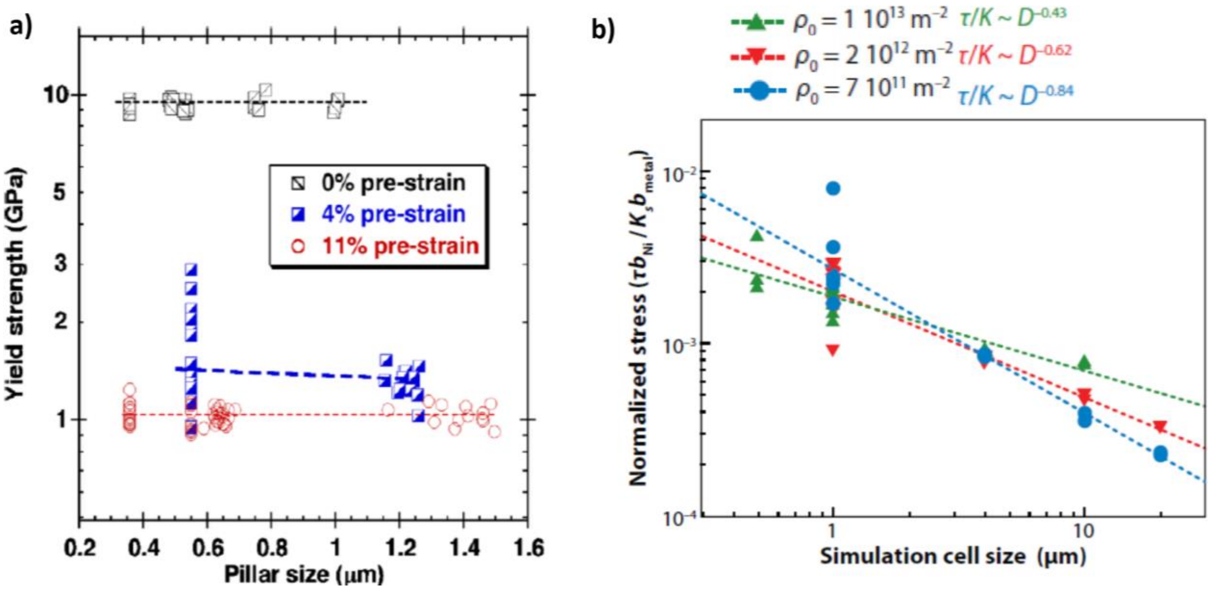

Figure 22: a) *Mo-alloy micropillars produced via eutectic solidification, free of dislocations, show yield strengths near the theoretical strength (0% pre-strain). No size dependence on the micropillar size is observed. It has to be noted that prestrained micropillars show lower strengths [Bei et al. (2008)].* ***b)*** *3-D discrete dislocations simulations (DDS) of FCC microcrystals on the degree of size-dependence of the yield strength on the initial dislocation density. The graph shows that a higher dislocation density results in a weaker size effect [Rao et al. (2008)]*

Moreover, pre-strained samples (4% and 11%) exhibited a yield strength lower than dislocation-free pillars, and might also exhibit a slight size-effect.

According to this, the second argument for the size effect observed in FIB milled pillars is the dependence on the pre-existing dislocations density [*Bei et al. (2008)*][*Rao et al. (2008)*]. Smaller specimens contain fewer dislocations (for a constant dislocation density) and are therefore expected to yield at higher strength. Consistently with Bei *et al.* results [*Bei et al. (2008)*], Rao et al. [*Rao et al. (2008)*] performed 3-D discrete dislocations simulations (DDS) of FCC microcrystals and showed that the initial dislocation density influences the degree of size-dependence of yield strength . Moreover both studies showed that once dislocations exit in the sample, the size effect is pronounced and a higher initial dislocation density results in a weaker size-effect, and vice-versa, as shown in ***Figure 22***-b. This higher initial dislocation density that results in a weaker size effect is explained by ¨forest hardening¨, a mechanism dominant in large specimens that strengthens the sample [*Rao et al. (2008)*].

This more pronounced size effect in samples containing low initial dislocation densities was also observed in experiments on alkali halide LiF crystals FIB-milled from bulk ultrapure LiF single crystals having a low initial dislocation density (10^9 m^{-2}) compared to the densities reported for fcc or bcc FIB-milled microcrystals ($10^{12\text{-}13} m^{-2}$) [*Nadgorny EM, (2008)*].

According to this, one may expect that size effect in the sub-microscale is only a dependence on the density of pre-existing dislocations. But other works on pristine (dislocation-free) gold nanoparticles showed a clear size effect in the sub-microscale [*Mordehai et al. (2011)*], as shown later in ***Figure 24***. Hence, the size dependence of the yield strength is not only dependent on the pre-existing dislocations densities, but seems also to be related to other specimen size characteristics.

III. Origin of the Size effect & Controlling Mechanisms

Many works try to investigate the origin of the size effect observed in single crystalline sub-micron materials and three dimensional nanostructures. One must know first that it is often considered that free surfaces are considered as sinks and sources of dislocations [*Greer & Nix (2006)*]. In the sub-microscale, due to the high surface/volume ratio, the role of these free surfaces becomes central.

In fact, there is no consensus for the mechanism leading to the size effect on the yield strength, and controlling mechanisms of this size effect in recent research studies is still debating on two approaches categorized as follows:

The first mechanism is the deformation via dislocation surface nucleation/ starvation [*Greer & Nix (2006)*], predominant in pristine (dislocation free) samples. In this approach, the size effect is pronounced due to the fact that the length of the generated dislocation segments is limited by the sample dimensions. As a consequence, it decreases when decreasing the sample size. Knowing that the dislocation generation stress is inversely proportional to the distance between both pining points of a dislocation line, this leads to a higher stress needed to generate smaller dislocations lines when decreasing the sample size. Hence, smaller pristine samples yield at higher stress than larger ones. Moreover, this limited segments length prevents the multiplication of dislocations, and causes their exhaustion through the close proximity of free surfaces in smaller samples. This phenomenon is called dislocation starvation. At this stage, one has to mention the phenomenon of “mechanical annealing”. For a typical dislocation density of 10^{12} m^{-2} in FIB milled micropillars; the average dislocation spacing is 1 µm [*Bei et al. (2005)*]. Thus, for pillars in the 1 µm range size or smaller, possibly existing mobile dislocations are all annihilated at the close proximity of free surfaces (by high image forces) at the early beginning of compression tests, without being trapped by the FIB damaged layer[*Shan et al. (2008)*]. New dislocations will then nucleate at the free surface. This corresponds to “mechanical annealing” of mobile pre-existing dislocations followed by dislocation nucleation/starvation. Such mechanism has been observed during *in situ* TEM nanocompression tests [*Shan et al. (2008)*]-[*Huang et al. (2010)*]

The second mechanism is the deformation via the motion of dislocations activated from a decreasing number of bulk dislocation sources when decreasing the sample size (Frank-Read sources or single-arm dislocation sources) [*Parthasarathy et al. (2007)*]. The activation stress of single arm source depends on the sample size [*Rao et al. (2008)*]. Thus, a higher stress has to be applied to operate the short single arm source in a smaller specimen. This leads to the observed size effect. This mechanism is predominant in specimens produced from bulk, by a top-down approach as FIB fabrication, as they already contain dislocations in the initial state.
Moreover, it may exist a critical size at which a transition from the second mechanism to the first mechanism occurs when decreasing sample size. This may explain different size effect exponents x for the same material in two different size regimes, as that observed in Mo-alloy nanopillars [*Huang et al. (2011)*], see ***Figure 21***

Finally, it has to be mentioned that the literature is well documented for size effects and responsible mechanisms for a wide range of metals, but few works are reported for hard materials as ceramics [*Korte (2011)*] [*Calvié (2012)*].

1.2.2 ¨Intermittent superplasticity¨: size effect on the plastic response (stress-strain curves)

As explained in **section 1.1.1**, experimental micro and nanocompression tests can be performed either in the displacement-control mode or in the load-control mode. Simulations are often displacement-control tests.
In the displacement-control mode, a maximum displacement is set and a force is read by a force sensor. Thus, at a dislocation nucleation event, a burst of displacement occurs in the sample and significantly changes the sample shape. As a consequence, the force drops at the occurrence of this burst of displacement due the temporary separation of the punch and the specimen. This results in stress-drops in the stress-strain curve, as shown in ***Figure 23***-a.
A different behavior is obtained from load-control mode tests, where a load is imposed and a displacement is read. Therefore, the load should remain constant while an avalanche of dislocation escapes takes place. During the avalanche of dislocations, the punch drops

downward until the specimen regains its ability to resist the same load as the one before the avalanche occurred. Thus during these dislocations events, no stress drops are recorded but a lack of data is often observed in stress-strain curves, as shown in ***Figure 23***-b.

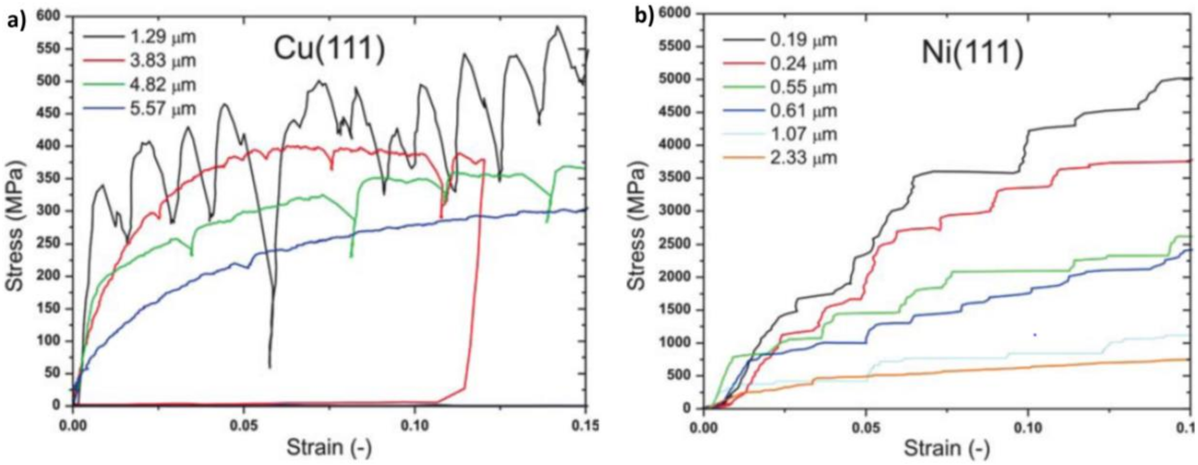

Figure 23: a) *Cu(111) samples loaded in the displacement-control mode. The stress-strain curves show stress-drops [D. Kiener et al. (2009)]* ***b)*** *Ni (111) samples loaded in the load-control mode. The strain bursts correspond to the plateaus [C.P. Frick et al. 2008].*

In both cases, the stress-strain curve is different than that of the bulk, for which a smooth stress-strain response is observed. This may be explained by different deformation mechanism and dislocations processes controlling plasticity in both cases. And by the fact that in the bulk, each displacement burst has a size which is much smaller than the sample dimension, and may not be captured in the stress-strain response.

It is noteworthy that sub-micron and nanoscale samples show large plastic strain before failure. This plastic strain is larger than the plastic strain range observed in bulk. The literature is well documented on these effects observed in metals at small scale.

In load-control mode tests, these stress drops cannot be observed in stress-strain curves, so most of the time, the size-effect on the magnitude and frequency of these jumps in the stress-strain curves have no clear description. In some displacement-control mode tests, especially on non-pristine specimens, they have been simply described by a stochastic nature of dislocation avalanches. [**Jennings** *et al. (2010)*] -[*Kaufmann, Kraft et al. (2011)*].

However, some studies introduce the effect of the specimen size on the stress-strain jump magnitude [*unpublished results of M.D Uchic, published in review Uchic (2009)*] and their occurrence frequency, and draw a correlation with different deformation mechanisms in smaller and/or larger specimens. For instance, microcompression of Copper micropillars, machined by FIB, [*unpublished results of Kauffmann, published in review Oliver Kraft (2010)*] of 5000 nm and 950 nm in diameter show smooth stress-strain responses described as bulk-like deformation, while pillars of 225 nm in diameter show serrated stress-strain curves with consecutive jumps. Similarly, compression tests performed on bcc metallic micropillars [***Ju**-Young Kim et al. (2010)*] showed that Nb and Mo micropillars of 900-850 nm in diameter exhibited continuous non-linear strain hardenings with no stress drop in stress-strain curves as the ones observed in smaller pillars. Moreover, Molecular Dynamics (MD) simulations and experimental compression tests on Au pristine single crystal nanoparticles [*Mordehai et al. (2011)*] reported a specimen size effect on the magnitude of these consecutive stress drops. They concluded that this is due to a predominance of one of the two main size-dependent deformation mechanisms described above and that result in the following: (i) dislocation nucleation and starvation in smaller samples due to high surface-to-volume ratio, with surfaces acting as sources and sinks of dislocations; (ii) multiple slip systems and dislocation interactions. In the first case, in small objects, the stress drops as an abrupt deformation occurs when dislocations nucleate and rapidly escape from free surfaces. Then, a new elastic regime takes place until another similar event takes place. One must mention here that when dislocations escape from surfaces, they leave atomic steps. These atomic steps act as new sources of dislocations and require less stress to accommodate further plastic deformation, which results in softening of the material rather than strain hardening, as shown in curves of smaller specimen sizes in ***Figure 24***. However this mechanism also occurs in larger specimens but because of the larger size, more surfaces act as dislocation sources, which give rise to the activation of multiple slip systems. Dislocations may then interact with each other, or be stored in the bulk as new dislocation sources. In this case, strain hardening may cause a steeper increase than simple elastic reload, as shown in curves of larger specimen sizes in ***Figure 24***.

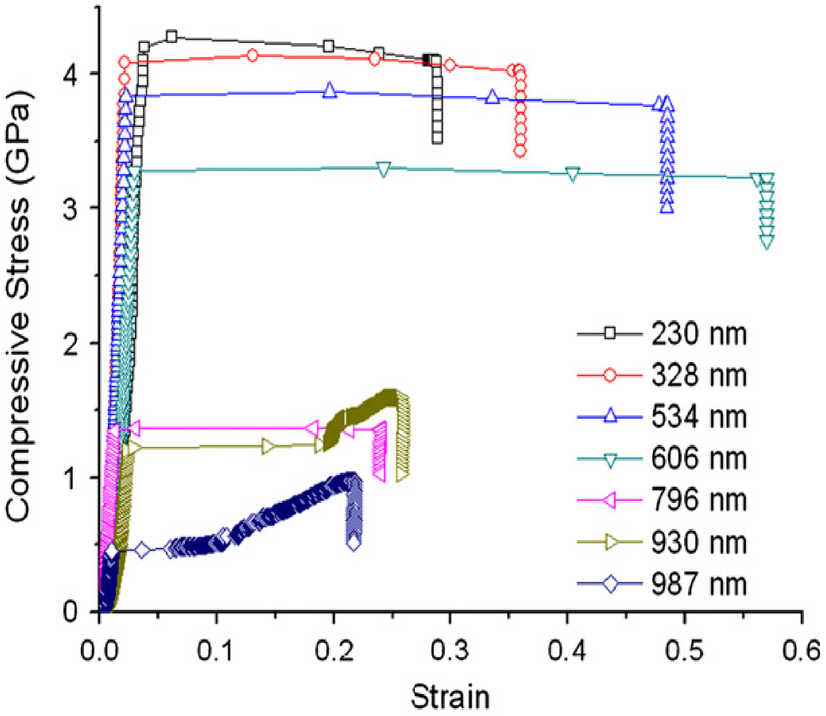

Figure 24: *large plastic strain in smaller nanoparticles with no strain hardening, whereas larger nanoparticles show strain hardening the predominance of different deformation mechanisms in smaller and larger samples.*

This different mechanism controlling the plastic deformation results indeed in different dislocations substructures in two different size regimes. This is observed in Nickel micropillars compression tests reinforced by TEM observations on post-mortem samples. [*Nortfleet DM, et al (2008*)]. TEM observations of dislocations structures in nickel micropillars showed that the dislocation structures on the active slip systems in pillars larger than 2 µm are comparable to the ones found in bulk samples deformed to a similar state, and different than those observed in smaller micropillars.

Again, most of the cited works deal with metals. As far as ceramics are concerned, MgO micropillars compressed along the <001> direction [*S. Korte 2011*] also show stress-strain curves with a clear specimen size effect on the stress-drops magnitudes.

General Conclusion of Chapter 1

Compression was presented as a power tool to study plasticity of materials at small scale. Anisotropic materials can be studied without ambiguity in resulting data and thus a target slip system can be studied. The mechanical properties (resolved shear stress) can be extracted without the major strain gradient often observed in nanoindentation tests.

***In situ* TEM nanocompression**, among *in situ* SEM and *ex situ* microcompression tests, is presented as a useful quantitative and accurate tool, with *high temporal and spatial resolutions*. This enables *the characterization of the dislocation substructure evolution and the determination of the deformation mechanism* at small scale. Moreover, it enables the description of a possible size effect on the essential mechanisms controlling the deformation of materials at small scale.

It was however shown that these *in situ* TEM tests performed on freestanding samples are not trivial task. For instance, it was shown that *spherical nanoparticles pose some challenges on the identification of the compression axis direction*, which prevents the analysis of the images contrasts or observed dislocations. Many other parameters make this task sophisticated and thus few statistical studies, on the size effects on the yield strength for example, are reported in literature.

Nevertheless, the literature is well documented on the dependence of the **controlling mechanisms** and the **yield strength** of metals on the specimen size in the micron and sub-micron scale. Experimental tests and theoretical simulations results show that higher yield stresses are obtained in smaller specimens. This is consistent with the findings that “smaller are stronger”. Larger plastic strains than that observed in bulk are observed at small scale, leading to the so-called superplasticity. Moreover, stress-strain curves show intermittent plastic behavior. However *few works on a possible superplasticity and size effect are reported on hard material as ceramics*, knowing that ceramics do not show any plastic strain at bulk.

Finally, it was shown that Top-Down approaches, *as FIB*, for micro and nanofabrication, may induce defects on samples surfaces and affect the mechanical properties and thus complicate the analysis.

This PhD Work

In this PhD work we use ***in situ* TEM nanocompression** to investigate **plastic deformation in ceramics nanoparticles.** Indeed, *ceramics* are known to be hard and brittle and thus plasticity in ceramics, which has been proven to exist at small scale, has been hardly studied. Yet, ceramics exhibit limiting critical size under which grinding is not possible. A special emphasis will be given on the quantification of the stress-stain curves and the images, to provide precise information on the deformation mechanism, as well as quantitative parameters of the mechanical behavior law.

Cubic shape has been chosen for single crystalline nanoobjects. Indeed, well defined oriented surfaces will help us to prevent ambiguity on the identification of the compression axis direction. Hence, we present a quantitative protocol including *in situ* TEM nanocompression tests, and data processing for the analysis of the stress-strain curves. Magnesium oxide (MgO), ceramic and model material is used. In order to avoid the formation of dislocations during FIB machining, single crystalline, pristine (dislocation-free) MgO nanocubes are synthesized by bottom-up approaches.

Thanks to its well-known structure, Molecular Dynamics (MD) simulations will be carried out. These MD simulations have been performed by Jonathan Amodeo and Julien Morthomas, from the group Metal in Mateis laboratory, in a collaboration work. The comparison of the MD simulations results with the experimental data will help us determining the deformation mechanisms.

Moreover, we present **a statistical study** of *in situ* TEM nanocompression tests performed on MgO nanocubes. It will be used to investigate a possible **size effect** on the yield strength and on the dislocation sub-structure in the sub-micron and nanoscale.

Finally, MgO is an ionic crystal. Knowing that ionic crystals are very sensitive to irradiation and show hardening, the influence of the electron beam has to be studied. Therefore, we perform *in situ* TEM nanocompression tests without the electron beam (beam-off tests) and other with electron (beam-on tests) in order to investigate possible changes in the mechanical properties (especially the yield strength).

A second part of this manuscript is devoted to transition alumina nanoparticles.

E. Calvié, in her PhD thesis, has shown that alumina nanoparticles exhibit large plastic deformation at the nanoscale. As alumina is extensively studied for the elaboration of transparent ceramics or for biomedical applications, taking plasticity into account during elaboration (mainly during the compaction step) is of prime importance.

E. Calvié showed that plasticity in alumina was not only due to the electron beam, since nanoparticles could be deformed in a compaction Belt apparatus. However, the deformation mechanism could not be determined from the *in situ* TEM nanocompression tests, because of the ambiguity on the identification of the compression axis direction. Moreover, quantitative parameters (Young modulus, yield stress) could be determined but no comparison was possible with data from the literature or with MD simulation results. Indeed, alumina at the nanoscale crystallizes in metastable phases which are different from the phase in the bulk. Moreover, MD cannot accurately model its defective structure.

In this work, we show an extensive TEM study of alumina samples compacted in a DAC at different pressures. The crystallographic phases are determined and possible textures analyzed. A comparison with the contrasts obtained during *in situ* TEM nanocompression tests give insights on the deformation mechanism. Moreover, phase transformation of metastable alumina with increasing pressure is identified and analyzed.

REFERENCES

- **Bei,** H., E. P. George, J. L. Hay, et G. M. Pharr. « Influence of Indenter Tip Geometry on Elastic Deformation during Nanoindentation ». Physical Review Letters 95, no 4 (19 juillet **2005**): 045501. doi:10.1103/PhysRevLett.95.045501.
- **Bei**, H., S. Shim, E. P. George, M. K. Miller, E. G. Herbert, et G. M. Pharr. « Compressive strengths of molybdenum alloy micro-pillars prepared using a new technique ». Scripta Materialia 57, no 5 (septembre **2007**): 397-400. doi:10.1016/j.scriptamat.2007.05.010.
- **Bei**, H., S. Shim, G.M. Pharr, et E.P. George. « Effects of Pre-Strain on the Compressive Stress–strain Response of Mo-Alloy Single-Crystal Micropillars ». Acta Materialia 56, no 17 (octobre **2008**): 4762-70. doi:10.1016/j.actamat.2008.05.030.
- **Bei**, H., S. Shim, M. K. Miller, G. M. Pharr, et E. P. George. « Effects of Focused Ion Beam Milling on the Nanomechanical Behavior of a Molybdenum-Alloy Single Crystal ». Applied Physics Letters 91, no 11 (**2007**): 111915. doi:10.1063/1.2784948.
- **Bouvier**, S., et A. Needleman. « Effect of the Number and Orientation of Active Slip Systems on Plane Strain Single Crystal Indentation ». Modelling and Simulation in Materials Science and Engineering 14, no 7 (**2006**): 1105. doi:10.1088/0965-0393/14/7/001.
- **Brenner**, S. S. « Tensile Strength of Whiskers ». Journal of Applied Physics 27, no 12 (1 décembre **1956**): 1484-91. doi:10.1063/1.1722294.
- **Brinckmann**, Steffen, Ju-Young Kim, et Julia R. Greer. « Fundamental Differences in Mechanical Behavior between Two Types of Crystals at the Nanoscale ». Physical Review Letters 100, no 15 (17 avril **2008**): 155502. doi:10.1103/PhysRevLett.100.155502.
- **Buzzi**, S., M. Dietiker, K. Kunze, R. Spolenak, et J. F. Löffler. « Deformation behavior of silver submicrometer-pillars prepared by nanoimprinting ». Philosophical Magazine 89, no 10 (1 avril **2009**): 869-84. doi:10.1080/14786430902791748.
- **Calvié,** E., J. Réthoré, L. Joly-Pottuz, S. Meille, J. Chevalier, V. Garnier, Y. Jorand, et al. « Mechanical behavior law of ceramic nanoparticles from transmission electron microscopy in situ nano-compression tests ». Materials Letters 119 (15 mars **2014**): 107-10. doi:10.1016/j.matlet.2014.01.002.
- **Calvié**, Emilie, Lucile Joly-Pottuz, Claude Esnouf, Philippe Clément, Vincent Garnier, Jérôme Chevalier, Yves Jorand, Annie Malchère, Thierry Epicier, et Karine Masenelli-Varlot. « Real time TEM observation of alumina ceramic nano-particles during compression ». Journal of the European Ceramic Society 32, no 10 (août **2012**): 2067-71. doi:10.1016/j.jeurceramsoc.2012.02.029.
- **Carlton**, C. E., et P. J. Ferreira. « In situ TEM nanoindentation of nanoparticles ». Micron, In situ TEM, 43, no 11 (novembre **2012**): 1134-39. doi:10.1016/j.micron.2012.03.002.
- **Choi,** Y.S., M.D. Uchic, T.A. Parthasarathy, et D.M. Dimiduk. « Numerical Study on Microcompression Tests of Anisotropic Single Crystals ». Scripta Materialia 57, no 9 (novembre **2007**): 849-52. doi:10.1016/j.scriptamat.2007.06.057.
- **Dehm**, Gerhard, James M. Howe, et Josef Zweck. **In-Situ Electron Microscopy**: Applications in Physics, Chemistry and Materials Science. John Wiley & Sons, 2012.chapter 11
- **Deneen**, Julia, William M. Mook, Andrew Minor, William W. Gerberich, et C. Barry Carter. « In Situ Deformation of Silicon Nanospheres ». Journal of Materials Science 41, no 14 (28 juin **2006**): 4477-83. doi:10.1007/s10853-006-0085-9.
- **Dimiduk**, D. M., M. D. Uchic, et T. A. Parthasarathy. « Size-affected single-slip behavior of pure nickel microcrystals ». Acta Materialia 53, no 15 (septembre **2005**):

4065-77. doi:10.1016/j.actamat.2005.05.023.

- **Dou**, R., et B. Derby. « A universal scaling law for the strength of metal micropillars and nanowires ». Scripta Materialia 61, no 5 (septembre **2009**): 524-27. doi:10.1016/j.scriptamat.2009.05.012.
- **Espinosa,** Horacio D., Rodrigo A. Bernal, et Tobin Filleter. « In Situ TEM Electromechanical Testing of Nanowires and Nanotubes ». Small 8, no 21 (5 novembre **2012**): 3233-52. doi:10.1002/smll.201200342.
- **Fleck**, N. A., G. M. Muller, M. F. Ashby, et J. W. Hutchinson. « Strain gradient plasticity: Theory and experiment ». Acta Metallurgica et Materialia 42, no 2 (1 février **1994**): 475-87. doi:10.1016/0956-7151(94)90502-9.
- **Frick,** C. P., B. G. Clark, S. Orso, A. S. Schneider, et E. Arzt. « Size effect on strength and strain hardening of small-scale [1 1 1] nickel compression pillars ». Materials Science and Engineering: A 489, no 1-2 (20 août **2008**): 319-29. doi:10.1016/j.msea.2007.12.038.
- **Gane**, N. « Microdeformation of Solids ». Journal of Applied Physics 39, no 3 (**1968**): 1432. doi:10.1063/1.1656376.
- **Gane**, N. « The Compressive Strength of Sub-Micrometre Diameter Magnesium Oxide Crystals ». Philosophical Magazine 25, no 1 (janvier **1972**): 25-34. doi:10.1080/14786437208229212.
- **Gane**, N. « The Direct Measurement of the Strength of Metals on a Sub-Micrometre Scale ». Proceedings of the Royal Society A: Mathematical, Physical and Engineering Sciences 317, no 1530 (23 juin **1970**): 367-91. doi:10.1098/rspa.1970.0122.
- **Gianola,** D. S., A. Sedlmayr, R. Mönig, C. A. Volkert, R. C. Major, E. Cyrankowski, S. a. S. Asif, O. L. Warren, et O. Kraft. « In situ nanomechanical testing in focused ion beam and scanning electron microscopes ». Review of Scientific Instruments 82, no 6 (1 juin **2011**): 063901. doi:10.1063/1.3595423.
- **Greer**, Julia R., et William D. Nix. « Nanoscale gold pillars strengthened through dislocation starvation ». Physical Review B 73, no 24 (12 juin **2006**): 245410. doi:10.1103/PhysRevB.73.245410.
- **Greer,** Julia R., Warren C. Oliver, et William D. Nix. « Size dependence of mechanical properties of gold at the micron scale in the absence of strain gradients ». Acta Materialia 53, no 6 (avril **2005**): 1821-30. doi:10.1016/j.actamat.2004.12.031.
- Gruber, Patric A., Christian Solenthaler, Eduard Arzt, et Ralph Spolenak. « Strong single-crystalline Au films tested by a new synchrotron technique ». Acta Materialia 56, no 8 (mai **2008**): 1876-89. doi:10.1016/j.actamat.2007.12.043.
- **Hall**, E. O. « The Deformation and Ageing of Mild Steel: III Discussion of Results ». Proceedings of the Physical Society. Section B 64, no 9 (**1951**): 747. doi:10.1088/0370-1301/64/9/303.
- **Haque**, M.a., H.d. Espinosa, et H.j. Lee. « MEMS for In Situ Testing—Handling, Actuation, Loading, and Displacement Measurements ». MRS Bulletin 35, no 05 (mai **2010**): 375-81. doi:10.1557/mrs2010.570.
- **Huang**, Ling, Qing-Jie Li, Zhi-Wei Shan, Ju Li, Jun Sun, et Evan Ma. « A new regime for mechanical annealing and strong sample-size strengthening in body centred cubic molybdenum ». Nature Communications 2 (22 novembre **2011**): 547. doi:10.1038/ncomms1557.
- **Issa**, Inas, Jonathan Amodeo, Julien Réthoré, Lucile Joly-Pottuz, Claude Esnouf, Julien Morthomas, Michel Perez, Jérome Chevalier, et Karine Masenelli-Varlot. « In situ investigation of MgO nanocube deformation at room temperature ». Acta Materialia 86 (**2015**): 295-304.
- **Jennings** Andrew T**.**, Michael J. Burek, et Julia R. Greer. « Microstructure versus

Size: Mechanical Properties of Electroplated Single Crystalline Cu Nanopillars ». Physical Review Letters 104, no 13 (2 avril **2010**): 135503.

- **Kaufmann**, D., R. Mönig, C.A. Volkert, et O. Kraft. « Size Dependent Mechanical Behaviour of Tantalum ». International Journal of Plasticity 27, no 3 (mars **2011**): 470-78. doi:10.1016/j.ijplas.2010.08.008.
- **Kendall**, K. « The Impossibility of Comminuting Small Particles by Compression ». Nature 272, no 5655 (20 avril **1978**): 710-11. doi:10.1038/272710a0.
- **Khan**, M. Y., L. M. Brown, et M. M. Chaudhri. « The Effect of Crystal Orientation on the Indentation Cracking and Hardness of MgO Single Crystals ». Journal of Physics D: Applied Physics 25, no 1A (**1992**): A257. doi:10.1088/0022-3727/25/1A/039.
- **Kiener,** D., C. Motz, et G. Dehm. « Dislocation-Induced Crystal Rotations in Micro-Compressed Single Crystal Copper Columns ». Journal of Materials Science 43, no 7 (avril **2008**): 2503-6. doi:10.1007/s10853-008-2531-3.
- **Kiener**, D., C. Motz, T. Schöberl, M. Jenko, et G. Dehm. « Determination of Mechanical Properties of Copper at the Micron Scale ». Advanced Engineering Materials 8, no 11 (novembre **2006**): 1119-25. doi:10.1002/adem.200600129.
- **Kiener**, D., C. Motz, T. Schöberl, M. Jenko, et G. Dehm. « Determination of Mechanical Properties of Copper at the Micron Scale ». Advanced Engineering Materials 8, no 11 (novembre **2006**): 1119-25. doi:10.1002/adem.200600129.
- **Kiener**, Daniel, Christian Motz, Gerhard Dehm, et Reinhard Pippan. « Overview on Established and Novel FIB Based Miniaturized Mechanical Testing Using in-Situ SEM ». International Journal of Materials Research 100, no 8 (août **2009**): 1074-87. doi:10.3139/146.110149.
- **Kim, Ju-Young**, Dongchan Jang, et Julia R. Greer. « Crystallographic Orientation and Size Dependence of Tension–compression Asymmetry in Molybdenum Nano-Pillars ». International Journal of Plasticity 28, no 1 (janvier **2012**): 46-52. doi:10.1016/j.ijplas.2011.05.015.
- **Kim, Ju-Young**, Dongchan Jang, et Julia R. Greer. « Tensile and compressive behavior of tungsten, molybdenum, tantalum and niobium at the nanoscale ». Acta Materialia 58, no 7 (**2010**): 2355-63.
- **Korte,** S., et W.J. Clegg. « Discussion of the Dependence of the Effect of Size on the Yield Stress in Hard Materials Studied by Microcompression of MgO ». Philosophical Magazine 91, no 7-9 (mars **2011**): 1150-62. doi:10.1080/14786435.2010.505179.
- **Kraft**, Oliver, Patric A. Gruber, Reiner Mönig, et Daniel Weygand. « Plasticity in Confined Dimensions ». Annual Review of Materials Research 40, no 1 (**2010**): 293-317. doi:10.1146/annurev-matsci-082908-145409.
- **Lee**, Subin, Jiseong Im, Youngdong Yoo, Erik Bitzek, Daniel Kiener, Gunther Richter, Bongsoo Kim, et Sang Ho Oh. « Reversible cyclic deformation mechanism of gold nanowires by twinning–detwinning transition evidenced from in situ TEM ». Nature Communications 5 (8 janvier **2014**). doi:10.1038/ncomms4033.
- **Legros**, M., D.s. Gianola, et C. Motz. « Quantitative In Situ Mechanical Testing in Electron Microscopes ». MRS Bulletin 35, no 05 (mai **2010**): 354-60. doi:10.1557/mrs2010.567.
- **Lloyd**, S. J., J. M. Molina-aldareguia, et W. J. Clegg. « Deformation under nanoindents in sapphire, spinel and magnesia examined using transmission electron microscopy ». Philosophical Magazine A 82, no 10 (1 juillet **2002**): 1963-69. doi:10.1080/01418610208235708.

- Maaß, Robert, Lucas Meza, Bin Gan, Sammy Tin, et Julia.R. Greer. « Ultrahigh

Strength of Dislocation-Free Ni3Al Nanocubes ». Small 8, nº 12 (25 juin 2012): 1869‑75. doi:10.1002/smll.201102603.

- **Maaß**, R., S. Van Petegem, D. Grolimund, H. Van Swygenhoven, D. Kiener, et G. Dehm. « Crystal rotation in Cu single crystal micropillars: In situ Laue and electron backscatter diffraction ». Applied Physics Letters 92, no 7 (18 février **2008)**: 071905. doi:10.1063/1.2884688.
- **Michler**, Johann, Kilian Wasmer, Stephan Meier, Fredrik Östlund, et Klaus Leifer. « Plastic Deformation of Gallium Arsenide Micropillars under Uniaxial Compression at Room Temperature ». Applied Physics Letters 90, no 4 (**2007**): 043123. doi:10.1063/1.2432277.
- **Minor**, Andrew M., S. A. Syed Asif, Zhiwei Shan, Eric A. Stach, Edward Cyrankowski, Thomas J. Wyrobek, et Oden L. Warren. « A new view of the onset of plasticity during the nanoindentation of aluminium ». Nature Materials 5, no 9 (septembre **2006**): 697-702. doi:10.1038/nmat1714.
- **Minor**, A. M., J. W. Morris, et E. A. Stach. « Quantitative in Situ Nanoindentation in an Electron Microscope ». Applied Physics Letters 79, no 11 (**2001**): 1625. doi:10.1063/1.1400768.
- **Mook**, W. M., C. Niederberger, M. Bechelany, L. Philippe, et J. Michler. « Compression of Freestanding Gold Nanostructures: From Stochastic Yield to Predictable Flow ». Nanotechnology 21, no 5 **(2010**): 055701. doi:10.1088/0957-4484/21/5/055701.
- **Mook**, W. M., J. D. Nowak, C. R. Perrey, C. B. Carter, R. Mukherjee, S. L. Girshick, P. H. McMurry, et W. W. Gerberich. « Compressive stress effects on nanoparticle modulus and fracture ». Physical Review B 75, no 21 (22 juin **2007**): 214112. doi:10.1103/PhysRevB.75.214112.
- **Mordehai,** Dan, Seok-Woo Lee, Björn Backes, David J. Srolovitz, William D. Nix, et Eugen Rabkin. « Size effect in compression of single-crystal gold microparticles ». Acta Materialia 59, no 13 (août **2011**): 5202-15. doi:10.1016/j.actamat.2011.04.057.
- **Nadgorny,** Edward M., Dennis M. Dimiduk, et Michael D. Uchic. « Size Effects in LiF Micron-Scale Single Crystals of Low Dislocation Density ». Journal of Materials Research 23, no 11 (novembre **2008**): 2829-35. doi:10.1557/JMR.2008.0349.
- **Ng, K. S**., et A. H. W. Ngan. « Stochastic nature of plasticity of aluminum micro-pillars ». Acta Materialia 56, no 8 (**2008**): 1712-20.
- **Norfleet**, D.M., D.M. Dimiduk, S.J. Polasik, M.D. Uchic, et M.J. Mills. « Dislocation Structures and Their Relationship to Strength in Deformed Nickel Microcrystals ». Acta Materialia 56, no 13 (août **2008**): 2988-3001. doi:10.1016/j.actamat.2008.02.046.
- **Östlund**, Fredrik, Philip R. Howie, Rudy Ghisleni, Sandra Korte, Klaus Leifer, William J. Clegg, et Johann Michler. « Ductile–brittle transition in micropillar compression of GaAs at room temperature ». Philosophical Magazine 91, no 7-9 (1 mars 2011): 1190-99. doi:10.1080/14786435.2010.509286.
- **Page**, Trevor F., Warren C. Oliver, et Carl J. McHargue. « The deformation behavior of ceramic crystals subjected to very low load (nano)indentations ». Journal of Materials Research 7, no 02 (**1992**): 450-73. doi:10.1557/JMR.1992.0450.
- **Parthasarathy**, Triplicane A., Satish I. Rao, Dennis M. Dimiduk, Michael D. Uchic, et Dallas R. Trinkle. « Contribution to size effect of yield strength from the stochastics of dislocation source lengths in finite samples ». Scripta Materialia 56, no 4 (février **2007**): 313-16. doi:10.1016/j.scriptamat.2006.09.016.
- **Petch**. N.J « The cleavage strength of polycrystals». Journal of Iron Steel Inst. 174:25–28 (**1953**)
- **Rao**, S. I., D. M. Dimiduk, T. A. Parthasarathy, M. D. Uchic, M. Tang, et C. Woodward. « Athermal mechanisms of size-dependent crystal flow gleaned from three-

dimensional discrete dislocation simulations ». Acta Materialia 56, no 13 (août **2008**): 3245-59. doi:10.1016/j.actamat.2008.03.011.

- **Richter**, G., Hillerich, K., Gianola, D.S., Mönig, R., Kraft, O., Volkert, C.A., **2009**. Ultrahigh Strength Single Crystalline Nanowhiskers Grown by Physical Vapor Deposition. Nano Lett. 9, 3048–3052. doi:10.1021/nl9015107
- **Romeis**, S., J. Paul, M. Ziener, et W. Peukert. « A Novel Apparatus for in Situ Compression of Submicron Structures and Particles in a High Resolution SEM ». Review of Scientific Instruments 83, no 9 (**2012**): 095105. doi:10.1063/1.4749256.
- **Rzepiejewska-Malyska**, K.a., G. Buerki, J. Michler, R.c. Major, E. Cyrankowski, S.a.s. Asif, et O.l. Warren. « In situ mechanical observations during nanoindentation inside a high-resolution scanning electron microscope ». Journal of Materials Research 23, no 07 (**2008**): 1973-79. doi:10.1557/JMR.2008.0240.
- **Schneider**, A. S., B. G. Clark, C. P. Frick, P. A. Gruber, et E. Arzt. « Effect of orientation and loading rate on compression behavior of small-scale Mo pillars ». Materials Science and Engineering: A 508, no 1-2 (20 mai **2009**): 241-46. doi:10.1016/j.msea.2009.01.011.
- **Shade**, P. A., R. Wheeler, Y. S. Choi, M. D. Uchic, D. M. Dimiduk, et H. L. Fraser. « A combined experimental and simulation study to examine lateral constraint effects on microcompression of single-slip oriented single crystals ». Acta Materialia 57, no 15 (septembre **2009**): 4580-87. doi:10.1016/j.actamat.2009.06.029.
- **Shan**, Z. W., Raja K. Mishra, S. A. Syed Asif, Oden L. Warren, et Andrew M. Minor. « Mechanical annealing and source-limited deformation in submicrometre-diameter Ni crystals ». Nature Materials 7, no 2 (février **2008**): 115-19. doi:10.1038/nmat2085.
- **SMITHD** A., and BOWKETTK,. M., **1968**, Fourth European Regional Conference on Electron Microscopy, Rome, Vol. 1 (Rome: Tipografia Poliglotti Vaticana), p. 261.
- **Stach,** Eric A., Tony Freeman, Andrew M. Minor, Doug K. Owen, John Cumings, Mark A. Wall, Tomas Chraska, et al. « Development of a Nanoindenter for In Situ Transmission Electron Microscopy ». Microscopy and Microanalysis: The Official Journal of Microscopy Society of America, Microbeam Analysis Society, Microscopical Society of Canada 7, no 6 (novembre **2001**): 507-17. doi:10.1017.S1431927601010492.
- **Stölken**, J. S., et A. G. Evans. « A microbend test method for measuring the plasticity length scale ». Acta Materialia 46, no 14 (1 septembre **1998**): 5109-15. doi:10.1016/S1359-6454(98)00153-0.
- **Sun,** Qiaoyan, Qiang Guo, Xi Yao, Lin Xiao, Julia R. Greer, et Jun Sun. « Size Effects in Strength and Plasticity of Single-Crystalline Titanium Micropillars with Prismatic Slip Orientation ». Scripta Materialia 65, no 6 (septembre **2011**): 473-76. doi:10.1016/j.scriptamat.2011.05.033.
- **Uchic,** Michael D., Dennis M. Dimiduk, Jeffrey N. Florando, et William D. Nix. « Exploring specimen size effects in plastic deformation of Ni3(Al, Ta) ». In Symposium BB – Defect Properties and Related Phenomena in Intermetallic Alloys, Vol. 753. MRS Online Proceedings Library, **2003.** doi:10.1557/PROC-753-BB1.4.
- **Uchic**, M. D. « Sample Dimensions Influence Strength and Crystal Plasticity ». Science 305, no 5686 (13 août **2004**): 986-89. doi:10.1126/science.1098993.
- **Uchic**, Michael D., et Dennis M. Dimiduk. « A methodology to investigate size scale effects in crystalline plasticity using uniaxial compression testing ». Materials Science and Engineering: A, Dislocations 2004An International Conference on the Fundamentals of Plastic Deformation, 400-401 (25 juillet **2005**): 268-78. doi:10.1016/j.msea.2005.03.082.
- **Volkert**, C. A., et E. T. Lilleodden. « Size effects in the deformation of sub-micron Au columns ». Philosophical Magazine 86, no 33-35 (21 novembre **2006**): 5567-79.

doi:10.1080/14786430600567739.

- **Williams,** David B., et C. Barry **Carter.** Transmission Electron Microscopy: A Textbook for Materials Science. 2. ed. New York: Springer, **2009.**chapter 2.
- **Ye, Jia**, Raja K. Mishra, Alan R. Pelton, et Andrew M. Minor. « Direct Observation of the NiTi Martensitic Phase Transformation in Nanoscale Volumes ». Acta Materialia 58, no 2 (janvier **2010**): 490-98. doi:10.1016/j.actamat.2009.09.027.
- **Zhang, H**., B.E. Schuster, Q. Wei, et K.T. Ramesh. « The Design of Accurate Micro-Compression Experiments ». Scripta Materialia 54, no 2 (janvier **2006**): 181-86. doi:10.1016/j.scriptamat.2005.06.043.
- **Zheng, Kun**, Chengcai Wang, Yong-Qiang Cheng, Yonghai Yue, Xiaodong Han, Ze Zhang, Zhiwei Shan, et al. « Electron-Beam-Assisted Superplastic Shaping of Nanoscale Amorphous Silica ». Nature Communications 1 (1 juin **2010**): 24. doi:10.1038/ncomms1021.

Part A

Chapter 2

In situ TEM Nanocompression of MgO Nanocubes: Material & Techniques

Magnesium oxide, or **magnesia**, has an empirical formula of MgO and consists of a lattice of Mg^{2+} ions and O^{2-} ions held together by ionic bonding. So far, it is an ionic **ceramic** with the B1 crystalline structure (NaCl structure, rock salt) which has been widely studied in the past decades for its potential application as a refractory material. The phase B1 of MgO is **stable** under high temperature until > 3000 K (T_f) and high pressure until 200 GPa. MgO is also considered as a **model material** of ionic crystal, due to the low electronegativity of magnesium and the high electronegativity of oxygen which implies the description of the structure by the unique interaction between punctual charged particles [*Matsui (1989)*]. Hence, it is a **model material**, for dislocation properties analysis in B1-structured alkali halides and other ionic ceramics (e.g. NaCl, LiF, KCl, CaO, etc.) [*Takeuchi et al. (2009)*]. Moreover, the surface the most stable is the surface formed with (100) crystallographic planes. Therefore a bottom-up approach used to form ***MgO single crystals*** results often with ***cubic objects,*** revealing the crystal growing along these planes.

This chapter provides a description of the ***crystallographic structure***, as well as the ***elastic*** and ***plastic properties*** of MgO. Two ***synthesis*** methods used to synthesize MgO nanocubes are presented, followed by a description of the different ***TEM and SEM modes*** Used for their characterization.

In a second part, the ***in situ TEM nanocompression technique*** is presented, going from a presentation of the sample holder and data acquisition. S***ubstrate treatments*** and ***material deposition*** optimization will also be described. ***DIC*** (Digital image Correlation) is also presented. It was used to correct a possible displacement of the diamond punch (fixed part of the setup test) and thus to obtain a real displacement (real deformation of the sample). Finally, a few pieces of information will be given regarding the potential used to perform Molecular Dynamics (***MD***) simulation.

2.1 MgO: Material characteristics

2.1.1 *Crystallographic Structure and Phase Stability*

MgO crystallizes in a cubic cell with a rock-salt structure (NaCl-type). This crystal structure consists in a Bravais Face centered cubic (FCC) lattice corresponding to the space group $Fm\bar{3}m$ (n° 225). The unit cell consists of a FCC lattice of O^{2-} ions with Mg^{2+} ions occupying all the octahedral sites (*or vice versa*), as shown *Figure 25*-a. Thus, it can be described also by two interpenetrating FCC structures of oxygen (blue FCC, in *Figure 25*-b) and Magnesium (Red FCC in *Figure 25*-b), displaced from each other by 0.5 of the body diagonal.

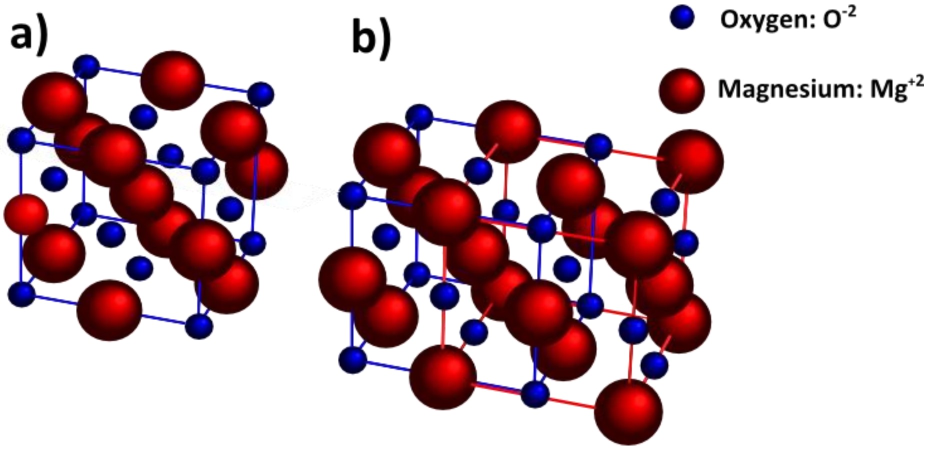

Figure 25: ***a)*** *Unit cell of MgO, B1 structure (NaCl-type), O in FCC lattice, Mg in octahedral sites.* ***b)*** *Two interpenetrating FCC structures of oxygen (blue FCC) and Magnesium (Red FCC) displaced from each other by 0.5 of the body diagonal.*

Atomic positions in a unit cell are given by Wyckoff positions 4a (0,0,0) and 4b (½, ½, ½) for oxygen and magnesium, respectively. The unit cell contains 4 atoms of oxygen and 4 atoms of magnesium.

This conventional structure B1 of MgO is ***stable at high pressure*** until 200 GPa [*Amodeo. J thesis (2011)*]. The unit cell lattice parameter a varies from 4.21and 3.75 Å under relative pressures from 0 to 100 GPa. No phase transformation has been observed experimentally even at high pressure (> 200 GPa reachable in DAC (Diamond Anvil Cell) [*Duffy et al. (1995)*]. However, computational calculations predict a phase transition from the B1 structure to the B2 one above 400 GPa (at 597 GPa [*Alfé (2005)*], at 712 GPa [*Habas et al. (1998)*]). Thus it is a stable material phase under very high pressures.

Moreover, ***melting temperature*** of MgO occurs in the range of ***3000 K at ambient pressure*** [*Amodeo. J thesis (2011)*]. It is shown that the melting temperature increases when the pressure increases. An increase of the melting temperature of MgO B1 structure of 1000K at 30 GPa was indeed observed in experiments performed in DAC [*Zerr & Boehler (1994)*]. So far, simulations showed a more rapid increase of the melting temperature with pressure, up to 8000 K at 140 GPa [*Alfé (2005)*]. Molecular Dynamics (MD) simulations [*Aguado & Madden (2005)*] could reproduce a less steep slope, closer to that obtained experimentally [*Zerr & Boehler (1994*] once the simulated MgO contained initially structural defects. Anyway, all these experimental and simulations show an increase of the melting temperature with increase pressure, which shows the high stability of the MgO B1 structure at ambient temperature.

2.1.2 *Elastic properties*

Elastic properties of crystals are described by a linear relationship between stress σ and strain ε. This linear relationship is characterized by elastic constants *C*. In a 3D crystal, the stress and the strain are described as tensors, which are defined as follows: ***Stress*** has the meaning of local applied "pressure". It has components σ_{ij}, showing that the force can be applied along 3 directions "*i*" and 3 faces "*j*". ***Strain*** determines relative atomic displacements and has components

$\varepsilon_{ij} = \frac{1}{2\left(\frac{du_i}{dx_j}+\frac{duj}{dx_i}\right)}$, Where u_i is the displacement in the "*i*" direction and x_j is the direction along which u_i may vary. Similar definitions apply for the displacement u_j along the direction x_i. In the general case, one can relate the stress and the strain in a 3D crystal by the general form of Hooke's law:

$$\sigma_{ij} = \sum_{kl} C_{ijkl}\varepsilon_{kl}$$

The most general form of the matrix *C* has 3x3x3x3=81 components. However, due to symmetries in the stress and strain tensors ($\sigma_{ij} = \sigma_{ji}$ or $\varepsilon_{kl} = \varepsilon_{lk}$), each of them is described by 6 independents components only ($\sigma_{xx,}\sigma_{yy}, \sigma_{zz}, \sigma_{yz}, \sigma_{zx}, \sigma_{xy}$) & ($\varepsilon_{xx,}\varepsilon_{yy}, \varepsilon_{zz}, \varepsilon_{yz}, \varepsilon_{zx}, \varepsilon_{xy}$). This reduces the matrix C to 36 elastic constants, as shown in **Figure 26**. There is a convention to denote elastic constants by C_{mn}, where the indices *m* and *n* are defined as 1=*xx*, 2=*yy*, 3=*zz* for the compression components and as 4=*yz*, 5=*zx*, 6=*xy* for the shear components. For example, $C_{xxxx} = C_{11}$, $C_{xxyy} = C_{12}$ and $C_{yzyz} = C_{44}$. For example, C_{yzyz} relates the shear stress on the face *y*, i.e. (010), along the z direction, and the strain on the same face, along the same direction. $C_{xxyy}=C_{12}$, relates the compressive stress on the face *x*, i.e. (100), along the *x* direction, and the strain on the face *y*, *i.e.* (010), along the *y* direction.

$$\begin{array}{ccccc}
 & & \begin{array}{cc}\text{compression} & \text{mixed}\end{array} & & \\
\begin{pmatrix}\sigma_{xx}\\ \sigma_{yy}\\ \sigma_{zz}\\ \hline \sigma_{yz}\\ \sigma_{zx}\\ \sigma_{xy}\end{pmatrix} & = & \left(\begin{array}{ccc|ccc} C_{11} & C_{12} & C_{13} & C_{14} & C_{15} & C_{16}\\ C_{21} & C_{22} & C_{23} & C_{24} & C_{25} & C_{26}\\ C_{31} & C_{32} & C_{33} & C_{34} & C_{35} & C_{36}\\ \hline C_{41} & C_{42} & C_{43} & C_{44} & C_{45} & C_{46}\\ C_{51} & C_{52} & C_{53} & C_{54} & C_{55} & C_{56}\\ C_{61} & C_{62} & C_{63} & C_{64} & C_{65} & C_{66}\end{array}\right) & \begin{pmatrix}\varepsilon_{xx}\\ \varepsilon_{yy}\\ \varepsilon_{zz}\\ \hline \varepsilon_{yz}\\ \varepsilon_{zx}\\ \varepsilon_{xy}\end{pmatrix} & \begin{array}{c}\text{compression}\\ \\ \\ \\ \text{shear}\end{array}\\
\text{stress} & & \begin{array}{cc}\text{mixed} & \text{shear}\end{array} & \text{strain} &
\end{array}$$

Figure 26: *C matrix of 36 components relating stress and strain tensors.*

In crystals, many of the C_{mn} components are the same due to symmetries in the crystallographic phase. In particular, in **cubic crystals**: $\mathbf{C_{11}} = C_{22} = C_{33}$**;** $\mathbf{C_{12}} = C_{21} = C_{23} = C_{32} = C_{13} = C_{31}$**;** $\mathbf{C_{44}} = C_{55} = C_{66}$ due the fact that *x*, *y*, and *z* axes are identical by symmetry. Also the off-diagonal shear components are null, i.e. $C_{45} = C_{54} = C_{56} = C_{65} = C_{46} = C_{64} = 0$, and mixed compression/shear coupling does not occur, i.e. $C_{14} = C_{41} = ... = 0$. This can be understood by simply drawing a cube, as in **Figure 27**-b, and by noticing the similarities between the groups of compression components and shear components. The absence of mixed components in a cubic crystal can also be understood this way. As a conclusion, the cubic elastic components matrix reduces to the form shown in **Figure 27**-a.

a)

$$\begin{pmatrix} C_{11} & C_{12} & C_{12} & & & \\ C_{12} & C_{11} & C_{12} & & 0 & \\ C_{12} & C_{12} & C_{11} & & & \\ & & & C_{44} & 0 & 0\\ & 0 & & 0 & C_{44} & 0\\ & & & 0 & 0 & C_{44}\end{pmatrix}.$$

b)

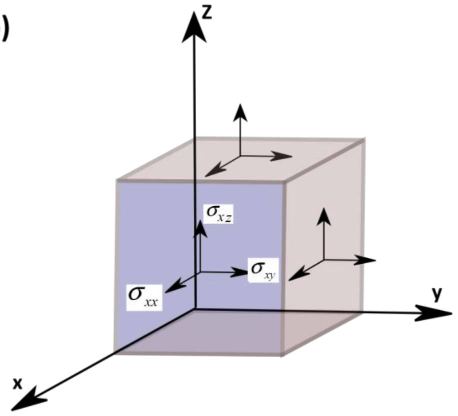

Figure 27: a) reduced C matrix for cubic crystals **b)** *Stress components on different faces along different directions.*

One can see that elasticity in cubic crystals can be described by only three components C_{11}, C_{12}, C_{44}. In general, C_{44} represents the shear resistance along the <100> direction and ½ (C_{11}-C_{12}) represents the shear resistance along the <110> direction.

In isotropic materials these two parameters are equal and C_{44} represents the shear modulus μ in this case. However, due to the symmetry in cubic systems along the <111> direction, cubic materials cannot be considered as isotropic and the components C_{44} and 1/2(C_{11}-C_{12}) are not equal. The degree of anisotropy is then described by the coefficient $A = \frac{2\,C_{44}}{(C_{11}-C_{12})}$.

MgO is anisotropic along the <100>, <110> and <111> directions and $A > 1$. Thus, the shear modulus is defined as μ=$\sqrt{c_{44}(\frac{C_{11}-C_{12}}{2})}$. Moreover, the Young's modulus is defined by E=$(c_{11}-c_{12})(\frac{2C_{12}+C_{11}}{C_{12}+C_{11}})$.

2.1.3 *Plastic properties (slip systems) & Critical Resolved Shear Stress (CRSS)*

MgO is more ductile than a conventional ceramic. Bulk MgO single crystals accommodate a slight amount of strain before failure (~7% for <100> oriented samples) at room temperature (RT), while larger deformation is reached at higher temperature [*Hulse and Pask (1960)*] [*Hulse et al. (1963)*].

I. Slip systems

In general, under a directional solicitation, plastic deformation in crystalline systems occurs through the activation of slip systems that identify dislocations motion and direction. Slip systems are defined by slip planes and slip direction. In general, s**lip planes** correspond to closed-packed planes (highest atomic density) and the **direction of the slip** corresponds to the shortest lattice translation (shortest interatomic distance), i.e. the Burgers vector.

In general, in FCC structures, slip occurs in the <110> direction. Therefore, dislocations have Burgers vectors of type ½<110> (**b**=$\frac{a}{2} < 110 >$), and slip planes are {111}, {110} and {100}. Depending on the solicitation direction and Schmid's law, slip plane families with the highest Schmid factor are preferentially activated. ***Table 1*** presents the Schmid factors corresponding to the slip plane families {111}, {110} and {100} in the FCC structure, for three solicitation directions : <100>, <110> and <111>.

Table 1: *Schmid factors "**S**" for slips systems in three slip planes {111}, {110} and {100} in FCC structure, depending on three solicitation directions <100>, <110> and <111>.*

Slip system / **Direction of Solicitation**	**½<110>{111}**	**½<110>{110}**	**½<110>{100}**
<100>	**S = 0.41** For 8/12 systems	**S = 0.5** For 4/6 systems	**S = 0** For all systems
<110>	**S = 0.41** For 4/12 systems	**S = 0.25** For 4/6 systems	**S = 0.35** For 4/6 systems
<111>	**S = 0.27** For 6/12 systems	**S = 0** For all systems	**S = 0.47** For 3/6 systems

In ionic crystals, a restriction on certain slip plans appears when displacing ions of the same charge near a certain inter-distance limit [*J. Gilman (1959)*]. Therefore dislocations in MgO glide more easily in {110} planes than in {100} and {111} ones, because of this restriction. in MgO, the activation of dislocations in {111} planes are rarely observed [*Clauer & Wilcox (1976)*]-[*Stretton et al. (2001)*].

Thus, it can be considered that MgO has two slip systems families: ½<110>{110} known as soft slip system family (*6 systems*), and ½<110>{100} known as hard slip system family (*6 systems*). Depending on the solicitation direction, the slip system with the highest Schmid factor is activated. Taking, for example, the <100> solicitation direction, the soft slip system family ½<110>{110} is activated. Indeed, it has a Schmid factor S=0.5 for 4/6 systems along {110} planes – S=0 for the two others ones, as shown in ***Figure 28***. On the contrary, S=0 for all the systems of the hard slip system type ½<110>{100}.

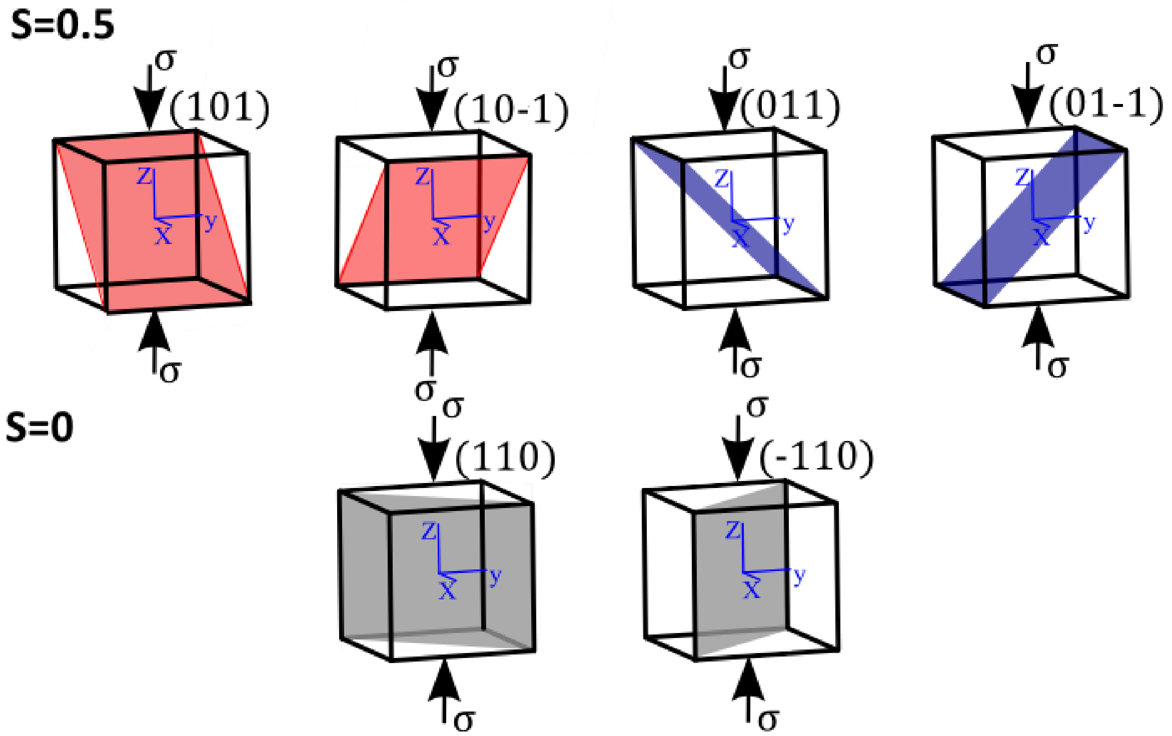

Figure 28: *6 systems of the soft slip system type ½<110>{110}. Solicitation direction is* ***[001]*** *(Z direction). 4 slip planes* ($(\mathbf{101}), (\mathbf{10\bar{1}}), (\mathbf{011})$& $(\mathbf{01\bar{1}})$) *over 6 are active in this case, with a Schmid factor 0.5. The two other systems, with* $(\mathbf{110})$ *and* $(\mathbf{\bar{1}10})$ *planes have a Schmid factor = 0.*

II. *Critical Resolved Shear Stress (CRSS)*

Slip occurs on a given slip system when the resolved shear stress (the projection of the applied stress onto the slip system) reaches the CRSS of this particular system. Thus, the **CRSS** is defined as $\boldsymbol{S} \mathbf{x}\, \boldsymbol{\sigma}$, where **σ** is the applied stress and **S** is the Schmid factor of the slip system in the orientation defined by the applied stress. For a given slip system, the CRSS itself is dependent on many factors, as the material nature, the slip system type and temperature.

For bulk single crystal MgO at room temperature, the CRSS is dependent on the competition between lattice friction and solution hardening on the two main slip system families, ½<110>{110} and ½<110>{100} of the crystalline structure. ½<110>{110} dislocation glide involves the nucleation of kink-pairs, typical of the lattice friction regime. This specific process leads to a characteristic dislocation microstructure made of rate-controlled long screw dislocations [*Appel et al. (1977)*] [*Messerschmidt (2010)*]. Above a transition temperature (~600 K for ½<110> {110} slip systems and 1500 K for ½<110>{100}), lattice friction is overcome and plastic strain is accommodated by curved dislocations [*Clauer & Wilcox*

(1976)][*Haasen et al. (1986)*], ruled by the strength of dislocation– dislocation “forest” interactions [*Copley & Pask (1965)*][*Amodeo-2014*].

The literature contain numerous studies on deformation of bulk single crystal MgO oriented along the <100> direction. This is due to the fact that {100} are the most stable surfaces of MgO and thus are known as cleavage planes in MgO {110} are the slip planes with the highest Schmid factor. Therefore one can find many experimental and simulations works on these slip systems [*Amodeo. J thesis (2011)*] at different temperatures and environmental pressures. At RT and ambient pressure, the CRSS of ½ <110>{110} slip systems in single crystal bulk MgO, in the <100> solicitation direction, is in the range ~ 0.5 x 50 MPa ≅ 25 MPa. [*C. Hulse et al. (1960)*].

As a conclusion, the mechanical properties of MgO are well known. In addition, MgO is stable at small scale and high pressure [Duffy et al. (1995)]-[Zerr & Boehler (1994)].

In the following section, we present two bottom-up approaches for the synthesis of MgO will be presented. We will see that they result in perfectly well-shaped single crystal MgO nanocubes edged by {100} faces (most stable faces of MgO, as mentioned previously).

This sharp geometry permits a standard [001] compression axis, and will simplify the identification of the slip systems. It will also reduce the misorientation issues commonly observed in nanospheres compression tests.

2.2 Synthesis Methods of MgO nanocubes & Characterizations

MgO formation from Mg and oxygen molecules (O_2) as base components is a well-known chemical reaction. Magnesium is heated in an environment rich enough in oxygen. Mg becomes hot enough and supplies enough energy for oxygen molecules to split up, i.e. to break the very strong O=O double bond. Each magnesium atom gives two electrons to an oxygen atom, so that magnesium oxide is made of magnesium ions, Mg^{2+}, and oxide, O^{2-} ions, bonded by ionic bonds.

The surface the most stable of MgO is the surface formed with {100} crystallographic planes. Laters are called cleavage planes. Therefore a bottom-up approach used to form MgO single crystal results often in a cubic shape revealing the crystal growing along these plans.

Herein, single crystal magnesium oxide (MgO) nanoparticles with a perfectly cubic shape are synthesized using two different bottom-up methods. The first method is simple and rapid, and was described by Takahashi [*Takahashi(2007)*]. It consists in growing MgO single crystal nanocubes on a glass substrate by means of a domestic microwave oven. The second synthesis method is simple and classic and consists in burning commercial magnesium chips, in air as described in the pioneer work of Heidenreich [*Heidenreich (1942)]*.

2.2.1 *Synthesis Methods of MgO nanocubes*

I. Microwave method

This method consists in growing MgO single crystal nanocubes on a glass substrate by means of a domestic microwave oven, using commercial magnesium (Mg) chips (4-30 mesh) and steel wool as starting materials. Steel-wool is used to create arc discharges by microwave. Mg chips and steel-wool (0.5 g each) are put in an alumina crucible of volume ~3.6 10^{-4}m^3.

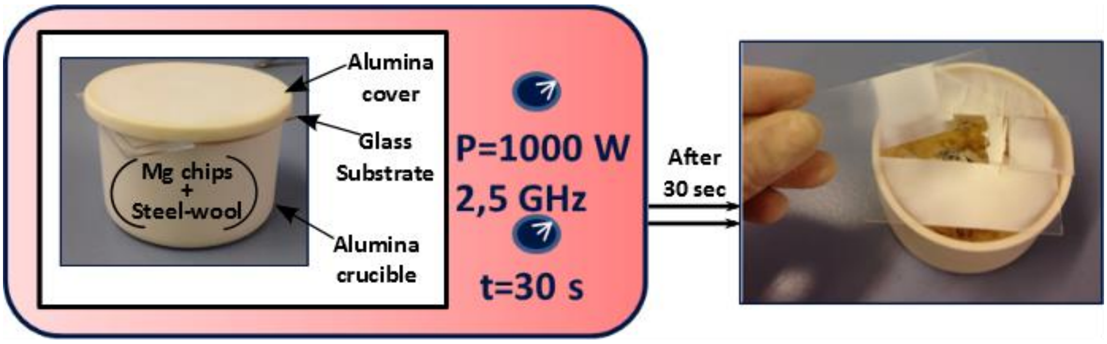

Figure 29 *Alumina crucible, containing 0.5 g of Mg chips and 0.5 g of steel-wool. The crucible is covered with a glass substrate and an alumina cap. Everything is placed in a domestic microwave operating at 2.45 GHz for 30 sec. This result in MgO nanocubes as a white powder deposited on the glass substrate.*

The glass substrate is put on the crucible and covered with an alumina cap, as shown in ***Figure 29***-left. This crucible is placed in a domestic microwave oven operating at 2.45 GHz. Microwave irradiation is carried out at the electric power level of 1000 W for 30 sec. The alumina crucible is taken out of the microwave oven after the crucible has cooled down to room temperature.

The MgO nanocubes, forming a white powder deposited on the glass substrate, as shown in ***Figure 29***-right, are characterized by Scanning Electron Microscopy (SEM) and dry deposited onto a TEM grid (Cu 300-mesh covered by a holey carbon film) for different TEM characterizations presented in the following sections. For the nanocompression experiments, the MgO nanocubes are either dry deposited on a sapphire substrate, or sometimes dispersed in ethanol before deposition on the sapphire substrate.

II. Burning Mg in air

The second synthesis method simply consists in burning the commercial magnesium chips in air, as described in the pioneer work of Heidenreich [*Heidenreich (1942)*] and shown in ***Figure 30***. This time, the smoke particles are caught directly on three substrates: a glass substrate for SEM imaging, a TEM grid for different TEM characterizations and the nanocompression sapphire substrate. The MgO nanocubes were sometimes dispersed in ethanol before deposition on the sapphire substrate.

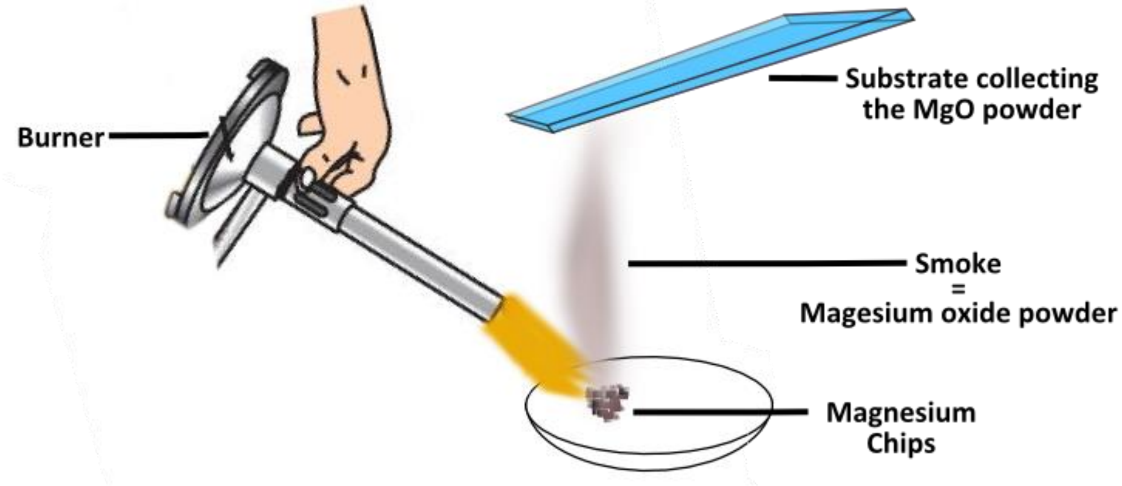

Figure 30: *Scheme of the ¨burning Mg chips in air¨ method. The smoke is caught on a glass substrate.*

For nanocubes synthesized by both methods described above, primary characterizations are carried out by SEM, Bright Field (BF)conventional TEM, Weak Beam Dark Field (WBDF-TEM), High Resolution TEM (HRTEM), and Energy-Dispersive Spectroscopy (EDS-TEM). Short descriptions of these TEM Modes are presented, especially since these modes, except HRTEM, are used during the in situ TEM nanocompression tests.

2.2.2 *SEM Characterizations of MgO nanocubes*

SEM images are acquired on a Zeiss Supra 55VP microscope. The acceleration voltage is fixed to 1 kV (sometimes to 3kV), and images are acquired with a secondary electron Everhardt–Thornley detector.

Typical SEM images of the white powder produced by the ***microwave*** method and deposited on the glass substrate are shown in *Figure 31*-b-c-d. This powder consists mostly of sharp nanocubes with edge sizes ranging from ∼10 to 500 nm, attached together by electrostatics forces edge-to-edge or surface-to-surface. The presence of particles smaller than 20 nm is clear from the SEM images (the smallest nanocubes detected by this method have sizes of 10 nm). This is confirmed by TEM observations.

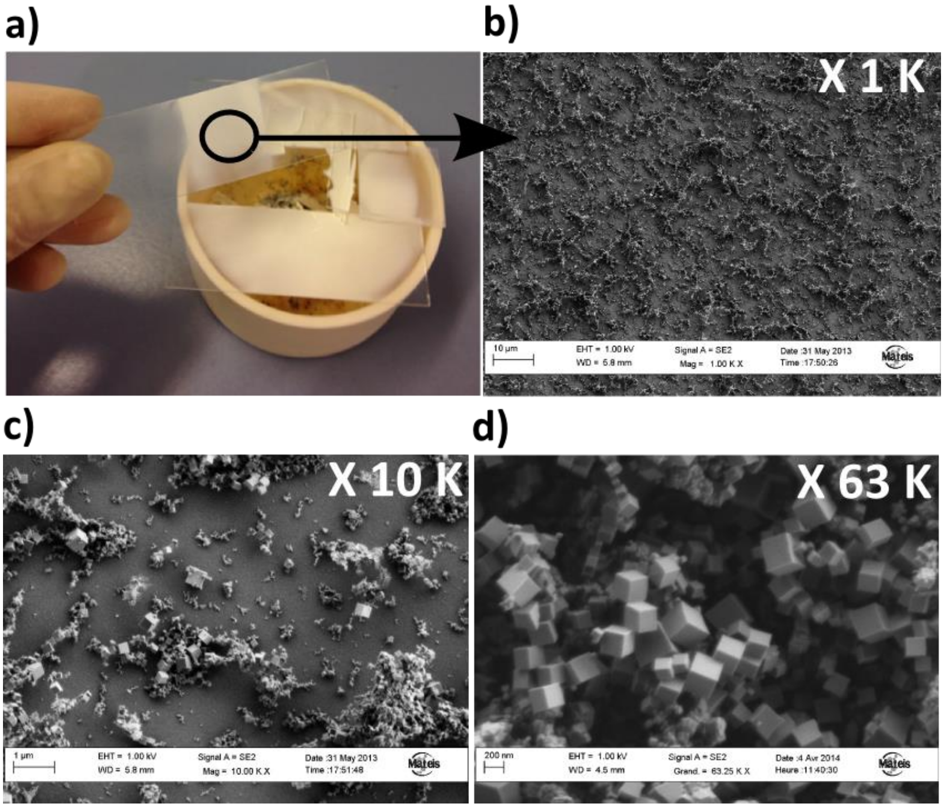

Figure 31: ***a)*** *MgO powder deposited on a glass substrate.* ***b-c*** *and* ***d)*** *SEM images of MgO nanocubes synthesized by ¨Microwave method¨.*

The powders produced by ***burning Mg in air*** also consist mostly of sharp nanocubes. The edge sizes lie in a narrower range: from 10 nm to ~ 200 nm. Typical SEM images of the white powder produced by this method and deposited on the glass substrate are shown in ***Figure 32***-a-b.

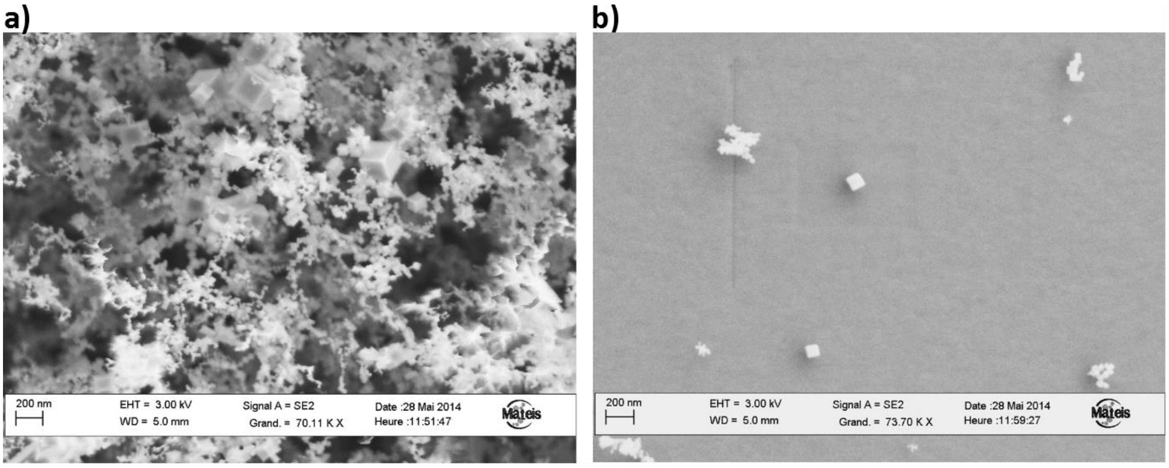

Figure 32: *SEM images of MgO nanocubes synthesized by ¨Burning Mg in air method¨.*

2.2.3 *TEM principles & different TEM Characterizations of MgO nanocubes*

In this section, and once for all the other parts of the dissertation; we present in detail TEM and its general layout components and functions, as well as the main observation modes used for the nanocube characterizations and during *in situ* nanocompression tests. Some of these modes are also used in works on transition alumina nanoparticles presented in the second part of the dissertation.

Different TEM characterizations carried out on MgO nanocubes are presented after each mode description.

I. TEM

Basically, TEM consists of passing a highly energetic and coherent electron beam travelling from an electron gun (the electron source in the JEOL 2010F is a ZrO/W sharp tip and works in field emission, thermally assisted) through a thin enough specimen (few nm to few 100s nm). Between the specimen stage and the electron gun, a condenser lens allows condensing and focusing the electron beam onto the specimen, as shown in *Figure 33*. A condenser aperture allows selecting the maximum visible area of the sample and is used to limit spherical aberrations. Herein, the diameter of the aperture often used is 70µm. Then the electron beam passes through the ultra-thin specimen. Thus, the highly energetic incident electrons interact with potentials in sample (nucleus of atoms and electrons), causing the scattering of incident electrons (elastic or inelastic scattering) through the crystal and provide composition, phase and crystallographic structural information on the sample. However, one must differentiate between two main considerations of electrons. So the electrons are either scattered by the sample atoms or diffracted by a family of planes *(hkl)* of the crystal. The

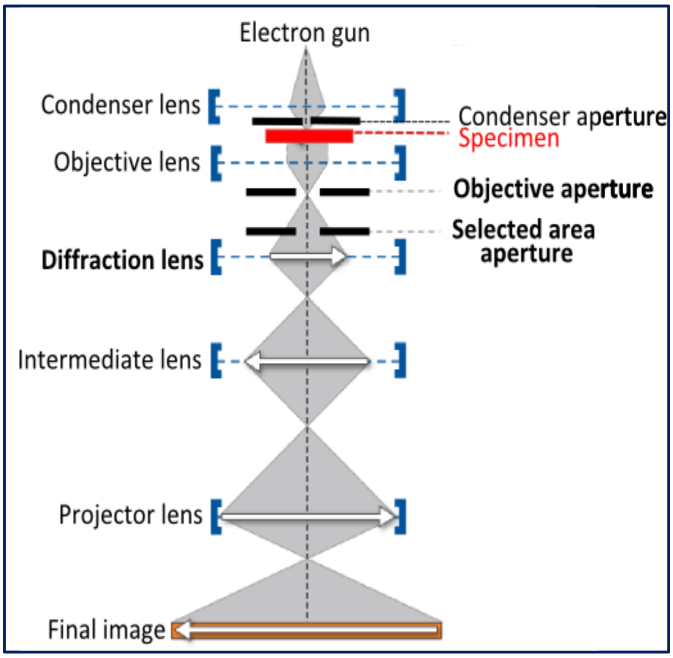

***Figure 33**: Layout of main components in a basic TEM and electron beam ray-diagram*

unscattered electrons (direct beam) are those that do not undergo interaction with the crystal or the sample.

Hence, two central modes exist in TEM, ***Imaging*** and ***Diffraction***. In both modes, an objective lens, the main magnifying lens, takes the electrons emerging from the exit surface of the specimen, disperses them to create a Diffraction Pattern (DP) in the back-focal plane (bfp) as shown in both ray-diagram in *Figure 34*, and recombines them to form an a magnified DP or a magnified image in the image plane.

Diffraction pattern (DP) is formed in the ***bfp*** of the objective lens and contains all information on the crystal structure (see *Figure 34*-a-b). Central beam is all direct (transmitted) beams, unaffected by the sample, and the diffraction spots are due to constructive interference of diffracted beams by *hkl* planes that satisfy the Bragg diffraction. Their distance from the central spot is inversely proportional to their inter-reticular distance. (It's a 2D representation of the reciprocal lattice). One can obtain the ***DP*** (see *Figure 34*-a) by using the selected area aperture that select a smaller area of the image plane (*image 1*) of the objective lens and thus reduces the intensity of the central beam relatively to the intensity of diffraction spots. To obtain as final image the ***DP***, the intermediate lens is weakened, that its focal length is made larger, in such a way its object plane become the back focal plane (***bfp***) of the objective lens that in turns coincides with the object plane of the projector lens (see red dot in *Figure 34*-a). A magnified representation of the ***DP*** is then produced on the fluorescent screen or the CCD camera.

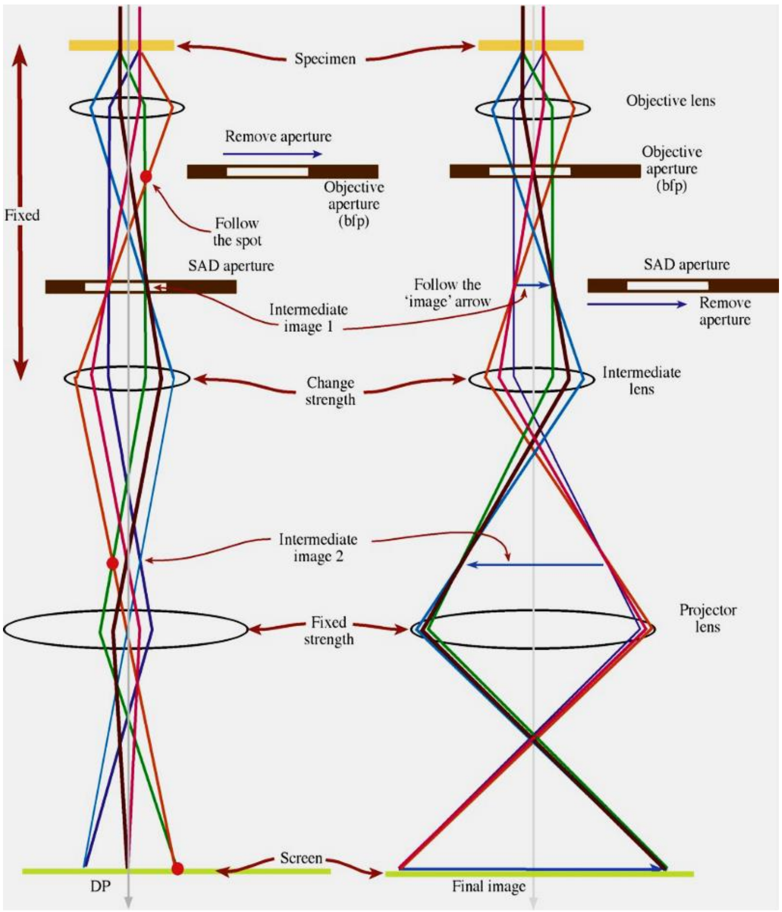

Figure 34: *Raydiagrams of the two basic operations for forming:* ***a)*** *DPs and* ***b)*** *contrast images of the sample in the TEM [William & Carter-book chap.9].*

In the ***imaging*** mode, the intermediate lens is readjusted so that its object plane becomes the image plane of the objective lens *(image 1)*; than the ***image 2*** is projected onto screen as final image (see *Figure 34*-b). The contrast in these conventional TEM images is mainly due to the diffraction/scattering contrast and mass-thickness contrast. Highly scattering regions are regions diffracting at high angles, heavy elements and thicker regions, all these appear darker. An objective aperture can be used to select smaller area of the ***bfp*** of the objective lens, thus its size controls selecting small angled diffraction beams and thus enhance contrast in image; in a way that area that are highly scattering appear darker. Thus it is often so-called contrast aperture or (diaphragm).

Conventional TEM images of MgO nanocubes were performed on a JEOL 2010F TEM to investigate the degree of perfection of the cubic shape of these MgO particles. Typical TEM images of MgO nanocubes synthesized by the microwave method described ***in section 2.2.1*** are shown in ***Figure 35***-a. The nanocubes synthesized by burning Mg in air are presented in the TEM image in ***Figure 35***-b. whatever the synthesis method, the MgO nanocubes are completely transparent to the electron beam and exhibit a perfect cubic shape. The dark and white lines observed in Figure-11-a are due to diffraction effect and (so-called Bragg lines).

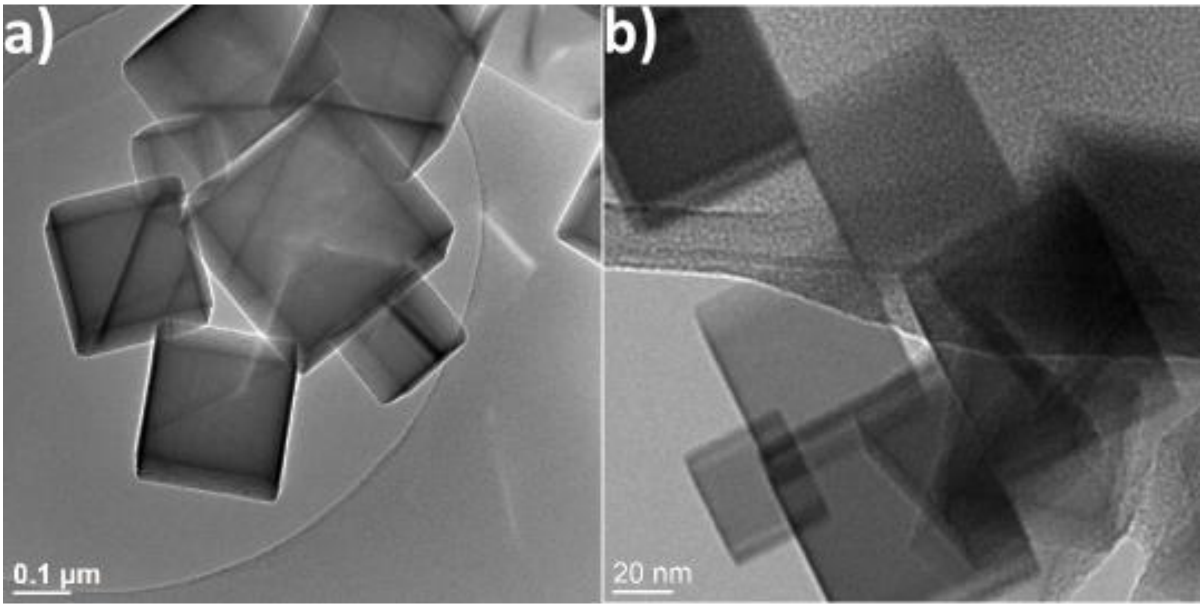

Figure 35: *Conventional BF TEM image of MgO nanocubes:* ***a)*** *Synthesized by Microwave Method and* ***b)*** *by Burning Mg in air.*

II. Bright Field & Dark Field Modes

The objective aperture allows, in the ***Diffraction*** mode, the choice of the central spot (direct beam) (see *Figure 36*-A) and later to switch into ***imaging*** mode. This allows forming a ***Bright Field (BF)*** image where all the non-diffracting areas appear bright-white and all the diffracting areas appear dark-black. Similarly, the choice of a specific ***diffraction*** spot in the ***DP*** (see *Figure 36*-B) and then switch to imaging mode leads to the formation of a ***Dark Field (DF)*** image, where all the areas containing the diffracting planes (*hkl)* appear bright-white while the other ones appear dark-black .

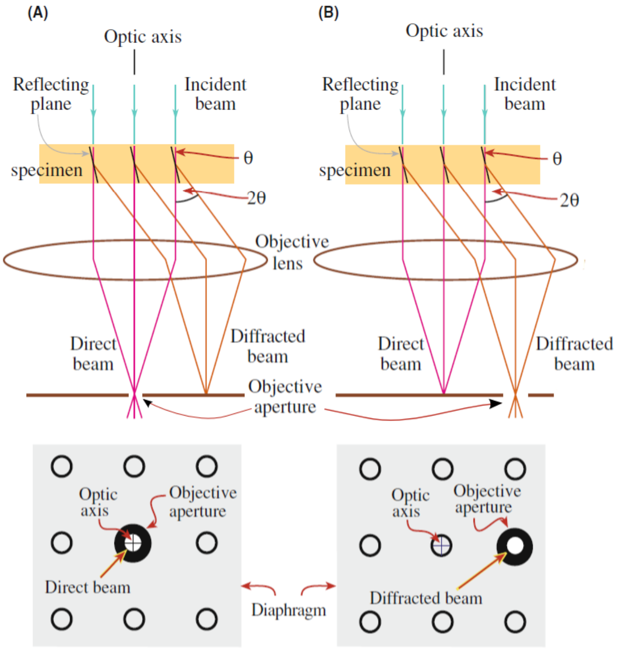

Figure 36: A) *Bright-field.* ***B)*** *off-axis Dark field (the on-axis is shown later in WBDF [William& Carter-book-chap.9]*

These two modes are the most often used in this PhD work, especially during the in situ nanocompression tests.

III. Weak Beam Dark Field (WBDF) Mode

Regarding the importance that dislocations have during all stages of plastic deformation, a large number of MgO nanocubes, synthesized by both synthesis methods, are characterized before any mechanical test using the **WBDF** mode. This will bring information about the crystallinity perfection of these single crystals MgO nanocubes, i.e. whether they are free of dislocation or not.

The WBDF technique is also used sometimes during in situ tests nanocompression to determine dislocation nucleation /path and the evolution of their microstructure and to determine its burgers vector in order to characterize its type (screw or edge). This is presented in section 2.3.2-IV.

WBDF (Weak Beam Dark Field) is a very useful technique to image dislocation lines with a narrow contrast and to determine its character. It is a DF mode under special tilt conditions.

First, a small and brief remind of some notions of diffraction patterns:

Normally, there are several planes *hkl* in the real space that obey to Bragg's condition for the specific orientation of the incident beam on the crystal. Diffraction patterns (DP) represent the intersection of the reciprocal lattice of a crystal with the Ewald sphere at reciprocal lattice points representing those *hkl* planes that are at Bragg condition ($2d_{hkl}\sin\theta=n\lambda$; constructive interference of diffracted beams). First, the incident beam is defined by a plane wave vector $\overrightarrow{k_0}$ of magnitude $\frac{1}{\lambda}$ (λ : electron beam wavelength). Bragg diffraction of planes *hkl*, means elastic scattering of the incident wave vector $\overrightarrow{k_0}$ by *hkl* planes with no energy loss, thus the diffracted beam $\vec{k}$ is equal in magnitude to $\overrightarrow{k_0}$ and its end lies on the Ewald sphere which radius is equal to $\boldsymbol{k_0}$(see ***Figure 37***-a). Thus Ewald Sphere intersections with reciprocal lattice points represent all possible diffraction of planes obeying to Bragg condition, and its center coincides with the origin of $\overrightarrow{k_0}$. ***Figure 37***-a shows planes *hkl* near Bragg conditions with a small magnitude of excitation error vector $\vec{S}$ but its intensity profile lies on the Ewald sphere and thus these planes are diffracting with a smaller intensity than what was if **S** was equal to zero. One can see from this ***Figure 37***-a, that $\vec{g}$ is the vector perpendicular to planes *hkl* and its magnitude $\mathbf{g}= 2\sin\theta.k_0=2\sin\theta /\lambda=1/d_{hkl}$.

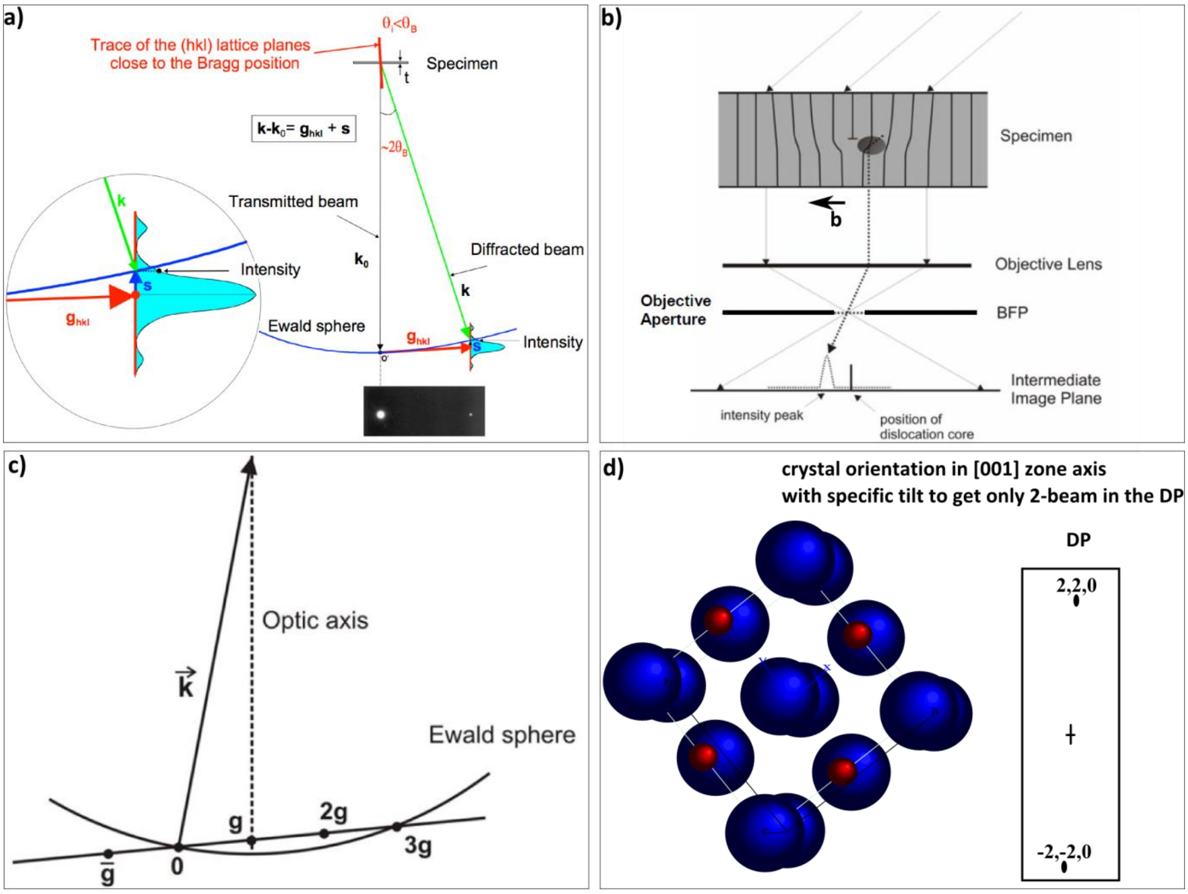

__Figure 37__: __a)__ (hkl) planes near Bragg conditions with a small magnitude of excitation error vector $\vec{S}$. [William & carter book] __b)__ path rays in WBDF method for an example of an edge dislocation. Perfect area is far from Bragg condition (large excitation error) whereas the area near the dislocation core is in exact Bragg condition.

The displacement field, caused by this dislocation core, in *hkl* planes is parallel to the burgers vector of this dislocation as shown in ***Figure 37***-b. WBDF consists of imaging a dislocation when the excitation error $\vec{S}$ is large enough (kinematical condition). So only the large displacement field near the dislocation core can give a slight contrast. Only DF mode is able to reveal this contrast (***Figure 37***-b).

Dislocations visibility criterion:

If the displacement field is parallel to *hkl* planes, i.e. **g** reflection of *hkl* planes is perpendicular to Burger's vector; this means that no phase changes occur in the diffracted beam and the dislocation will be invisible. This is called criterion for dislocation invisibility where is $\vec{g}.\vec{b}=0$, and otherwise ($\vec{g}.\vec{b} \neq 0$) the dislocation is visible with specific beam tilts.

To make the dislocation visible, first the incident beam must be tilted in a way that the **g** reflection of *hkl* planes become far from the Bragg condition, i.e. increase the excitation error **S** of *hkl* planes of the undistorted area of the sample and get the distorted area exactly in Bragg conditions as shown in the dislocation (pure edge) of ***Figure 37***-b&c. This occurs by tilting the incident beam (of 2 θ) in a way to get **g** reflection in the optical axis with a large excitation error as shown in ***Figure 37***-c, and only the distorted area obeying to Bragg condition will be exactly in diffraction condition. Making a DF image with the central spot (**g** with large excitation error; small intensity of *hkl* planes but higher for its distorted area) will give a dark background of perfect crystal and a sharp thin line of diffracting beam of the distorted area near the dislocation core.

Procedure:

-Choose a specific zone axis, in our case we choose [001] (see ***Figure 37***-d).

-Tilt the sample in a way to get rid of all other reflections and get only two beams in the DP (so-called 2-beam condition) as shown in ***Figure 37***-d, the direct beam (**0**) and the specific **g** reflection in DP. If we choose the **g** (220) where all possible dislocations in MgO will be visible depending on the visibility criterion as shown in ***Table 2***.

-Tilt the incident beam to translate the central spot (**0**) into **–g**, i.e. to get **g** in the optical axis with large excitation error as shown in ***Figure 37***-c.

-Then with the objective aperture, we choose the central spot (**g** with weak intensity), and make a **DF image**. Then, all possible dislocations in MgO will appear bright-white if exists on a dark background representing the perfect area of the crystal.

Table 2: *Screw and edge Burgers vector in slip planes {110} and {101}. $\vec{g}.\vec{b}$ Visibility criterion with g (200) and g (220).*

Slip Planes	type	**Burgers vector $\vec{b}$**	Vector line	*g*	$\vec{g}.\vec{b}$	*visibility*	**g**	$\vec{g}.\vec{b}$	**visibility**
(101)	screw	**½[10$\bar{1}$]**	[10$\bar{1}$]	*200*	*1*	*YES*	**220**	**1**	**YES**
(10$\bar{1}$)	screw	**½[101]**	[101]	*200*	*1*	*YES*	**220**	**1**	**YES**
(011)	screw	**½[01$\bar{1}$]**	[01$\bar{1}$]	*200*	*0*	*NO*	**220**	**1**	**YES**
(01$\bar{1}$)	screw	**½[011]**	[011]	*200*	*0*	*NO*	**220**	**1**	**YES**
(101)	edge	**½[10$\bar{1}$]**	[010]	*200*	*1*	*YES*	**220**	**1**	**YES**
(10$\bar{1}$)	edge	**½[101]**	[010]	*200*	*1*	*YES*	**220**	**1**	**YES**
(011)	edge	**½[01$\bar{1}$]**	[100]	*200*	*0*	*NO*	**220**	**1**	**YES**
(01$\bar{1}$)	edge	**½[011]**	[100]	*200*	*0*	*NO*	**220**	**1**	**YES**

Images in ***Figure 38*-a&b** are acquired with the diffraction spot (220), that allows the detection of dislocations having Burgers vector equal to [10$\bar{1}$], [101], [01$\bar{1}$], and [011], as shown in *Table 2*. Under such conditions, dislocations can be imaged as narrow lines which are approximately 10–15 nm wide depending of the wave excitation condition [*D.J.H. Cockayne (1969)]*.

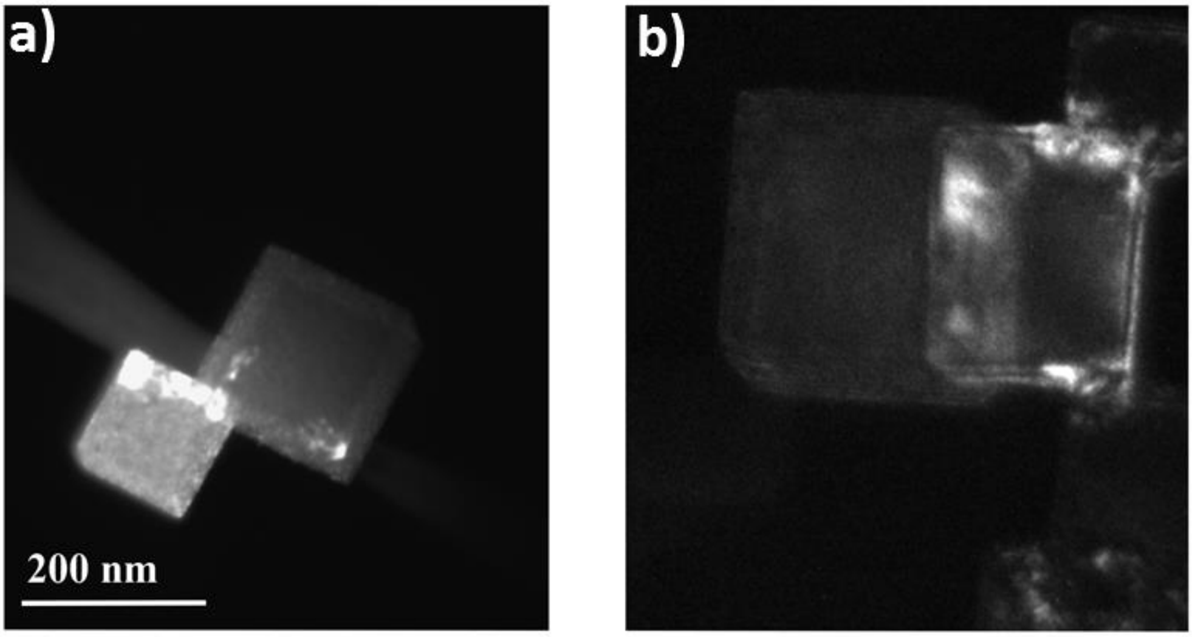

Figure 38: *WBDF image of MgO nanocubes synthesized by **a)** microwave method, and **b)** burning Mg method*

WBDF images show no bulk lattice defect such as dislocations, grain boundaries or twinning. Contrasts are only observed at the contact points with other nanocubes or with the carbon film of the TEM grid, and can be attributed to the stress field induced by the elastic compression of the lattice [*A. Thölén (2006)*]. None of the nanocubes imaged is found to contain bulk lattice defects. Similar samples are used for *in situ* nanocompression testing will thus be considered as initially dislocation-free.

IV. High Resolution TEM Mode

High-resolution transmission electron microscopy (HRTEM) is an imaging mode that allows the imaging of the crystallographic structure of a sample at the atomic scale. The incident beam must be the most parallel and a large objective aperture has to be selected that allows many beams including the direct beam to pass. The image is formed by the interference of the diffracted beams by the planes (*hkl*) with the direct beam (phase contrast) as shown in *Figure 39*. If the point resolution of the microscope is sufficiently high and a suitable crystalline sample oriented along a zone axis, then HRTEM images are obtained. The obtained images consist of the crystal imaging at atomic scale.

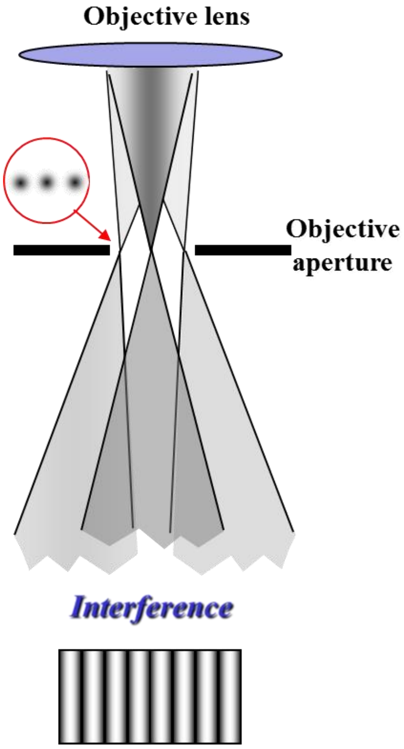

Figure 39 : *example of a lattice plane imaging from 3 waves interference [**Esnouf,**Claude–Book-2011:]*

The contrast formation in HRTEM images can only be explained by the wave nature of electrons and the change of phase when transmitted through the sample. More details on this mode and the theory beyond are available in [*William& Carter- book-ch.28*]. However, Vibrations in the TEM instruments should be minimized to optimize resolution in a HRTEM image.

HRTEM characterizations are carried out on MgO nanocubes using a JEOL 2010F TEM microscope equipped with a field emission gun and operating at 200 kV. Electronic diffraction patterns will be calculated using the Fourier Transforms of regions of interest in the HRTEM images.

HRTEM mode is not possible during the in situ nanocompression tests on MgO nanocubes due to vibrations in the sample holder.

However, in the second part of the dissertation on transition alumina, HRTEM images are used to investigate the crystallographic orientations of alumina nanoparticles after compaction in DAC. Electronic diffraction patterns are also obtained and analysed.

A typical HRTEM image of a MgO nanocube is presented in *Figure 40*. In the inset, the diffraction pattern shows {200} crystallographic planes with a lattice spacing of 2.15 Å. By both synthesis methods, the nanocubes obtained are fully crystalline and are single crystals. Surfaces are oriented along the <100> directions. This allows an easy identification of the crystallographic compression axis during *in situ* nanocompression tests. It corresponds to the <100> direction when the nanocubes are flat on the substrate.

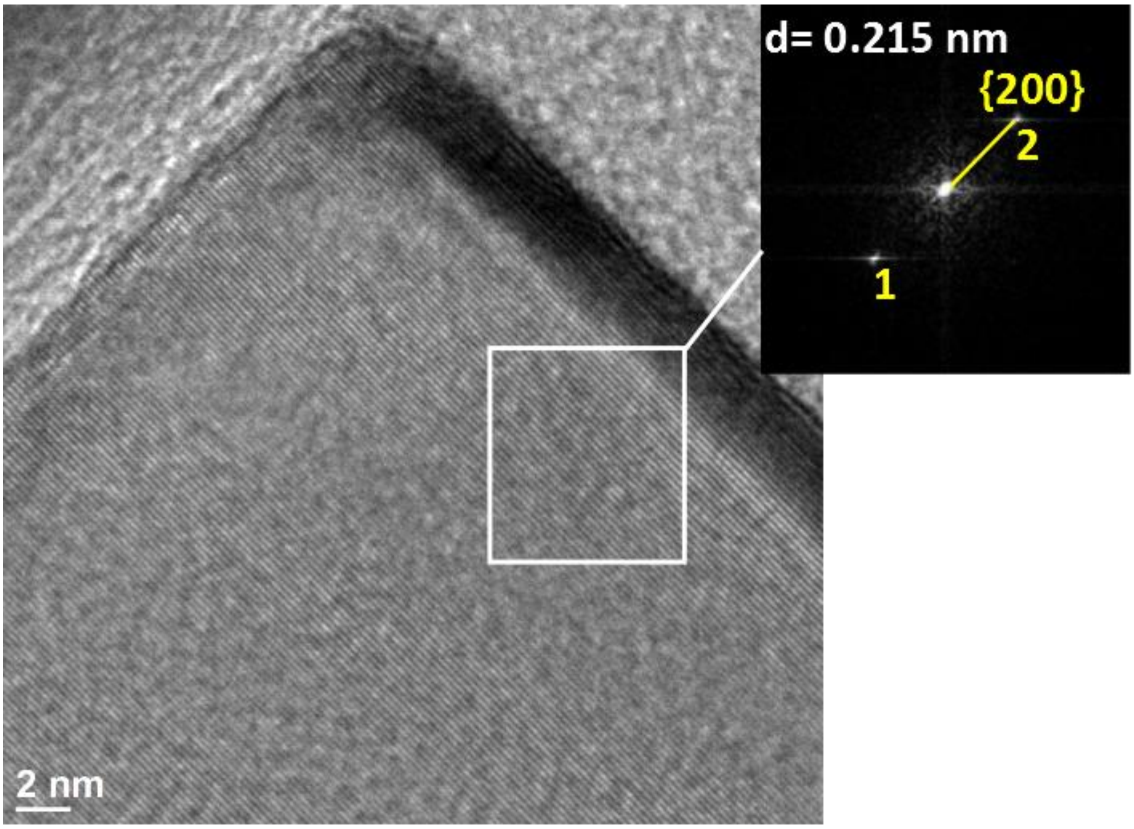

Figure 40 *A typical HRTEM image of a MgO nanocube. In the inset, the diffraction pattern shows {200} crystallographic planes with a lattice spacing of 2.15 Å*

V. Energy-dispersive spectroscopy (EDS)-TEM Characterizations

Energy-Dispersive Spectroscopy (**EDS**), or sometimes called **Energy-Dispersive X-ray Spectroscopy EDXS** is a technique used for elemental characterizations of a sample. Its characterization capability is due to the fundamental principle that each element has a unique atomic structure allowing unique set of peaks on its X-ray emission spectrum. It consists in stimulating the emission of characteristic X-rays from a specimen, by focusing a high-energy beam of charged particles such as electrons or protons , or a beam of X-rays into electron the sample [*Wikipedia*]. The number and energy of the X-rays emitted from a specimen can be measured by a detector used to convert X-ray energy into voltage signals; this information is sent to a pulse processor, which measures the signals and passes them onto an analyser for data display and analysis in the form of an EDS spectrum. EDS spectrum consists of number of x-ray photons as a in function of the characteristic X-ray energy of elements.

Herein, EDS characterisations are carried out in the TEM JEOL 2010F, thus the electron beam (200KeV) was the source of X-ray excitation in MgO nanocubes. The TEM is equipped with an 80 mm^2 SSD detector from Oxford Instruments.

EDS is performed on MgO nanocubes to characterise the presence of impurities, knowing the importance of impurities on mechanical properties of a crystal specimen. For MgO, it is observed that the CRSS increases with increasing fractions of iron impurities. This is due mainly to the spatial distribution of iron and its oxidation state (Fe^{3+}), which have an effect on dislocation movement [Amodeo. J thesis (2011)]. It is reported that high concentrations of iron and high precipitation acts as barriers for dislocations and prevent their activation at lower stress and thus increases the CRSS.

EDS spectra shown in Figure 41 acquired during HRTEM observations indicate that the nanocubes are exclusively composed of MgO (99.9± 0.1 at. % MgO). Some randomly dispersed impurities in microwave samples, mainly iron, can be detected but with very low fractions. The impurities concentrations however lie within the measurement uncertainty.

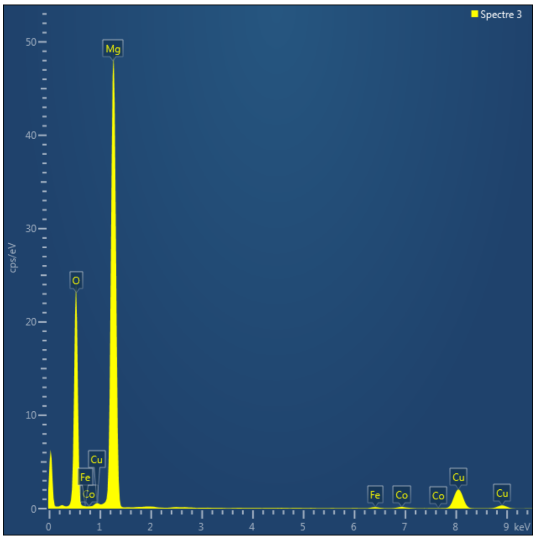

Figure 41: Typical EDS spectra of MgO nanocubes synthesized by microwave method.

So far, MgO nanocubes synthesized in both methods are single crystals, pure MgO with very low concentrations of impurities – without any segregation. Most importantly, the MgO nanocubes are free of dislocation.

2.3 *In situ* TEM nanocompression of MgO nanocubes

In situ nanocompression tests are carried out using a dedicated sample holder from Nanofactory Instruments fitted in a JEOL 2010F microscope operating at 200 kV.

2.2.1 *In Situ TEM Sample Holder & Experiments Control*

I. Technical description of the sample holder

The sample holder from Nanofactory is shown in ***Figure 42***. The sample holder consists of three main parts: the front piece, the rod and the end piece. It allows both nanoindentation and nanocompression tests, depending on the front piece components (geometry of the diamond tip and the sample configuration).

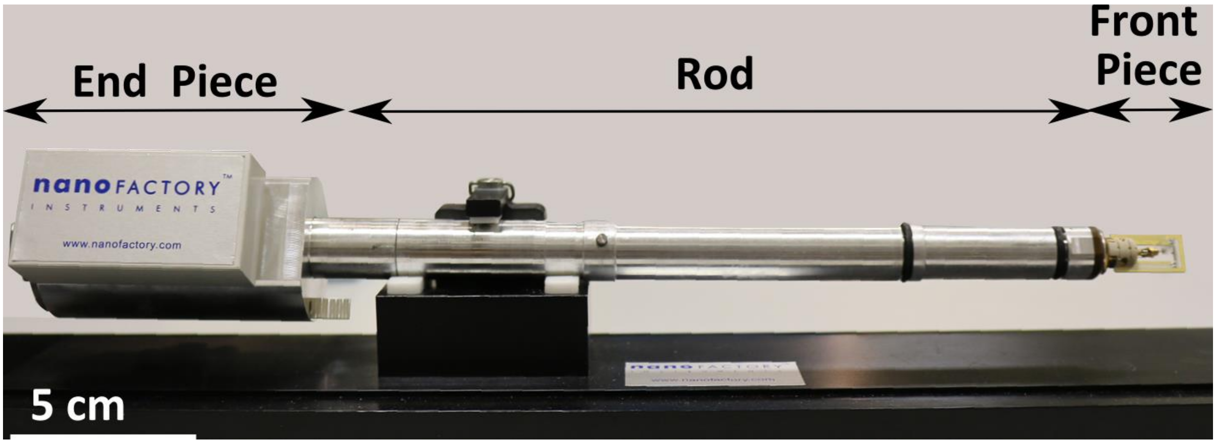

Figure 42: Nanofactory Sample holder

Herein, for a Jeol TEM 2010F (field emission TEM) with a gap between ultra-high resolution pole pieces of only 2 mm wide, the dedicated sample holder from Nanofactory is equipped with a front piece that is a very thin ceramic piece, as shown in ***Figure 43***-b.

Moreover, the front piece contains all the main components for the tests: force sensor, tip, substrate and sample. Depending on the test type (nanoindentation or nanocompression), the substrate and sample geometries change (blue text in ***Figure 43***-a). Herein, for nanocompression tests of MgO nanocubes, nanocubes are deposited on a sapphire substrate that is glued, with epoxy, to a gold wire of ~1 cm long. The latter is screwed to a hat having six legs, placed on a ball which is the end of the ceramic piezo-tube. These are mobile parts of the front piece (green text in ***Figure 43***-a).We use a front piece equipped of a ***punch*** diamond tip of surface area 500*500 nm^2. The diamond tip is fixed on the front piece. Behind the diamond tip is the load cell (MEMs device) based on Hook’s law, with springs (SiO_2) of known stiffness (3500 N/m), used for force and displacements measurements. The diamond tip and force sensor are the fixed part of the front piece, whereas the substrate is mobile.

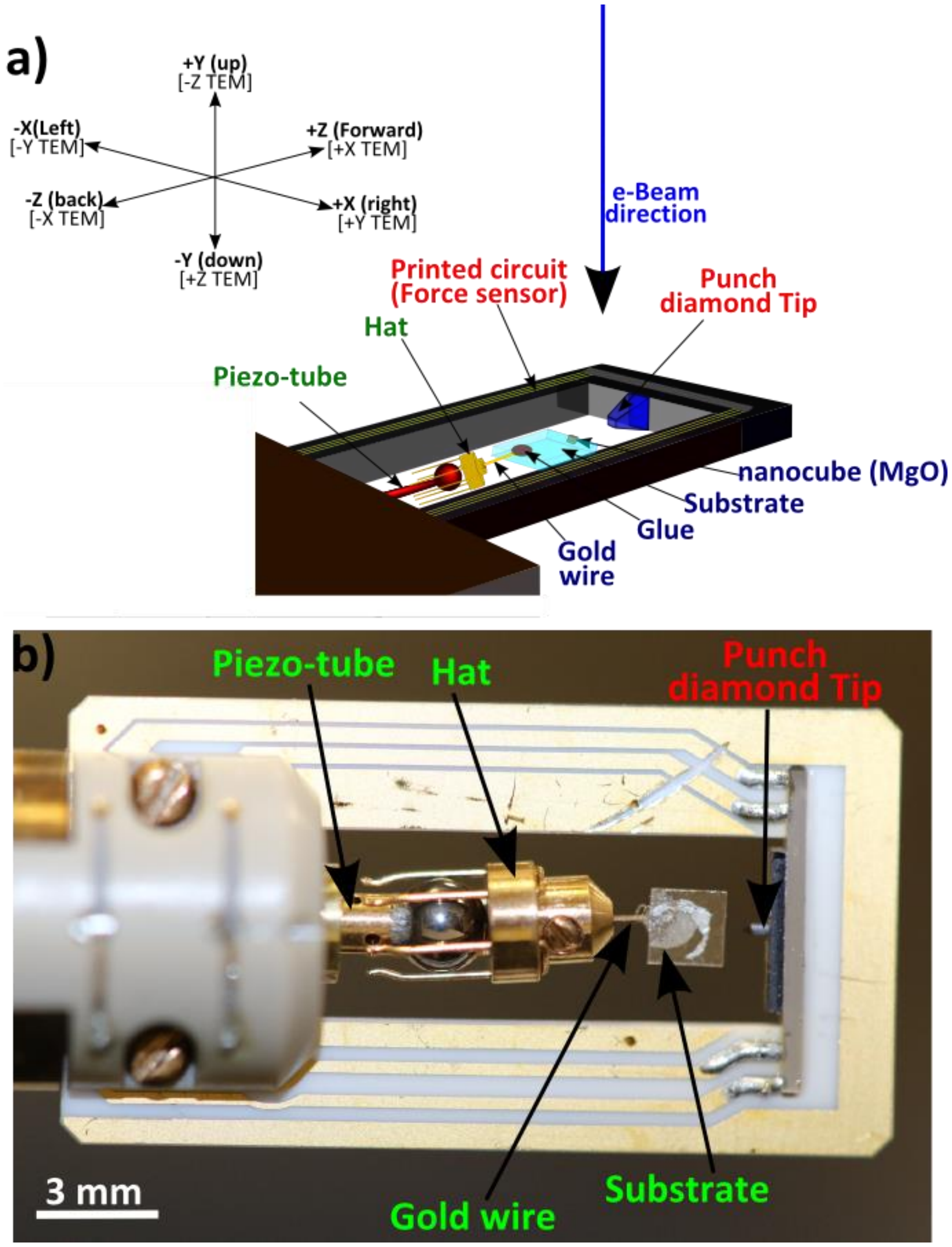

***Figure 43: Front Piece**. **a)** Scheme that represents the main parts of a front piece with the possible direction of the sample with respect to the electron-beam direction. Dimensions (especially the MgO nanocube size) are not respected in this scheme. **b)** Front piece with real dimensions.*

The coarse movements of the hat (i.e. of the substrate the sample) are ensured by piezo-tube pulses that induce stick-slip motion of the hat over the ball. Fine movements are of a shorter range and are acquired by a constant displacement of the piezo-tube. Coarse and fine movements of the sample are of a sub-Angstrom resolution and can be done in three +/− directions with respect to the sample holder (see ***Figure 43***-a), and to the electron beam direction once the sample holder is inserted in the TEM.

The end piece is the part of the sample holder containing all the connectors.

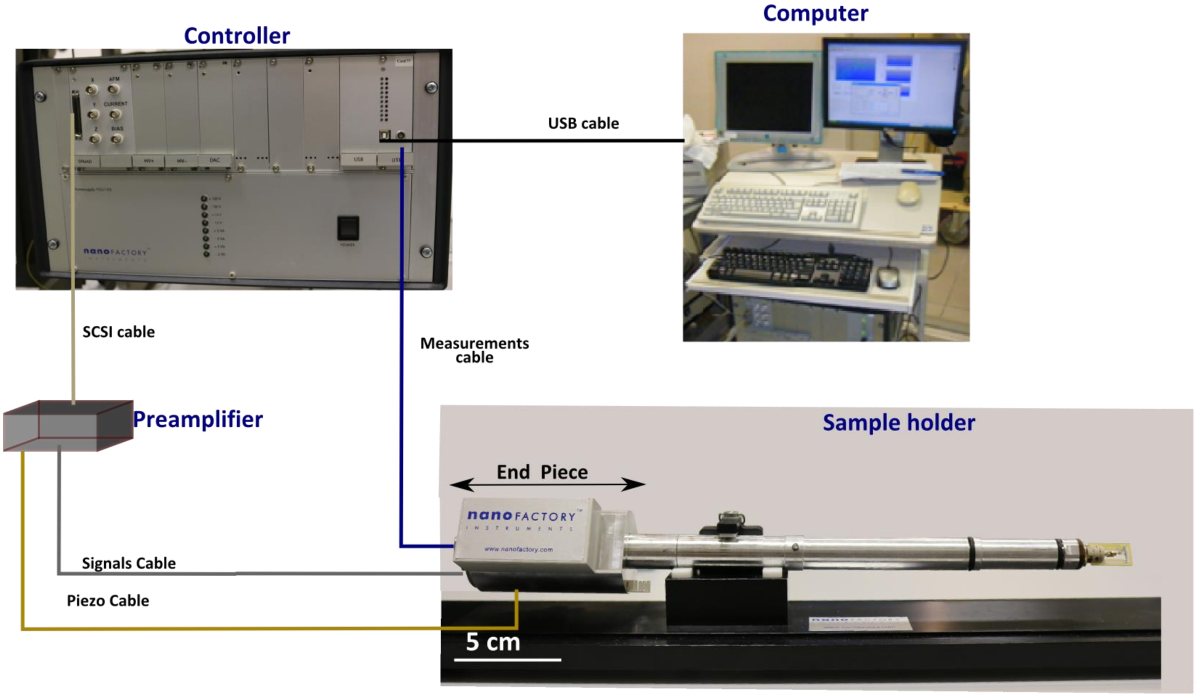

Figure 44: *Sample holder, controller and PC connections.*

The controller contains electronics that allow the process of the signals sent and received from the sample holder. It provides the pulses which induce the sample movements via a piezo connector and thus controls the piezo-tube movements. Also, the controller receives signals via the signal and measurements cables for force and displacements measurements. The measurements cable does not pass through the preamplifier to minimize the noise level.

The preamplifier converts low level signals from the holder to high level signals in the +/-10 V range.

II. Experiment Control and Data Acquisition:

Since, the controller is connected to a computer via a USB cable, the user controls an *in situ* TEM nanocompression (or nanoindentation) experiment via the software NFC3 from Nanofactory for nanocompression tests commands and the software Digital Micrograph for TEM images display. The TEM 2010F is equipped with a Gatan Orius 200 CCD camera.

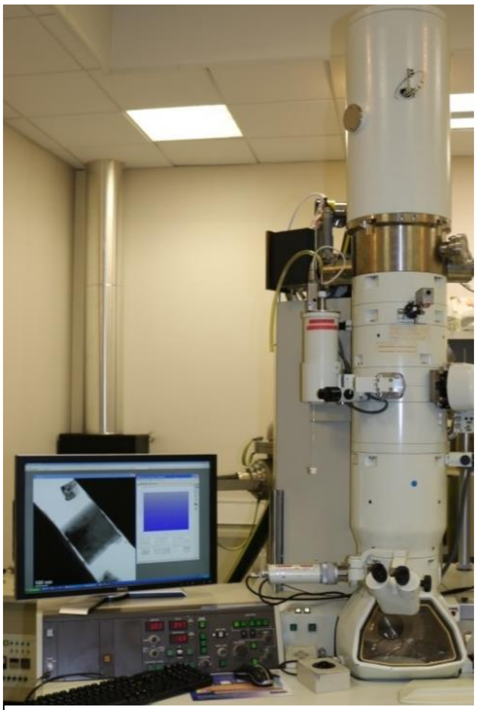
Figure 45 : TEM 2010F

All the commands necessary for the movements of the sample are available in the NFC3 software:

- **Alignments** in three directions (see arrows in **Figure 46**) of the sample to come in front of the punch diamond tip. This is performed via coarse movements of the piezo-tube and commands are given by the user via a joystick.
- Once the sample (MgO nanocube) is in face of the diamond tip as shown in **Figure 46**, **a nanocompression test** at constant displacement rate is performed via fine and constant movements of the piezo. For MgO nanocubes nanocompression tests, we often used displacement rates of 2nm/s and 1nm/s. At this time, TEM images and corresponding movies are recorded.

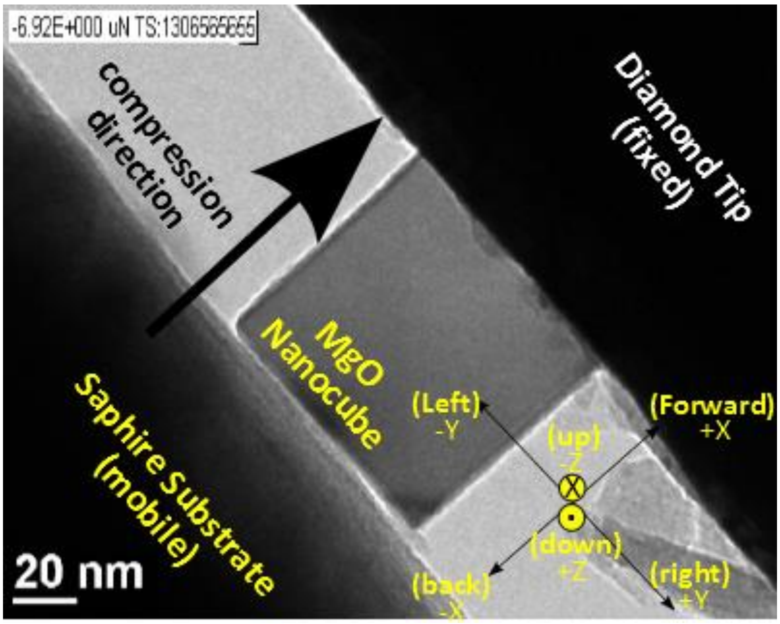

Figure 46: *MgO nanocube ready to be compressed in situ TEM. Arrows show possible movements of the sample*

- **Calibration of the piezo-tube sensitivity** (nm/V) (especially the Backward/Forward (B/F) factor sensitivity). This is done before any test, to adjust the theoretical displacement of the piezo to become equal to the real one. This is obtained by commanding a Backward displacement $-d_{test}$, and resetting to a position 0. A TEM image (1) is taken for the position 0. Then a command of a Forward displacement $+d_{test}$ equal to a theoretical movement of the piezo is given, and a TEM image (2) is taken. Measurement of the real displacement d_{real} is done by calculating the difference between TEM images 1 and 2. If $d_{real} \neq d_{test}$, adjusting of the sensitivity factor is done by getting the new sensitivity factor $(B/F)_{new} = \frac{d_{real}}{d_{test}} * (B/F)_{old}$.

More details on the *in situ* TEM nanocompression tests on MgO nanocubes performance are available in **section 2.3.2 (I).**

Moreover, the NFC3 software provides data of a given experiment by displaying:

- Displacement in function of time
- Force in function of time
- Force in function of displacement

As shown in ***Figure 47***. It is noteworthy that the displacement, in the displacement-time curve, corresponds to the displacement of the piezo-tube. However, the displacement in the force-displacement curve corresponds to an estimated displacement of the substrate. This corresponds in fact to the displacement of the piezo-tube corrected by a spring rate (one of the characteristics of the tip, provided by Nanofactory).

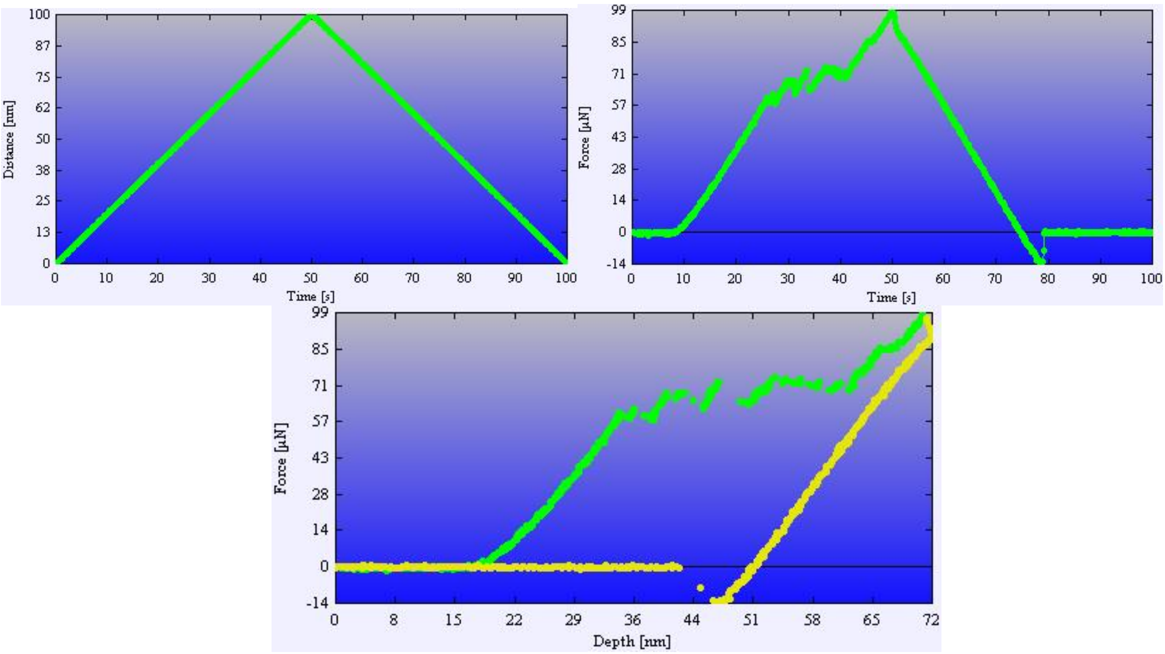

Figure 47: *Force-time-displacement data of a nanocompression test*

III. Substrate and Nanoparticles deposition

- **Substrate**

The substrate chosen for these tests is a commercial sapphire substrate. Sapphire is known for its high hardness and thus it is suitable for such investigations. The sapphire substrate is a 2mm*2mm square (see ***Figure 48***-a) and its thickness is of 75 µm, as shown in the SEM image in ***Figure 48***-b.

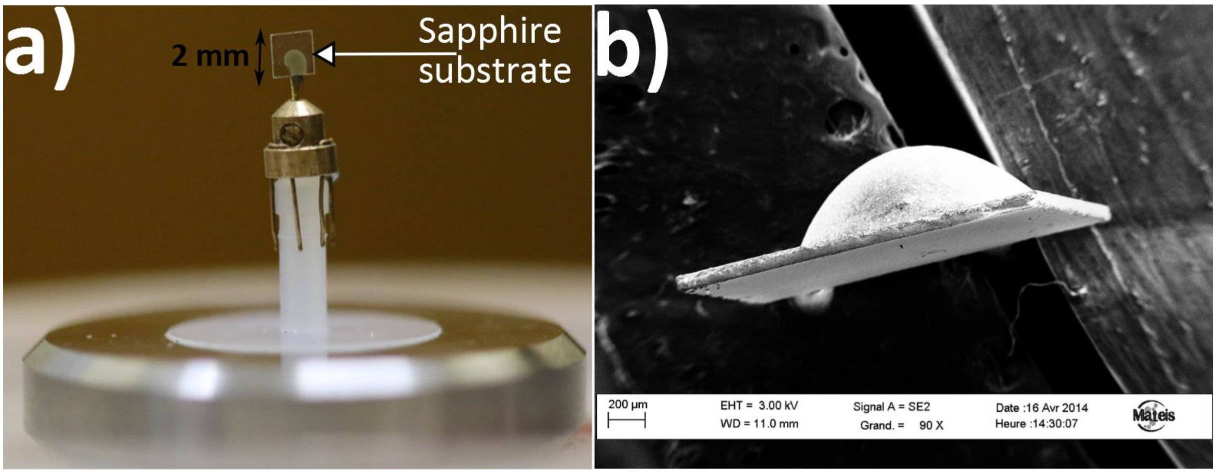

Figure 48:a) *Sapphire substrate is of 2mm*2mm square.* ***b)*** *SEM image of the thin edge of the sapphire substrate.*

- **MgO Nanocubes Deposition**

MgO nanocubes are deposited on the 75 µm*2mm lateral surface (see *Figure 49*) either by contact with the glass substrate (nanocubes of microwave synthesis) or by passing the substrate in the smoke during the second synthesis method. These two ways precludes the use of solvents that may modify the surface structure of MgO samples [*R.O. Kagel (1968)]*. However a few tests are performed on nanocubes dispersed by ethanol for two reasons. The first reason is to have a lower quantity of MgO nanocubes on the substrate. This facilitates finding a clean surface on the substrate during *in situ* TEM tests to perform the nanocompression between two clean plateaus: the diamond tip and the clean surface of the substrate. The second reason is to investigate the ethanol effect on MgO, especially on elastic properties as the Young Modulus. MgO is indeed known for its very high sensitivity to humidity that may modify its surface structure [*R.O. Kagel (1968)*]. However, trial and error TEM observation just before experiments are required to test if quantity of MgO nanocubes is very high or sufficiently good.

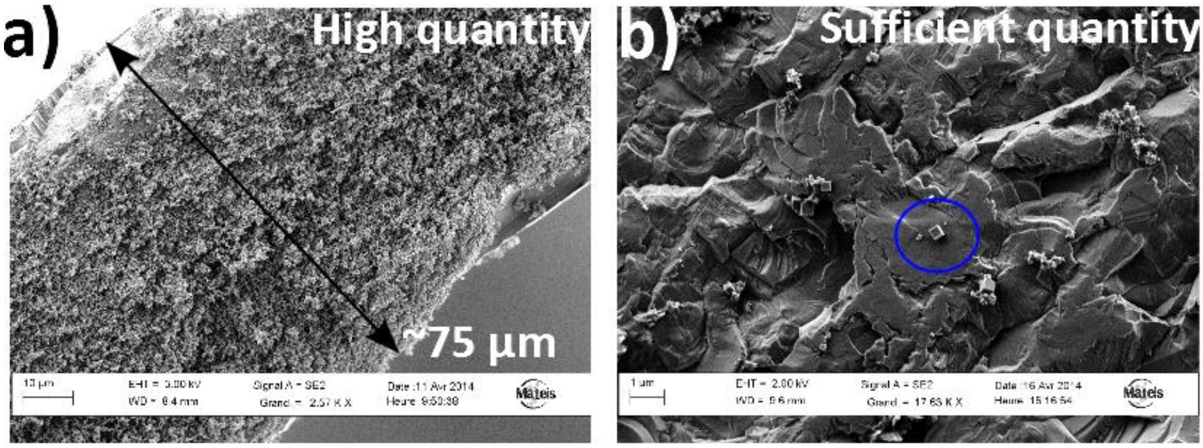

Figure 49:* *a) *Very high quantity of MgO nanocubes on the sapphire substrate that make isolation and compression of a MgO nanocube on a clean surface a very difficult task.* ***b)*** *Sufficient quantity of MgO nanocubes. a MgO nanocube seems ready for nanocompression on a clean surface.*

SEM images of MgO nanocube dispersions are often taken before *in situ* TEM nanocompression tests. This is useful to qualitively check the quantity of MgO nanocubes. If the nanocube quantity is too high, it is possible to lower it by gently passing an optic lenses filter on its surface. Thus by this procedure we save much time for *in situ* TEM tests. ***Figure 49***-b shows a cleaned substrate with an optimized quantity of MgO nanocubes. A MgO nanocube is shown to be well positioned for a nanocompression test.

- **Sapphire substrate polishing using an Ilion II polisher (Gatan)**

First SEM images of the sapphire substrate, showed ***Figure 49***, reveal the large surface roughness of the substrate. This may pose more challenges for *in situ* TEM tests for two reasons. First, once the substrate is inserted in the TEM, the observation direction (Z direction in ***Figure 43***-a) prevents observation of holes in the substrate (along the Y direction). As a consequence, one cannot easily identify, during a nanocompression test, if the nanocube is gliding into a certain hole or if it is deforming by compression. Moreover, probably due to this gliding effect, many cubes are lost during tests. The second reason is related to mechanics. From a mechanical point of view, stress localisation can occur in the MgO nanocube during compression if it is deposited on a rough substrate. This induces a non-uniform plastic deformation and poses ambiguity on data analysis.

For these reasons, cross-sectioning polishing by means of Argon ions beam milling of the substrate surface is done by Ilion II polisher from Gatan. The sapphire substrate is glued to a titanium alloy blade using silver paint. Only ~25 µm of the sapphire substrate was in the field of the incident Ar^+ beam, as shown in ***Figure 50***, and this is the part of the substrate that is milled. As the ion beam is partially blocked by the blade, the resultant milling area propagates in a "flat and horizontal" plane above the blade edge.

The polishing is done in Mateis Laboratory by Thierry Douillard and Bérangère Lesaint.

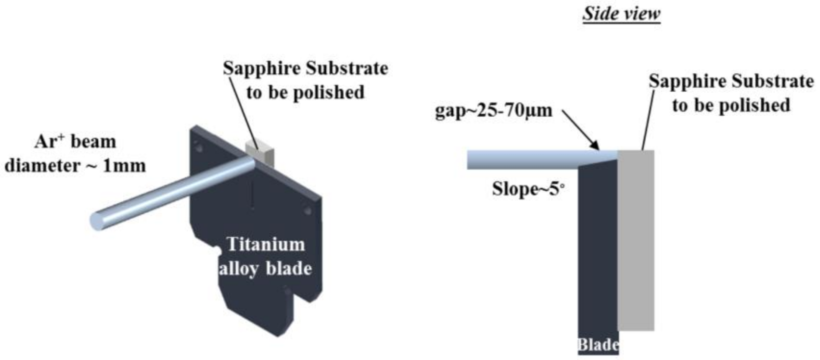

Figure 50: Scheme of Argon ions beam milling of the substrate surface by Ilion II polisher from Gatan.

The polishing of the sapphire provided a very smooth surface, as shown in *Figure 51*-c. The low surface roughness removes ambiguities during *in situ* TEM nanocompression and saves time for locating clean surfaces and positioning properly a nanocube, as it will be shown in the following section.

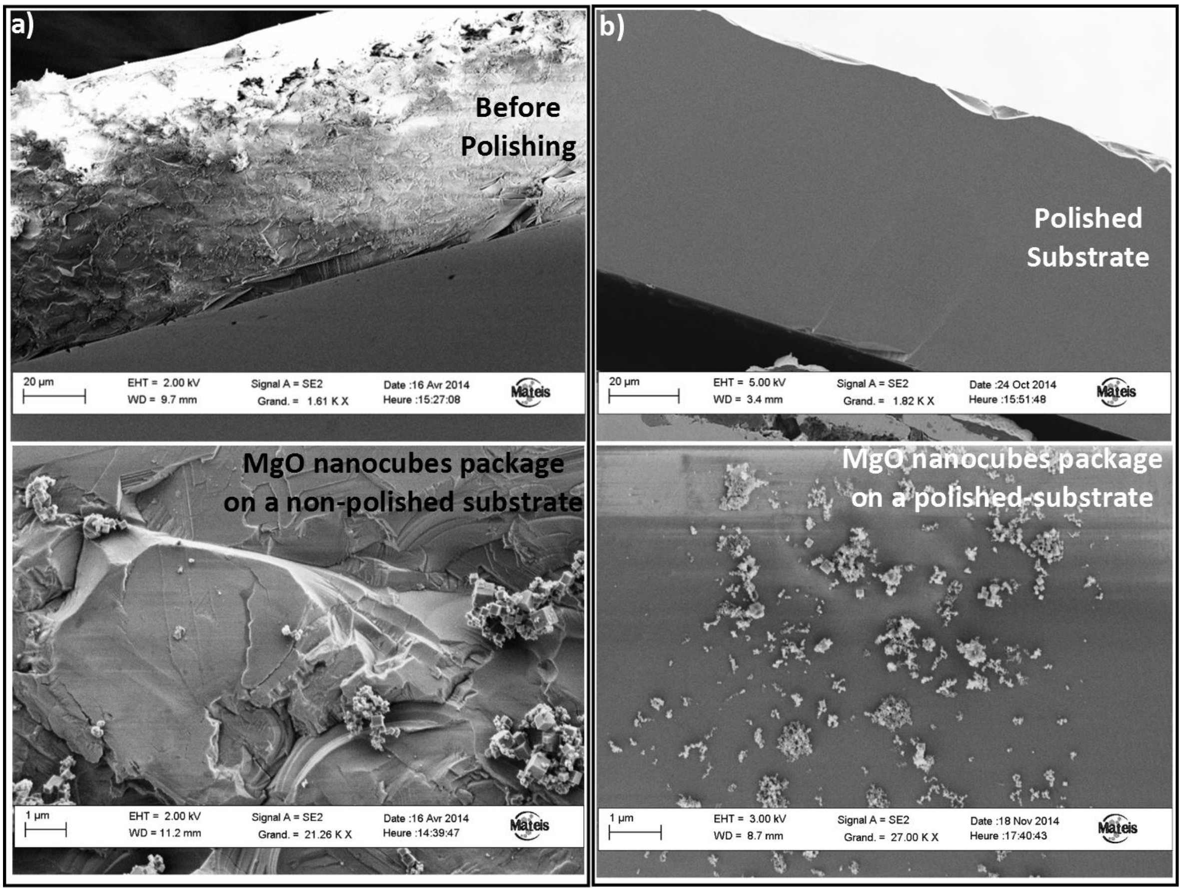

***Figure 51: a)** SEM images of the non-polished sapphire substrate surface. Lower SEM image showing agglomerates of MgO nanocubes in cavities. **b)** Smooth surface of the polished sapphire. Lower SEM Image showing MgO nanocubes deposited on smooth surface.*

2.2.2 *Experimental description of In situ TEM nanocompression of MgO nanocubes and Data Analysis*

I. Experimental Technique

Following the procedure for an optimum MgO nanocubes powder deposition on the sapphire substrate as described above, the substrate is glued on a gold wire. As mentioned above, the other end of the gold wire is screwed to the hat which is then placed on the ball (see ***Figure 43***-b), representing the end of the piezo-tube of the sample holder.

The sample holder is then inserted in the TEM. Aligning the tip and a nanocube is not a trivial task because of the microscope depth of field.

First, the tip is the part that remains fixed, thus preliminary settings of the TEM are done on the tip that it is placed at a reference height $Z_{(r)}$, which usually is the eucentric position. The coordinates ($X_{(r)}$; $Y_{(r)}$), of the tip are noted to relocate more easily the tip. Then, one must locate a MgO nanocube well positioned on a clean surface on the sapphire substrate. As the latter is the moving part, setting its Z position to the eucentric position is performed by continuously using the image wobbler while the X and Y positions are set progressively until the nanocube become in front of the tip. As TEM images are 2D images, Bragg fringes can be used to know if the MgO nanocube is above or below the tip. All these movements of the moving part (sample) are ensured by commands of the piezo-tube.

Since MgO nanocubes exhibit {100} surfaces, nanocubes can be easily oriented to compression in the [001] direction. Manipulation of the nanocubes is possible by means of electrostatic forces between the diamond tip and the crystals and so a particular nanocube can be transferred to a clean region of the substrate surface. Van der Waals forces are usually sufficient to prevent nanocubes from falling off the substrate in the electron beam transmission direction, but not all the times. MgO nanocubes are often agglomerated, thus a series of manipulations by means of electrostatic forces is needed until a unique MgO nanocube remains on the tip or on the substrate and thus become ready for a nanocompression test. An example of de-agglomeration is shown in ***Figure 52***, where a few cubes are visible above the substrate ***Figure 52***-a. Once the substrate is brought closer to the tip and a few cubes become attracted, the substrate is moved backward. A huge agglomerate of nanocubes often appears, which was probably hidden below or above the substrate, as shown in ***Figure 52***-b. After many manipulations (in three directions) aiming to isolate one cube, finally, only one nanocube may remain on the tip (see ***Figure** 52*-c). This nanocube is then compressed on a clean surface of the sapphire substrate, as shown in **Figure 46**.

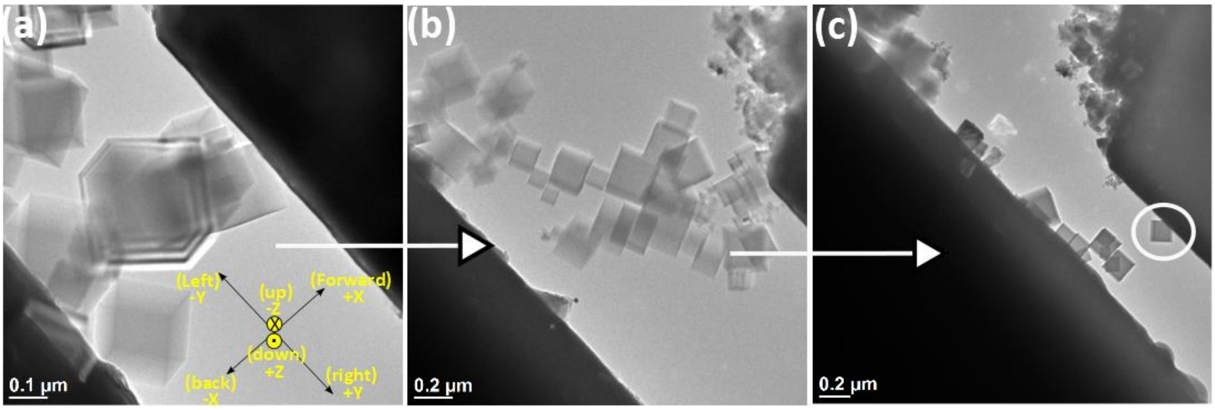

***Figure 52:** Sequence of TEM images showing steps of de-agglomeration of MgO nanocubes until only one nanocube remain at the end on the tip or on the substrate for nanocompression test.*

II. Experimental Parameters

During the *in situ* mechanical test itself, the substrate is moved toward the tip at a controlled displacement rate of 2 nm.s^{-1} (1 nm.s^{-1} for only two cases), which is equivalent to an engineering strain rate of 0.02 s^{-1} for a 100 nm nanocube. The cycle of a test is composed of a loading part and an unloading part, both at the same displacement rate. Several loading-unloading cycles often are done. Movies and loading-displacement F_i (L_0-L_i) curves (as shown in *Figure 46*) can be acquired simultaneously. F_i is the instantaneous force and L_i is the instantaneous position of the substrate with respect to the tip, i.e. the instantaneous sample size.

III. Stress-Strain Curves and Digital Image Correlation (DIC)

In order to investigate mechanical parameters of compressed MgO nanocubes, load-displacement curves are converted into engineering stress-strain curves. First, load-displacement curves obtained from the NFC3 software consist of the instantaneous force (F_i), provided by the force sensor, in function of the instantaneous displacement (d_i) of the substrate provided by the actuator.

One can obtain the engineering stress by calculating $\sigma_E = F_i/A_0$, where $A_0=L_0^2$ and L_0 is the initial position of the substrate with respect to the tip, i.e. the initial nanocube size. L_0 is measured from TEM images. The engineering strain is obtained by calculating (d_i/L_0) as if calculating (L_0-L_i)/L_0 where L_i is the instantaneous size of the nanocube. By doing this, one assume that the sample holder is infinitely stiff with respect to the tested nanocube. This is not the case since one can observe motion of the tip, supposed to be fixed, during tests. This motion is shown in ***Figure 53***, by following the position of the tip while the substrate is moving toward in stages (i), (ii) and (iii) of loading.

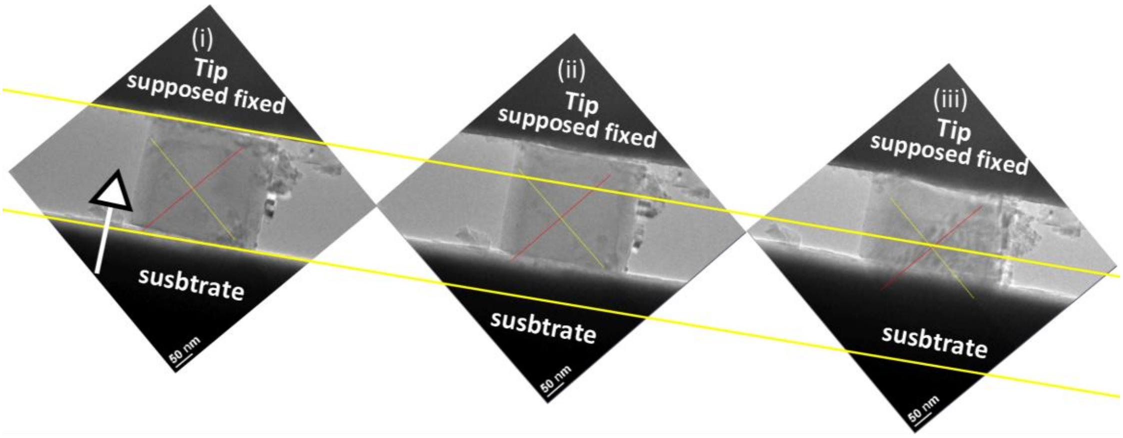

Figure 53: *Three stages captured from a displacement of the substrate toward the tip supposed fixed. The two lateral lines allow observing the movement of the substrate but also of the tip supposed fixed.*

In order to remove these ambiguities in displacement data and determine the real displacement of the substrate and thus the real deformation of the sample, DIC (Digital Image Correlation) is used. The DIC technique used herein consists of treating a rigorous comparison of grey level transitions between the tip, the samples and the substrate performed on successive images. DIC allows arbitrary displacement fields to be estimated with a sub-pixel resolution (1/100 pixel). From the actual displacement of the substrate and the diamond tip edges, the real instant size of the sample (L_i) as shown in ***Figure 54*** is estimated. This time, the longitudinal engineered strain is obtained by calculating $(L_0-L_i)/L_0$, with corrected L_i. The corrected longitudinal strain at each instant is synchronized with the stress value at each frame (instant). Therefore, engineering stress–strain curves with correlated images at each instant can be obtained.

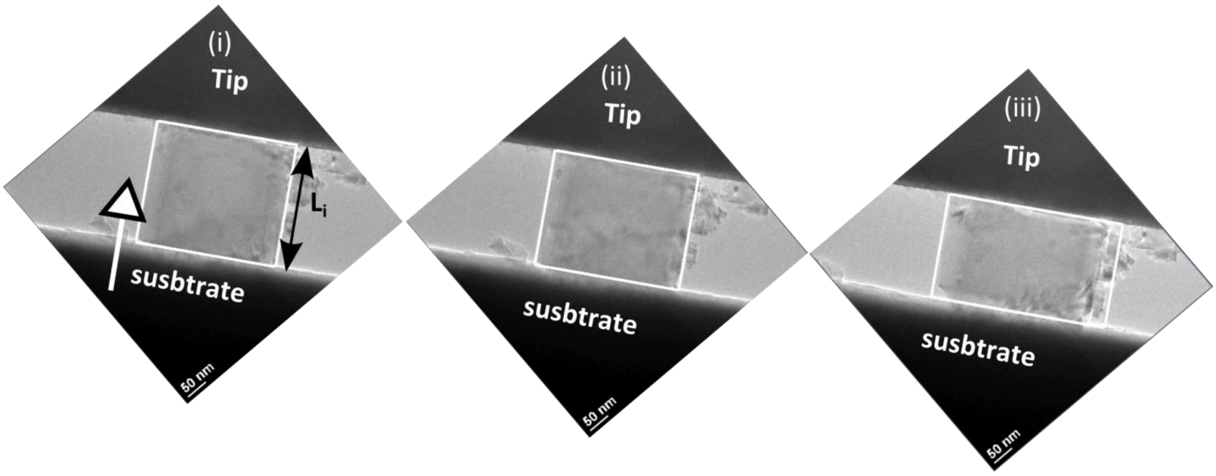

Figure 54: *Three stages captured from a displacement of the substrate toward the tip supposed fixed. The white borders following the nanocube's instantaneous longitudinal (Li) and lateral deformations. Latter allow obtaining instantaneous variation of the lateral surface and thus the true stress can be calculated.*

DIC principle is shown in *Figure 54*, longitudinal and lateral deformations are followed on successive images in function of time in movies and thus true stress- true strain curves can be obtained. Supposing that lateral deformation is the same in both directions (parallel to the diamond tip edge and in depth), this allows obtaining A_i. Thus, true stress σ is obtained by calculating F_i/A_i. True strain is defined as the Hencky strain Ln (L_i/L_0). Therefore true stress–true strain curves can be also obtained and images are correlated at each point of the curve (see *Figure 55*).

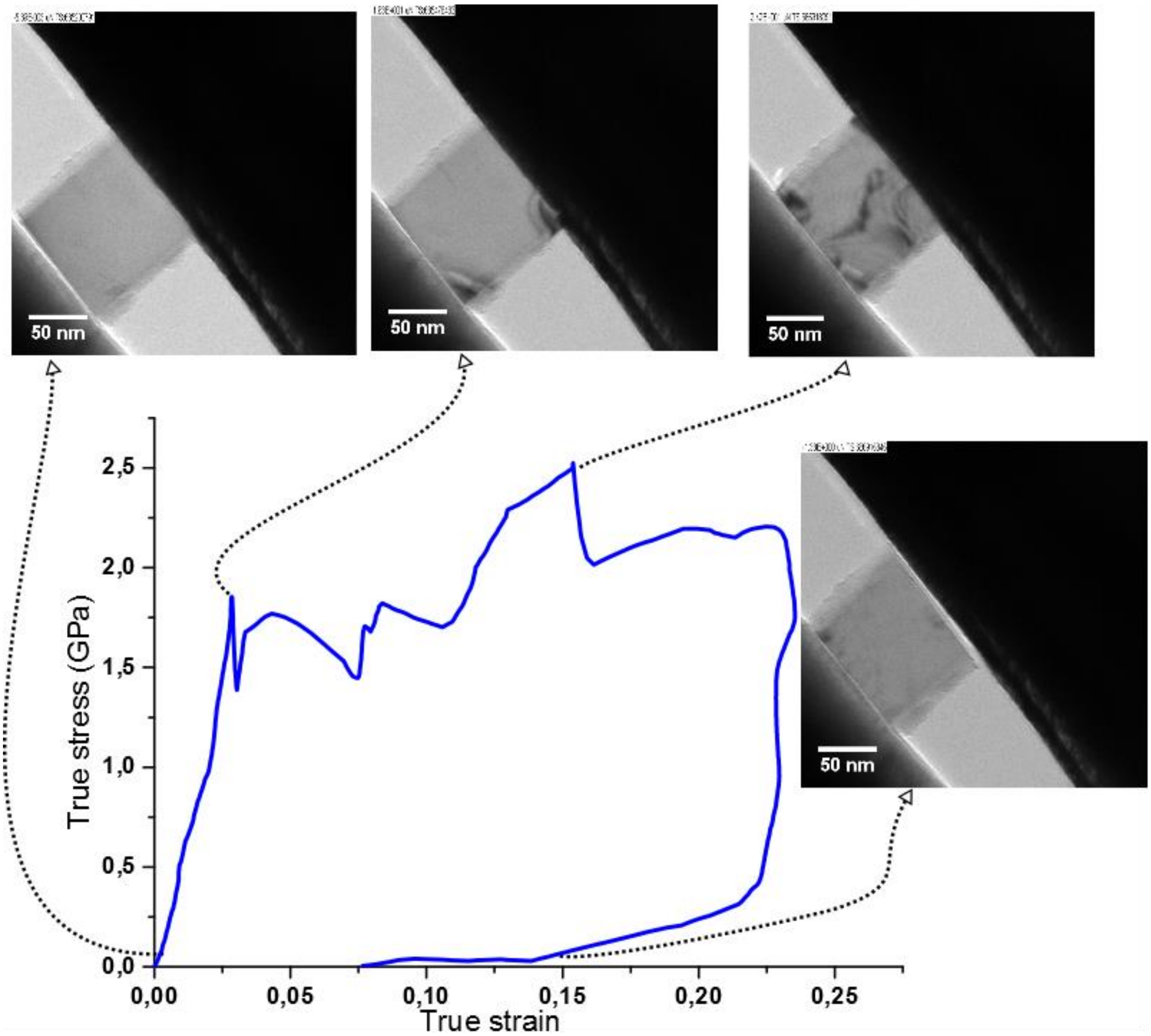

Figure 55: True stress- strain Obtained by DIC for a MgO nanocubes of 114 nm. TEM images are correlated at corresponding instants.

DIC is performed using Matlab code by a model developed by my supervisor Julien Réthoré from LAMCOS Laboratory.

IV. TEM images Analysis (Dislocation Characterisation)

In order to determine the possible deformation mechanism of MgO single crystals nanocubes, it is important to characterize the dislocations.

As mentioned previously, HRTEM is not possible with this sample holder due to vibrations in the system. Moreover, the sample holder is a simple tilt one, and the gap between the TEM pole pieces is only 2mm. Thus, only few degrees of tilt around one crystallographic direction is possible (y direction see ***Figure 56***).

However, due to the simple cubic shape of these single crystals MgO, one already can know that the compression axis corresponds to the <100> crystallographic direction, and the electron beam direction, i.e. the zone axis, is also near the <100> direction. As a consequence, 4 slip systems out of 6 may be active, as shown in *Figure 56*.

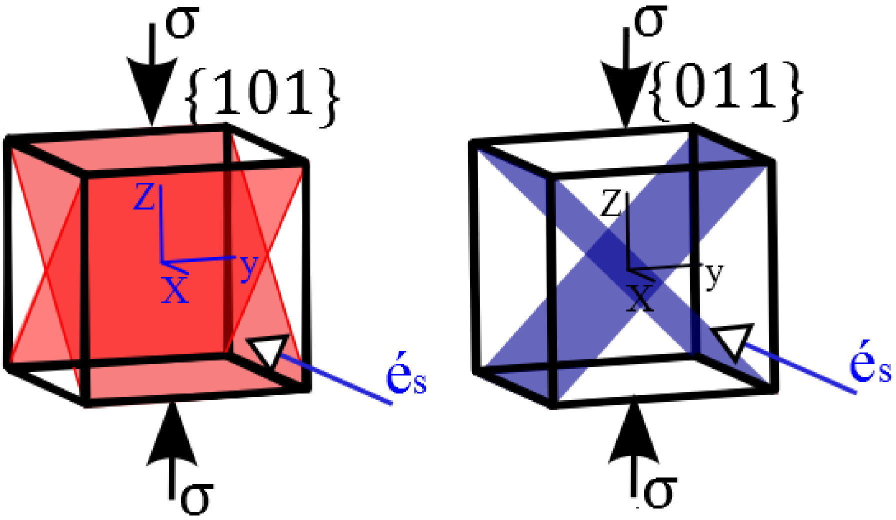

Figure 56 *MgO nanocubes with faces oriented along {100} compressed in the [001] direction (Z direction). Planes highlighted in the scheme are 4/6 slip planes* $((101), (10\bar{1}), (011) \& (01\bar{1}))$ *active in [001] compression with a Schmid factor 0.5. An arrow* (*é*$_s$) *shows the direction of the Electron beam in the TEM, during the in situ tests, with respect to the nanocube and the compression axis.*

Let us present the dislocation characterizations in MgO nanocubes during compression through an example:

A WBDF image is displayed in *Figure 57*-a. The compression axis corresponds to the [001] direction. The zone axis is near the [100]direction, and the WBDF is acquired with the diffracting wave **g** (0, 0, 2).

As mentioned before, 4/6 slip systems can be active in MgO when the solicitation direction is along the [001] direction. These slip systems correspond to the planes (101), $(10\bar{\mathbf{1}})$, and (011) and $(01\bar{\mathbf{1}})$, which are schematically shown in *Figure 56*. Thus, the possible dislocations Burgers vectors are $[10\bar{\mathbf{1}}]$, [101], $[01\bar{\mathbf{1}}]$ and [011]. The **g.b** ≠ **0** criterion is satisfied for all Burgers vectors, thus all the dislocations of these slip systems can be visible. The prefect area in the cube appear dark, and during compression the dislocations lines appear as white thin lines as shown in *Figure 57*-a.

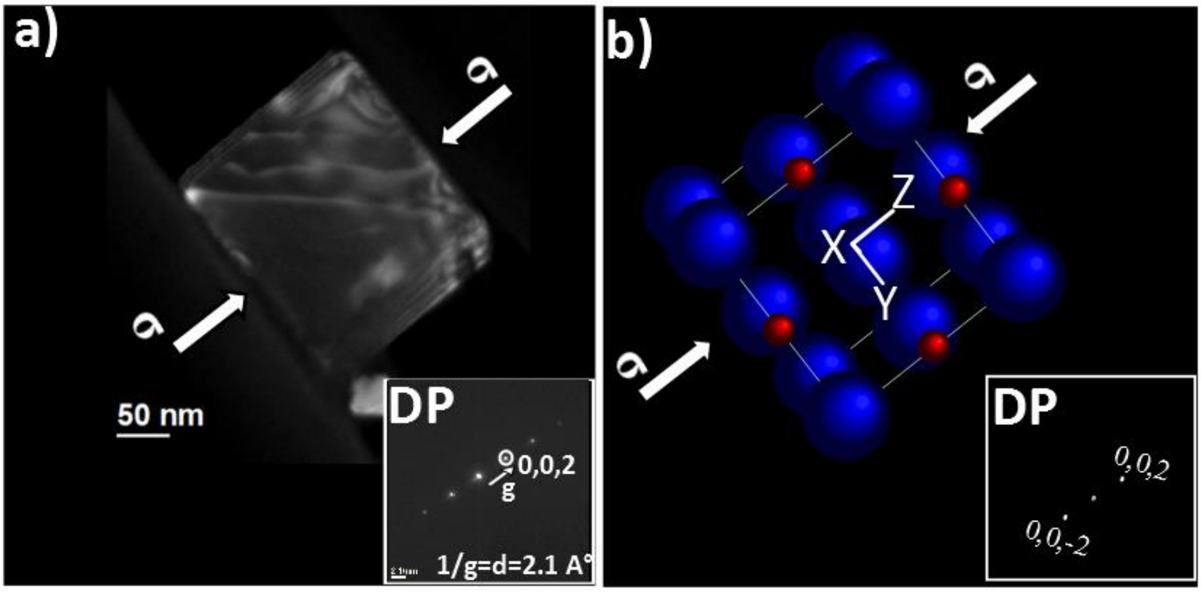

***Figure 57: a)** MgO sized 195 nm compressed in WBDF mode. First dislocations produced at early compression appear as thin white lines .Inset is DP. **b)** Crystal oriented to match the one shown in a) until the simulated DP matches the experimental one.*

With the software *CaRine Crystallography*, it is possible simulate the tilt of the crystal, so that it coincides with the experimental image. This is done by tilting the simulated crystal near the [100] zone axis until the 2-beam condition is satisfied, as shown in ***Figure 57***-b (direct beam and **g** (0, 0, 2).

By calculating the equations of the straight lines representing the 8 possible dislocations in MgO, it is possible to draw these lines in a cubic 3-D cell by using also the software *CaRine Crystallography*. ***Figure 58*** gives the example of a screw dislocation ½[01$\bar{1}$](011), then one can tilt the cube until it represents the most possible the experimental position of the nanocube as shown in ***Figure 59***, ***Figure 60*** & ***Figure 61***.

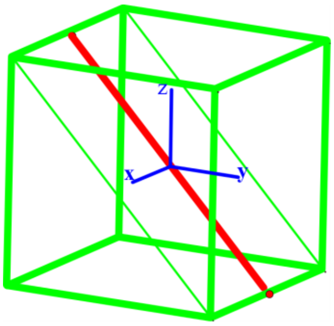

***Figure 58:** ½[01$\bar{1}$] (011) screw dislocation (3D Scheme)*

Figure 59 shows the lines corresponding to 4 screw dislocations (lines parallel to the Burgers vectors) and 4 edge dislocations (lines perpendicular to the Burgers vectors) in the 4 active slip systems.

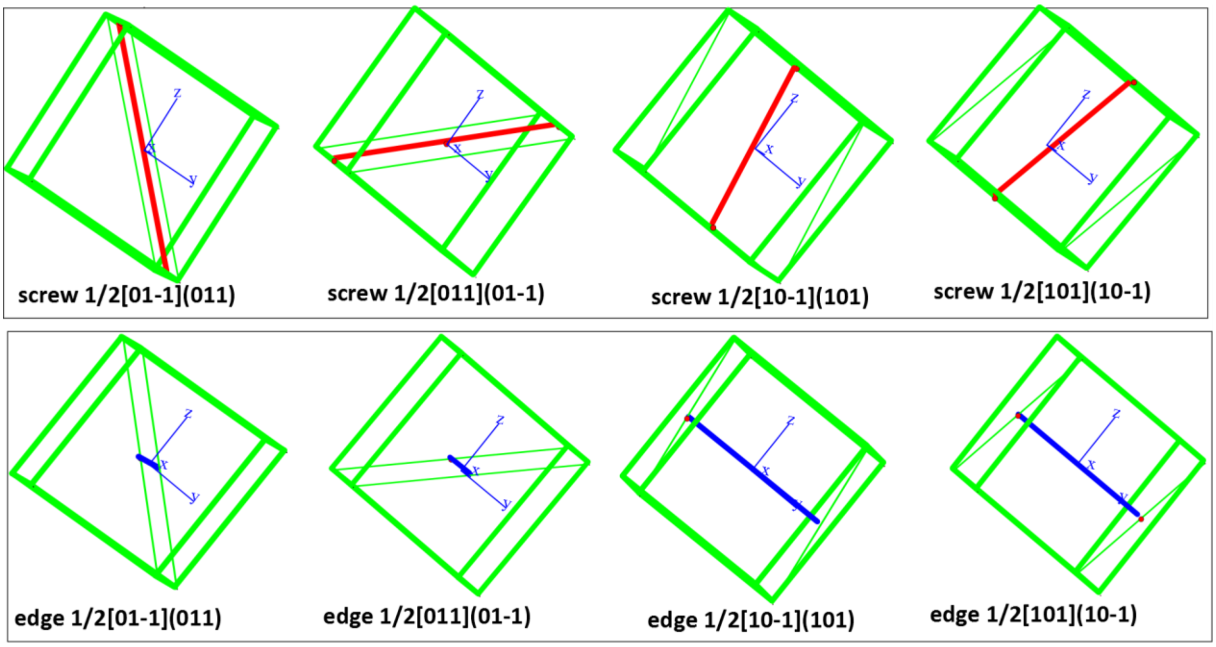

Figure 59: *schemes of 4 screw (red) and 4 edge (blue) possible dislocations lines in {011} and {101} planes nanocubes when compressed in <001> direction.*

With this usual configuration of nanocubes during *in situ* TEM nanocompression of MgO, the following reference orientation is considered:

The compression direction is always along [001] and the zone axis (e-beam direction) is along [100] or near it (often small degree of tilt around [001]). This makes WBDF images possible with **g** (002) as showed above or even with (022) or (331), as it will be shown in **chapter 3.** With these g reflections, we get **g.b≠0** for all possible dislocations in 4/6 active slip systems ({011} and {101} where Burgers are $[01\bar{1}]$, [011], $[10\bar{1}]$ and [101]) respectively.

In *Figure 60*, the WBDF image obtained with the diffracting wave **g** (0,0,2), the dislocations in the nanocube can be compared with the eight possible dislocations lines showed in *Figure 59*. One can see that a pure $1/2[011](01\bar{1})$ screw dislocation (red line in *Figure 60*) reproduces only dislocation in the experimental WBDF image. Moreover, the curved dislocation on the top of the nanocube could be a mixed screw and edge 1/2[011] dislocation in the slip plane $(01\bar{1})$.

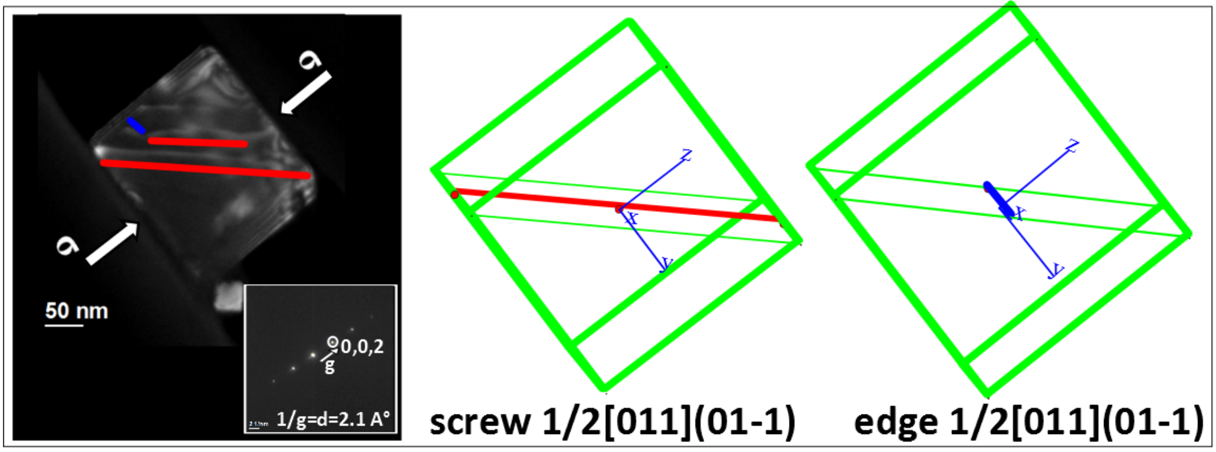

Figure 60: ***a****-WBDF TEM image of a 195 nm sized nanocube at early compression where dislocations appear. Their characteristics are determined in the inset*

DF image shown in ***Figure 60***, exhibit a bright contrast for dislocation lines. Such imaging is performed with small excitation of diffracting waves (kinematical condition), so called Classical WBDF. In this case, the contrast is weak but originated from core region of dislocations (narrow contrast for dislocation line). In the case of classical DF condition, the contrast appears dark due to dynamical effect in the electron propagation waves.

DF images are performed with the diffracting waves **g** (002), (022) or (331). In these cases, the perfect crystal is bright and the dislocations are darker than the perfect crystal, as shown in ***Figure 61***-a.

Later on, tests will also be presented for statistical purposes (size effect on the yield stress for example). Such tests are also carried out in conventional BF images. However, an objective aperture is used to have a contrast which is good enough for the observation of dislocations, as shown in ***Figure 61***-b, where dislocations exhibit a classical dark contrast. The dislocations observed experimentally can also be compared to the lines of dislocations in the 3D cubic cell as shown ***Figure 61***-b.

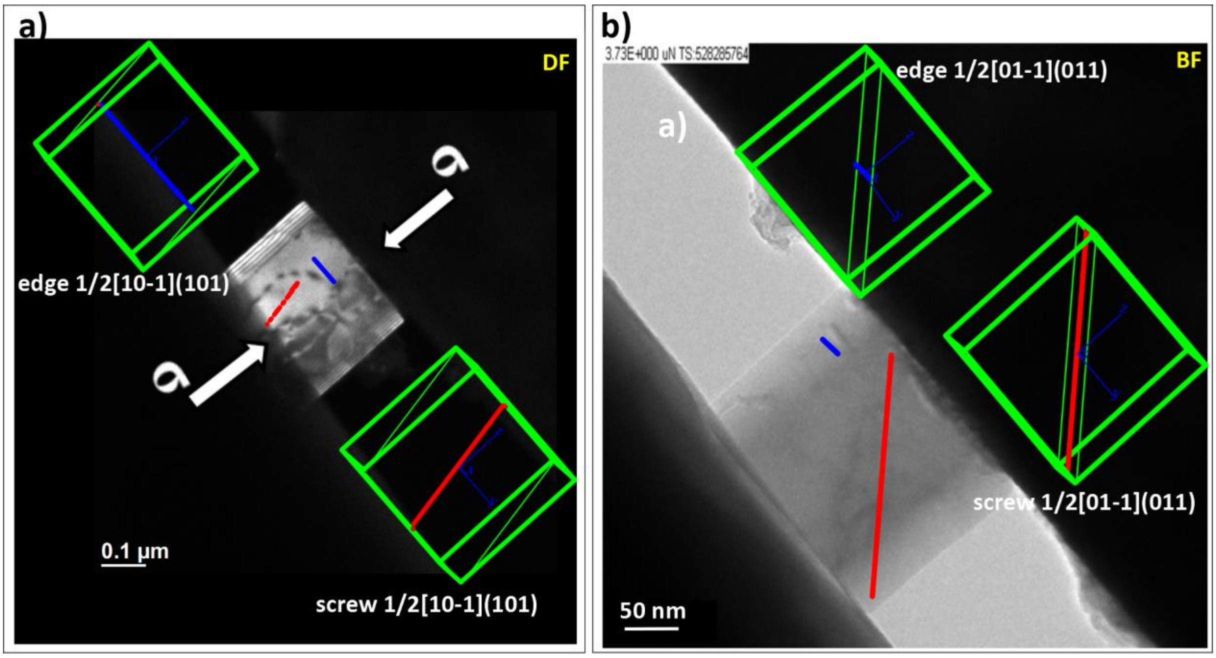

Figure 61: a) *DF image of a MgO nanocubes. Dislocations lines are compared lines of dislocations in the 3D cubic cell.* ***b)*** *Similar interpretation for the BF TEM image of a 170 nm sized nanocube.*

V. Molecular Dynamics (MD) Simulations

MD simulations have been performed by Jonathan Amodeo and Julien Morthomas from group Metal in Mateis Laboratory in a collaboration work.

- **MD Potential Characteristics**

MD simulations are performed to investigate the elementary deformation mechanisms of initially dislocation-free MgO nanocubes under compression at room temperature. The code LAMMPS is used for such simulations. Atomic interactions are described using a rigid ion model:

$$v_{ij}(r_{ij}) = A_{ij}exp\left(\frac{-r_{ij}}{\rho_{ij}}\right) - \frac{c_{ij}}{r_{ij}^6} + \frac{q_i q_j}{r_{ji}}$$

That includes a Buckingham term: $A_{ij}exp\left(\frac{-r_{ij}}{\rho_{ij}}\right) - \frac{c_{ij}}{r_{ij}^6}$, where $A_{ij}exp\left(\frac{-r_{ij}}{\rho_{ij}}\right)$ describes short term repulsion energy and $\frac{c_{ij}}{r_{ij}^6}$ is used for Van der Waals energy, in addition to long-range Coulombic interactions $\frac{q_i q_j}{r_{ji}}$. The Coulombic term increases the simulations time compared to the potential conventionally used for metals.

Three potentials are tested, as shown in ***Table 3***. The Ball and Grimes potential ($B-G\pm 1.7e$) is chosen because it reproduces the elastic constants of MgO obtained elsewhere in the literature (see ***Table 4***).

Table 3: *Elastic constants calculated with three potentials tested.*

	C11 (GPa)	*C12 (GPa)*	*C44 (GPa)*
L-C ±2e	404.38	143.73	85.60
B-G ±2e	466.75	146.58	90.95
B-G ±1.7e	282.61	138.09	137.98

Table 4: $\boldsymbol{B-G\pm 1.7e}$ *potential reproduces elastic constants of MgO obtained elsewhere in the literature.*

		C11 (GPa)	*C12 (GPa)*	*C44 (GPa)*
This work	**SM (LAMMPS)**	282.61 (282.75)	138.09 (138.03)	137.98 (138.03)
Carrez et al. To be published	**SM (GULP)**	283.63	138.03	137.97
Carrez et al. MSEA 2009	***Ab initio (VASP)***	279	93	146
Sinogeikin & Bass PEPI 2000	**Exp (Brillouin)**	297.9	95.8	154.4

Thus, with this potential, the Young's modulus in the [100] direction is calculated to be $E_{[100]}$=191.96 GPa and the shear modulus is μ=99.85 GPa.

Moreover, the $B-G\pm 1.7e$ potential reproduces the dislocation properties of MgO (γ -surfaces energies) obtained by [*[P. Carrez et al. (2014)]*.γ Surfaces are usually considered as an important concept to understand dislocation formation and plastic deformations. Indeed, the γ surface energy is described by the surface energy that results from disturbing the potential of a perfect crystal when translating its upper half part relatively to its lower half part along a glide plane, by a magnitude vector lying in the glide plane, as shown for example in ***Figure 62***.

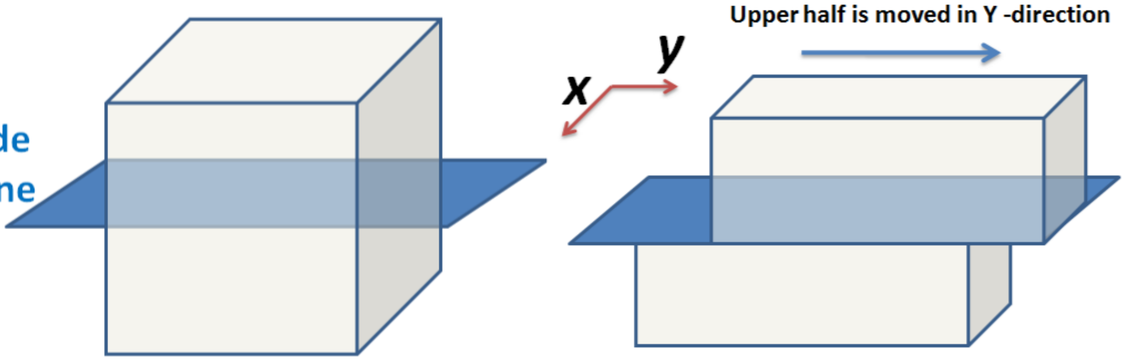

Figure 62: *translating an upper half part relatively to its lower half part along a glide plane.*

γ surface energies in {100} and {110} planes in function of the magnitude of a translation vector, equal to a factor of Burgers vector of ½<110> dislocation, are calculated with the potential chosen (Ball and Grimes). These calculated γ surface energies in {100} and {110} planes coincide with *ab initio* calculations by [*[P. Carrez et al. (2014)]*.and show a lower γ surfaces energies in {110} planes (See ***Figure 63***).

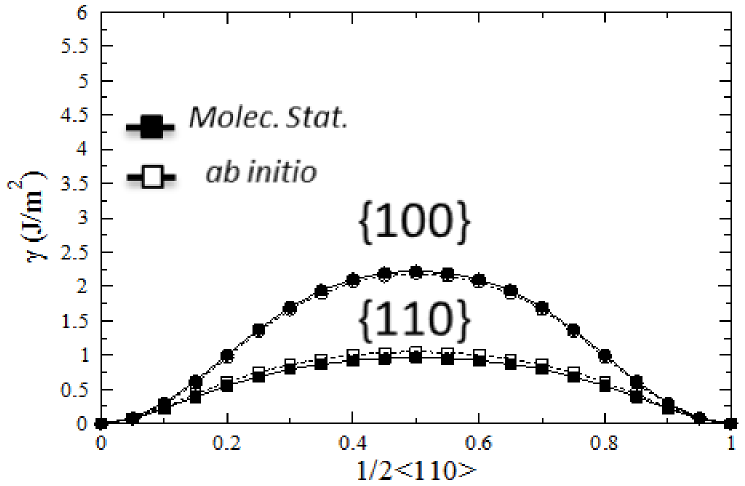

Figure 63: *Generalized Stacking Fault energy γ along ½ 〈1 1 0〉 in {1 1 0} and {1 0 0}. The calculations have been done at 0 GPa* [*P. Carrez et al. (2014)*].

All these elastic and dislocations properties of MgO are key points for interatomic potential transferability towards nanomechanical test simulations.

- **MD Compression method**

Cubic samples with edge lengths from 4.2 nm to 12.7 nm are shaped with free surfaces oriented along the <100> directions, as suggested by the experiment.

The MD compression tests of MgO nanocubes are performed using two external potentials (see ***Figure 64***) which model an infinite flat punch and the substrate.

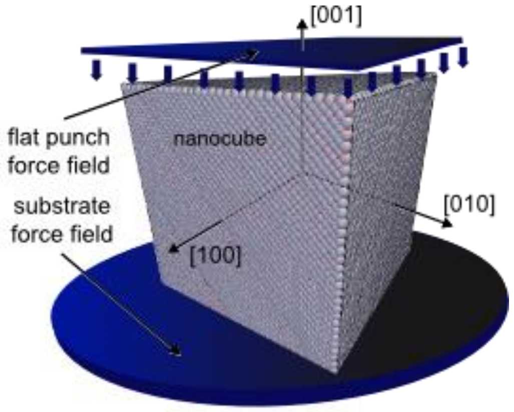

Figure 64: *Scheme of the MD nanocompression simulation set-up, made of two force fields to respectively sustain and compress the nanocube*

To model uniaxial compression along the [001] direction, the top indenter is subjected to a constant displacement rate equivalent to an engineering strain rate of $10^8 s^{-1}$. The bottom potential is kept fixed to sustain the sample. During compression simulations, time steps down to 2 fs are used and a Nose´–Hoover thermostat imposed a temperature of 300 K. The true strain is calculated as in the experiment and the compressive stress is computed as the ratio between the force experienced by the indenter and the instantaneous contact area drawn by the last upper atomic layers.

Simulations are analysed using Atom Viewer, a tool which combines a modified bond-angle method to identify crystalline structures, a Nye-tensor analysis for dislocation Burgers vector definition and a skeletonization algorithm for dislocation reconstruction.

General Conclusion of Chapter 2

In this chapter we presented the MgO characteristics, from its crystallographic structure B1 to the phase stability at ambient temperature and high pressures. Elastic properties (elastic constants, shear and Young moduli) and plastic properties (slip systems, CRSS) of MgO were also presented. Two synthesis methods of MgO single crystals nanocubes were used, namely ‘’Microwave method’’ and ‘’Burning Mg in air method’’. They result in MgO nanocubes in size ranges of [10 - 500 nm] and [10 - 200 nm], respectively.

Characterisations of MgO nanocubes synthesized by both methods were presented. SEM and Conventional BF TEM characterizations revealed the perfect cubic shape of these MgO nanocubes. HRTEM and WBDF characterisations showed that these MgO nanocubes are single crystals and free of dislocations. EDS revealed the low fraction and homogeneous distribution of impurities existing in these MgO nanocubes (99.9± 0.1 at. % MgO). TEM basics concepts and main TEM modes (Conventional TEM BF, BF, DF, WBDF and HRTEM) used in this PhD work were also presented.

In Situ TEM nanocompression tests of MgO nanocubes are carried out on the TEM 2010F (Field-emission 200 KeV) with a dedicated sample holder. The sample holder from Nanofactory was described. Substrate surface treatment by ion polishing and the optimisation of the nanocube deposition have been described. *Then, the main steps of the in situ* TEM nanocompression tests have been presented. They include the alignment of the tip and the substrate, the positioning of MgO nanocubes as well as data acquisition. In order to extract the mechanical parameters of MgO nanocubes compressed in situ, DIC has been presented, as it takes into account the displacement of the diamond punch (assumed to be fixed). Moreover, the principles of TEM images analysis, especially for dislocations characterisations, by WBDF, DF and even BF are explained. Finally, in order to investigate elementary deformation mechanisms of initially dislocation-free MgO nanocubes under compression at RT, we presented the characteristics of the MD simulations performed in a collaboration work.

References

- **Aguado,** Andrés, et Paul A. Madden. « New Insights into the Melting Behavior of MgO from Molecular Dynamics Simulations: The Importance of Premelting Effects ». Physical Review Letters 94, nº 6 (18 février **2005**): 068501. doi:10.1103/PhysRevLett.94.068501.
- **Alfè**, Dario. « Melting Curve of MgO from First-Principles Simulations ». Physical Review Letters 94, nº 23 (15 juin **2005**): 235701. doi:10.1103/PhysRevLett.94.235701.
- **Amodeo**, J., B. Devincre, Ph. Carrez, et P. Cordier. « Dislocation reactions, plastic anisotropy and forest strengthening in MgO at high temperature ». Mechanics of Materials 71 (avril **2014**): 62‑73. doi:10.1016/j.mechmat.2014.01.001.
- **Amodeo,** Jonathan. Modélisation multi-échelle de la déformation plastique de MgO monocristallin : du laboratoire au manteau terrestre. Lille 1, **2011**. http://www.theses.fr/2011LIL10080.
- **Appel**, F., H. Bethge, et U. Messerschmidt. « Dislocation Motion and Multiplication at the Deformation of MgO Single Crystals in the High Voltage Electron Microscope ». Physica Status Solidi (a) 42, nº 1 (16 juillet **1977**): 61‑71. doi:10.1002/pssa.2210420104.
- **Carrez**, Ph., J. Godet, et P. Cordier. « Atomistic simulations of ½ 〈1 1 0〉 screw dislocation core in magnesium oxide ». Computational Materials Science 103 (1 juin **2015**): 250‑55. doi:10.1016/j.commatsci.2014.10.019.
- **Clauer**, A. H., et B. A. Wilcox. « High Temperature Tensile Creep of Magnesium Oxide Single Crystals ». Journal of the American Ceramic Society 59, nº 3‑4 (1 mars **1976**): 89‑96. doi:10.1111/j.1151-2916.1976.tb09438.x.
- **Cockayne**, D. J. H., I. L. F. Ray, et M. J. Whelan. « Investigations of dislocation strain fields using weak beams ». Philosophical Magazine 20, nº 168 (1 décembre **1969**): 1265‑70. doi:10.1080/14786436908228210.
- **Copley**, Stephen M., et Joseph A. Pask. « Plastic Deformation of MgO Single Crystals up to 1600°C ». Journal of the American Ceramic Society 48, nº 3 (1 mars **1965**): 139‑46. doi:10.1111/j.1151-2916.1965.tb16050.x.
- **Duffy**, Thomas S., Russell J. Hemley, et Ho-kwang Mao. « Equation of State and Shear Strength at Multimegabar Pressures: Magnesium Oxide to 227 GPa ». Physical Review Letters 74, nº 8 (20 février **1995**): 1371‑74. doi:10.1103/PhysRevLett.74.1371.
- **Esnouf**, Claude. *Caractérisation microstructurale des matériaux: analyse par les rayonnements X et électronique*. Lausanne: Presses polytechniques et universitaires romandes, 2011.
- **Gilman**, J. J. « Plastic anisotropy of lif and other rocksalt-type crystals ». Acta Metallurgica 7, nº 9 (1 septembre **1959**): 608‑13. doi:10.1016/0001-6160(59)90130-0.
- **Haasen**, P., U. Messerschmidt, et W. Skrotzki. « Proceedings of the International Conference on Low Energy Dislocation Structures Low energy dislocation structures in ionic crystals and semiconductors ». Materials Science and Engineering 81 (1 août **1986**): 493‑507. doi:10.1016/0025-5416(86)90286-7.
- **Habas,** Marie-Pierre, Roberto Dovesi, et Albert Lichanot. « The ##IMG## [http://ej.iop.org/images/0953-8984/10/31/008/toc_img1.gif] Phase Transition in Alkaline-Earth Oxides: A Comparison of Ab Initio Hartree-Fock and Density Functional Calculations ». Journal of Physics: Condensed Matter 10, nº 31 (**1998**): 6897. doi:10.1088/0953-8984/10/31/008.

- **Heidenreich**, Robert D. « Electron Reflections in MgO Crystals with the Electron Microscope ». Physical Review 62, nº 5‑6 (1 septembre **1942**): 291‑92. doi:10.1103/PhysRev.62.291.
- **Hulse**, C. O., S. M. Copley, et J. A. Pask. « Effect of Crystal Orientation on Plastic Deformation of Magnesium Oxide ». Journal of the American Ceramic Society 46, nº 7 (1 juillet **1963**): 317‑23. doi:10.1111/j.1151-2916.1963.tb11738.x.
- **Hulse**, Charles O., et Joseph A. Pask. « Mechanical Properties of Magnesia Single Crystals Corn Pression ». Journal of the American Ceramic Society 43, nº 7 (1 juillet **1960**): 373‑78. doi:10.1111/j.1151-2916.1960.tb13674.x.
- **Kagel**, R. O., et Robert G. Greenler. « Infrared Study of the Adsorption of Methanol and Ethanol on Magnesium Oxide ». The Journal of Chemical Physics 49, nº 4 (15 août **1968**): 1638‑47. doi:10.1063/1.1670289.
- **Matsui**, Masanori. « Molecular Dynamics Study of the Structural and Thermodynamic Properties of MgO Crystal with Quantum Correction ». The Journal of Chemical Physics 91, no 1 (**1989**): 489. doi:10.1063/1.457484.
- **Messerschmidt**, Ulrich. Dislocation Dynamics During Plastic Deformation. Vol. 129. Springer Series in Materials Science. Berlin, Heidelberg: Springer Berlin Heidelberg, **2010**. http://link.springer.com/10.1007/978-3-642-03177-9.
- **S. Takeuchi,** H. Koizumi, T. Suzuki, Peierls stress and kink pair energy in NaCl type crystals, Mater. Sci. Eng. A 521(**2009**) 90–93.
- **Stretton**, Iona, Florian Heidelbach, Stephen Mackwell, et Falko Langenhorst. « Dislocation creep of magnesiowüstite (Mg0.8Fe0.2O) ». Earth and Planetary Science Letters 194, nº 1‑2 (30 décembre **2001**): 229‑40. doi:10.1016/S0012-821X(01)00533-7.
- **Takahashi**, Naoyuki. « Simple and rapid synthesis of MgO with nano-cube shape by means of a domestic microwave oven ». Solid State Sciences 9, nº 8 (août **2007**): 722‑24. doi:10.1016/j.solidstatesciences.2007.05.007.
- **Thölén**, Anders. « Stress Fields at Boundaries between Contacting Particles ». Journal of Materials Science 41, nº 14 (29 juin **2006**): 4466‑76. doi:10.1007/s10853-006-0092-x.
- **Williams, David B., et C. Barry Carter**. Transmission Electron Microscopy: A **Textbook f**or Materials Science. 2. ed. New York: Springer, 2009.
- **Zerr**, A., et R. **Boehler.** « Constraints on the Melting Temperature of the Lower Mantle from High-Pressure Experiments on MgO and Magnesioüstite ». Nature 371, nº 6497 (6 octobre **1994**): 506‑8. doi:10.1038/371506a0.

Chapter3: Results on *In Situ* TEM Nanocompression of MgO Nanocubes

In this chapter**,** we present in first part the results on the elementary deformation mechanism by coupling experimental and MD simulations results. The second part deals with a statistical experimental study revealing the effect of the nanocube size on the yield strength. The effect of the electron beam on the yield strength is also studied. Moreover, the behavior of the stress-strain curves (stress-drops) in small and larger nanocubes is discussed in function of the dislocation characteristics deduced from the TEM images.

In the following, as both synthesis methods gave nanocubes with similar characteristics (absence of dislocation, impurity fraction), the nanocubes will not be sorted by their synthesis method.

3.1. Deformation Mechanism of MgO nanocubes

3.1.1. Experimental and MD Results of In Situ Compression of MgO nanocubes

I. Mechanical Behavior of MgO Nanocubes

The mechanical response of a 140 nm edge size MgO nanocube compressed *in situ* in TEM at room temperature, with a constant displacement rate of 2 nm/s (deformation rate 1,43.10^{-02}) is displayed in *Figure 65*-a. The compression test is composed of five successive loads–unload cycles.

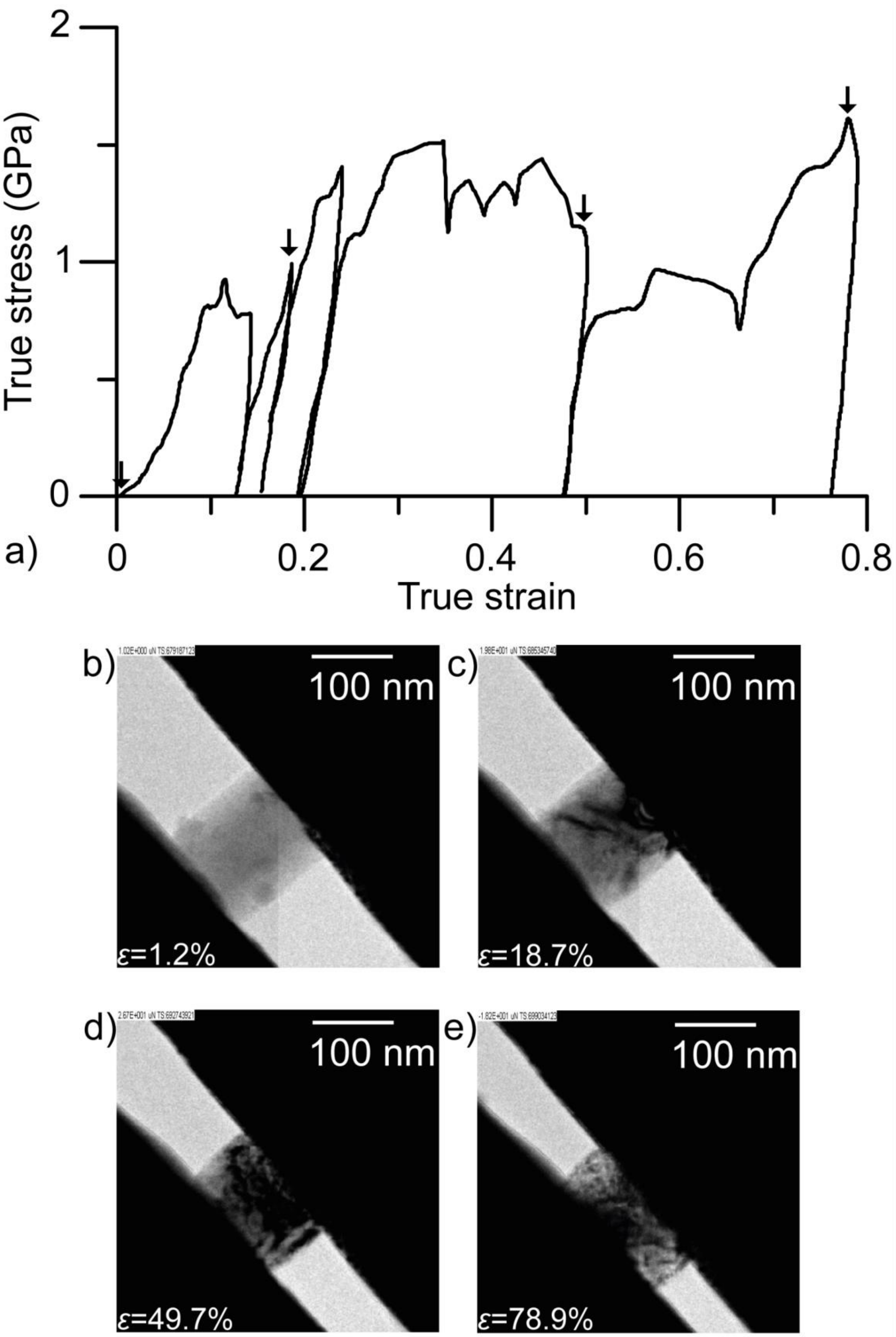

Figure 65: ***(a)*** *Experimental true stress–strain curve for a 140 nm sized MgO nanocube compressed in situ in TEM. Five loading–unloading cycles are shown.* ***(b–e)*** *Images at ε = 1.2%, ε = 18.7%, ε = 49.7% and ε = 78.9% true strain are represented. The positions of the images are indicated as black arrows on the stress-strain curve.*

In addition to the stress–strain curve, four on-the-fly images are presented in *Figure 65* b–e for true strain of about ε= 1.2%, ε = 18.7%, ε = 49.7% and ε = 78.9%, respectively. The sample is deformed up to ε = 79.0% before final unload.

Early in the first cycle, the stress–strain dependency is nonlinear and noisy. This transitory stage reflects the accommodation regime between the substrate, the sample and the tip up to ε = 3.5%. Then, the curve exhibits an elastic-like behavior up to ε = 9.0% and a true stress of about σ = 0.78 GPa. A Young's modulus of about $E_{[001]}$ = 141.9 GPa is deduced from the early beginning of the first unload. From this point and during the rest of the whole compression test, mobile contrast bands are observed in the nanocube.

Contrast bands may appear for several reasons, e.g. elastic deformation of the lattice or presence of mobile/sessile dislocations. In the following, we will focus only on contrast bands that are believed to be the signature of dislocations. These contrast bands may be recognized by their peculiar curved shape as well as their specific orientation, e.g. the two angled contrast bands observed on the image at ε= 18.7% in ***Figure 65***-c.

One can note that all the residual contrasts accumulated during the first load cycle, up to ε = 13.1%, vanish during the first unload. This phenomenon occurs because of both compressive stress relaxation and surface image forces, believed to be particularly effective in nanometer sized samples. This leads to a perfectly refreshed microstructure comparable to the one observed in ***Figure 65***-b.

At ε = 18.7%, one may see two freshly nucleated, linear and parallel contrast bands (***Figure 65***-c). These bands are tilted at ~45° from the [001] nanocube surfaces, which might be an evidence for dislocation glide in {110} slip planes.

After their emergence from a surface and/or an edge, both traces escape from the opposite side of the nanocube. Further contrast bands can be observed during the third cycle and the beginning of the fourth one where the true stress rises up to σ= 1.51 GPa.

During the fourth cycle, successive stress drops take place. Similar stress drops are often described in the literature *[S.H. Oh et al. (2009)] [D. Kiener et al. (2011)] [F. Csikor (2007)] [M. Uchic et al. (2004)*] and are attributed to dislocation nucleation or multiplication peaks and subsequent severe sudden plastic deformation. Although the deformed nanocube becomes very thick during the fourth cycle, these severe plastic deformation events are still recognizable by the high contrast they produce, see for instance on the ε = 49.7% image (***Figure 65***-d). Nevertheless, it is not possible to analyze slip contrasts from the middle of cycle four up to the end of the fifth cycle because of their high density (***Figure 65***-e). Finally, the sample is unloaded after the fifth cycle and a total deformation of about ε = 79.0%. No sign of failure has been observed during or after unload.

II. Focus on the Early Stages of Deformation

In order to investigate further the elementary mechanisms responsible for the first stages of MgO nanocubes deformation, two supplementary *in situ* compressions tests are studied. Stress–strain curves of 90 and 120 nm sized nanocubes compressed *in situ* in TEM at constant displacement rate 2 nm/s (2,22 .10^{-02} and 1,67. 10^{-02} deformation rate respectively) are represented in *Figure 66*.

As the main features of the stress–strain curve of the 140 nm sized MgO nanocube have been described in the previous section, we will focus only on new outcomes in the following.

We observe that both samples are characterized by a strain burst occurring at higher stress than in the case of the 140 nm sized sample. At this point, the true stress is equal to ~2.72 and 5.03 GPa, respectively, for the 120 and the 90 nm sized samples.

In the inset of *Figure 66*, an image at ε = 7.3%, i.e. during the initial strain burst, of the 120 nm sized nanocube is shown. Once again, we observe an inclined and straight contrast band, tilted at ~45° from the indenter and generated from the surface and/or an edge of the nanocube, similarly to what was observed in the case of the 140 nm sized sample (*Figure 65*).

Further experiments performed in WBDF mode and showing 45° tilt from [001] of the nanocubes is shown in **chapter 2**. WBDF technique confirms that these dislocations are gliding in $(01\bar{1})$ glide planes and its burgers vector could be identified.

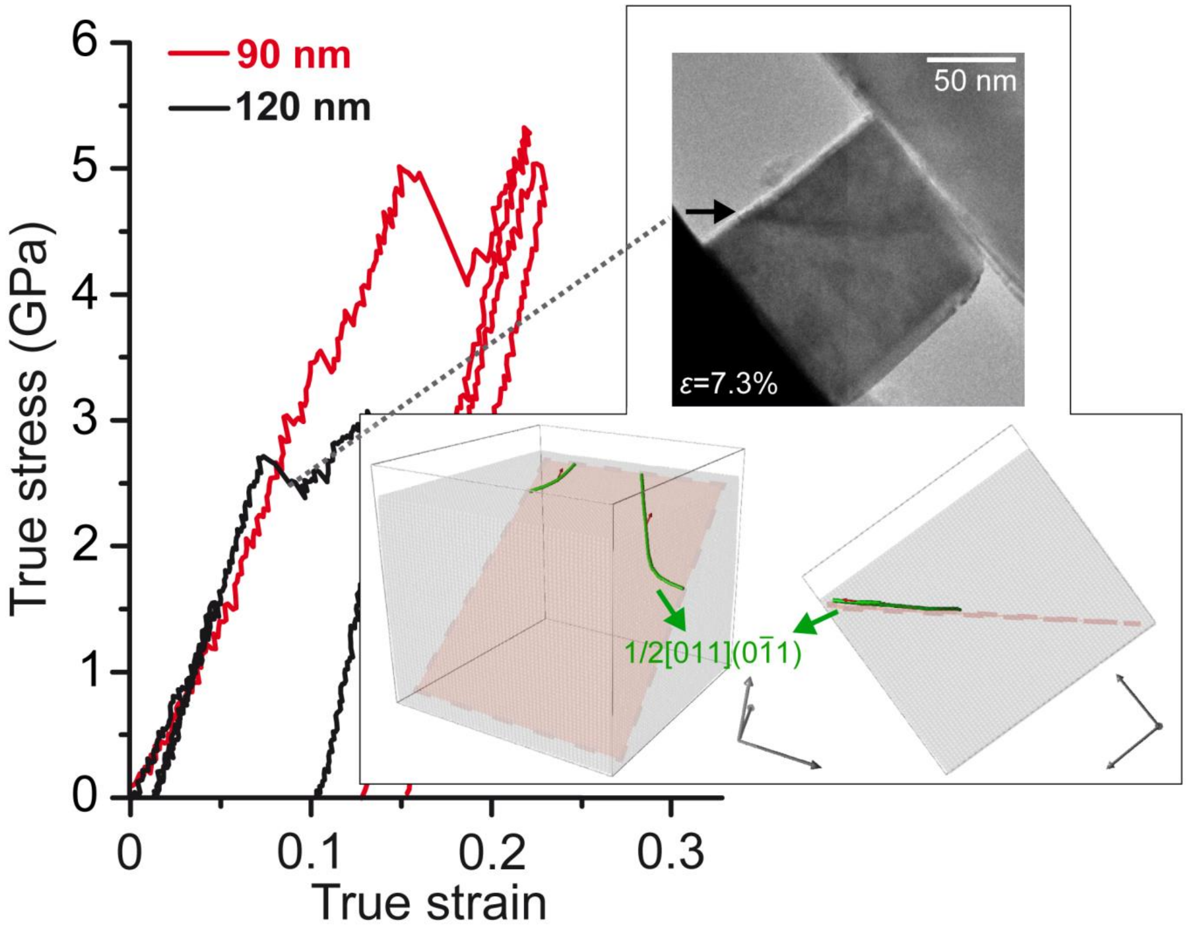

Figure 66: *Experimental stress–strain curves for two MgO nanocubes of 90 (red line) and 120 (black line) nm edge lengths. In the inset: TEM image of a 120 nm sized sample during compression, ε = 7.3%. The black arrow shows a contrast band corresponding to dislocations that emerge from the surface of the cube. Two MD simulation snapshots of a 12.6 nm sized nanocube are also represented. Reconstructed ½<110>{110} dislocations are in green. The slip plan is in red. Atoms are shown in transparent light gray for the sake of clarity. The coordinates system is oriented along the cubic directions.*

MD simulations are performed in order to identify elementary deformation mechanisms of MgO nanocubes. Although the compression rate that can be computed is far higher than in the experiment, and the maximum size of the sample is smaller (especially in the case of ionic systems), MD simulations are known to provide a qualitative basis for the identification and interpretation of elementary mechanisms possibly responsible for the deformation of nano-objects [*D. Mordehai et al. (2011)*]- **[***T. Zhu et al.(2008)*] – [*T. Zhu et al. (2010)*]. Figure 66 shows early nucleated dislocations during the compression of a 12.6 nm sized nanocube by MD. Here, dislocations are nucleated from two lateral edges (contrarily to the other top and bottom planar edges) of the nanocube. The slip plane is $(0\bar{1}1)$ and the Nye tensor analysis leads to dislocations characterized by a 1/2[011] Burgers vector. ½<110> Burgers vectors are characteristic of perfect dislocations in the B1 structure.

Similar compression tests have been performed for 10.1, 7.6, 5.9 and 4.2 nm sized cubes. Corresponding stress–strain curves are presented in Figure 67.

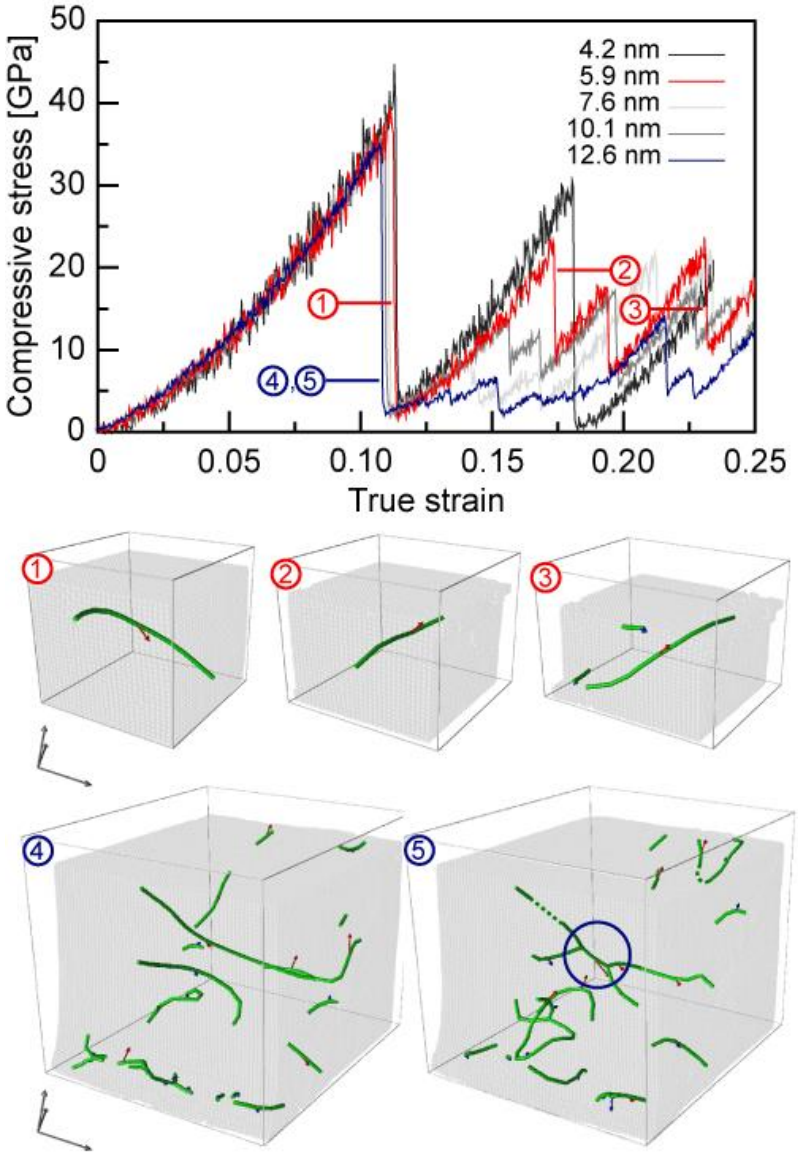

Figure 67: *Stress–strain curves of MgO nanocubes from MD compression simulations. ❶-❺: Images of nanocubes during compression. Green lines correspond to dislocations and red arrows represent ½<110> Burgers vector orientation. ❶-❸ show the evolution of the 5.9 nm sized sample. ❹ and ❺ show the dislocation organization at the end of the first nucleation peak of the 12.6 nm sized sample. The blue circle shows a dislocation junction embryo. The coordinates system is oriented along the cubic directions.*

They are first characterized by a linear elastic regime up to $\varepsilon\sim3\%$. $E_{[001]}$ values are displayed in ***Table 5***. In order to compare $E_{[001]}$ to bulk Young's modulus $E_{[001]}^{bulk}$, bulk elastic constants are calculated. Results lead to C_{11} = 282.8 GPa, C_{12} = 138.0 GPa and C_{44} = 138.0 GPa. These results are in good agreement with recent calculations using the same interatomic potential *[Carrez et al. (2014)]*. We deduce $E_{[001]}^{bulk}$ = 192.3 GPa using the anisotropic elastic theory.

***Table 5**: Young's moduli and yield stresses for MD compression simulations, plus sites and slip systems of the first nucleated dislocations. $E_{[001]}^{bulk}$ = 192.3 GPa is deduced from the elastic constants and the anisotropic elastic theory. For the 7.6 nm sized particle, two dislocations nucleate simultaneously.*

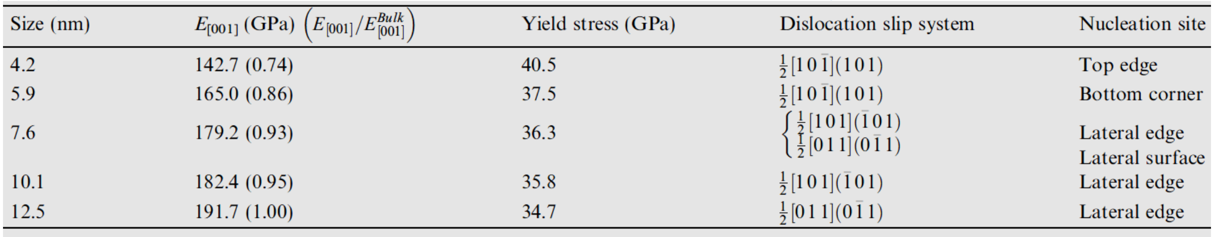

Size (nm)	$E_{[001]}$ (GPa) $\left(E_{[001]}/E_{[001]}^{Bulk}\right)$	Yield stress (GPa)	Dislocation slip system	Nucleation site
4.2	142.7 (0.74)	40.5	$\frac{1}{2}[10\bar{1}](101)$	Top edge
5.9	165.0 (0.86)	37.5	$\frac{1}{2}[10\bar{1}](101)$	Bottom corner
7.6	179.2 (0.93)	36.3	$\begin{cases}\frac{1}{2}[101](\bar{1}01)\\ \frac{1}{2}[011](0\bar{1}1)\end{cases}$	Lateral edge Lateral surface
10.1	182.4 (0.95)	35.8	$\frac{1}{2}[101](\bar{1}01)$	Lateral edge
12.5	191.7 (1.00)	34.7	$\frac{1}{2}[011](0\bar{1}1)$	Lateral edge

Afterwards, the elastic regime becomes non-linear up to 10.8% < ε< 11.4%, depending on the size of the sample.

This phenomenon is commonly observed at the nanoscale and is attributed to surface forces and anharmonicity *[M.T. McDowell et al.(2008)] [Y.J. Wang, et al.(2013)].* The yield stress varies continuously from 40.5 to 35.2 GPa, when decreasing the size of the sample, and dislocations nucleate. Nucleation can be inferred from the simulated stress–strain curves by the correlated stress drops. When dislocations nucleate (or escape), top or bottom surfaces of the sample are rearranged, leading to a slight increase in the distance between the sample top surface and the indenter. As the flat punch force varies inversely with this distance, the stress drops down.

The onset of plastic deformation is controlled by ½<110>{110} dislocations only, nucleated either from an edge, a surface or a corner of the nanocube. A detailed analysis of the localization of dislocation nucleation first events is summarized in ***Table 5***.

No dislocation is observed in the {100} or {111} glide planes during the simulations. This result is in agreement with early 45° tilted contrast bands described on the TEM images of *Figure 65*, *Figure 66*, and later on with dislocations analysis of WBDF TEM images. This confirms that the initial elementary process that governs the deformation of <100> oriented and pristine MgO nanocubes under uniaxial compression is the nucleation of ½ <110> perfect dislocations, gliding later in {110} slip planes.

3.1.2. Discussion

I. Toward small-size effects on MgO mechanical properties

In contrast to their bulk counterpart, nanometer-sized MgO particles deform up to large strain, beyond ε = 78.9% in the experiment. No sign of crack has been observed during and after the compression of the nanocubes.

These results apply also to the case of MD compression simulation using the Ball and Grimes interatomic potential. In the simulation, we observe a strong effect of the size on the elastic regime. For particles with sizes lower than 10 nm, $E_{[001]}$ decreases when reducing the size (Table 1). Furthermore, the elastic regime becomes non-linear. This phenomenon is weaker for larger particles and is thus not expected in the experiments (at least for the sizes we investigate here).

Nevertheless, $E_{[001]}$ is lower in the experiment (~142 GPa for the 140 nm sized particle) compared to the experimental bulk value $E_{[001]}^{bulk}$ ~248 GPa *[M.A. Durand et al. (1936)]* [*D.-H. Chung (1963)*]. We believe that this variation is not a size-effect but may rather be an extrinsic effect as e.g. electron-beam assisted deformation [*M. Mačković et al (.2014)*][*K. Zheng et al. (2010)*][*J. Zang et al. (2011)*]. *Zheng et al.* point out that the force required to deform amorphous silica (a-SiO_2) NPs at a given elastic strain is lowered by a factor 2 to 3 in the case of electron-beam-on tests compared to electron- beam-off ones [*K. Zheng et al. (2010)*]. In the work of *Mačković et al.*, a-SiO_2 NPs are pre-irradiated and then compressed under beam-on/off conditions. Results show that the Young's modulus is increased by a factor 2 (whatever the conditions) compared to the low-dose/beam-off reference conditions with a maximum load force of 50% up to 500% the original one [*M. Mačković et al.(2014)*]. Similar observations have been made by *Zhang et al.* in crystalline zinc tin oxide nanowires where electron-beam irradiation is believed to change elastic and electrical conductivity properties [*J. Zang et al. (2011)*]. Nevertheless, despite the fact that similar processes might influence the Young's modulus in our experiments, we believe that they should not modify the elementary mechanisms responsible for plastic deformation. However in the following **section 3.2** we present result on the electron beam effect on the yield strength.

While we have performed several compression tests, only perfectly aligned and homogeneously deformed samples are presented here. Therefore, alignment should not be a strong source of bias. Furthermore, we did not notice any significant influence of the variations of the aspect ratio φ, during the deformation of the 140 nm sized sample, on the subsequent elastic reloads. This is shown in ***Figure 68***. Unloads are used for a better evaluation of E [001] as the indenter-to sample contact is more accurate during unloads compared to the accommodation regime observed during the early beginning of the first load.

As a corollary, no effect of the beam exposure time has been deduced from the analysis of elastic reloads. The aspect ratio effect on the subsequent elastic portions observed in the simulations has also been investigated without significant outcome.

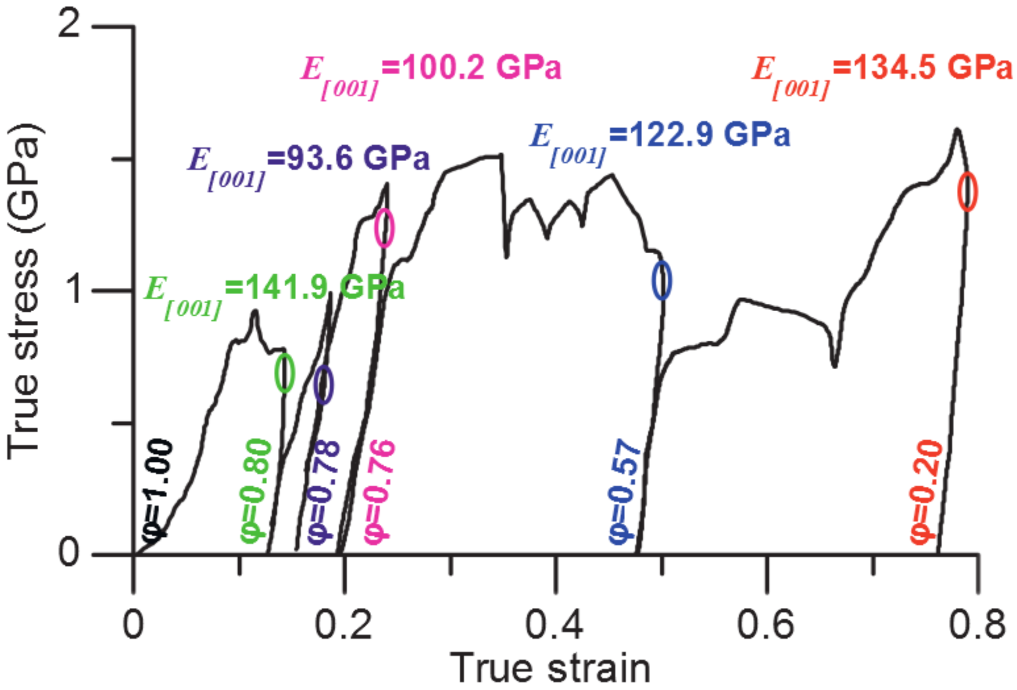

Figure 68: *Evaluation of effective Young's moduli during elastic reloads for the 140 nm sized sample. Circled zones refer to regions where Young's moduli have been evaluated. Size aspect ratio φ has been evaluated from the beginning of each unloads using DIC.*

Finally, the flow stress is also influenced by downscaling, and raises up in comparison to bulk <100> compression tests at RT i.e. from ~ 50 MPa in bulk conditions [*C. Hulse et al. (1960)*] [*F. Sato et al.1980*] [*C. Barthel thesis 1984*] [*J. Amodeo et al.2011*] up to the GPa range for the nanocubes (***Figure 65**-**Figure 66***). These results confirm that lowering the scale permits an increase in both strength and ductility, even for originally brittle ceramics. More specifically, yield stresses from experiments and simulations seem to exhibit a size effect of ~10 and 100 nm. ***In section 3.2, we present a statistic experimental study on the size effect on the yield strength***. In the following, we will further focus on the special features of the plastic deformation regime of MgO nanocubes.

II. Dislocation nucleation and slip systems in nanosized MgO

Both *in situ* TEM compression tests and MD simulations agree that {110} dislocations are responsible for plastic deformation in the MgO nanocubes. MD compression simulations lead to full ½<110> Burgers vectors. Neither dislocations in the {100} or {111} slip planes nor twinning dislocations are observed in both the experiments and the simulations .

1/2<110>{110} dislocation glide is also one known mechanism responsible for the deformation of MgO micropillars [*S. Korte et al. (2011), Philos.Mag*][*S. Korte et al.(2011),acta*] and bulk single crystals [*C. Hulse et al. (1960)*] [*F. Sato et al. (1980)*] [*S. Copley et al.(1965)*] [*J. Amodeo et al.(2011)*] [*F. Appel et al.(1985)*].

Indeed, for <100>-compressions, only ½<110>{110} and 1/2<110>{111} slip system families may contribute to the deformation. As mentioned **in chapter 2,** the Schmid factor for these slip system families is about $S_{\{110\}}$= 0.50 for 4 over 6 ½<110>{110} slip systems and $S_{\{111\}}$= 0.41 for 8 over 12 ½<110>{111} slip systems, others being null. Although both slip system families exhibit comparable Schmid factors, ½<110>{111} slip is unfavored due to charge repulsion between ions in the case of NaCl-type ionic materials as MgO [*J. Gilman 1959*]. This phenomenon leads to a surprisingly high shear stress for the {111} slip planes compared to what is generally observed, e.g. in fcc metals. With this orientation, {100} slip can only occur in the case of misorientations or local rotations. Nevertheless, ½<110>{100} slip is believed to be effective under a rather higher shear stress than ½<110>{110} in RT compression experiments [*C Hulse et al. 1963*] [*C. Barthel thesis 1984*] [*F. Appel et al.1985*], which does not make {100} slip planes suitable candidates to accommodate deformation in our study.

To further investigate the relative role of {100}, {110} and {111} glide planes, we have calculated the GSF (Generalized Stalking-Fault) energies (the so-called $\gamma -$surfaces) using the same interatomic potential as that for the MD compression simulations, as previously mentioned in **chapter 2**. GSF energies are computed by simply shifting the atoms contained in the upper half of a simulation cell relatively to its lower half by an appropriate translation vector owned by the boundary plan. GSF energies provide a good estimate of the sensitivity of a slip plane to be sheared in a given direction. As shown in e.g. *Carrez et al.* [*P. Carrez et - 2009*], GSF energies calculated in the {110} and the {100} planes of MgO do not exhibit the characteristic, “fcc-like”, stable stacking fault energy (sSFE) that allows ½<110> undissociated dislocations only. This corroborates the results inferred from the Nye tensor analysis during the MD compression simulations where perfect dislocations only are observed (*Figure 66*& ***Figure 67***).

III. Deformation regimes and dislocation network

While the nucleation process and the propagation of ½ <110>{110} dislocations are at the onset of plastic deformation of initially pristine MgO nanocubes, it is interesting to see if dislocation networks can be formed. *Figure 69* shows four supplementary TEM images of the 140 nm sized nanocube (already described previously) during the first load cycle. In this figure, one can identify at least two mechanisms that operate simultaneously. Indeed, red lines on *Figure 69* emphasize a dislocation contrast that escapes progressively the sample from the surface, just after it nucleates from the other side of the sample. This process of dislocations nucleation and escape from surfaces is observed also in other experiments that are presented in the following in **section 3.2.**

This process of nucleation-exhaustion of dislocations is often observed when dislocation glide is not precluded [*J. Greer et al. 2006*] [*S.H. Oh et al. 2009*]. In some cases, it can be the unique rate controlling mechanism, see for instance the MD compression simulations for nanocube edge lengths size lower than 10 nm, shown in ***Figure 67***. Indeed, for the 4.2 nm and the 5.9 nm sized simulated samples, stress–strain curves clearly show consecutive stress drops. These peaks are due to the nucleation of one or very few dislocations that induce localized deformation and directly escape from the cube after their nucleation, as observed in ***Figure 67***. This dislocation starvation process is less pronounced in the 7.9 nm sized sample and disappears nearly from the 12.6 nm sized sample.

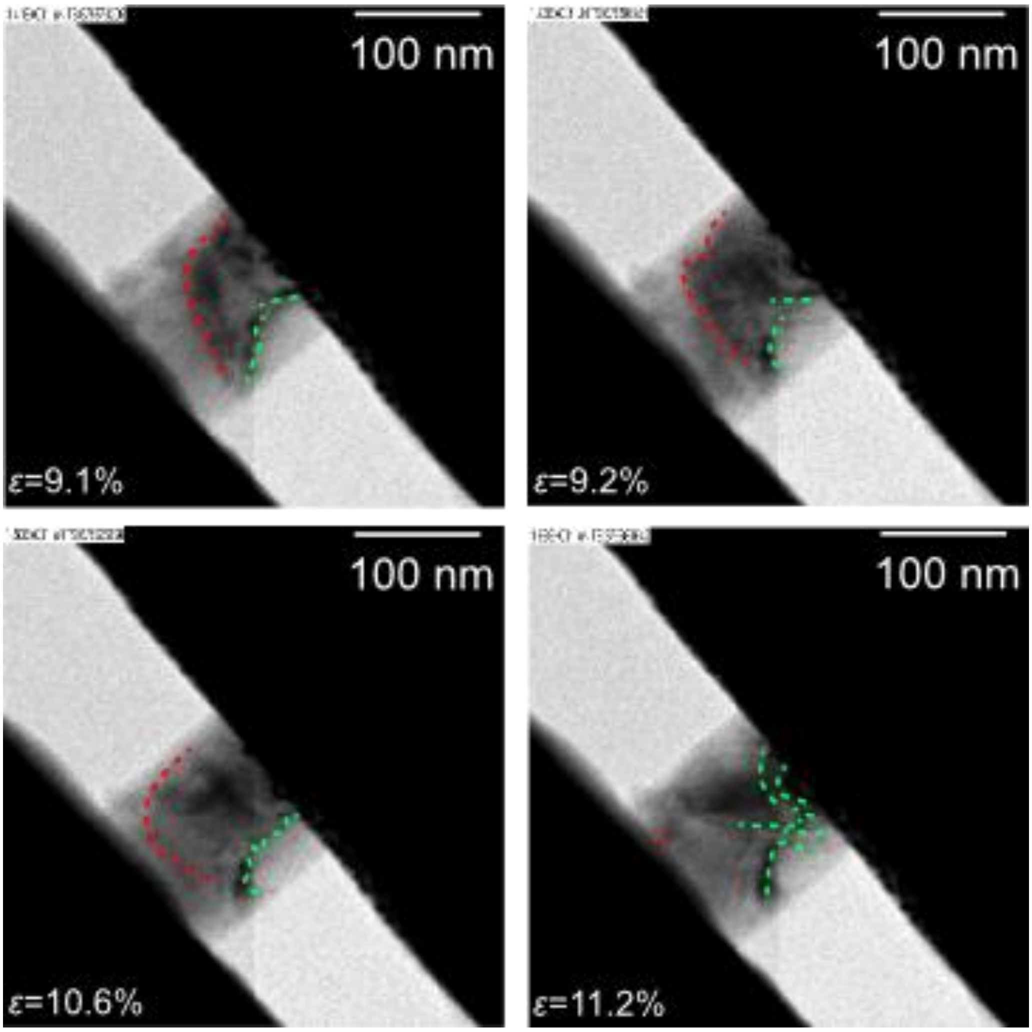

Figure 69: *TEM images of a 140 nm sized MgO nanocube during the first cycle of load. Dashed red lines show a contrast band that escapes progressively the sample. Green lines show an arrangement of contrast bands that may be attributed to the formation of a dislocation network.*

Actually, in the case of the 12.6 nm sized sample, deformation is homogeneous and dislocations nucleate from multiple slip systems during the first stress drop. In this case, gliding dislocations intersect and react, which can be viewed as the critical step of the dislocation network formation (***Figure 67***). This process is strongly different from the dislocation starvation process described above, as it does not require further dislocation nucleation, i.e. dislocations later unlock from the dislocation network and multiply to accommodate further deformation. One should note that the lack of subsequent large stress drops on the 12.6 nm sized sample stress–strain curve is due not only to this last microstructural process but also to the increase of the sample size. Indeed, following a simple first order approach, one can approximate the average shear $\bar{\gamma}$ produced by a $\{110\}$ gliding dislocation in a cube of edge length l by Eq. (1):

$$\bar{\gamma} = b\frac{\bar{S}}{V} = b\frac{\sqrt{2}}{2l} \qquad \text{Eq. 1}$$

where b is the Burgers vector length, $\bar{S}$ is the averaged {110} surface area swept by the dislocation and V is the volume of the sample. From Eq. (1), the amount of shear produced by a dislocation decreases as the size of the nanocube increases. As a consequence, and assuming a constant strain rate, the stress response to a shear increment will be smoother for large samples than for a small one.

Both deformation regimes described above and their respective transition have already been observed in metallic nano-objects [*J. Greer et al. 2006 phys. rev*][*I. Ryu et al. 2013*], and may apply also to B1-structured ceramics.

Finally, clear signs of curved dislocations appear during the *in situ* TEM compression tests as in the MD compression simulations. These results are in contradiction with RT TEM observations performed in bulk MgO after compression [*U. Messerschmidt 2010*], where dislocation patterns merely consist in long, straight and screw dislocation segments, characteristic of a Peierls lattice friction regime. As the Peierls stress (stress necessary to generate dislocation glide at 0 K) is ~150 MPa in the {110} slip planes and 1600 MPa in the {100} planes in MgO [*C. Barthel, thesis 1984*] [*J. Amodeo et al. 2011*] [*F. Appel 1985*] [*P. Carrez et al. 2009*], we believe that the lattice friction is overcome in both the experiments and in the simulations on MgO nanocubes, leading to more isotropic dislocation lines.

This topological property is of primary importance because contact reactions between straight screw dislocations may sometimes not lead to the formation of junction locks. This particularly applies in the case of the bcc structure [*L. Kubin 2003*] and for the B1 structure of MgO as shown in recent DDD simulations [*J. Amodeo et al. 2014*]. Actually, non-screw dislocations are required to generate a dislocation junction in MgO. ***Figure 67*** shows images of a 12.6 nm sized nanocube deformed in MD simulations where two curved dislocations with 60° tilted Burgers vectors react with each other to create a junction embryo following the reaction path ½$[10\bar{1}](101)$ + ½ $[01\bar{1}](011)$ → ½$[11\bar{2}](\bar{1}10)$. This local interaction process is not observed in smaller samples where all the deformation is accommodated by only a few dislocations that never intersect (***Figure 67***). This result confirms that the probability of dislocations intersecting is more likely in larger samples due to a higher number of defects. Finally, one can see in ***Figure 67*** that contact interactions between dislocations (e.g. junctions, crossed or repulsive states) enhance the build-up of a dislocation network during the deformation of the 12.6 nm sized nanocube.

In summary, and contrary to what is observed in bulk MgO at RT, the high stress reached during the nanocompression tests could allow dislocations to overtake the lattice friction and thus increase the possibility of contact reactions between dislocations. This process improves the formation of a dislocation network, as it is observed in the compression simulations of the 12.6 nm sized nanocube (***Figure 67***). We believe that a similar process is likewise the source of the persistent contrast bands observed during the *in situ* TEM compression tests (***Figure 65***&*Figure 69*).

Further *in situ* TEM nanocompression tests on MgO nanocubes on a wider size range are performed. Correlation between stress-strain curves and TEM images provide further information on the effect of the nanocube size on the measured yield stress and on both deformation mechanism regimes. This is presented in **section 3.2.**

IV. Implications for Nano Crystalline (NC) ceramics

The results presented above have direct potential future impact for the processing (i.e. compaction, ball milling) or the design (i.e. mechanical properties) of nanostructured bulk ceramics. Indeed, knowing the plastic deformation mechanisms and mechanical constitutive laws of ceramic nanoparticles (NPs) are of key importance for phenomena such as third body wear particle in contact mechanics, milling of NPs which may exhibit a plastic behavior below a certain size or particle compaction during green body preparation of ceramics. It is for example usually considered that ceramic nanopowders just rearrange without plasticization during compaction [*R. Oberacker-2012*] The results presented here for MgO nanocubes and previously for transition alumina nanospheres by E. Calvié et al. [*E. Clavié et al. 2012*] [*Emile Calvié et al. 2014*] prove that wide plastic flow of ceramic NPs can occur during compaction at RT. This propensity to plastic deformation during compaction opens a new route to deformable ceramics, even at RT. In other words, it would be possible to use plastic deformation of ceramic NPs to obtain green bodies with very high densities and small pores, and sinter them at temperatures well below the ones currently used [*J. Zheng et al. 1989*]. Sintering at much lower temperatures would then keep the nanoscale specificities after the whole process chain, leading to higher mechanical or peculiar functional properties. This might then apply to orthopedic devices, with ceramics exhibiting high wear and crack resistance, but also for transparent polycrystalline ceramics for which the quest is today to reach the highest density with the smallest grains [*A. Krell et al.2009*].

3.1.3. Conclusion: Deformation Mechanism Investigation of MgO Nanocubes by in situ TEM Nanocompression and MD simulations

In summary, we have investigated the mechanical behavior of <100>-oriented and initially dislocation-free MgO nanocubes using original *in situ* TEM compression tests in the 100 nm size range and MD simulations. Results show high strength as homogeneous and wide deformation without failure. The analysis of TEM contrast bands suggests possible {110} slip. These results are confirmed by the MD compression simulations, in which the nucleation of ½<110>{110} perfect dislocations is at the onset of the plastic deformation. Schmid factor analysis and considerations based on GSF energy calculations consolidate these results. Dislocations nucleate from edges, corners or surfaces of the nanocubes. Contrary to what is observed in bulk MgO single crystals at RT, dislocations are curved in both the experiment and the simulation, which is due the high stress experienced by the sample during the nanocompression test. This property could enhance the formation of a dislocation network that is generally a high temperature like process in bulk MgO. Further experiments performed in WBDF mode confirm these results. This will be presented in the following.

3.2. Size effects in single crystal MgO nanocubes

After identification of the deformation mechanism via TEM observations and MD simulations, [*Issa et al (2015)*] which revealed the surface dislocation nucleation controlling mechanism, we focus in the following on the effect of the nanocube size on the deformation behaviour observed in stress-strain curves after the onset of plasticity. The predominance of dislocation starvation in smaller nanocubes and the dislocation interactions that become predominant in larger nanocubes, responsible of such stress-strain response, will be discussed in light of TEM observations. Moreover, the size effect on the yield stress is studied. And the electron beam effect on the yield stress.

More than twenty five MgO nanocubes are tested *in situ* TEM nanocompression tests. Due to misalignment problems [*Shan ZW et al. (2008)*][*Zhang et al (2006)*] that induce non-uniaxial nanocompression and may lead to a local increase in stress and so to a non-accurate measurement of the flow stress, experimental results presented herein are restricted to only seventeen tests (***Table 6***). In latter cases, TEM observations show a good alignment between the flat punch, the nanocubes and the substrate.

3.2.1. Stress-Strain Curves

Engineering stress-strain curves of several MgO nanocubes of different sizes (90, 120, 170, 262 and 450 nm), compressed along the [001] direction, are shown in *Figure 70*. For the two smallest nanocubes, several loading-unloading cycles are performed but only the first cycles are presented for clarity. As previously shown in section **3.1** [*Issa et al. 2015*], MgO nanocubes show large plastic deformation (more than ε=50% for the cube of 450 nm) without failure.

An increase in the yield stress level is observed when decreasing the size of the nanocubes. A detailed discussion on the size-effect on the yield stress is available in **section 3.2.3**. In this section, we focus on the size-effect on the stress-strain behavior after the yield stress.

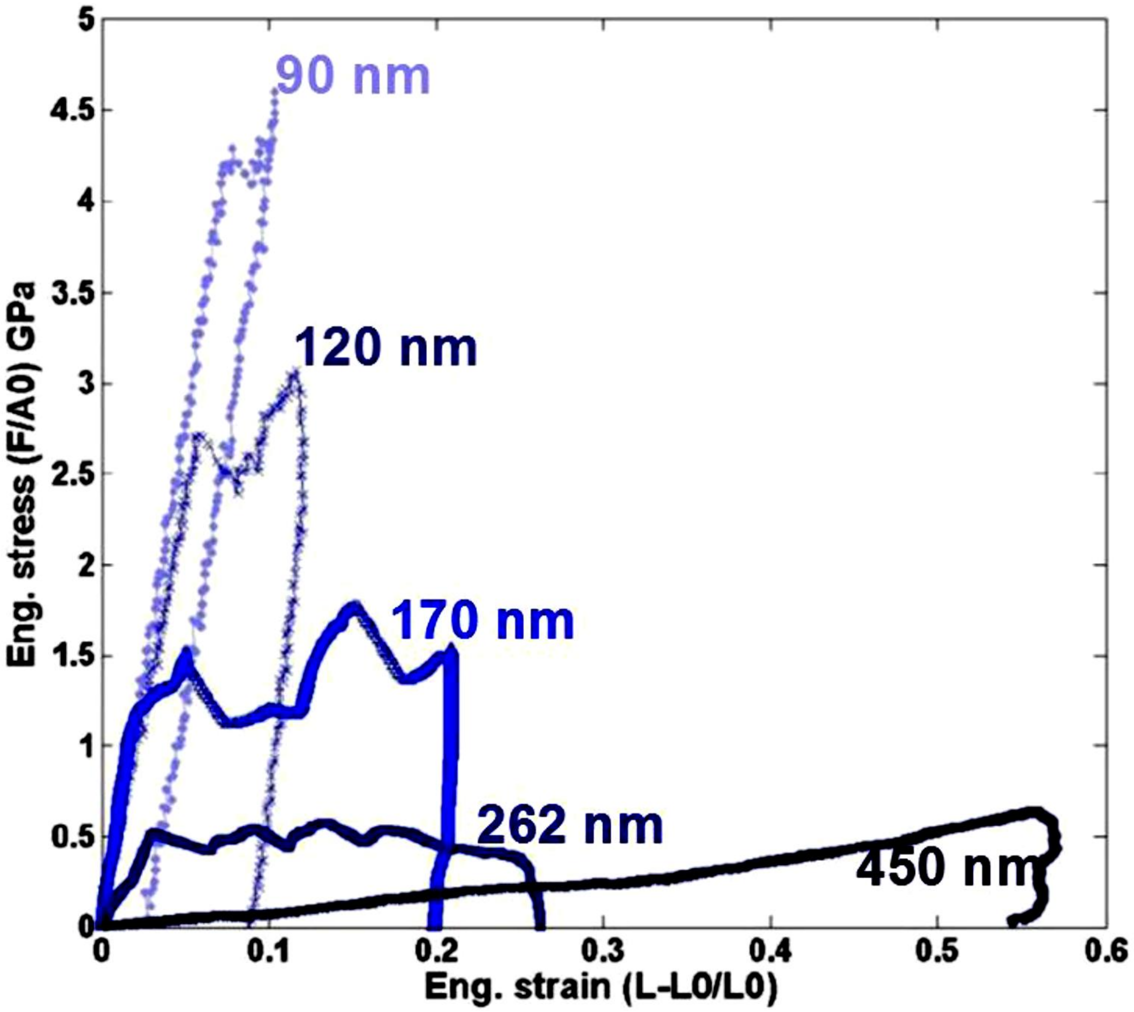

Figure 70: *Size effect on the yield stress of MgO nanocubes: Experimental engineering stress-strain curves of MgO nanocubes of different sizes, all compressed along the [001] direction. A clear size effect on the plastic behavior of nanocubes is evidenced by large stress drops in smaller sizes and by a smoother stress-strain response in larger nanocubes.*

After a linear stress-strain behavior, believed to be the elastic response of the nanocubes, the stress reaches a yield. The strain at yield decreases with increasing nanocube sizes. The yield occurs almost at ε=7% for nanocubes of 90 nm and below for the 120 and 170 and 262 nm sized nanocubes. As far as the 450 nm sized nanocube is concerned, the elastic regime is not clear and the yield limit cannot be determined. From Figure *70,* it is obvious, for all curves (except for the 450 nm sized nanocube), that the elastic regime vanishes by a large stress drop, which is normally observed during compression tests of nearly mobile-dislocation free nano-objects (i.e. non pre-strained objects). [[*Bei et al. (2007)- Effects of focused ion beam milling on the nanomechanical behavior of a molybdenum-alloy single crystal*]. –[*Mordechai et al. (2011)*]. Note that the elastic regime in the stress-strain curve of the 170 nm sized nanocube vanishes by a small strain hardening part before the first stress drop. We believe that this is an artificial strain hardening due to a temporary lack of stability in the system at that moment, i.e. non stability of TEM images that was measured in DIC and thus appears in the stress-strain curve. Moreover, it clearly appears in experimental stress-strain curves, in *Figure 70* after the first stress drop, that the plastic regime contains consecutive stress drops. This discontinuous behavior of the stress-strain response becomes smoother when increasing the nanocube size. In other words, stress drops observed in stress-strain curves of larger nanocubes are of far smaller magnitude than those observed in the curves of smaller nanocubes.

In the literature, regardless the densities of dislocations in specimens before any mechanical tests, these consecutive stress drops during plastic deformation are observed during compression tests performed on single crystal micropillars and nanopillars machined by FIB, or on nanowires fabricated by templated electrodeposition from FCC metals. They are referred to strain bursts [*J.R. Greer, Oliver, Nix,(2005)]- [J.R. Greer, NIX (2006)] –[Volkert et al. (2006)] – [D.M. Dimiduk et al. (2005)]- [C.P. Frick et al. (2008)] – [K.S. Ng et al. (2008).*]. They are usually characterized by a negative slope of the stress-strain curve followed by a nearly elastic reload in a displacement-control mode tests (stress drops) and by a lack of data points in load-control mode (strain bursts). These stress jumps have also been observed in compression tests performed on single crystal micropillars of bcc metals [*Kim et al. (2010)] –* **[***Kauffman, Kraft (2011)]-[Ling Huang et al. (2011)]-[unpublished results of M.D Uchic, published in Uchic(2009)]* and also in a few works on hcp metals [*Sun et al. (2011)*].
Especially in load-control mode tests, the magnitude of these stress drops cannot be observed in stress-strain curves, so most of the time, the size-effect on the magnitude and frequency of these jumps in the stress-strain curves have no clear description. In some displacement-control mode tests, especially on non-pristine specimens, they have been simply described by a stochastic nature of dislocation avalanches. [*Andrew T (2010)*] [*Kaufmann a, Kraft (2011)*]. However some studies introduce the effect of the specimen size on the stress-strain jump magnitude [*unpublished results of M.D Uchic, published in Uchic et al. (2009)*] and their occurrence frequency, and draw a correlation with different deformation mechanisms in smaller and/or larger specimens. For instance, microcompression of Copper micropillars, machined by FIB, [(*unpublished results of Kauffmann, published in review Kraft et al.(2010)]* of 5000 nm and 950 nm in diameter show smooth stress-strain responses described as bulk-like deformation, while pillars of 225 nm in diameter show serrated stress-strain curves with consecutive jumps in the stress-strain behavior. Similarly, compression tests

performed on bcc metallic micropillars [***Ju**-Young Kim et al.(2010)*] showed that Nb and Mo micropillars of 900-850 nm in diameter exhibited continuous non-linear strain hardenings with no stress drop in stress-strain curves as the ones observed in smaller pillars. Moreover, Molecular Dynamics (MD) simulations and experimental compression tests on Au pristine single crystal nanoparticles [*Mordehai et al. (2011)*] reported a specimen size effect on the magnitude of these consecutive stress drops. They concluded that two main size-dependent deformation mechanisms occur in such submicron scale specimens: (i) dislocation nucleation and starvation in smaller nanoparticles due to high surface-to-volume ratios, with surfaces acting as sources and sinks of dislocations; (ii) multiple slip systems and dislocation interactions. In the first case, in small objects, the stress drops as an abrupt deformation occurs when a dislocation nucleates and rapidly escapes from free surfaces. The stress drop is followed by a new elastic regime which takes place until another similar dislocation nucleation-escape event takes place.

This mechanism also occurs in larger specimens but because of the larger size, more surfaces act as dislocation sources, which give rise to the activation of multiple slip systems. Dislocations may then interact with each other, and be stored in the bulk as new dislocation sources. In this case, strain hardening may cause a steeper increase than simple elastic reload. This was observed in Nickel micropillars compression tests and reinforced by TEM observations. [*Nortfleet et al.(2008)*]. TEM observations of dislocation structures in nickel micropillars showed that the dislocation structure on the active slip systems in pillars larger than 2 µm is comparable to the one found in bulk samples deformed to a similar state.

On MgO, single crystal micropillars of 0.5 to 5 µm in diameter were compressed in the <001> direction [*S. Korte et al. 2011]* and stress-strain curves show a clear specimen size effect on the stress-strain behavior. In addition, the different slip systems can be activated individually by changing the solicitation direction.

In **section 3.1** , we showed *In situ* TEM compression tests on MgO nanocubes (similar to the ones presented here) and MD simulations that confirmed that the onset of plasticity in pristine MgO nanocubes compressed in <001> direction, is governed by the nucleation and propagation of 1/2<110>{110} dislocations [*Issa et al. 2015*]. It can therefore be considered that the first stress drop observed in all curves, regardless the nanocube size, is correlated to a first dislocation nucleation/escape process. Moreover, MD simulations showed that in small nanocubes (4.2 nm, 5.6 nm and 7.6 nm), dislocation nucleate and escape through free surfaces, leaving atomic steps. This process leads to a negative slope in the stress-strain curve as there is no resistance to the load (because of lack of storage of dislocations). Such negative slope corresponds to a large stress drop. However, in the case of a larger nanocube (12.6 nm), MD simulations showed that dislocations are nucleated from multiple slip systems. In this case, and due to the curved nature of dislocations, gliding dislocations intersect and form a network. Due to the storage of intersecting dislocations, the nanocube rapidly resists the load. This process, predominant in larger nanocubes, does not require further dislocation nucleation to accommodate further deformation and thus lead to smoother stress-strain response, with less visible stress drops.

We believe that both mechanisms occur in the experiments on nanocubes. A critical size may be found, above or below which a predominance of one of these two mechanisms exists. It seems that this critical size is near ~200 nm. This will be presented in the following.

*Figure 73*a-b show typical TEM images of nanocubes smaller than 200 nm (195 nm and 170 nm respectively) at early compression, where few dislocations are nucleating from contact surfaces and traversing the nanocube with increasing strain. Further experimental evidence for dislocation identification are given in *Figure 73*-**a&b** and it is presented in the following section. Dislocations traversing the nanocubes can be identified as 1/2<110>{110} dislocations just before the first stress drop. It seems that the first stress drop appears simultaneously with the escape of a large number of these early dislocations. They leave atomic steps on the surfaces of smaller nanocubes (< ~200 nm). Moreover, the rather uniform grey level all over the nanocube suggest that only few dislocations remain in the nanocube after the cycle at zero load. In larger nanocubes (> ~200 nm), a higher density of nucleated dislocations appear at early compression from multiple sites from contact surfaces. This high density of dislocations seems to promote their interaction and entanglement rather than their escape through a surface. Once again, it seems that these two mechanisms occur simultaneously but with a predominance of one or the other depending on the nanocube size.

For further evidence, in *Figure 71*, we present the stress-strain curve of a 170 nm sized cube. The positions of the TEM images are indicated on the stress-strain curve. At early compression (linear elastic behavior), few dislocations are nucleated from surfaces or edges (blue dotted lines in *Figure 71*-1). With increasing load, these dislocations are observed traversing the nanocube surface (see red dotted lines *Figure 71*-2, representing the new positions of the blue dotted lines in Figure 3.7-1). In *Figure 71*-2, the green dotted lines present new dislocations that are just nucleated. The dislocation density highly increases until the yield stress (*Figure 71*-3). Consecutively and just after the yield stress, the dislocation density decreases (see *Figure 71*-4). It seems that at this point, i.e. just after the yield stress, these dislocations escape the nanocube from the upper and left surfaces. Moreover, a severe deformation (sudden drop in the punch clearly observed in movie of the test) is simultaneously observed. The stress-strain curve shows the first stress drop (the double parallel arrows in *Figure 71*-4 show the sudden change in the nanocube length before and after the sudden drop, with the same color code for dislocations). *Figure 71*-5 and *Figure 71*-6 show a similar effect before and after the second drop. Indeed, dislocations contrasts highly decrease at the early beginning of the second stress drop. Both figures also reveal the dislocation escape from the surface. *Figure 71*-7 shows the nanocube after compression (i.e at zero load) and it seems nearly free of dislocation (at least, in this consistent condition of diffraction). An atomic step appears on the left side of the nanocube, and reveals the dislocation escape process.

Figure 71 : 170 nm MgO nanocube, TEM Images are correlated to stress strain curve by DIC.

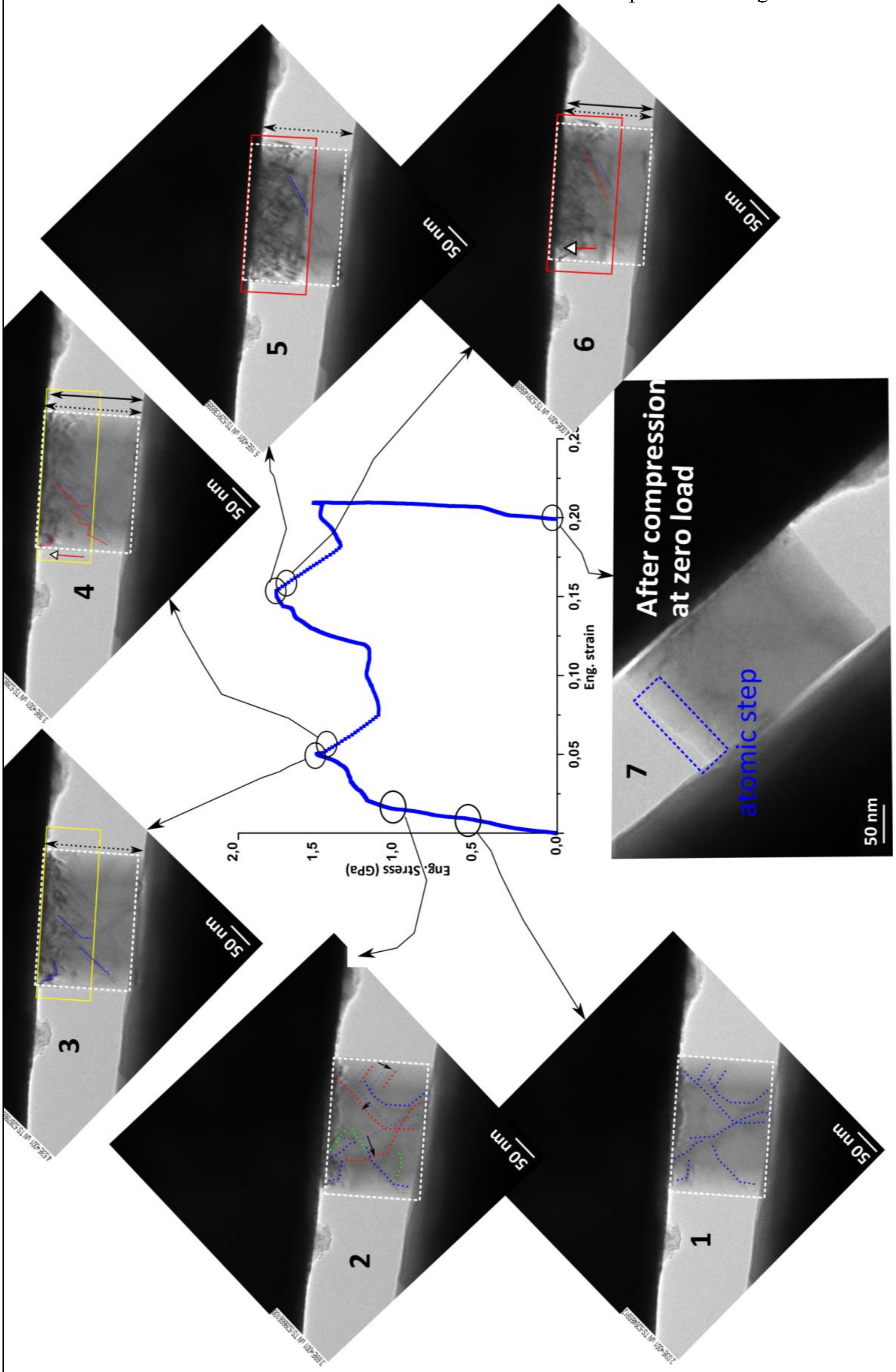

The behavior of a larger nanocube of 316 nm (larger than 200nm) is illustrated in *Figure 72*. The stress-strain curve show a smaller stress drop (*Figure 72*-B), and the reload after the stress drop shows some strain hardening (*Figure 72*-C dotted rectangle) believed to be due to the higher density of interacting dislocations. Note that in this test, no objective diaphragm was used, thus contrasts are not optimum. However, at zero load (*Figure 72*-D), the presence of a high contrast in the nanocube obviously reveals the presence of dislocations. Thus, even though lateral surfaces may show height steps, the dislocations storage process is clearly more intense than what was observed in the 170 nm sized nanocube in *Figure 71*-7.

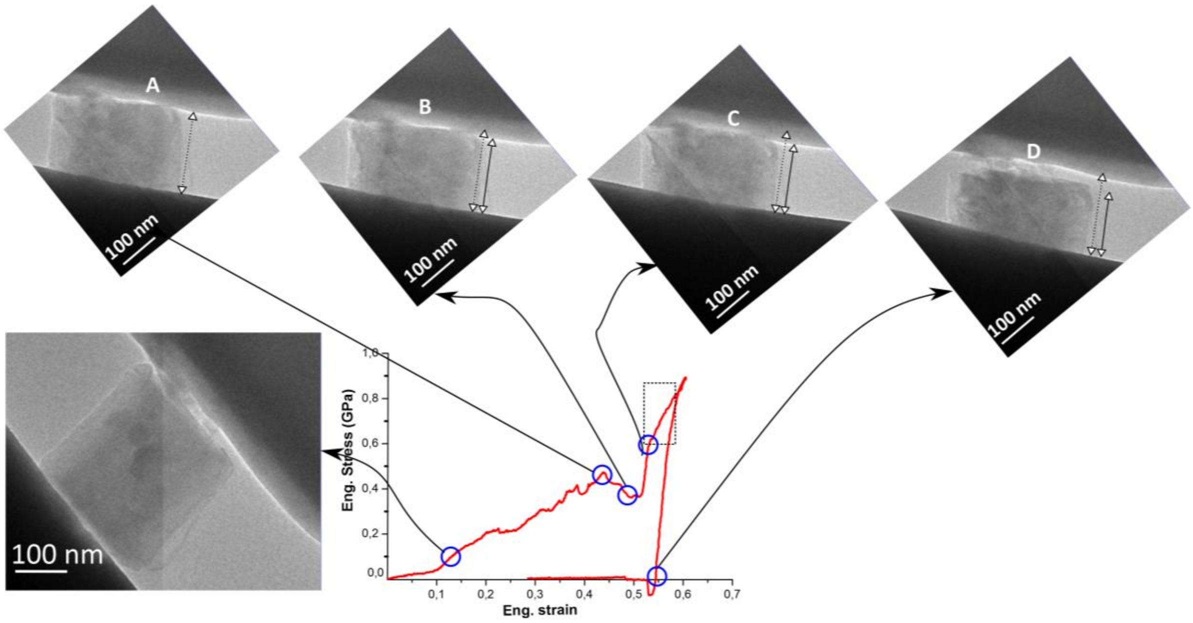

Figure 72: TEM images of a 316 nm MgO nanocube correlated to its stress-strain curve

For further evidence of the higher remaining density in larger nanocubes (>~200nm, we present), in *Figure 76*-a a typical BF TEM of a nanocube larger than 200 nm (355 nm) at early compression. A large number of dislocations nucleate in different slip systems from multiple sites near the bottom surface. A reload on the same nanocube is performed and a WBDF TEM image of the cube at the end of the test (zero load) is shown in *Figure 76*-b. The WBDF TEM image reveals the presence of a high density of entangled dislocations remaining in the nanocube at zero load.

One can notice that despite the difference in size between the nanocubes tested in MD simulations and those tested experimentally, TEM images in *Figure 74* and ***Figure 75*** (formation of steps due to the dislocation escape in nanocubes smaller than 200 nm with very low dislocation contrasts after the cycle), and *Figure 76* (persistent entangled dislocations in nanocubes larger than 200 nm and high density of dislocations remaining in nanocubes after the cycle) reveal the existence of both mechanisms described in MD. By relating these TEM observations with experimental stress-strain curves, we report that the predominance of the mechanism of dislocation nucleation/starvation becomes less pronounced in large nanocubes (larger than 200 nm), while the storage of dislocation as new dislocations sources results in the rapid resistance of the nanocube to the indenter and so to smaller stress drops. Furthermore, in nanocubes smaller than 200 nm, the predominant mechanism involves dislocation nucleation/starvation via dislocations escape with severe and sudden stress drops, which give rise to the large stress drops on the stress-strain curves.

In ***Figure 75*** we present a BF image of a 160 nm sized cube. From this image, it can be notice that entangled dislocations occur in smaller nanocubes but with lower densities. Indeed, TEM images show that at large strain (>50%), the contrast increases due to multiple dislocations remaining in the nanocubes, but the network formed seem to be far less dense than those observed in large nanocube even at smaller strains.

The lack of large subsequent stress drops in large nanocubes is not only due to the microstructural process described above but may also be related to the increase of the cube size. Indeed, and as it was mentioned previously in section **3.1**, the average shear strain $\bar{\gamma}$ produced by a {110} gliding dislocation in a cube of edge length l produced by a dislocation decreases as the size of the nanocube increases (see Eq. 1 in section **3.1**.) As a consequence, and assuming a constant strain rate, the stress response to a shear increment will be smoother for large samples than for a small one.

3.2.2. TEM Observations and Dislocation Characterizations

Dislocations observed in TEM compression tests are mostly, not always, curved (mixed: screw and edge) due to the overcome of the lattice friction. As the Peierls stress (stress necessary to move screw dislocation glide at 0 K) is ~150 MPa in the {110} slip planes and 1600 MPa in the {100} in MgO [*C. Barthel- thesis (1984)*] – [J. Amodeo et al. (2011)] – [*F. Appel (1985)]* - [*P. Carrez et al. (2009)*], we believe that in the compression tests of MgO nanocubes we overcome the Peierls stress and curved dislocations lines are more favorable rather than straight lines as the one observed in macroscopic tests on MgO at room temperature. [*Messerschmidt (2010)*]. These dislocation structures favor the contact and intersection between dislocations.

However, in *Figure 73*-a the WBDF TEM image of a 195 nm sized nanocube at the onset of plasticity, obtained with the diffraction vector $\vec{g}$ (0,0,2) shows somehow straight lines corresponding to dislocations. Regarding all possible cases of dislocations (screw or edge) projected along the electron beam axis; one can recognize the dislocation character and its slip plane in WBDF mode as shown in **chapter 2.** The Burgers vectors determined correspond to ½ [011] $(01\bar{1})$ screw dislocation (red in *Figure 73*-a). Moreover the upper dislocation shows a curved nature and can be identified as a mixed dislocation of screw and edge 1/2[011] dislocation in the slip plane $(01\bar{1})$. (screw (red) and edge (blue) parts). The oscillating contrast along the dislocation may be due to the curvature of the screw dislocation part in the transmitted plane. In the inset of *Figure 73*-a, such screw and edge dislocations are schematically represented in a 3D cube gliding in its $(01\bar{1})$ plane and the cube is rotated to the same configuration of the single crystal nanocube in TEM. A similar calculation can be carried out for the 170 nm sized nanocube presented in *Figure 73*-b. The dislocations are a screw $1/2[01\bar{1}]$ (011) dislocation (red line in the schemed cube) and an edge $1/2[01\bar{1}]$ (011) dislocation (blue line in the schemed cube).

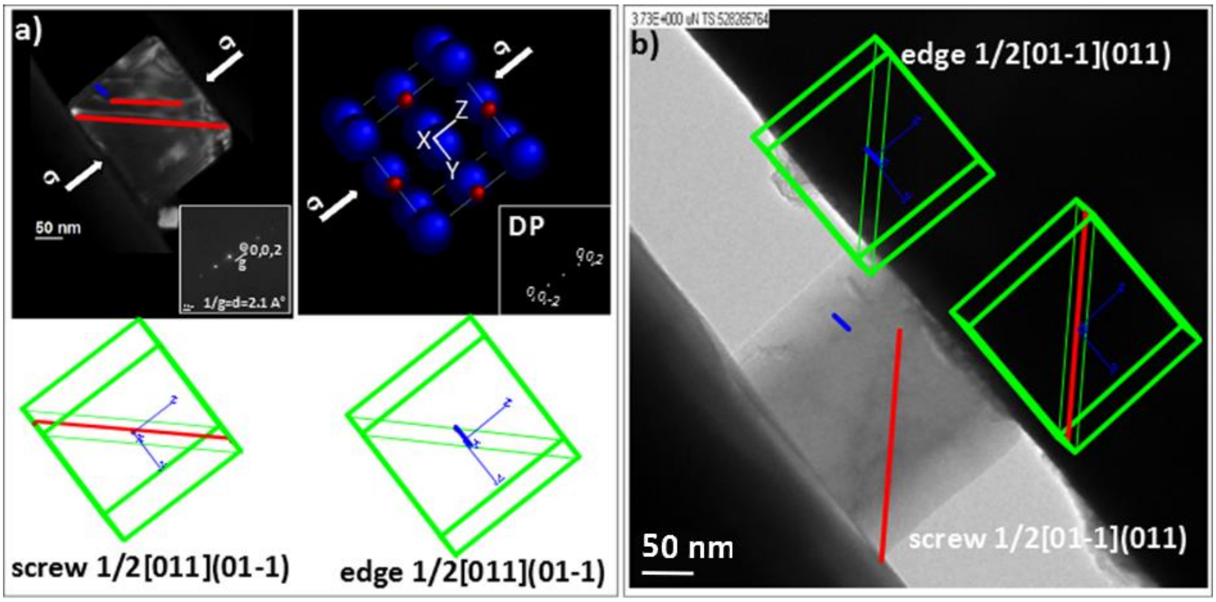

Figure 73*: **a**-WBDF TEM image of a 195 nm sized nanocube at yield stress where few lines of dislocations appear. Their characteristics are determined in the inset. **b**- Similar interpretation for the BF TEM image of a 170 nm sized nanocube.*

As mentioned in the previous section, in nanocubes smaller than 200 nm, the escape of dislocations is much more observed. It leads to the formation of surface steps, as shown in the

Figure 74-b (black arrows) of the 170 nm sized cube after compression (zero load). Another example for atomic steps is presented in ***Figure 75***-b for the 160 nm sized cube (*Lomer dislocations observed in Figure 75-a, remain in the nanocube until the last cycle of loading-unloading*). We believe that these atomic height steps serve as new sites for dislocations nucleation, which requires a lower stress. This process leads to the softening behavior observed in nanocubes with large strains instead of fracture or failure.

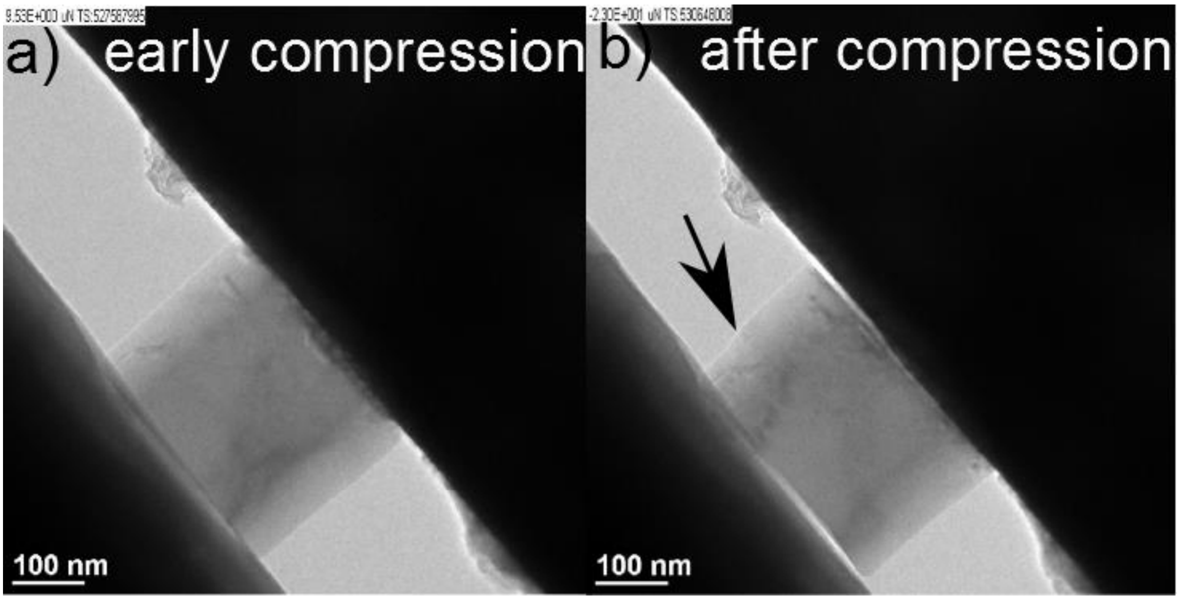

Figure 74: *BF TEM image of the 170 nm sized nanocube **a-** at early compression and **b)** after compression, at zero load. Clear surface steps can be observed after compression.*

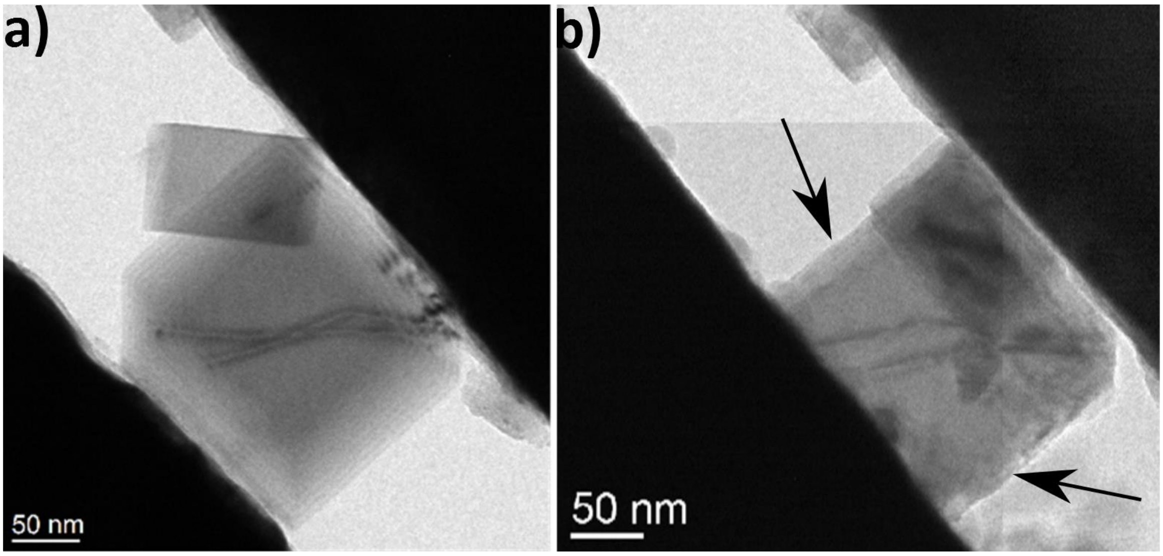

Figure 75: ***BF TEM Image of a 160 nm sized nanocube*** *a-* ***before compression;*** *b-* ***after a few percents of strain under compression along the [001] direction. Two lines correspond to entangled dislocations remaining in the nanocubes.***

Figure 76- a is a BF TEM of 355 nm at zero load after few percent of strain, avalanches of dislocations nucleated from bottom contact of the nanocube with the substrate are observed. *Figure 76*-b is a WBDF TEM image ($\vec{g}\ [1, \bar{3}, \bar{3}]$), of the same cube at zero load after a second cycle of load-reload. With this **g**, only dislocations of Burgers vector ([101] and [10$\bar{1}$]) are visible**,** i.e. 4/8 possible dislocations (see **chapter 2)**. Persistent entangled dislocations are observed which reveal the predominance of the storage of entangled dislocations in larger nanocubes. This also explains strain hardening in larger nanocubes rather than softening. This was clearly observed in the stress-strain curve of the 450 nm nanocube represented in *Figure 70* and in the reload part after the stress drop of the 316 nm cubes (*Figure 72*; dotted rectangle).

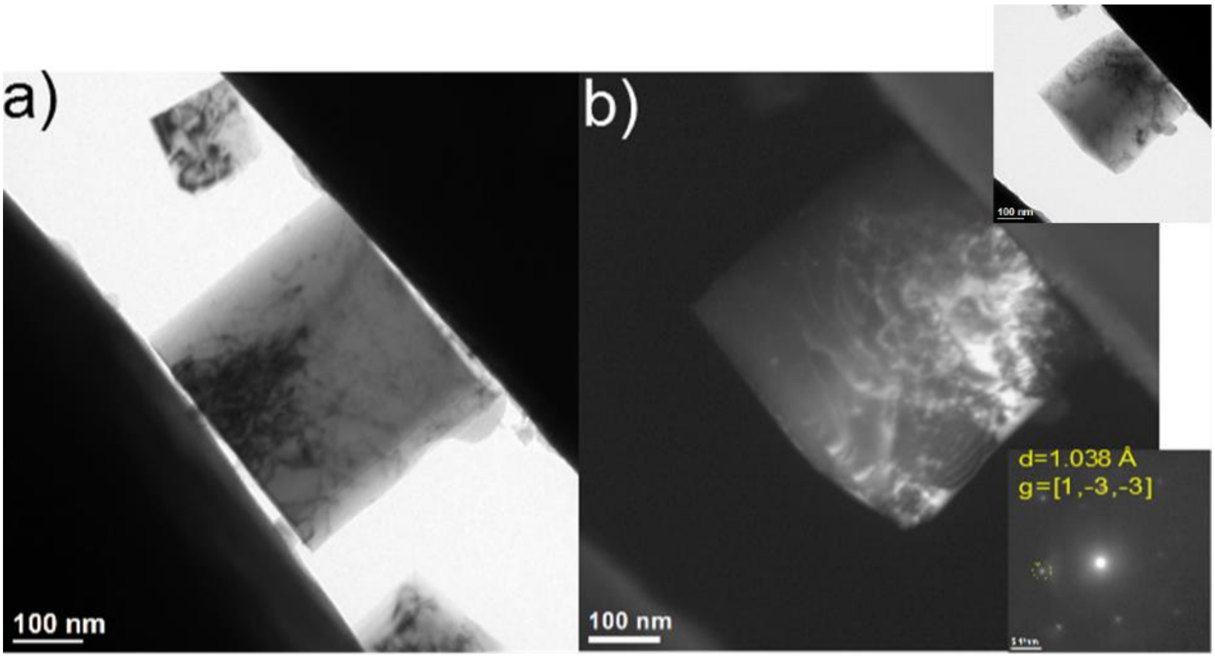

Figure 76: a) *A BF TEM image of a 355 nm nanocube at zero load shows many dislocations nucleating from the bottom surface. b) WBDF image showing dislocations persistent in the nanocube after the second cycle of loading-unloading.*

At this stage, it can be mentioned that clear homogeneous deformation is observed in nanocubes at early plastic deformation, until large strain values. This is significantly different from the prismatic deformation observed during the compression tests on micropillars. Indeed, nanocubes exhibit an aspect ratio of 1:1 which is a low aspect ratio (relative to micropillars). As a consequence, a large fraction of slip systems are confined between the indenter and the substrate and thereby multiple nucleation and glide of dislocations along the same slip plane is limited. Dislocation glide instead occurs in various slip systems, from different locations with equal nucleation activity, and leads to the homogenous deformation.

3.2.3. *Nanocubes Size-Effect on the Yield Stress or Strength*

The macroscopic yield stress of bulk MgO tested in compression at room temperature along the <001> direction is ~50 MPa [*Hulse (1960)*]. The yield stresses measured at the onset of plastic deformation (7 ± 1% strain for 90 nm and decreasingly lower % of strain for larger nanocubes), for all the MgO nanocubes tested experimentally along the <001> direction, are presented in ***Table 6***.

It is obvious that the yield stress is influenced by downscaling. Measured yield stresses for MgO nanocubes exceed the macroscopic yield stress of bulk MgO, by a factor of ~4 in larger nanocubes and up to ~60 times in smaller nanocubes. Moreover, the critical resolved shear stress in <110> {110} slip planes, in the smallest nanocube for example, is $\frac{\sigma_y}{2} = 1.545\ GPa$ which represents 1/10 of the theoretical resolved shear stress of MgO $\frac{\mu}{2*\pi} = 15.89\ GPa$ where μ = 99.89 GPa (shear modulus) is taken as $\frac{1}{2}(C_{11} - C_{12})$, as calculated by MD by J. Amodeo.

I. *Electron Beam Effect on the Yield Stress (Strength)*

Before ascribing this increase in strength to a crystal size effect, one must consider the possibility of hardening of an ionic crystal due to electron irradiation. This has to be taken into account especially for experiments performed *in situ* in TEM (operating at 200 keV). Indeed, it is well known that ionic crystals are very sensitive to irradiation damage, which can lead to a hardening effect. This was for example observed in microhardness experiments on Lithium Fluoride crystals which critical resolved shear stress was increased by an order of magnitude by irradiation with 1MeV electrons [*WHAPHAM (1960)]*. However, it seems that it is not the case for MgO crystals when irradiated by an electron beam inside TEM operating at 100KeV [*N. Gane 1972*]. On the contrary, in amorphous silica SiO_2 [*K. Zheng et al. (2010)*], MD simulations revealed that during compression, the electron beam causes structural and bonding defects throughout the sample and facilitates plasticity. This effect is called ionization damage and is due to electron-electron interaction giving rise to Auger processes and bonding defects. The conclusions drawn from MD simulations were reinforced by calculations of the energy transferred to the sample from a 200 kV electron beam. The energy transferred to an oxygen atom is equal to 33 eV, whereas it is equal to 19 eV for a silicon atom. This energy is responsible of the cleavage of the Si-O bond (4.4 – 6.2 eV) and is larger than the displacement energy in silica (25 eV). Thus, it causes bonding defects and is believed to facilitate plasticity in silica. In our case, The threshold voltage above which MgO exhibits oxygen vacancies is 460 kV at room temperature [*Pells 1982*]. Herein, we work with a TEM operating at 200kV. However, we observe a similar softening of the MgO nanocubes during electron beam irradiation as that observed in silica. Indeed, *Figure 77* displays stress-strain curves obtained when compressing a 150 nm sized MgO nanocube without any electron beam (beam-off). The measured yield stress in the first cycle is equal to 1 GPa.

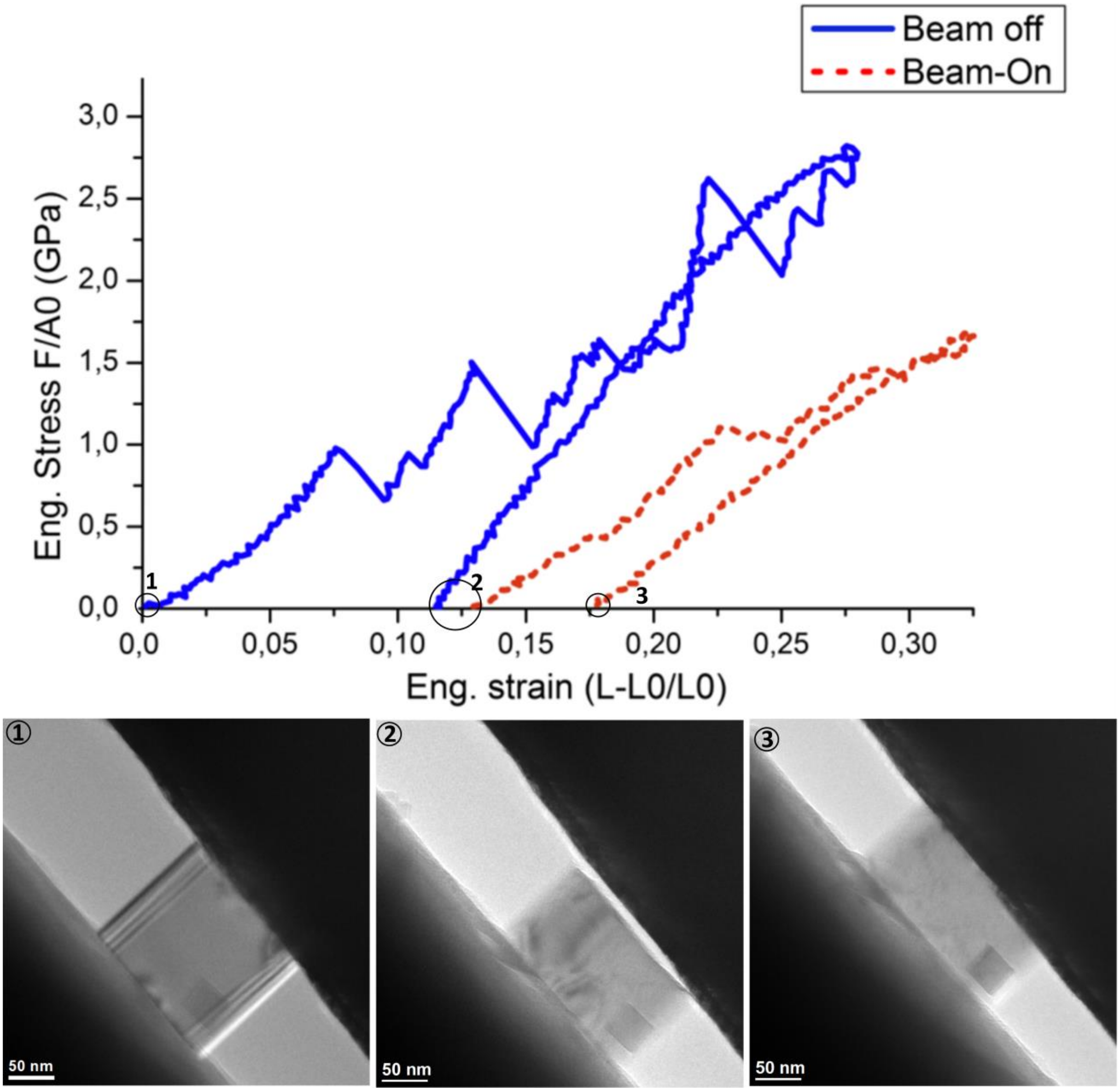

Figure 77: *Loading-unloading cycle of a 150 nm sized nanocube. The blue curve (solid line) corresponds to a beam-off test whereas the red curve (dashed line) is the second cycle of loading-unloading on the same cube with beam-on.*

The unloading cycle of the beam-off test reveals that the strain is under-estimated. This may be due to electronic problems during the displacement of the substrate away from the tip. Of course, as no image is acquired (beam-off test), it is not possible to carry out DIC. A second cycle performed on the same cube under electron illumination (beam-on), reveals that the yield stress is reached at 1.1 GPa. Knowing that in the second cycle the yield stress must be reached at the highest stress level achieved in the plastic regime of the first cycle (*i.e.* 2.78 GPa), the electron beam is estimated to reduce the yield strength of MgO nanocubes by a factor ~ 2.5. Therefore we believe that the measured yield stresses in all beam-on tests are under-estimated.

Nevertheless, the beam-off/beam-on tests reveal that the electron beam illumination does not induce any hardening effect on MgO nanocubes. Therefore we attribute the high strength observed in MgO crystals, at small scale, to a size effect especially in pristine samples, where the lack of dislocations in MgO single crystals nanocubes promotes a higher stress needed to generate dislocations rather than lower stress needed to move them from Frank-Read sources. However, if dislocations exist, their processes in these small volumes may be different than in the bulk. For instance, strengths higher than in the bulk were observed in FIB milled micropillars of fcc and bcc metals despite the presence of initial dislocations produced during FIB preparation or already existing from the bulk [*Uchic et al. (2009)*].

II. Size-Effect on the Yield stress (Strength)

In order to understand the origin of this size effect, one must investigate first the magnitude of this effect and compare it to what was obtained in other materials structures, when taking into account many gradients that may affect strongly the size effect such as the initial dislocations densities, the strain rate and the material structure.

Table 6: nanocubes tested sizes, measured yield stress, displacement rate and strain rate. The effect of the electron beam on the measured yield stress is calculated for all nanocubes.

Nanocube size (nm)	**σ_y (GPa)**	**electron beam effect corrected σ_y (Gpa)**	**displacement rate (nm/s)**	**strain rate (/s)**
62	3,09	7.725	2	3,23E-02
90	4,28	10.7	2	2,22E-02
97	1,8	4.5	2	2,06E-02
99	1,2	3	1	1,01E-02
110	1,8	4,5	2	1,82E-02
114	1,8	4,5	2	1,75E-02
120	2,7	6,75	2	1,67E-02
138	2,47	6,175	2	1,45E-02
140	0,8	2	2	1,43E-02
150	1,4	3,5	2	1,33E-02
150 (beam-off)	1	1	2	1,33E-02

160	0,713	1,7825	1	6,25E-03
170	1,5	3,75	2	1,18E-02
262	0,51	1,275	2	7,63E-03
316	0,47	1,175	2	6,33E-03
355	0,41	1,025	2	5,63E-03
450	0,2	0,5	2	4,44E-03

In order to evaluate the size-effect, the yield stress is plotted in function of the nanocubes size, as shown in *Figure 78***.** The results are fitted with a power law often used in the literature to quantify the size-effect on the yield stress. The data are extrapolated until the bulk yield stress of MgO along the <001> direction, σ_0 =0.05GPa (~50 MPa):

$$\sigma_y = AL^{-x} + \sigma_0 \qquad \text{Eq. (3)}$$

Where σ_y is the yield stress, L the nanocube edge size, A is a fit constant and x is the power-law exponent. The best fit over the entire range of nanocubes size is found for x = 1.31. To better evaluate and visualize the power-law exponent, a log-log plot is shown in the inset of *Figure 78***.**

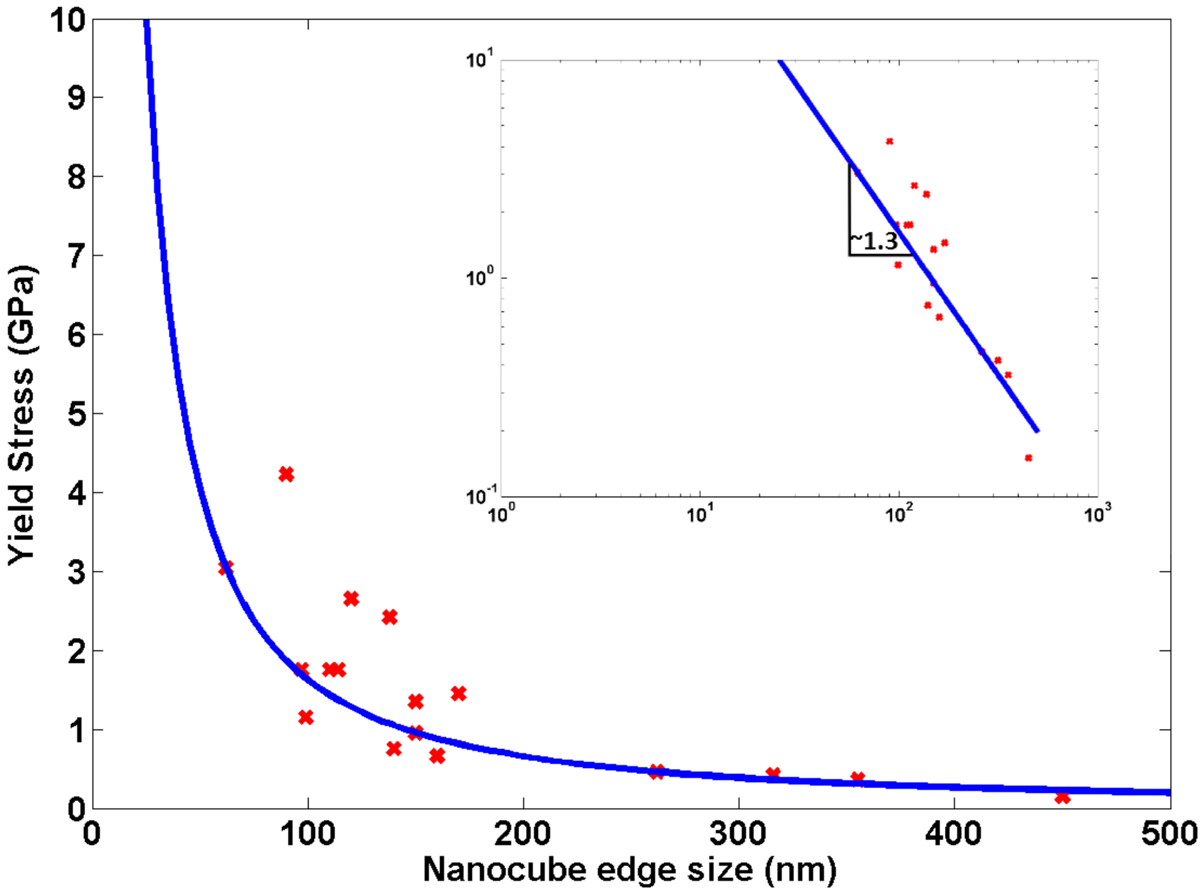

Figure 78: *Plot of the yield stress versus the nanocube size (17 nanocubes tested in situ). The inset shows the corresponding log-log plot.*

The value of the exponent x obtained is higher than the exponents measured on fcc metals single crystalline nano- and micropillars (0.6 - 0.97) [*D.M. Dimiduk et al. (2005)*]- [*Volkert et al. (2006)*] [*Brinckmann et al. (2008)*] [*Frick CP et al. (2008)*] [*A.T. Jennings et al. (2010)*], or fcc nanoparticles (~0.77) [*Dan Mordehai et al. 2(011*)]. It is also obviously higher than bcc crystals (W, Mo and Ta), where the power exponent varies from 0.22 to 0.48 for an average crystal size ranging from several microns to 200 nm [*J.Y. Kim et al. (2010)*] [*Schneider et al. (2009)*]. However, [*Ling Huang et al. (2011*] reported two different regimes on FIB milled Mo micropillars of diameter > 200 nm. They found a power exponent (0.3) in agreement with other studies [*J.Y. Kim et al. (2010)*] [*Schneider et al. (2009)*]. However, they reported a transition critical size (D_C~200nm) below which the size effect is highly pronounced and x becomes equal to ~1.

Interestingly, Bei et al [*Bei et al (2007)-Compressive strengths of molybdenum alloy micro-pillars prepared using a new technique*] [*Bei. et al (2008)*] carried out experiments on Mo-alloy micropillars (bcc metal) , produced via eutectic solidification followed by chemical etching. The pillars were believed to be free of dislocations and no size dependence of the yield stress on the micropillars size could be evidenced. Moreover, 3-D discrete dislocations simulations (DDS) of fcc microcrystals performed by Rao et al. [*Rao SI et al. (2008)*] showed that the degree of size-dependent strengthening is dependent on the initial dislocation density. These two studies on Mo-alloy showed that once dislocations exist in the sample, the size effect is pronounced and a higher starting dislocation density results in a weaker size-effect (and vice-versa), (**see chapter 1, section1.2**) . This larger size effect in specimens with low starting densities of dislocations was also observed in experiments on alkali halide LiF [*Nadgorny EM, (2008)]* crystals FIB-milled from bulk ultrapure LiF single crystals having a very low initial dislocation density (10^9 m^{-2}) compared to the densities reported for fcc or bcc Fib milled microcrystals ($10^{12-13}m^{-2}$).

In our case, with MgO single crystalline nanocubes initially dislocation-free, compressed *in situ* in TEM, a strong size-effect can be observed.

For nanocubes larger than 200 nm, the onset of plasticity (at yield stress) occurs through the predominant mechanism in this size regime that involves movement of dislocation networks. Thus the size effect on the yield stress may depend on the dislocation density nucleated at early compression.

For nanocubes smaller than 200 nm, the deformation mechanism observed involves dislocation nucleation and starvation. Several dislocations can be observed simultaneously but the dislocation density is low to that observed in larger nanocubes (from dislocation contrasts observed in TEM images). It is thought that in this case, only few dislocations can form a networkAs a consequence, the size effect observed below 200 nm could not be only attributed to different dislocation densities nucleated at early compression.

The observed dependence of the yield stress with the nanocube size could be also highly pronounced due to different strain rates. Indeed, it is well known in strain-rate sensitive materials that yield stress increases with increasing strain rate. In our experiments, the displacement rate is kept equal to 2nm/s in almost all tests, except for two tests where the displacement rate is set to 1 nm/s. A constant displacement rate leads to an increase in strain rate: from ~ 4.44. 10^{-3}/s in the 450 nm sized cube to 3.2 10^{-2}/s in the 62 nm sized cube. Thereby, the yield stress would be expected to rise faster with decreasing the nanocube size and lead to this strong size effect presented in the high power-law exponent ~ 1.31.

Table 6 shows that the different strain rate might explain the increase of the yield stress. The exponent x may thus be overestimated because of the varying strain rates. Nevertheless, when comparing the yield stresses measured on nanocubes of different sizes but with similar strain rates (e.g. 160 and 316 nm, at 6.25 10^{-3} and 6.33 10^{-3} /s, respectively) it seems that an effect of the size still exists.

As it was shown that dislocations nucleate from the nanocube surfaces or edges, a possible explanation of the size effect would involve the probability to find a defect on a nanocube surface or edge, which would induce dislocation nucleation decreases when the nanocube size decreases. We suppose that going to the nanoscale, the ratio $\frac{S}{V} \propto \frac{1}{L}$ increases and, as mentioned above, the role of surfaces become central. However, smaller nano-object means smaller surfaces and less sites for dislocation nucleations which induce higher yield stresses. Hence, $\sigma_y \propto \frac{S}{V} \propto \frac{1}{L}$ and in this ideal case, the power-law exponent must be equal to maximum 1. This later case may be obtained idealy in free-defects nanosamples [*Dunstan & Bushby 2013*]. However, in the literature, the most often studied geometries for the investigation of the size effect on the yield stress are cylinders and spheres (Pillars and spherical micro/nanoparticles). We believe that in both cases, where surfaces border the whole geometry (not edges), decreasing the size of the nanosample induces the variation of the yield stress σ_y proportionally to $\frac{S}{V} \propto \frac{1}{L}$. Regarding the dislocations state pre-existing in the nanosamples studied in the literature, the power-law exponent is often smaller than 1. For e.g. for fcc metals it is often close to 0.6 for samples machined by FIB [*Volkert et al. 2006*]. However Mordehai et al. [*Mordehai et al. 2011*] reported compression tests on Au nanoparticles, obtained by solid state dewetting and free of dislocations. In this case, the power-law exponent x obtained is equal to ~ 0.8.

In the case of the nanocubes studied here, it may be considered that the exponent is equal to 1, the other 0.3 being attributed to the different strain rates. However, it has to be mentioned that the edges might also play an important role as sites for dislocations nucleation. Thus the yield stress in the case of a cube geometry might not only vary proportionally to $\frac{S}{V} \propto \frac{1}{L}$, but also to $\frac{L}{V} \propto \frac{1}{L^2}$. Hence, the power-law exponent x obtained in the case of MgO nanocubes (free of dislocations) would be expected to be in the range $[1-2]$, which might also justify the exponent $x = 1.3$ obtained herein.

3.2.4. Conclusion

In this work, we investigated, *in situ* in TEM, the effect of the size on the deformation behavior and the yield strength of single crystal MgO nanocubes under uniaxial compression along the [001] direction. Initially, MgO single crystals are perfectly cubic and free of dislocations.

MgO nanocubes in the size range of [62-450 nm] show large strain up to 70% without fracture or crack. Most of nanocubes yielded at high stresses in the range of GPa. Stress-strain curves clearly show a size effect in the plastic regime, where stress drops are large in smaller nanocubes and stress-strain curves become smoother in larger nanocubes. Reinforced with DF and WBDF TEM observations, it was shown that such behavior was correlated to the predominance of dislocation starvation mechanism in smaller nanocubes (<200 nm). In larger nanocubes, it seems that dislocation interactions become predominant, which reduces the dislocation nucleation mechanism in order to accommodate further deformation and so smoother stress response was observed.

The size effect was described by a power law extrapolated to bulk MgO yield stress where the best fit was found with the power law exponent $x = 1.31$. This is consistent but remains stronger than the size effect observed in fcc and bcc single crystals FIB milled or directional solidified nano-/micropillars and pristine nanoparticles. We believe that the observed size effect cannot be fully explained by the variations of the strain rates. We instead propose that it is related to the probability to find a defect on the MgO surfaces or edges, which would induce dislocation nucleation.

Finally, it has to be mentioned that the effect of the electron beam has been investigated. A large effect was found on the plastic behavior. The electron beam is estimated to reduce the yield strength of MgO nanocubes by a factor ~ 2.5. Therefore we believe that the measured yield stresses in all beam-on tests are under-estimated.

References:

- **Amodeo,** J. C. Begau, E. Bitzek, Sup mat: atomistic simulations of compression tests on Ni3Al nanocubes, Mater. Res. Lett. (**2014**) 1–6
- **Amodeo**, J., Ph. Carrez, B. Devincre, et P. Cordier. « Multiscale modelling of MgO plasticity ». *Acta Materialia* 59, n° 6 (avril **2011**): 2291-2301. doi:10.1016/j.actamat.2010.12.020.
- **Andrew T, Jennings**, Michael J. Burek, et Julia R. Greer. « Microstructure versus Size: Mechanical Properties of Electroplated Single Crystalline Cu Nanopillars ». Physical Review Letters 104, no 13 (2 avril **2010**): 135503.
- **Appel**, F., et B. Wielke. « Low temperature deformation of impure MgO single crystals ». *Materials Science and Engineering* 73 (1 août **1985**): 97-103. doi:10.1016/0025-5416(85)90299-X.
- **Bei**, H., S. Shim, E. P. George, M. K. Miller, E. G. Herbert, et G. M. Pharr. « Compressive strengths of molybdenum alloy micro-pillars prepared using a new technique ». Scripta Materialia 57, no 5 (septembre **2007**): 397-400. doi:10.1016/j.scriptamat.2007.05.010.
- **Bei**, H., S. Shim, G.M. Pharr, et E.P. George. « Effects of Pre-Strain on the Compressive Stress–strain Response of Mo-Alloy Single-Crystal Micropillars ». Acta Materialia 56, no 17 (octobre **2008**): 4762-70. doi:10.1016/j.actamat.2008.05.030.
- **Bei**, H., S. Shim, M. K. Miller, G. M. Pharr, et E. P. George. « Effects of Focused Ion Beam Milling on the Nanomechanical Behavior of a Molybdenum-Alloy Single Crystal ». Applied Physics Letters 91, no 11 (**2007**): 111915. doi:10.1063/1.2784948.
- **Brinckmann**, Steffen, Ju-Young Kim, et Julia R. Greer. « Fundamental Differences in Mechanical Behavior between Two Types of Crystals at the Nanoscale ». Physical Review Letters 100, no 15 (17 avril **2008**): 155502. doi:10.1103/PhysRevLett.100.155502.
- C. **Barthe**l, Plastiche anisotropie von Bleisulfid und magnesiumoxid (Diploma thesis), University of Gottingen, **1984.**
- **Calvié,** E., J. Réthoré, L. Joly-Pottuz, S. Meille, J. Chevalier, V. Garnier, Y. Jorand, et al. « Mechanical behavior law of ceramic nanoparticles from transmission electron microscopy in situ nano-compression tests ». Materials Letters 119 (15 mars **2014**): 107-10. doi:10.1016/j.matlet.2014.01.002.
- **Calvié**, Emilie, Lucile Joly-Pottuz, Claude Esnouf, Philippe Clément, Vincent Garnier, Jérôme Chevalier, Yves Jorand, Annie Malchère, Thierry Epicier, et Karine Masenelli-Varlot. « Real time TEM observation of alumina ceramic nano-particles during compression ». Journal of the European Ceramic Society 32, no 10 (août **2012**): 2067-71. doi:10.1016/j.jeurceramsoc.2012.02.029.
- **Carrez**, Ph., J. Godet, et P. Cordier. « Atomistic simulations of ½ 〈1 1 0〉 screw dislocation core in magnesium oxide ». *Computational Materials Science* 103 (1 juin **2015**): 250-55. doi:10.1016/j.commatsci.2014.10.019.
- **Carrez**, Philippe, Denise Ferré, et Patrick Cordier. « Peierls–Nabarro Modelling of Dislocations in MgO from Ambient Pressure to 100 GPa ». *Modelling and Simulation in Materials Science and Engineering* 17, n° 3 (**2009**): 035010. doi:10.1088/0965-0393/17/3/035010.
- **Chung,** Dae-Hyun. « Elastic moduli of single crystal and polycrystalline MgO ». *Philosophical Magazine* 8, n° 89 (1 mai 1963): 833-41. doi:10.1080/14786436308213840.
- **Copley**, Stephen M., et Joseph A. Pask. « Plastic Deformation of MgO Single Crystals up to 1600°C ». Journal of the American Ceramic Society 48, n° 3 (1 mars **1965**): 139−46. doi:10.1111/j.1151-2916.1965.tb16050.x.
- **Csikor**, Ferenc F., Christian Motz, Daniel Weygand, Michael Zaiser, et Stefano Zapperi.

« Dislocation Avalanches, Strain Bursts, and the Problem of Plastic Forming at the Micrometer Scale ». Science 318, nᵒ 5848 (10 décembre **2007**): 251‑54. doi:10.1126/science.1143719.

- **Dimiduk**, D. M., M. D. Uchic, et T. A. Parthasarathy. « Size-affected single-slip behavior of pure nickel microcrystals ». Acta Materialia 53, no 15 (septembre **2005**): 4065-77. doi:10.1016/j.actamat.2005.05.023.
- **Dunstan**, D.J., et A.J. Bushby. « The Scaling Exponent in the Size Effect of Small Scale Plastic Deformation ». *International Journal of Plasticity* 40 (janvier 2013): 152-62. doi:10.1016/j.ijplas.2012.08.002.
- **Durand,** Milo A. « The Temperature Variation of the Elastic Moduli of NaCl, KCl and MgO ». *Physical Review* 50, nᵒ 5 (1 septembre **1936**): 449-55. doi:10.1103/PhysRev.50.449.
- **Frick,** C. P., B. G. Clark, S. Orso, A. S. Schneider, et E. Arzt. « Size effect on strength and strain hardening of small-scale [1 1 1] nickel compression pillars ». Materials Science and Engineering: A 489, no 1-2 (20 août **2008**): 319-29. doi:10.1016/j.msea.2007.12.038.
- **Gane**, N. « The Compressive Strength of Sub-Micrometre Diameter Magnesium Oxide Crystals ». Philosophical Magazine 25, no 1 (janvier **1972**): 25-34. doi:10.1080/14786437208229212.
- **Gilman**, J. J. « Plastic anisotropy of lif and other rocksalt-type crystals ». Acta Metallurgica 7, nᵒ 9 (1 septembre **1959**): 608‑13. doi:10.1016/0001-6160(59)90130-0.
- **Greer**, Julia R., et William D. Nix. « Nanoscale gold pillars strengthened through dislocation starvation ». *Physical Review B* 73, nᵒ 24 (12 juin **2006**): 245410. doi:10.1103/PhysRevB.73.245410.
- **Greer,** Julia R., Warren C. Oliver, et William D. Nix. « Size dependence of mechanical properties of gold at the micron scale in the absence of strain gradients ». Acta Materialia 53, no 6 (avril **2005**): 1821-30. doi:10.1016/j.actamat.2004.12.031.
- **Huang**, Ling, Qing-Jie Li, Zhi-Wei Shan, Ju Li, Jun Sun, et Evan Ma. « A new regime for mechanical annealing and strong sample-size strengthening in body centred cubic molybdenum ». Nature Communications 2 (22 novembre **2011**): 547. doi:10.1038/ncomms1557
- **Hulse**, C. O., S. M. Copley, et J. A. Pask. « Effect of Crystal Orientation on Plastic Deformation of Magnesium Oxide ». Journal of the American Ceramic Society 46, nᵒ 7 (1 juillet **1963**): 317‑23. doi:10.1111/j.1151-2916.1963.tb11738.x.
- **Hulse**, Charles O., et Joseph A. Pask. « Mechanical Properties of Magnesia Single Crystals Corn Pression ». Journal of the American Ceramic Society 43, nᵒ 7 (1 juillet **1960**): 373‑78. doi:10.1111/j.1151-2916.1960.tb13674.x.
- **Issa**, Inas, Jonathan Amodeo, Julien Réthoré, Lucile Joly-Pottuz, Claude Esnouf, Julien Morthomas, Michel Perez, Jérome Chevalier, et Karine Masenelli-Varlot. « In situ investigation of MgO nanocube deformation at room temperature ». Acta Materialia 86 (**2015**): 295-304.
- **Jennings, Andrew T**., Michael J. Burek, et Julia R. Greer. « Microstructure versus Size: Mechanical Properties of Electroplated Single Crystalline Cu Nanopillars ». *Physical Review Letters* 104, nᵒ 13 (1 avril **2010**): 135503. doi:10.1103/PhysRevLett.104.135503.
- **Kaufmann**, D., R. Mönig, C.A. Volkert, et O. Kraft. « Size Dependent Mechanical Behaviour of Tantalum ». International Journal of Plasticity 27, no 3 (mars **2011**): 470-78. doi:10.1016/j.ijplas.2010.08.008.
- **Kiener**, D., et A. M. Minor. « Source Truncation and Exhaustion: Insights from Quantitative in situ TEM Tensile Testing ». Nano Letters 11, nᵒ 9 (14 septembre **2011**): 3816‑20. doi:10.1021/nl201890s.

- **Kim, Ju-Young**, Dongchan Jang, et Julia R. Greer. « Crystallographic Orientation and Size Dependence of Tension–compression Asymmetry in Molybdenum Nano-Pillars ». International Journal of Plasticity 28, no 1 (janvier **2012**): 46-52. doi:10.1016/j.ijplas.2011.05.015.
- **Korte**, S., et W. J. Clegg. « Discussion of the dependence of the effect of size on the yield stress in hard materials studied by microcompression of MgO ». *Philosophical Magazine* 91, n^o 7-9 (1 mars **2011**): 1150-62. doi:10.1080/14786435.2010.505179.
- **Korte,** S., M. Ritter, C. Jiao, P. A. Midgley, et W. J. Clegg. « Three-dimensional electron backscattered diffraction analysis of deformation in MgO micropillars ». *Acta Materialia* 59, n^o 19 (novembre **2011):** 7241-54. doi:10.1016/j.actamat.2011.08.022.
- **Kraft**, Oliver, Patric A. Gruber, Reiner Mönig, et Daniel Weygand. « Plasticity in Confined Dimensions ». Annual Review of Materials Research 40, no 1 (**2010**): 293-317. doi:10.1146/annurev-matsci-082908-145409.
- **Krell,** A., J. Klimke, et T. Hutzler. « Transparent compact ceramics: Inherent physical issues ». *Optical Materials* 31, n^o 8 (juin **2009**): 1144-50. doi:10.1016/j.optmat.2008.12.009.
- **Kubin**, Ladislas P., Ronan Madec, et Benoit Devincre. « Dislocation Intersections and Reactions in FCC and BCC Crystals ». In *Symposium W – Multiscale Phenomena in Materials - Experiments and Modeling Related to Mechanical Behavior*, Vol. 779. MRS Online Proceedings Library Archive, **2003**. doi:10.1557/PROC-779-W1.6.
- **Mačković,** M., F. Niekiel, L. Wondraczek, et E. Spiecker. « Direct observation of electron-beam-induced densification and hardening of silica nanoballs by in situ transmission electron microscopy and finite element method simulations ». *Acta Materialia* 79 (15 octobre **2014**): 363-73. doi:10.1016/j.actamat.2014.05.046.
- **McDowell,** Matthew T., Austin M. Leach, et Ken Gall. « On The Elastic Modulus of Metallic Nanowires ». *Nano Letters* 8, n^o 11 (**2008**): 3613-18. doi:10.1021/nl801526c.
- **Messerschmidt**, Ulrich. Dislocation Dynamics During Plastic Deformation. Vol. 129. Springer Series in Materials Science. Berlin, Heidelberg: Springer Berlin Heidelberg, **2010**. http://link.springer.com/10.1007/978-3-642-03177-9.
- **Mordehai,** Dan, Seok-Woo Lee, Björn Backes, David J. Srolovitz, William D. Nix, et Eugen Rabkin. « Size effect in compression of single-crystal gold microparticles ». Acta Materialia 59, no 13 (août **2011**): 5202-15. doi:10.1016/j.actamat.2011.04.057.
- **Nadgorny,** Edward M., Dennis M. Dimiduk, et Michael D. Uchic. « Size Effects in LiF Micron-Scale Single Crystals of Low Dislocation Density ». Journal of Materials Research 23, no 11 (novembre **2008**): 2829-35. doi:10.1557/JMR.2008.0349.
- **Ng, K. S**., et A. H. W. Ngan. « Stochastic nature of plasticity of aluminum micro-pillars ». Acta Materialia 56, no 8 (**2008**): 1712-20.
- **Norfleet**, D.M., D.M. Dimiduk, S.J. Polasik, M.D. Uchic, et M.J. Mills. « Dislocation Structures and Their Relationship to Strength in Deformed Nickel Microcrystals ». Acta Materialia 56, no 13 (août **2008**): 2988-3001. doi:10.1016/j.actamat.2008.02.046.
- **R. Oberacker,** Powder compaction by dry pressing, in: R. Riedel, I. Chen (Eds.), Ceramics Science and Technology, Wiley-VCH, Weinheim, **2012**, pp. 1–37.
- **Oh**, Sang Ho, Marc Legros, Daniel Kiener, et Gerhard Dehm. « In Situ Observation of Dislocation Nucleation and Escape in a Submicrometre Aluminium Single Crystal ». *Nature Materials* 8, n^o 2 (février **2009**): 95-100. doi:10.1038/nmat2370.
- **Pells,** G. P. « The Temperature Dependence of the Threshold Displacement Energy in MgO ». *Radiation Effects and Defects in Solids* 64, n^o 1 (1 septembre 1982): 71-75. doi:10.1080/00337578208222990.
- **Rao**, S. I., D. M. Dimiduk, T. A. Parthasarathy, M. D. Uchic, M. Tang, et C. Woodward. « Athermal mechanisms of size-dependent crystal flow gleaned from three-dimensional

discrete dislocation simulations ». Acta Materialia 56, no 13 (août **2008**): 3245-59. doi:10.1016/j.actamat.2008.03.011.

- **Ryu,** Ill, William D. Nix, et Wei Cai. « Plasticity of bcc micropillars controlled by competition between dislocation multiplication and depletion ». *Acta Materialia* 61, n° 9 (mai 2013): 3233-41. doi:10.1016/j.actamat.**2013.**02.011.
- **Sato,** Fumio, et Koji Sumino. « The Yield Strength and Dynamic Behaviour of Dislocations in MgO Crystals at High Temperatures ». *Journal of Materials Science* 15, n° 7 (juillet **1980**): 1625-34. doi:10.1007/BF00550578.
- **Schneider**, A. S., B. G. Clark, C. P. Frick, P. A. Gruber, et E. Arzt. « Effect of orientation and loading rate on compression behavior of small-scale Mo pillars ». Materials Science and Engineering: A 508, no 1-2 (20 mai **2009**): 241-46. doi:10.1016/j.msea.2009.01.011.
- **Shan**, Z. W., Raja K. Mishra, S. A. Syed Asif, Oden L. Warren, et Andrew M. Minor. « Mechanical annealing and source-limited deformation in submicrometre-diameter Ni crystals ». Nature Materials 7, no 2 (février **2008**): 115-19. doi:10.1038/nmat2085.
- **Sun,** Qiaoyan, Qiang Guo, Xi Yao, Lin Xiao, Julia R. Greer, et Jun Sun. « Size Effects in Strength and Plasticity of Single-Crystalline Titanium Micropillars with Prismatic Slip Orientation ». Scripta Materialia 65, no 6 (septembre **2011**): 473-76. doi:10.1016/j.scriptamat.2011.05.033.
- **Uchic**, M. D. « Sample Dimensions Influence Strength and Crystal Plasticity ». Science 305, no 5686 (13 août **2004**): 986-89. doi:10.1126/science.1098993.
- **Uchic,** Michael D., Paul A. Shade, et Dennis M. Dimiduk. « Plasticity of Micrometer-Scale Single Crystals in Compression ». *Annual Review of Materials Research* 39, n° 1 (août **2009**): 361-86. doi:10.1146/annurev-matsci-082908-145422.
- **Volkert**, C. A., et E. T. Lilleodden. « Size effects in the deformation of sub-micron Au columns ». Philosophical Magazine 86, no 33-35 (21 novembre **2006**): 5567-79. doi:10.1080/14786430600567739.
- **Wang,** Yun-Jiang, Guo-Jie J. Gao, et Shigenobu Ogata. « Size-dependent transition of deformation mechanism, and nonlinear elasticity in Ni3Al nanowires ». *Applied Physics Letters* 102, n° 4 (28 janvier **2013**): 041902. doi:10.1063/1.4789528.
- **Whapham,** A. D., et M. J. Makin. « The Hardening of Lithium Fluoride by Electron Irradiation ». *Philosophical Magazine* 5, n° 51 (mars **1960**): 237-50. doi:10.1080/14786436008235839.
- **Zang,** Jianfeng, Lihong Bao, Richard A. Webb, et Xiaodong Li. « Electron Beam Irradiation Stiffens Zinc Tin Oxide Nanowires ». *Nano Letters* 11, n° 11 (9 novembre **2011**): 4885-89. doi:10.1021/nl2027519.
- **Zhang**, H., B. E. Schuster, Q. Wei, et K. T. Ramesh. « The design of accurate micro-compression experiments ». *Scripta Materialia* 54, n° 2 (janvier **2006**): 181-86. doi:10.1016/j.scriptamat.2005.06.043.
- **Zheng,** Jingmin, et James S. Reed. « Effects of Particle Packing Characteristics on Solid-State Sintering ». *Journal of the American Ceramic Society* 72, n° 5 (1 mai **1989**): 810-17. doi:10.1111/j.1151-2916.1989.tb06222.x.
- **Zheng, Kun**, Chengcai Wang, Yong-Qiang Cheng, Yonghai Yue, Xiaodong Han, Ze Zhang, Zhiwei Shan, et al. « Electron-Beam-Assisted Superplastic Shaping of Nanoscale Amorphous Silica ». Nature Communications 1 (1 juin **2010**): 24. doi:10.1038/ncomms1021.
- **Zhu,** Ting, et Ju Li. « Ultra-strength materials ». *Progress in Materials Science* 55, n° 7 (septembre **2010**): 710-57. doi:10.1016/j.pmatsci.2010.04.001.
- **Zhu**, Ting, Ju Li, Amit Samanta, Austin Leach, et Ken Gall. « Temperature and Strain-Rate Dependence of Surface Dislocation Nucleation ». *Physical Review Letters* 100, n° 2 (15 janvier **2008**): 025502. doi:10.1103/PhysRevLett.100.025502.

Part B

Coupling of the Mechanical Behaviour of Transition Alumina Nanoparticles Compressed *in situ* in TEM and in a Diamond Anvil Cell

B- Introduction

The plastic behaviour of a brittle material such as alumina is not observed at bulk. However, transition alumina nanoparticles compressed *in situ* in TEM show large plastic deformation under high load [*E. Calvié et al. (2014)*] (***Figure 80***-a).

Kun Zeng *et al* [*K. Zeng e al. 2010*] showed that the electron beam, during *in situ* TEM nano-compression tests of a-silica nanoparticles, creates structural and bonding defects throughout the entire sample and facilitates the plasticity of the nanoparticles. In this work, consecutive tests of beam-off and beam-on are conducted respectively on a-silica nanoparticle [*K. Zeng et al. (2010)*] (*Figure 79*-b-c: TEM images after each type of test). It is shown that the yield stress is highly affected by the electron beam (beam-on test) and thus plasticity is facilitated with electron-beam illuminations (*Figure 79*-d). The electron-beam effect on Si-O bonds is simulated by MD and is assumed to be presented by the creation of structural and bonding defects facilitating silica plastic deformation *[K. Zeng et al. (2010)]*. In the previous part on MgO nanocubes, we showed that the mechanical behaviour is also affected by the electron beam (decrease of the yield stress by a factor of ~2).

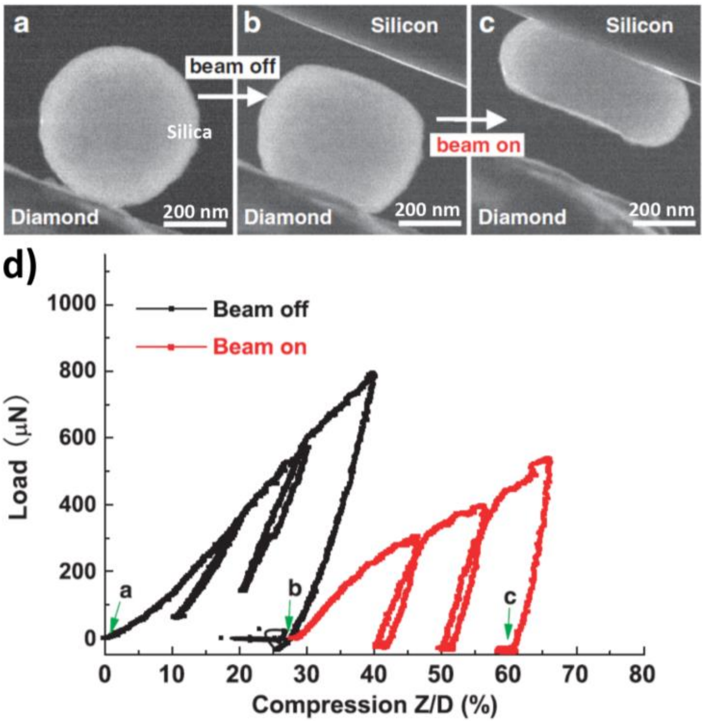

Figure 79: *Nanocompression of silica-amorphous particle in situ in TEM [K. Zeng et al. (2010)].* ***a)*** *The particle is stuck to the diamond punch.* ***b)****, the particle is imaged after it has been pressed without any illumination.* ***c)*** *Subsequently, with the beam on, the particle can be largely compressed with a moderate force.* ***d)*** *Load versus percent compression for the nanocompression test of silica-amorphous nanoparticle. The points (a, b & c) correspond to the three panels above.*

During her PhD at MATEIS, Emilie Calvié also investigated the electron beam effect on the plasticity of *in situ* TEM compressed transition alumina. This investigation was performed by compacting alumina nanoparticles in a Belt apparatus at uniaxial 5 GPa pressure, at ambient temperature. TEM observations on thin foils of these compacted nanoparticles, prepared by FIB, revealed the plastic deformation of the alumina nanoparticles (***Figure 80***-b). Therefore, it was suggested that the plasticity of the compressed alumina nanoparticles inside the TEM was not only an artefact due to the presence of the electron beam.

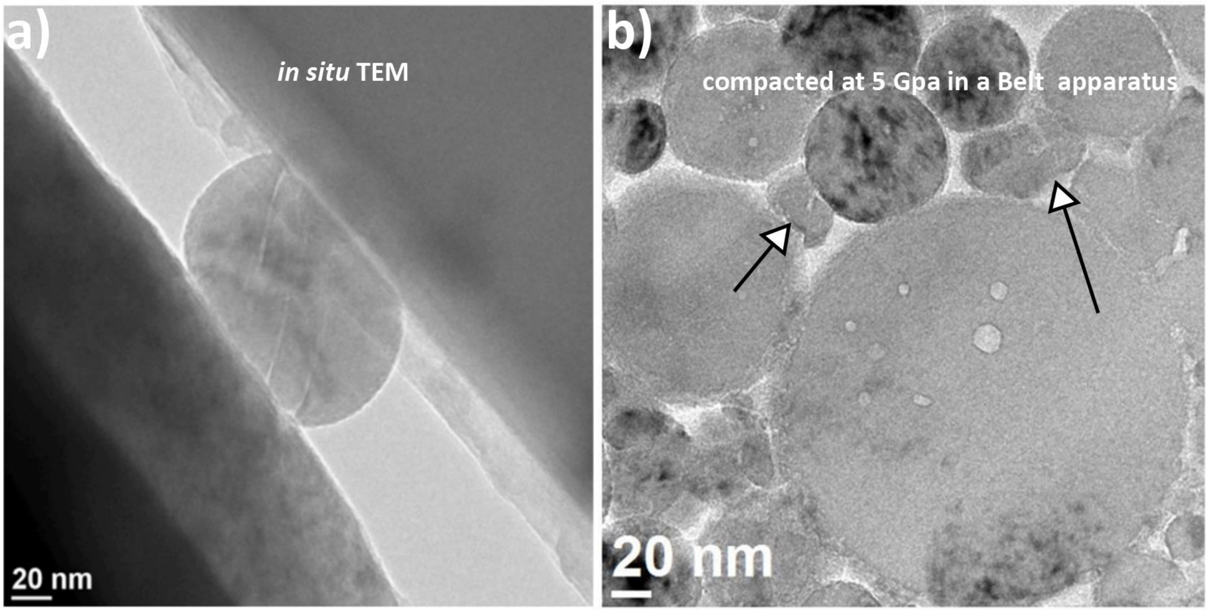

Figure 80: ***a)*** *TEM image of a transition alumina nanoparticle compressed in situ in TEM* [*E. Calvié et al. (2014)*] **b)** *TEM image showing plastic deformation of alumina nanoparticles in a powder compact during a pressing experiment at ambient temperature, under a pressure of 5 GPa. Arrows indicate highly deformed nanoparticles.*

Investigating the deformation mechanism controlling the plasticity of single crystalline alumina nanoparticles requires information on the crystallographic orientation of the nanoparticles with respect to the solicitation direction. This is necessary not only to identify the slip planes, but also to run simulations that would reproduce the experimental conditions. Due to vibrations in the *in situ* TEM sample holder, acquiring HRTEM images is not possible during the *in situ* tests, thus it is not possible to identify the crystallographic solicitation direction. Due to this and to the spherical shape of nanoparticles, image contrasts considered as dislocations signatures could not be analysed in [*E. Calvié et al. (2014)*]. As a consequence, the identification of elementary mechanisms responsible for plastic deformation in transition alumina nanospheres compressed *in situ* in TEM could not be determined. Finite Elements (FE) simulations could instead be used to reproduce the experimental conditions and to determine a constitutive law for transition alumina at the nanoscale [*Calvié et al. (2014)*].

In this part, we aim to investigate the deformation mechanism controlling the plasticity of transition alumina nanoparticles. We present experiments on transition alumina nanoparticles similar to those studied by E. Calvié. This time, the nanoparticles are compacted in a Diamond Anvil Cell (DAC) at room temperature under different uniaxial pressures, namely 5GPa, 15GPa and 20GPa. In **Chapter 4**, we describe the transition alumina crystallographic structure and main characteristics. The DAC technique and conditions chosen to conduct the compaction experiments are presented. Finally, the preparation of thin foils by FIB is also presented.

Foils of these compacted nanoparticles, prepared by FIB for HRTEM and electron diffraction (Debye Scherrer kind) observations, are studied and results obtained on the thin foils, using HRTEM and electron diffraction are presented in **Chapter 5**.

Chapter 4: Material and Techniques

4.1. Nanocrystalline (NC) ceramics

NC ceramics are ceramics with grain sizes smaller than ~100 nm. They are widely used in orthopedic applications. These ceramics present interesting mechanical properties compared to their conventional counterparts (with larger grain sizes). They present higher hardness and resistance to crack propagation. This is due, in principle, to a smaller space available for dislocation to pile-up and thus to the higher stress needed to move dislocations from smaller grains than larger grains [*Hall 1951*] [*Petch 1953*].

In general, a synthesis process of such ceramics is composed mainly of three steps, as described in *Figure 81*.

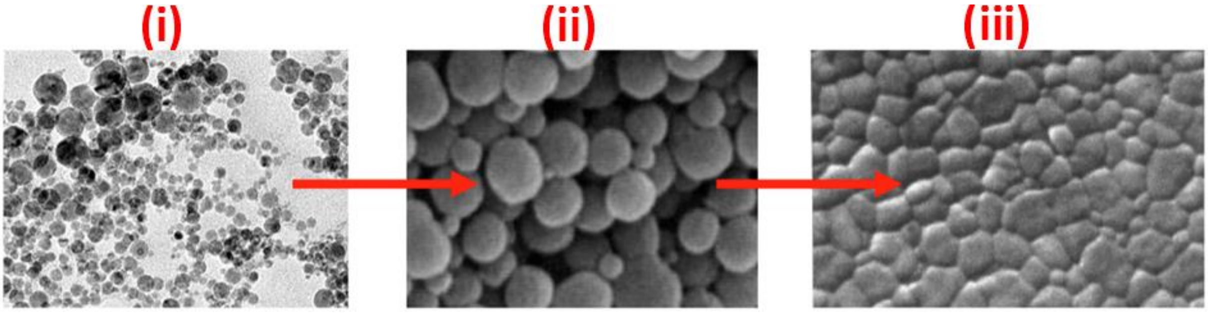

Figure 81: *Synthesis process of NC ceramics:* ***(i)*** *decrease nanoparticles size,* ***(ii)*** *compaction and* ***(iii)*** *sintering.*

The first step (i) is used to decrease the nanoparticle size by grinding techniques as ball milling. In the second step (ii), compaction is used to reduce the porosity and increase the density. Finally, the third step (iii) is a sintering step. It consists of high temperature and/or pressure treatments for ceramic. This step provides a maximum removing of the remaining porosity to produce a final ceramic with a high density. This final density of the NC ceramic is a key point for the mechanical properties (higher density indeed means better mechanical properties).

4.2. Alumina

Even though zirconia is considered as the main ceramic used for orthopedic applications, alumina is also widely used for such applications. This is due to its mechanical and biocompatibility properties. Indeed, alumina (Aluminium Oxide, Al_2O_3) presents a very good biocompatibility [*Bozentka (1993)*], and high resistance to compression [*William G (1996)*]. Compared to zirconia, alumina presents a higher hardness and a good resistance to ageing. Also, alumina presents surfaces with low roughness, which prevents in vivo inflammations. However, alumina presents a lower resistance to cracks compared to zirconia *[Heros R & Willmann G 1998]*.

4.2.1. Alpha-Alumina and Transition Alumina

Alumina (Aluminium Oxide, Al_2O_3) exists in many metastable phases (Transition alumina: Al_2O_3–γ, Al_2O_3–δ, Al_2O_3–θ…) beside the thermodynamically stable phase, α-alumina [*Levin et al. (1998)*]. α-alumina is the only phase of alumina that is stable at bulk, under a wide range of pressures and temperatures [*Chen et al. (2002)*].

At the nanoscale, α-alumina nanoparticles have a vermicular structure. This vermicular structure prevents the high density of final ceramics. Liao et al [*Liao, S.C et al. (1998)*] indeed showed that the compaction of transition alumina (perfectly spherical nanoparticles) improves the density of the final ceramic. They attributed the higher density to a possible partial plastic deformation of transition alumina nanoparticles. Thus, transition alumina nanoparticles carry great potential for many applications such as orthopedic ones, among others (catalysts, adsorbents, catalyst carries, coatings due to their high catalytic activity of their high surface areas) [*Levin et al. (1998)*].

These transition phases are not stable at bulk and during sintering step; Transition alumina experiences phase transition to α phase.

It exists many processing routes to obtain these phases of Alumina, the common one is a sequence of high temperature processes that enables phase transformations from boehmite, passing by transition alumina (metastable phases of alumina) to α-Alumina [*Levin et al. (1998)*]:

$$\gamma\text{AlOOH (Boehmite)} \xrightarrow{300°\text{-}500°C} Al_2O_3\text{-}\gamma \xrightarrow{700°\text{-}800°C} Al_2O_3\text{-}\delta \xrightarrow{900°\text{-}1000°C} Al_2O_3\text{-}\theta \xrightarrow{1000°\text{-}1100°C} Al_2O_3\text{-}\alpha \qquad \text{Eq. 2}$$

Each phase obtained by a sequence of transition is stable when temperature is decreased to room temperature. So far, these transformations are not reversible. Some other intermediate phases (δ*, δ') can also be found, that are cited in the *Table 7*, and will be discussed later in the text.

4.2.2. Crystallographic structures

Alumina has a chemical formula: Al_2O_3. Due to stoichiometry and crystallographic structures adopted by Alumina phases, Alumina structure contains Al^{3+} vacancies.

For example transition alumina phases are described by a spinel structure defined by the chemical formula AB_2O_4, thus Al_3O_4. But due to stoichiometry, Alumina is described by the chemical formula Al_2O_3. This means that the structure contains Al^{3+} vacancies.

In general, the alumina crystallographic structures can be divided into two main categories:

(i) For α-Al_2O_3, the oxygen anions are in a near HCP (Hexagonal Compact) arrangement: the cations fill 2/3 of the octahedral sites and vacancies are present in 1/3 of these sites in an ordered array and well-known sequence along a rhombohedral structure axis ($2Al^{3+}$-vacancy-$2Al^{3+}$...). The unit cell contains 10 atoms, and its symmetry is described by the space group ($R\bar{3}c$, N°167). Wyckoff positions of oxygen anions are 18*c* (0.306, 0, 1/4) while alumina cations occupy 12*c* positions with coordinates (0, 0, 0.35228) [*N. Ishizawa-1980]*.

(ii) For Transition Alumina (spinel structure), the oxygen anions are in a FCC arrangement: However, cations are occupying octahedral and tetrahedral sites. Each phase of transition alumina presents a specific percentage of cations occupation of the octahedral sites over the tetrahedral sites. This induces a different structure of cations arrangement in each phase. Structural parameters of these phases, with α-Al_2O_3, are given in ***Table 7***.

Table 7: Alpha and Transition alumina structural characteristics and parameters. The phases concerned in this work are highlighted.

Name	O-structure	Al-structure	Lattice Parameters (Å)			
			a	b	c	β
α	**HCP**	**Rhombohedral**	**4.758**		**12.991**	
γ (JCPDS file-50-741)	**FCC**	**Cubic**	**7.939**			
δ	**FCC**	**Tetragonal**	**5.599**		**23.657**	
δ’(JCPDS file-47-1770)	**FCC**	**Tetragonal**	**7.943**		**23.50**	
δ* (JCPDS file-46-1215)	**FCC**	**Orthorhombic**	**7.934**	**7.956**	**11.711**	
θ	**FCC**	**Monoclinic**	**5.62**	**2.906**	**11.79**	**103 °8’**

Structural data obtained on transition alumina, especially by neutron diffraction, give percentages of occupation of octahedral and tetrahedral sites with random distributions of cations on these sites. This makes running simulations (ab initio, MD) on these metastable phases of alumina complicated.

As, in this work, γ-Al_2O_3, δ-Al_2O_3 and δ*-Al_2O_3 are concerned, we present the structural characteristics of these three phases.

- **γ-Al_2O_3**

γ-Al_2O_3 is defined as a defect spinel structure. The ideal spinel structure (AB_2O_4) is an FCC arrangement of oxygen anions (Wyckoff positions: 32*e*) and cations occupy octahedral (Wyckoff positions: 8*a*) and tetrahedral sites (Wyckoff positions: 16*d*). The symmetry of the spinel structure is described by the space group Fd$\bar{3}$m (N°227). For Al_2O_3, the unit cell includes 32 oxygen atoms. The stoichiometry of Al_2O_3 is respected with 32*(2/3) = 64/3 =21+1/3 aluminium cations, occupying octahedral and tetrahedral sites. This means that γ-Al_2O_3 structure presents 8/3 vacancies in the octahedral and tetrahedral sites of an ideal spinel. The occupied sites have Wyckoff positions with fraction of occupancy given in *Table 8*.

Table 8: Structural parameters and Wyckoff positions of γ-Al_2O_3

Site		**Occupancy**	***x***	***y***	***z***
O	32*e*	1	0.2547	0.2547	0.2547
Al	16*d* (octahedral)	0.58	0.5	0.5	0.5
Al	8*a* (tetrahedral)	0.84	0.125	0.125	0.125
Al	32*e* (octahedral)	0.17	0.0272	0.0272	0.0272

Thus the ratio of occupancies in the tetrahedral and octahedral sites is $\frac{Tetrahedral\ sites}{Octahedral\ sites} = \frac{8*0.84}{16*0.58+32*0.17} = 0.45$. This ratio determines the degree of stability of the phase. For example the most stable phase α has this ratio equal to zero with alumina in the tetrahedral sites.

The γ-Al_2O_3 is considered as a partially disordered spinel structure and its unit cell is still described by the Fd$\bar{3}$m (N°227) space group with a volume of 500 Å^3.

- **δ-Al_2O_3**

δ-Al_2O_3 was described by Y. Replin and E. Hosson from an X-Ray Diffraction (XRD) procedure [*Repelin & Hosson (1990)*]. The unit cell symmetry is described by the P$\bar{4}$m2 space group (N°115) of volume 741.62 Å^3. Oxygen ions are in a near FCC arrangement (as for all transition alumina) (48 atoms). Al ions are distributed over octahedral and tetrahedral sites (32 atoms). The Al vacancies are randomly distributed over octahedral sites (4 Al vacancies) with a ratio $\frac{Tetrahedral\ sites}{Octahedral\ sites} = 0.7$. The Wyckoff positions are given in **appendix 1**.

The following relations can be written with the lattice parameters of γ and δ-alumina: $a_\delta = b_\delta \approx \frac{\sqrt{2}}{2} a_\gamma$ and $c_\delta \approx 3a_\gamma$. ($c_\delta/a_\delta \approx 4.22$).

- **δ*-Al_2O_3**

δ*-Al_2O_3 is sometimes called orthorhombic δ-Al_2O_3, as cited in [*Levin et al.(1998)*]. Few works have identified this phase by TEM Convergent-Beam Electron diffraction (CBED) and XRD. The unit cell symmetry is described by the $P2_12_12_1$ space group (N°16) of volume 739.23 $Å^3$. Oxygen ions are in a near FCC arrangement. Al atoms are distributed on octahedral and tetrahedral sites with 4 Al vacancies randomly distributed on octahedral sites.

The following relations can be written with the lattice parameters of γ and δ*-alumina : $a_{\delta*} \approx b_{\delta*} \approx a_\gamma$ and $c_{\delta*} \approx 1.5a_\gamma$. ($c_{\delta*}/a_{\delta*} \approx 1.5$)

Interestingly Levin and Brandon [*Levin et al. (1998)*] reviewed the phase transformation mechanisms between metastable phases. They indicated that transition from one phase to another occurs by migration of cations between octahedral and tetrahedral sites. It was suggested the transformation from γ-Al_2O_3 to δ*-Al_2O_3 (orthorhombic) occurs before the cubic spinel structure collapse and exhibits a tetragonal character. This is followed by a monoclinic structure transformation and finally at higher temperatures the trigonal structure α-Al_2O_3 is obtained (without any tetrahedral sites for Al atoms). Thus the sequence proposed is in the following form:

$$\gamma AlOOH\ (Boehmite) \longrightarrow \gamma\text{-}Al_2O_3 \longrightarrow \delta^*\text{-}Al_2O_3 \longrightarrow \delta\text{-}Al_2O_3 \longrightarrow \theta\text{-}Al_2O_3 \longrightarrow \alpha\text{-}Al_2O_3 \qquad \text{Eq. 3}$$

However, one must mention that other phases of Alumina (metastable) may be produced by different synthesis processes (for example: plasma spray……).

4.3. Transition Alumina Nanoparticles

The Transition Alumina nanoparticles used in this work are a commercial transition alumina powder (NanoTek, Nanophase Technologies Corporation, Romeoville, IL, USA). It is produced by Physical Vapor Synthesis (PVS).

4.3.1. HRTEM Characterisations: nanoparticle crystallinity

Figure 82 displays typical HRTEM images of the NPs. They are well crystallized and single crystalline. Very few of them eventually contain twin boundaries, believed to be growth defects.

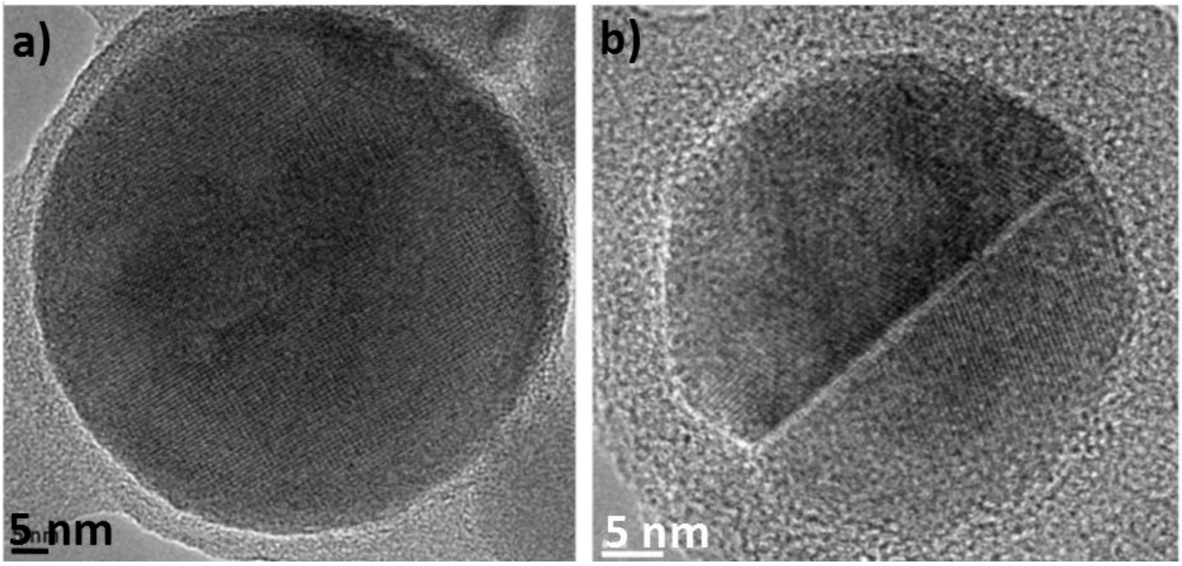

Figure 82: *a) HRTEM of a Transition alumina NP.* ***b)*** *HRTEM of a Transition alumina NP containing a twin [Calvie et al. (2014)]*

4.3.2. XRD Characterisations: Phases Identification

Experimental X-ray Diffraction (XRD) diffractogram on the thermally treated powder reveals the presence of the γ-Al_2O_3 and δ^*-Al_2O_3 phases (see *Figure 83*). The experimental XRD diffractogram can be compared to the theoretical one (obtained by the software *Carine Crystallography 3.1*) of these two phases with different proportions. The theoretical composition that gives the best fit with the experimental diffractogram 70 wt.% of γ-Al_2O_3 and 30 wt.% of δ^*-Al_2O_3. It is noteworthy that the inter-reticular distances of γ-Al_2O_3, δ-Al_2O_3 and δ*-Al_2O_3 are very close. However at 2θ Bragg diffraction angles in the range [44°-48°], one can differentiate peaks of these three phases. Thus we also compared the experimental XRD to a mixture of γ-Al_2O_3 (70%)/ δ-Al_2O_3 (30%). However, a linear combination of the XRD spectra does not reproduce the experimental peaks obtained at 2θ=45.57° or 46.5°(see *Figure 83* and *Figure 84*.). These peaks are observed in the theoretical diffractogram of γ-Al_2O_3 (0.7)/ δ^*-Al_2O_3 (0.3) at 2θ= 45.57°, 46.49° and ~ 47.6° and corresponds to peaks of δ^*-Al_2O_3. Thus we can conclude that the powder is composed of single crystal transition alumina nanoparticles with 70% of γ-Al_2O_3 and 30% of δ^*-Al_2O_3.

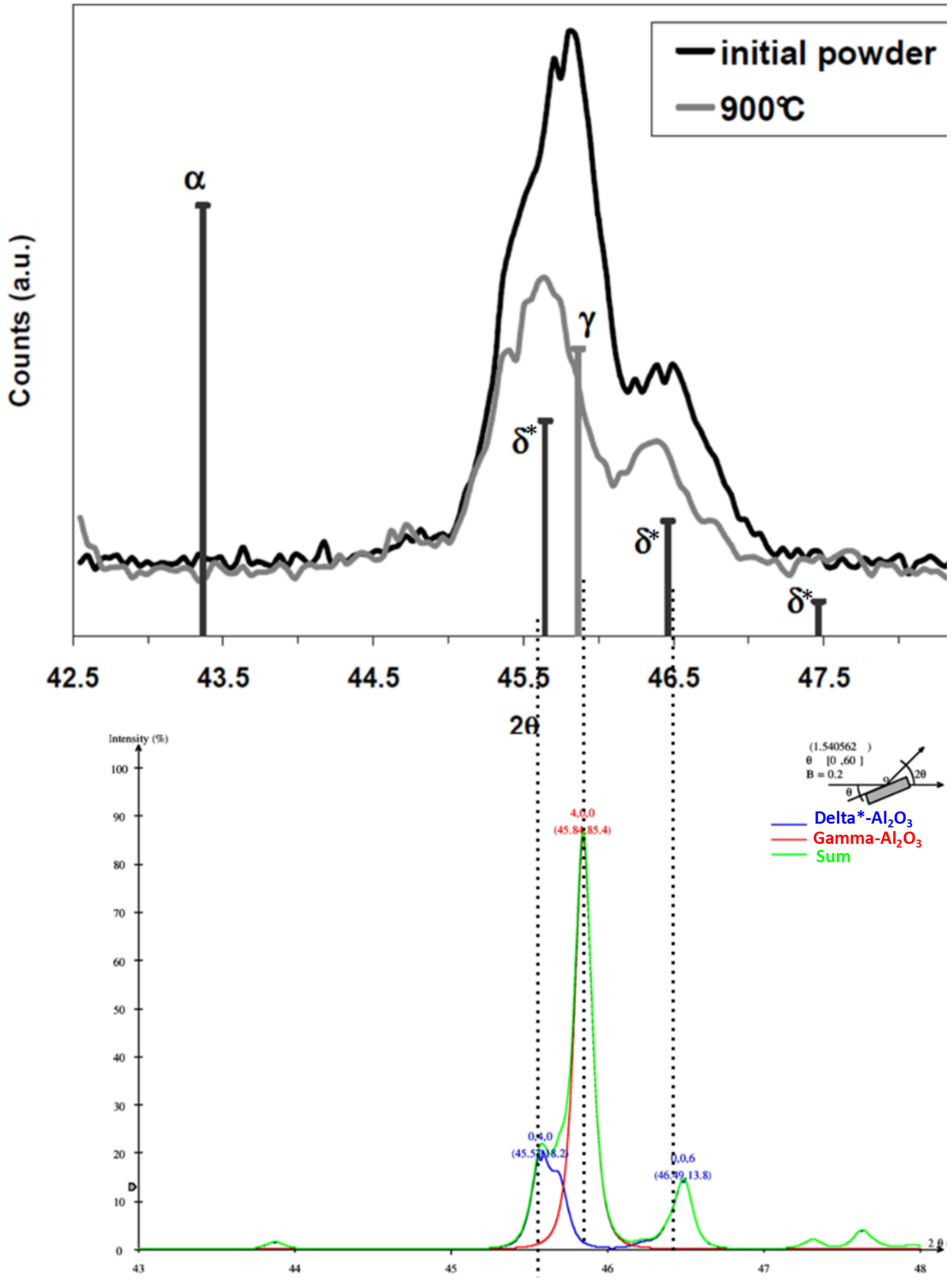

Figure 83: *Upper diffractogram : experimental X-Ray diffraction of the powder Nanotech. The powder used for the experiments is thermally treated at 900 °C. The lower diffractogram is theoretical XRD diffractogram for a mixture of* γ*-*Al_2O_3 *(70%) and* δ**-*Al_2O_3 *(30%). The dotted lines at approximately* $2\theta = 45.57°$ *and* $46.49°$ *correspond to (040) and (006) planes in* δ**-*Al_2O_3*. The line at* $2\theta \sim 45.8°$ *correspond to the (400) planes of* γ*-*Al_2O_3*.*

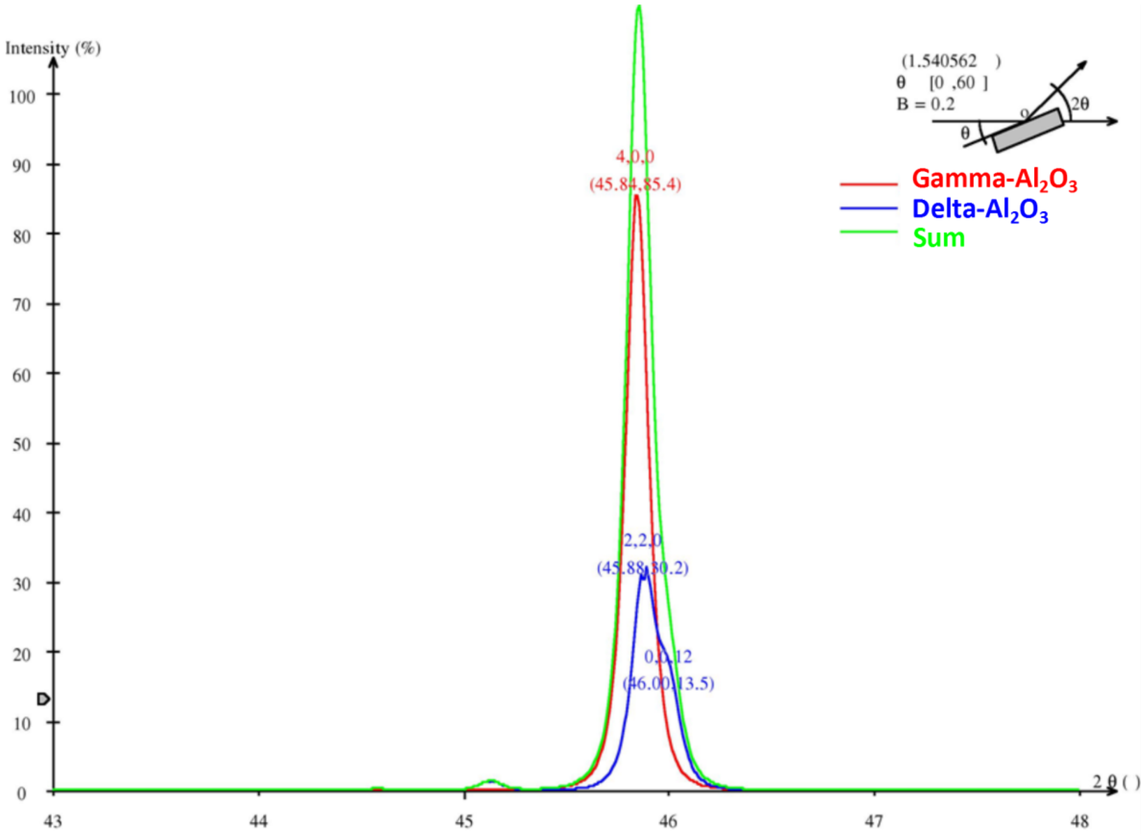

Figure 84 Theoretical XRD diffractogram for a mixture γ-Al2O3 (0.7) - δ-Al2O3 (0.3).

4.3.3. Nanoparticle Size Distribution

The diameter of these nanoparticles ranges from a few nm to 200 nm, as shown *Figure 85*. This size distribution is obtained by measuring diameters of nanaoparticles (1000 nps) on a large number of TEM images during the PhD thesis of Mirella AZAR at MATEIS laboratory [*AZAR Mirella PhD thesis INSA of lyon 2009*].

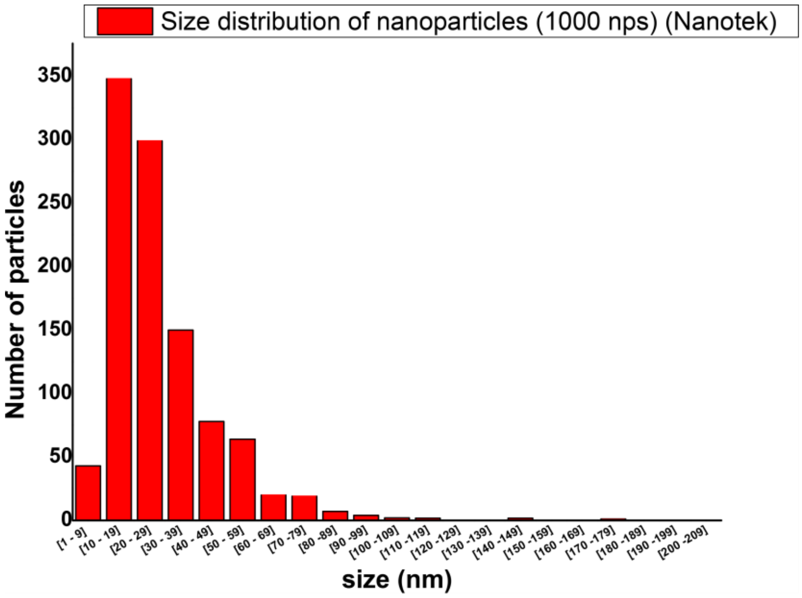

Figure 85 *Size distribution performed on 1000 nanoparticles from Nanotek powder.*

4.4. Uniaxial Compression in DAC

There are many high pressure techniques but the revolution in this field after the Bridgman anvils (anvils made of tungsten-carbon alloy), which produces few GPa of pressure, was the Diamond Anvil Cell (DAC). The DAC is the only technique that generates pressures higher than 5GPa thanks to single crystal diamond anvils. DAC is mainly used for powder compaction. Developments in the DAC field include the introduction of metal gaskets technique for hydrostatic pressure generation and the use of ruby fluorescence for pressure calibration (used in this work). Transmitting media for hydrostatic pressures are sometimes used to generate pressures higher than 50 GPa in the gasketed anvil. All these innovations have turned the DAC into a fine quantitative tool for powder compaction researches [*A. Jayaraman (1983)]*.

In this work we used DAC with a gasket technique at room temperature and a ruby fluorescence for pressure calibration.

A steel gasket of 1.5 cm in diameter and 200 µm in thickness is used. In Figure 86, a scheme shows the different steps of DAC experiments. An imprint is made in the center of the gasket with two culet flat diamonds. As shown in Figure 86-C, a hole of 60 µm in thickness and 300µm in diameter is drilled in the imprint by electroerosion.

The gasket is supported by one culet flat diamond from one side. while granules of transition alumina nanoparticles (obtained by atomization) are poured in the hole. A ruby is inserted in the hole for pressure calibration. No transmitter media was used. This favours free motion and stacking of the nanoparticles.

The samples are then compressed between two culet flat diamonds. The pressure is increased by steps to the desired pressure. Three experiments of compression are performed at 5 GPa, 15 GPa and 20 GPa at ILM University Claude Bernard Lyon1 in a collaboration work with Denis MACHON and Sylvie LEFLOCH.

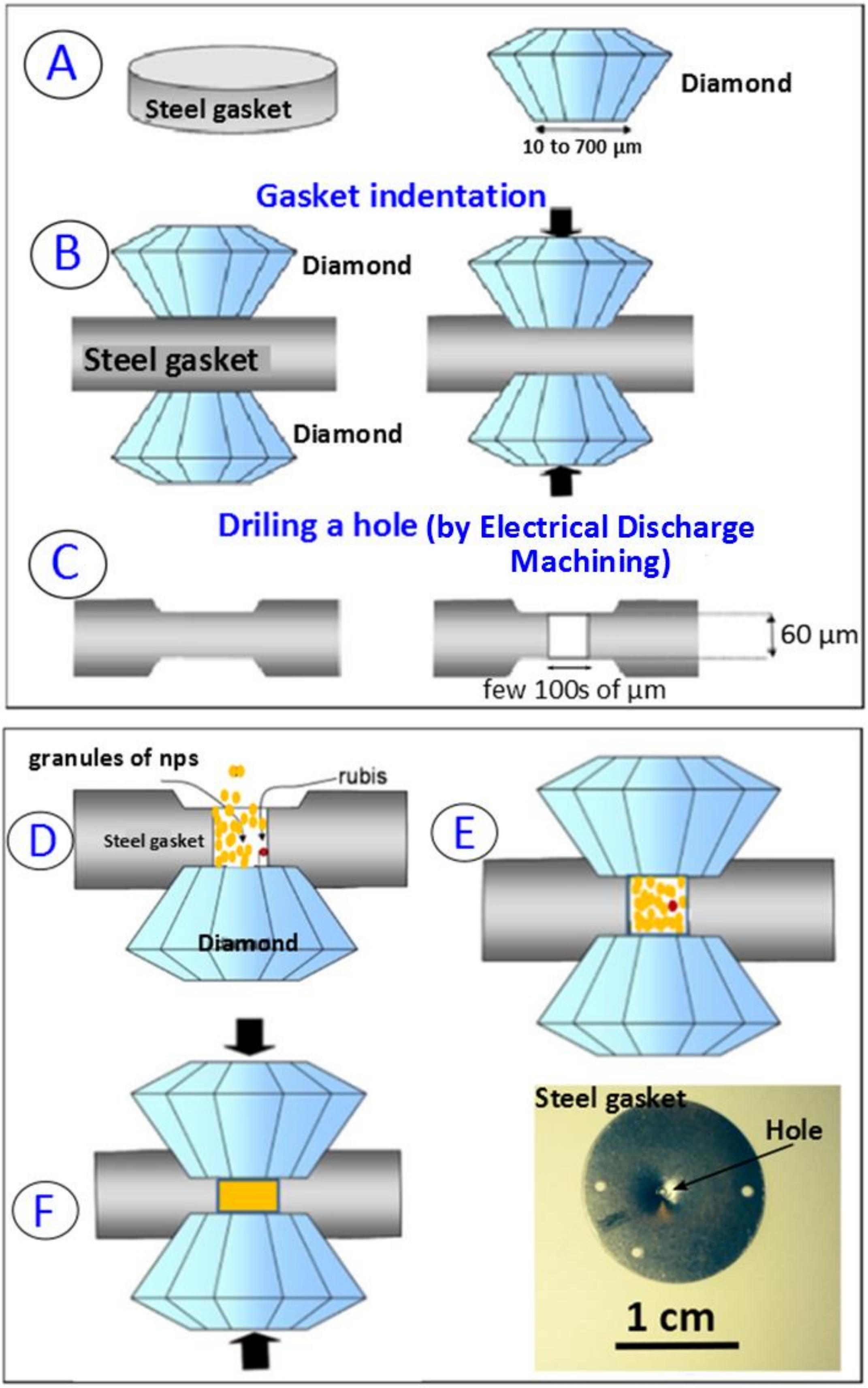

Figure 86: *Steps of the compaction procedure in DAC.*

4.5. Thin Foils preparation by FIB:

Thin Foils have been prepared by Thierry Douillard from the MATEIS Laboratory.

Thin foils are extracted from the compacted samples using a FIB/SEM (NVision 40; Carl Zeiss Microscopy GmbH, Oberkochen, Germany), combining a SIINT zeta FIB column (Seiko Instruments Inc. NanoTechnology, Japan) with a Gemini I column. The NVision 40 platform is also equipped with a multi-nozzle SIINT gas injection system (GIS). The *in situ* lift-out of the foils is carried out with a Cartesian nano-robotic manipulator (Klocke Nanotechnik GmbH, Aachen, Germany). To minimize the curtain effect introduced by the gallium ion beam milling and to protect the sample surface from implantation, an *in situ* ion beam induced deposition is first performed over the area of interest with tungsten carboxyl $W(CO)_6$ as a precursor gas (sputter-resistant layer of about 1µm). Trenches are milled to enable the extraction of 1-2 µm thick lamellas which are then transferred, using the manipulator, and glued, using the GIS, onto a TEM copper grid for further thinning. In this work, settings for 30 kV ion accelerating voltage with decreasing beam currents (700 pA to 40 pA) and probe sizes are used to reach a suitable foil thickness for TEM analysis (around 100 nm). At each step, milling is carried out using an adjusted grazing incidence to compensate for the ion beam tails in order to achieve near parallel foil top and bottom surfaces over a large zone. Finally, to reduce the amorphous layer due to the high energy ion beam, a final low-kV ion polishing at 2 kV/50 pA is performed.

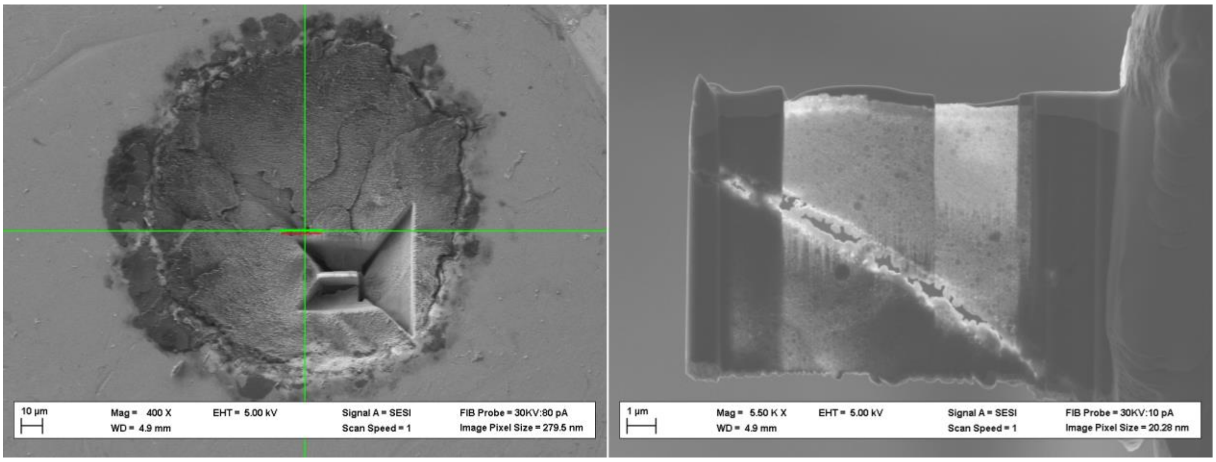

Figure 87: SEM images of the thin foil extracted by FIB

References:

- **Azar** M. PhD INSA de Lyon (2009) Mise en forme et frittage des poudres de céramique nanostructurées : Cas d'une alumine de transition
- **Calvié**, E., J. Réthoré, L. Joly-Pottuz, S. Meille, J. Chevalier, V. Garnier, Y. Jorand, et al. « Mechanical behavior law of ceramic nanoparticles from transmission electron microscopy in situ nano-compression tests ». *Materials Letters* 119 (15 mars **2014**): 107-10. doi:10.1016/j.matlet.2014.01.002.
- **Bozentka, David J.** « Biological Performance of Materials: Fundamentals of Biocompatibility ». *Journal of Hand Surgery* 18, n° 6 (1 novembre **1993**): 1130. doi:10.1016/0363-5023(93)90416-Z.
- **Carlton,** C. E., et P. J. Ferreira. « In situ TEM nanoindentation of nanoparticles ». *Micron*, In situ TEM, 43, n° 11 (novembre **2012**): 1134-39. doi:10.1016/j.micron.2012.03.002.
- **Chen, B**., D. Penwell, L. R. Benedetti, R. Jeanloz, et M. B. Kruger. « Particle-Size Effect on the Compressibility of Nanocrystalline Alumina ». *Physical Review B* 66, n° 14 (4 octobre 2002). doi:10.1103/PhysRevB.66.144101.
- **Hall**, E. O. « The Deformation and Ageing of Mild Steel: III Discussion of Results ». *Proceedings of the Physical Society. Section B* 64, n° 9 (**1951**): 747. doi:10.1088/0370-1301/64/9/303.
- **Heros** R, Willmann G. Ceramics in total hip arthroplasty: history, mechanical properties, clinical results andcurrent manufacturing state of the art. Seminars Arthroplasty 1998;9:114–22
- **Ishizawa N**., T. Miyada, I. Minato, F. Marumo and S. Iwai. Acta Crysta.(**1980**),B36, 228-230.
- **Jayaram**, V., et C.G. Levi. « The Structure of δ-Alumina Evolved from the Melt and the γ → δ Transformation ». *Acta Metallurgica* 37, n° 2 (février **1989**): 569-78. doi:10.1016/0001-6160(89)90240-X.
- **Jayaraman,** A. « Diamond anvil cell and high-pressure physical investigations ». *Reviews of Modern Physics* 55, n° 1 (1 janvier **1983**): 65-108. doi:10.1103/RevModPhys.55.65.
- **Levin,** Igor, et David Brandon. « Metastable Alumina Polymorphs: Crystal Structures and Transition Sequences ». *Journal of the American Ceramic Society* 81, n° 8 (1 août **1998**): 1995-2012. doi:10.1111/j.1151-2916.1998.tb02581.x.
- **Liao,** S. -C., Y. -J. Chen, B. H. Kear, et W. E. Mayo. « High pressure/low temperature sintering of nanocrystalline alumina ». *Nanostructured Materials* 10, n° 6 (août **1998**): 1063-79. doi:10.1016/S0965-9773(98)00125-1.
- **Petch**. N.J « The cleavage strength of polycrystals». Journal of Iron Steel Inst. 174:25–28 (**1953**)
- **Repelin,** Y., et E. Husson. « Etudes structurales d'alumines de transition. I-alumines gamma et delta ». *Materials Research Bulletin* 25, n° 5 (1 mai **1990**): 611-21. doi:10.1016/0025-5408(90)90027-Y.
- **Willmann, G**. « Development in medical-grade alumina during the past two decades ». *Journal of Materials Processing Technology*, International Conference on Advances in Material and Processing Technologies, 56, n° 1-4 (janvier **1996**): 168-76. doi:10.1016/0924-0136(96)85101-6.

- **Zheng**, Kun, Chengcai Wang, Yong-Qiang Cheng, Yonghai Yue, Xiaodong Han, Ze Zhang, Zhiwei Shan, et al. « Electron-Beam-Assisted Superplastic Shaping of Nanoscale Amorphous Silica ». *Nature Communications* 1 (1 juin 2010): 24. doi:10.1038/ncomms1021.

Chapter 5: Results on Transition Alumina Compacted by DAC

We present here the results obtained on the thin foils prepared from Transition Alumina nanoparticles compacted compacted at 5, 15 and 20 GPa in DAC. The sample compacted in a Belt apparatus at uniaxial 5 GPa pressure (from E. Calvié's PhD) is also studied. A series of images performed in different TEM modes (Conventional BF, HRTEM, Conventional Diffraction and Powder Diffraction (Debye-Scherrer) are studied.

5.1. Plastic Behavior

5.1.1. Plastic Deformation and Size Distribution

First, a series of conventional TEM images at low magnifications of the sample compacted at 5 GPa (5 GPa, Belt apparatus) are studied. The TEM image shown in **Chapter 4** is a typical image of this sample. Some nanoparticles are obviously plastically deformed. *Figure 88* displays the size distribution of the initial nanoparticles and that of the deformed nanoparticles, extracted from the TEM image series.

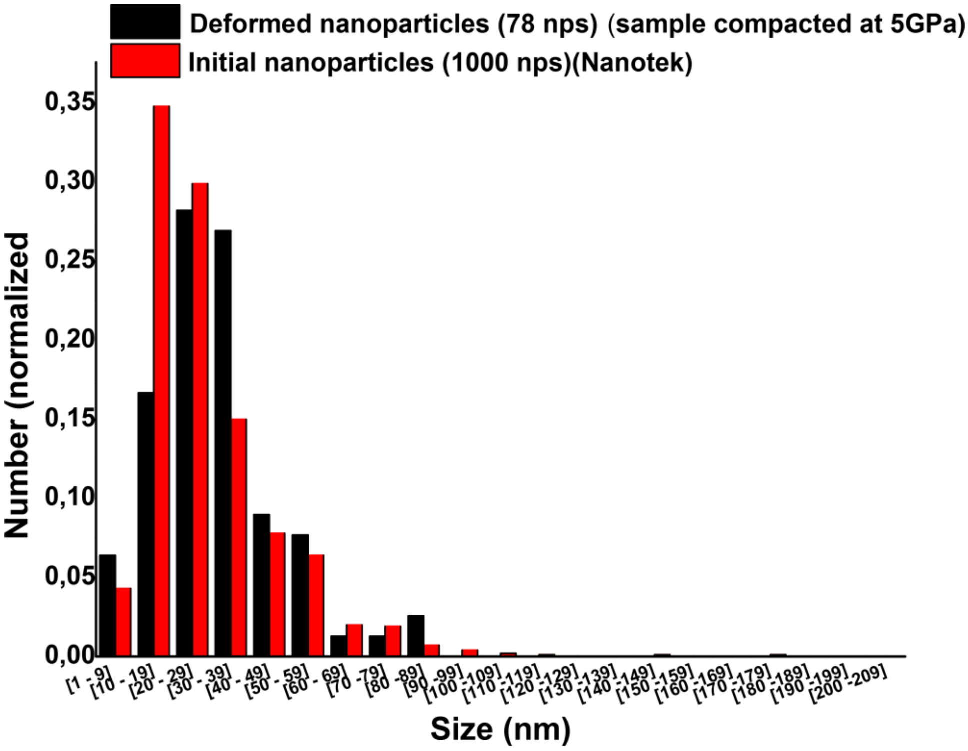

Figure 88: Size distribution of initial nanoparticles (statistics on 1000 nps) and size distribution of deformed nanoparticles (statistics on 78 nps).

The diameters of deformed nanoparticles are obtained by calculating the minor (d) and the major (D) diameters of the ellipse (deformed nanoparticle). The area of the ellipse is assumed to be equal to the area of the initial circle (before deformation) and hence equal to $A = \left(\pi * \left(\frac{d}{2}\right)^2 * \left(\frac{D}{2}\right)^2\right)$. The diameter of the np is assumed to be equal to $d' = \left(2 * \sqrt{\left(\frac{A}{\pi}\right)}\right)$.

Both size distributions may be described by log-normal laws. It is worthy to notice that more than 50% of the nanoparticles have diameters in the size range [10 nm-30 nm], while more than 50% of the nanoparticles deformed at 5 GPa have diameters in the size range [30 nm-40 nm]. Such discrepancy is not really surprising when considering granular stacking. Indeed, the smallest nanoparticles are more likely positioned in the voids between the biggest nanoparticles ([100 nm -200 nm]), which form the stacking arches. As a consequence, the smallest nanoparticles are less likely to encounter any force and undergo any deformation.

At this stage, one has to mention that the biggest deformed nanoparticle in the sample compacted at 5 GPa has a diameter of 89 nm, which is far smaller than the maximum nanoparticle size. This can be explained by the fact that the local pressure is higher on smaller nanoparticles than on bigger ones. So 5 GPa may not be a large enough pressure to deform larger nanoparticles.

Indeed, similar analyses of the samples compacted at 5, 15 and 20 GPa in DAC reveal that at 15 and 20 GPa, almost all nanoparticles are deformed, including the biggest ones (and the smallest ones), as shown in ***Figure 89*** .

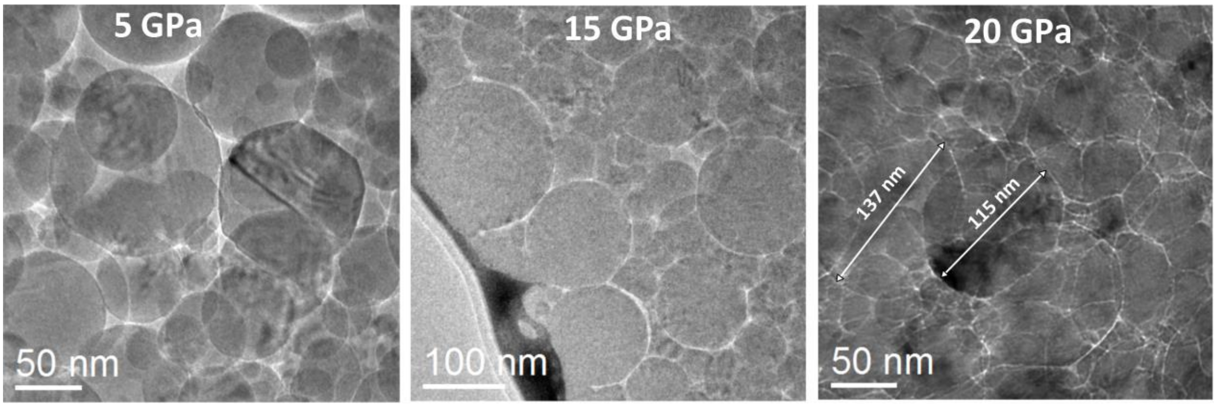

Figure 89: TEM images of thin foils prepared from samples compacted at 5, 15 and 20 GPa. Transition alumina nps undergo plastic deformation at room temperature and the population and sizes of deformed nps become more important at high pressures.

Finally, as bulk alumina is known to be brittle at room temperature, it is worthy to notice that almost no fracture could be observed in the nanoparticles, even after compaction at 20 GPa.

This is known to be a consequence of the DAC configuration, which favors plastic deformation of materials and exclude possible fractures.

In the sample compacted at 20 GPa, facets are observed to be parallel to each other and to the principal solicitation force (see *Figure 90*).

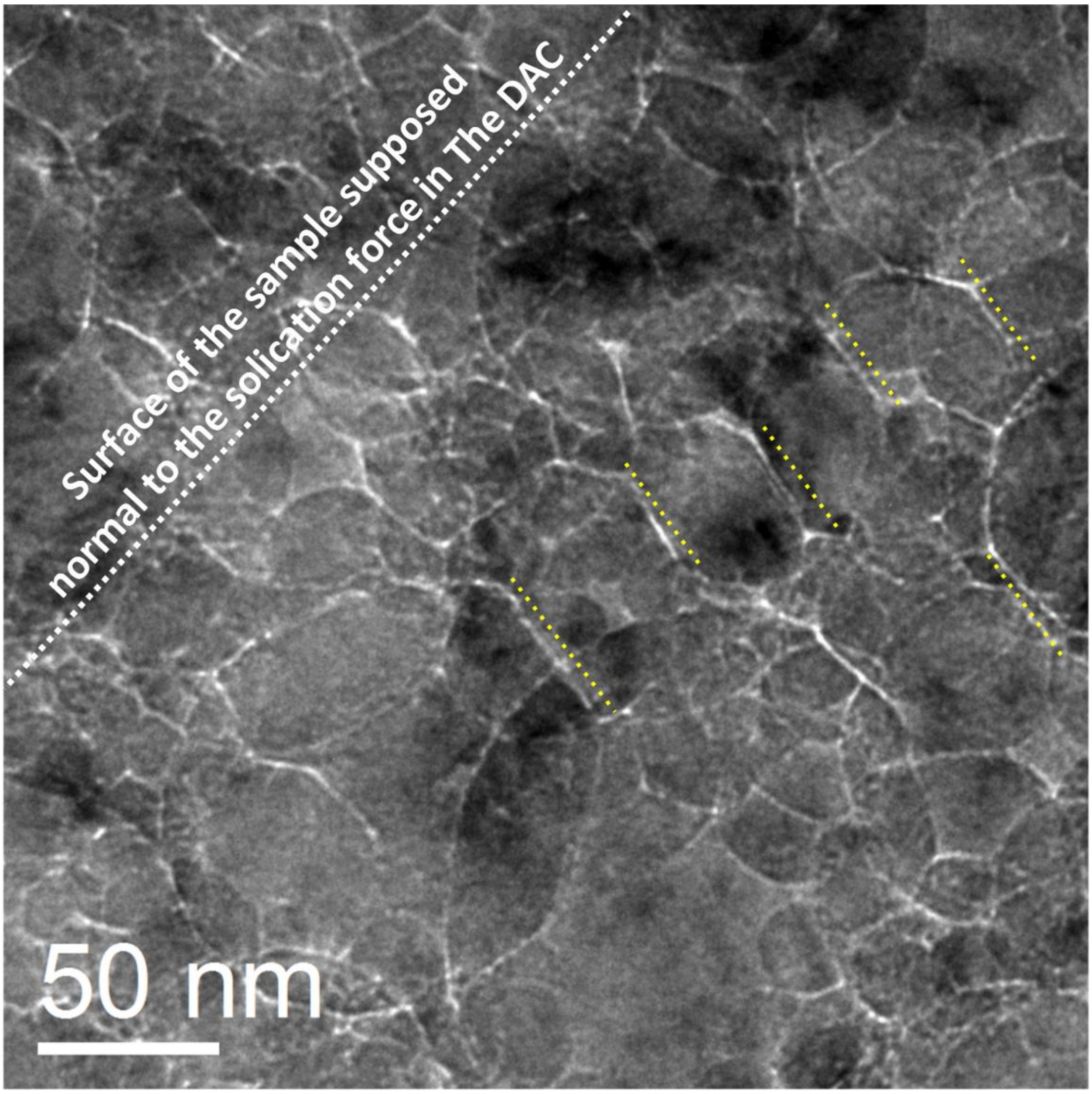

Figure 90: TEM image of the sample compacted at 20 GPa showing texture. Facets are observed parallel to the solicitation force direction.

This texture is observed until 1µm below the sample surface (see *Figure 91*). Below this depth, the texture is more likely to be localized in small domains of several nanoparticles. These domains are not perfectly aligned one to other. This is due to the fact that the uniaxial force of the DAC becomes less uniaxial at a certain distance below the surface (formation of arches in the granular assembly of nanoparticles). Here this distance is estimated to be more or less 1 µm.

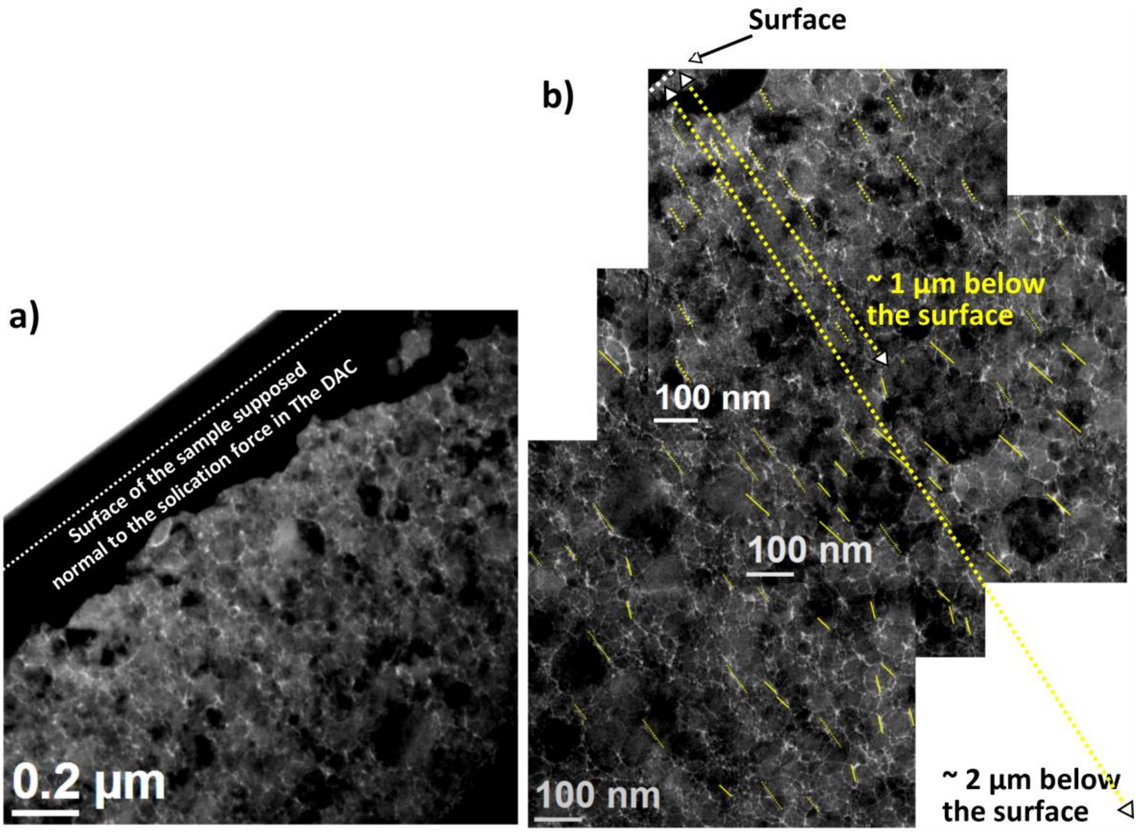

Figure 91: a) *TEM image of the zone directly below the surface.* ***b)*** *Series of TEM images of the sample compacted at 20 GPa from the zone directly below the surface, showing texture until ~ 1 µm below the surface. Facets are observed parallel to the solicitation force direction.*

5.1.2. Crystallographic Texture

Series of HRTEM images are taken of the surface contacts between two deformed nanoparticles on samples compacted at 5 GPa, 15 GPa and 20 GPa, Fourier Transform (FT) reproducing diffraction pattern of specific zone are indexed. Indexations are based on inter-reticular distances and angles between planes. One must mention that the density of the sample compacted at 15 GPa is very high and at 20 GPa no porosity is observed. Because of the high density of the sample compacted at 20 GPa, it is hardly possible to perform high resolution imaging. Few HR images are taken on this sample. As a consequence, classical selected area diffraction patterns of the sample compacted at 20 GPa are acquired and indexed. JCPDS files used for indexation of diffraction patterns can be found in **appendix 2, 3 and 4.**

- **At 5 GPa**

Representative images of the sample compacted at 5GPa are displayed in ***Figure 92*** with the corresponding FT of a squared zone in nanoparticles. All the deformed nanoparticles are found to be in the γ-phase at 5 GPa (see ***Figure 92***). Interestingly, a preferred crystallographic orientation is observed for the deformed nanoparticles in both samples (compacted with DAC and Belt apparatus).The planes {220} of the γ phase of Transition Alumina are indeed found to be parallel to the surface contact with the neighbor nanoparticle. This preferential crystallographic orientation, with the {220} planes parallel to the contact surface, is reproduced in almost all indexed HRTEM images of deformed nanoparticles with clear contact surfaces (see ***Figure 92***).

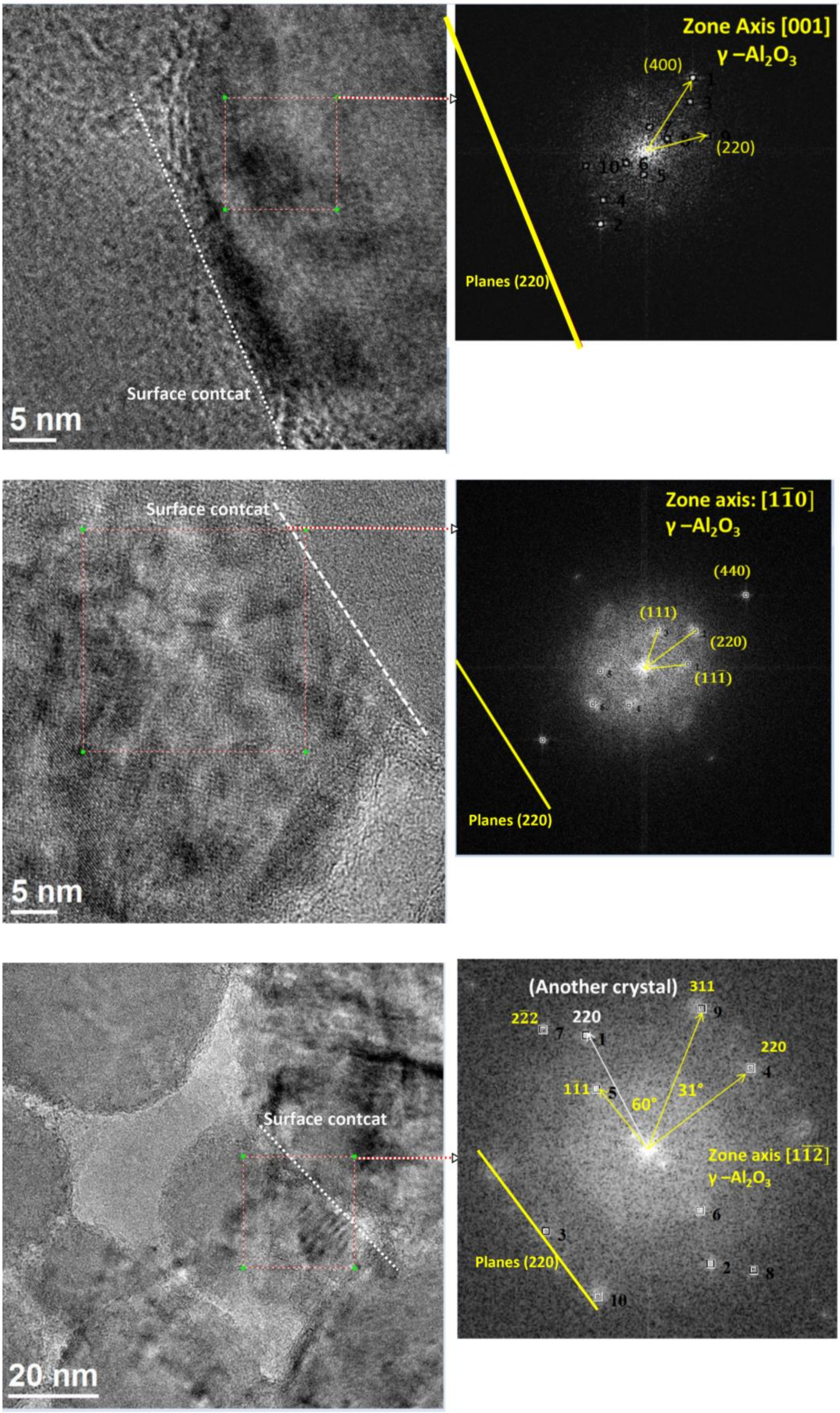

***Figure 92** HRTEM images of deformed nanoparticles of the sample compacted at 5 GPa. The indexation of the Fourier Transform reveals the phase γ-Al_2O_3 with preferred crystallographic orientation of planes {220} parallel to the surface in contact with the neighboring nanoparticle.*

HRTEM are performed mainly on deformed nanoparticles. Even though these HRTEM images reveals that nanoparticles deformed at 5GPa are mainly γ-Al_2O_3, but Debye Scherrer pattern performed on a wide zone of the sample shows that δ^*-Al_2O_3 could be identified (see *Figure 93*).

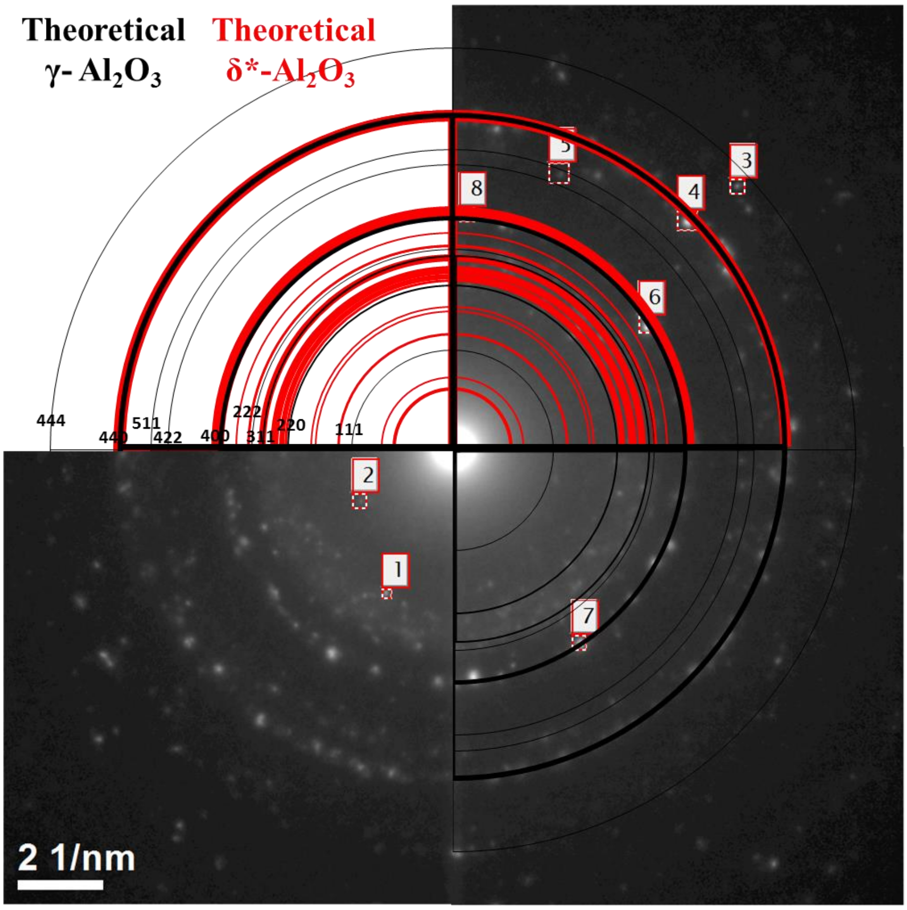

Figure 93: *Debye Scherrer of the sample compacted at 5GPa. Both phases*γ-Al_2O_3, δ^*- Al_2O_3 are identified.

However δ^*-Al_2O_3 is not identified in the deformed nanoparticles observed in HRTEM. ***Thus, one can suggest that at 5 GP, δ^*- Al_2O_3 nanoparticles did not undergo plastic deformation but only the γ-Al_2O_3 nanoparticles did. However, a larger statistics from HRTEM images should provide more information (9 deformed nanoparticles are indexed in HRTEM as γ-Al2O3, all showed a preferential {220} orientation parallel to the surface in contact with the neighboring nanoparticle).***

- **At 15 GPa**

Series of HRTEM images of the deformed nanoparticles in the sample compacted at 15 GPa indicate that the deformed nanoparticles are γ-Al_2O_3 and δ^*-Al_2O_3. For almost all nanoparticles identified as γ-Al_2O_3, again, a preferred crystallographic orientation is observed with the planes {220} parallel to the surface in contact with the neighboring nanoparticles. ***Figure 94*** displays a representative HRTEM image of these nanoparticles. Both deformed nanoparticles are presenting a preferred crystallographic orientation with their planes {220} parallel to their contact surface (white dotted line). The insets correspond to Fourier Transforms indexed for each nanoparticle. Moreover, in this HRTEM, the nanoparticle on the right (bordered by the dotted white and yellow lines) shows facets at ~120° which represents an angle between {220} planes. This indicates that the facets of this nanoparticle are oriented along {220} planes. Moreover, planes {220} are parallel to the surface in contact with the neighboring nanoparticle in the upper left corner of the image. In fact, this type of γ-Al_2O_3 nanoparticles presenting facets oriented along {220} in the sample compacted at 15 GPa is reproducible.

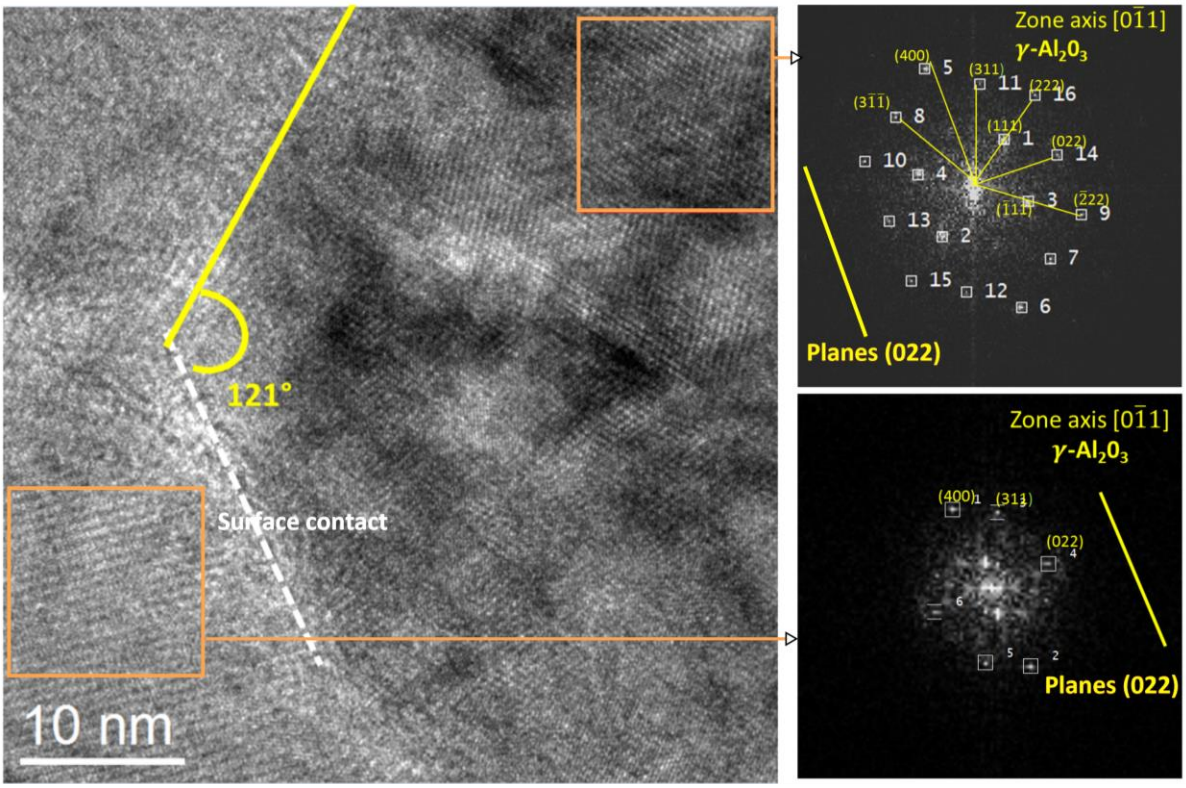

__Figure 94:__ HRTEM image of deformed nanoparticles of the sample compacted at 15 GPa. The indexation of the Fourier Transform reveals the phase γ-Al_2O_3 with preferred crystallographic orientation of planes {220} parallel to the surface in contact with the neighboring nanoparticle.

Other deformed nanoparticles could be indexed as δ^*-Al_2O_3. No preferential crystallographic orientation could be observed in those nanoparticles. However in this sample the number of deformed nanoparticles indexed as δ^*-Al_2O_3 exceeds somehow the number of nanoparticles of γ-Al_2O_3 (10/8) in comparison to the sample compacted at 5GPa where only deformed nanoparticles with γ phase could be indexed. ***Table 9*** summarizes all phases indexed in the 15 GPa sample with eventual preferential crystallographic orientation.

Table 9: summary on the crystallographic phases and eventual preferred crystallographic orientation in the sample compacted at 15 GPa.

	Number of nps	Specific crystallographic orientation
γ-Al_2O_3	**8**	**{220} // contact surface**
δ^*-Al_2O_3	**10**	**none**
Mixed nanoparticles	**2**	

From the above-mentioned observations, we suggest that phase transformation from γ-Al_2O_3 to δ^*-Al_2O_3 occurs at high pressure. If so, we assume that planes $\{220\}_\gamma$ will correspond to certain planes $\{hkl\}_{\delta*}$. Calculations for the corresponding $\{hkl\}_{\delta*}$ are made and presented in **appendix 5.**

In fact, we can rarely observe $\{hkl\}_{\delta*}$ planes corresponding to $\{220\}_\gamma$ ones. For example in ***Figure 95***-a, we studied the zone in contact between two deformed nanoparticles. Two white lines show the TEM image rotation by 30° when increasing the magnification from 100K to 120K (***Figure 95***-b) in order to ensure a good configuration of the planes indexed at high magnification with respect to the contact surface . In ***Figure 95***-c, the Fourier Transform of the red square in the nanoparticle on the left reveal that this nanoparticle corresponds to δ^*-Al_2O_3. We can draw the possible orientation of planes $(023)_{\delta*}$, normally at 60° from planes $(220)_{\delta*}$ and we observe that the former planes are parallel to the surface in contact between both nanoparticles. Relying on the calculations presented in **appendix 5**, planes $(023)_{\delta*}$ could correspond to planes $(022)_\gamma$ if we assume that this nanoparticle undergoes phase transformation from γ-$Al_2O_3$to δ^*-Al_2O_3 at high pressure.

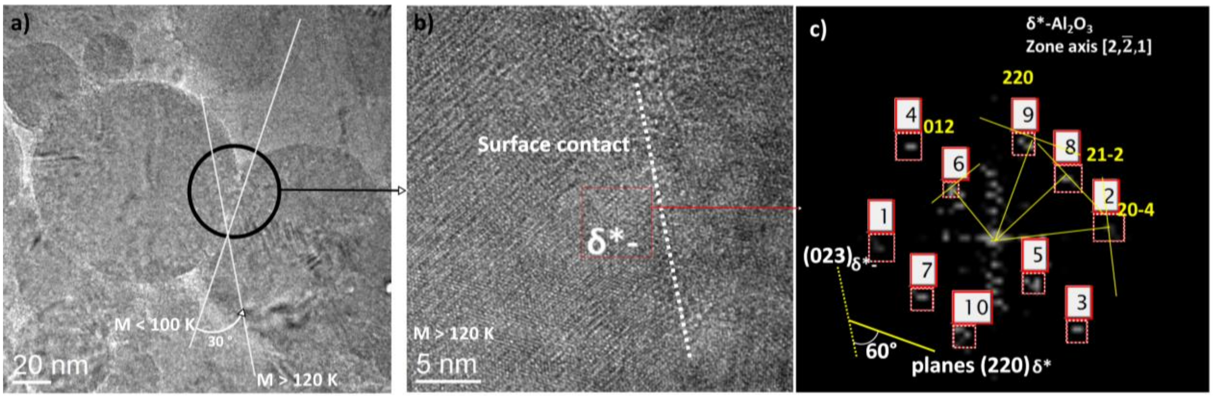

Figure 95 a) *TEM image of two deformed nanoparticles of the sample compacted at 15 GPa. The Magnification (M) is less than 100K.* ***b)*** *HRTEM image of deformed nanoparticles with the white dotted line indicating the contact direction at a magnification higher than 120K. The indexation of the Fourier Transform reveals the phase* δ^*-Al_2O_3.

Moreover, mixed nanoparticles are observed, with δ^*-Al_2O_3 and γ-Al_2O_3 found together in the same nanoparticle. The nanoparticle surfaces are supposed to be zones that experience high friction with the neighboring nanoparticle surfaces. As a consequence, one can assume that a higher energy is supplied to nanoparticle surfaces. If a phase transition occurs, it is thus supposed to start first near the surface. This is observed in one nanoparticle, where the core of the nanoparticle is indexed as γ phase (with planes {220} parallel to the surface contact) while the contact surface is indexed as δ^*phase. Surprisingly, one nanoparticle shows the inverse. In ***Figure 96***, HRTEM images of two zones of a deformed nanoparticle are studied. The zone near the surface contact is indexed as γ phase and the zone near the core is indexed as δ^*phase.

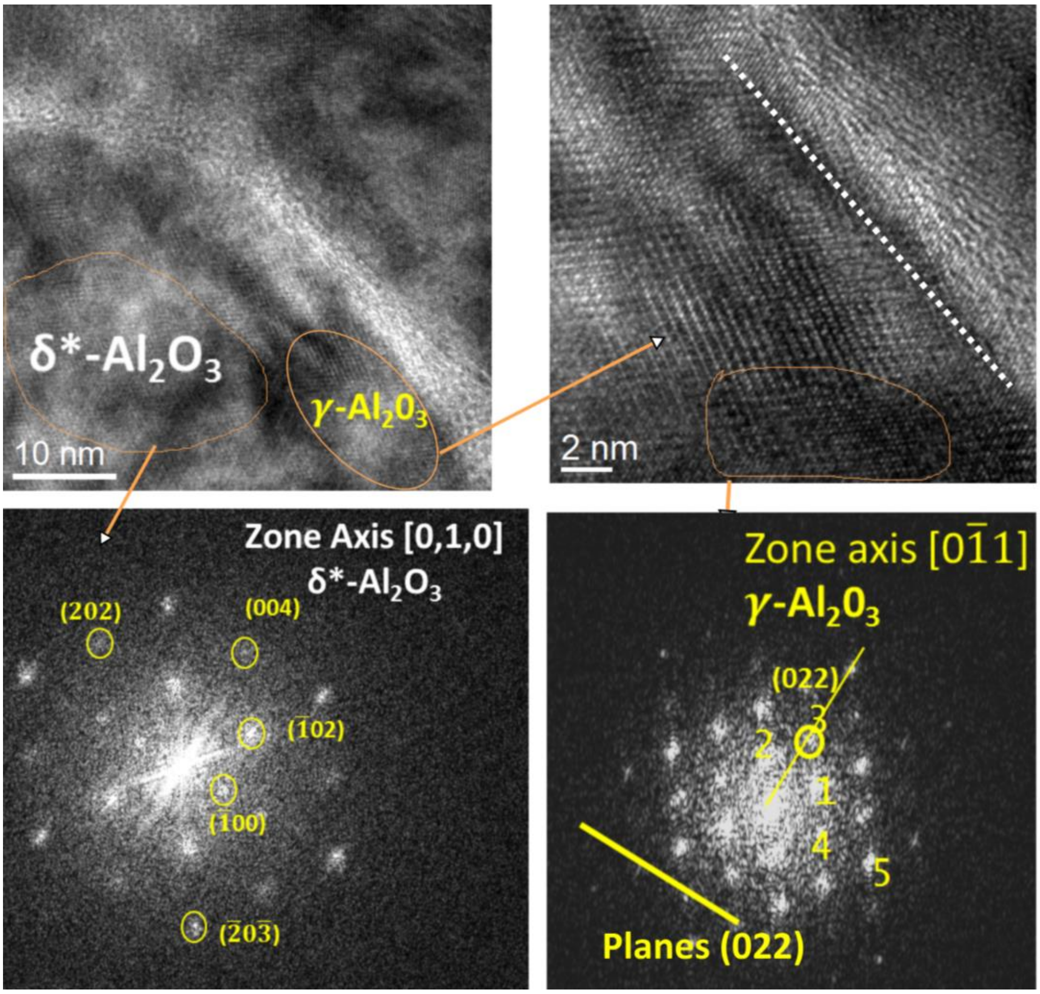

Figure 96 *HRTEM image of deformed nanoparticle. Two zones are studied and corresponding FT indexation reveal the phase* **δ^***-Al_2O_3 *near the core of the nanoparticle and the phase* **γ**-*Al2O3near the surface.*

Mixed nanoparticles are rare, so we will not conclude on this aspect because we believe that the statistics is not good enough.

- **At 20 GPa**

As far as the sample compacted at 20 GPa is concerned, the superposition of grains in the sample thickness hinders the acquisition of HRTEM images and/or the indexation of the electronic diffraction patterns. As a consequence, a series of classical selected area diffraction patterns is performed on several nanoparticles of this sample. Note that in this sample; almost all nanoparticles undergo plastic deformation. Diffraction patterns of several nanoparticles reveal that some nanoparticles are in the γ-phase with a clear texture . Indeed, {220} planes are found to be parallel to the solicitation direction in DAC or sometimes parallel. In general in a cubic system, {220} are 12 planes. For each plane from the family {220}, there is another plane from the same family that is parallel to it and two others that are perpendicular to it. The 8 remaining planes are either at 120° or 60°. This is shown in the ***Table 10***.

Table 10: *Angles between planes {220} of a cubic system*

	Planes {220}	Angle with (220)
(220)	(202)	60°
	$(\bar{2}02)$	120°
	$(20\bar{2})$	60°
	$(\bar{2}0\bar{2})$	120
	$(\bar{2}20)$	90°
	$(2\bar{2}0)$	90
	$(\bar{2}\bar{2}0)$	180
	(022)	60°
	$(0\bar{2}2)$	120°
	$(02\bar{2})$	60
	$(0\bar{2}\bar{2})$	120

One must mention that these classical diffraction patterns are not easy to index. The smallest selection area aperture of the TEM is often bigger than the desired nanoparticle. Thus diffracting planes from other nanoparticles can be involved in the diffraction pattern, which may pose ambiguities on indexation and analysis.

Figure 97 displays a typical diffraction pattern of nanoparticles that are identified as γ-Al_2O_3. Indexation of the diffraction pattern is based on verification of angles and inter-reticular distances but is also compared to Debye-Scherrer rings of γ-Al_2O_3. The planes {440} seem parallel to some facets in the nanoparticle (bold lines parallel to facets of the particle, ***Figure 97***). Two planes of this family are parallel to the surface of the sample, which is supposed to be perpendicular to the solicitation direction. However the diffraction pattern contains no diffraction spot corresponding to planes that are parallel to the solicitation direction. This could be due to the fact that we have only a 2D image/diffraction pattern of a 3D sample. Nevertheless, as mentioned above, we may conclude that such planes exist. In fact the dotted lines in the TEM image in ***Figure 97*** are planes at 90 ° to the planes which are parallel to the surface of the sample. The angles between such planes are equal to the angles between {220} planes. Thus it can reasonably be considered that {220} planes of nanoparticles are parallel to the solicitation direction.

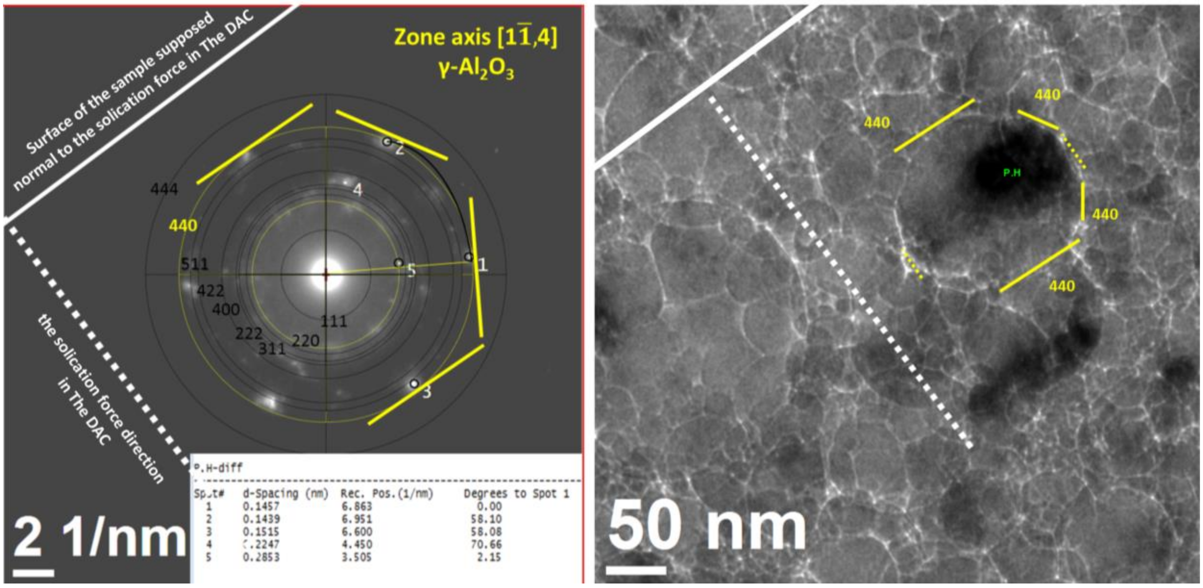

```
P.H-diff
-----------------------------------------------------------------
Spot#    d-Spacing (nm)  Rec. Pos.(1/nm)     Degrees to Spot 1
  1      0.1457          6.863                  0.00
  2      0.1439          6.951                 58.10
  3      0.1515          6.600                 58.08
  4      0.2247          4.450                 70.66
  5      0.2853          3.505                  2.15
```

Figure 97: *Selected area diffraction pattern of a selected particle shown in the TEM image at the right.*

The analysis on {220}γ planes can also be performed on Debye Scherrer patterns, acquired on a large number of particles. One of these Debye-Scherrer patterns is displayed in ***Figure 98***. The indexation clearly revealed the presence of the γ-phase. Moreover, the intensity along the {220}γ ring is not constant but maxima can be detected, which correspond to a preferential crystallographic orientation. By taking into account the fact that in this image, several nanoparticles are deformed, with contact surfaces parallel to each other and parallel to the compression axis, it can be concluded once again that the {220} planes in these nanoparticles are parallel to the contact surfaces, and thus to the compression direction during compaction in the DAC. Moreover it seems from ***Figure 98*** that some nanoparticles show some preferential orientation of the planes {400}, for which the Debye Scherrer ring does not have a uniform intensity. Note that the intensities of the theoretical rings of Debye Scherrer are proportional to the theoretical intensities of diffraction rings obtained with the JEMS software for γ-Al_2O_3.

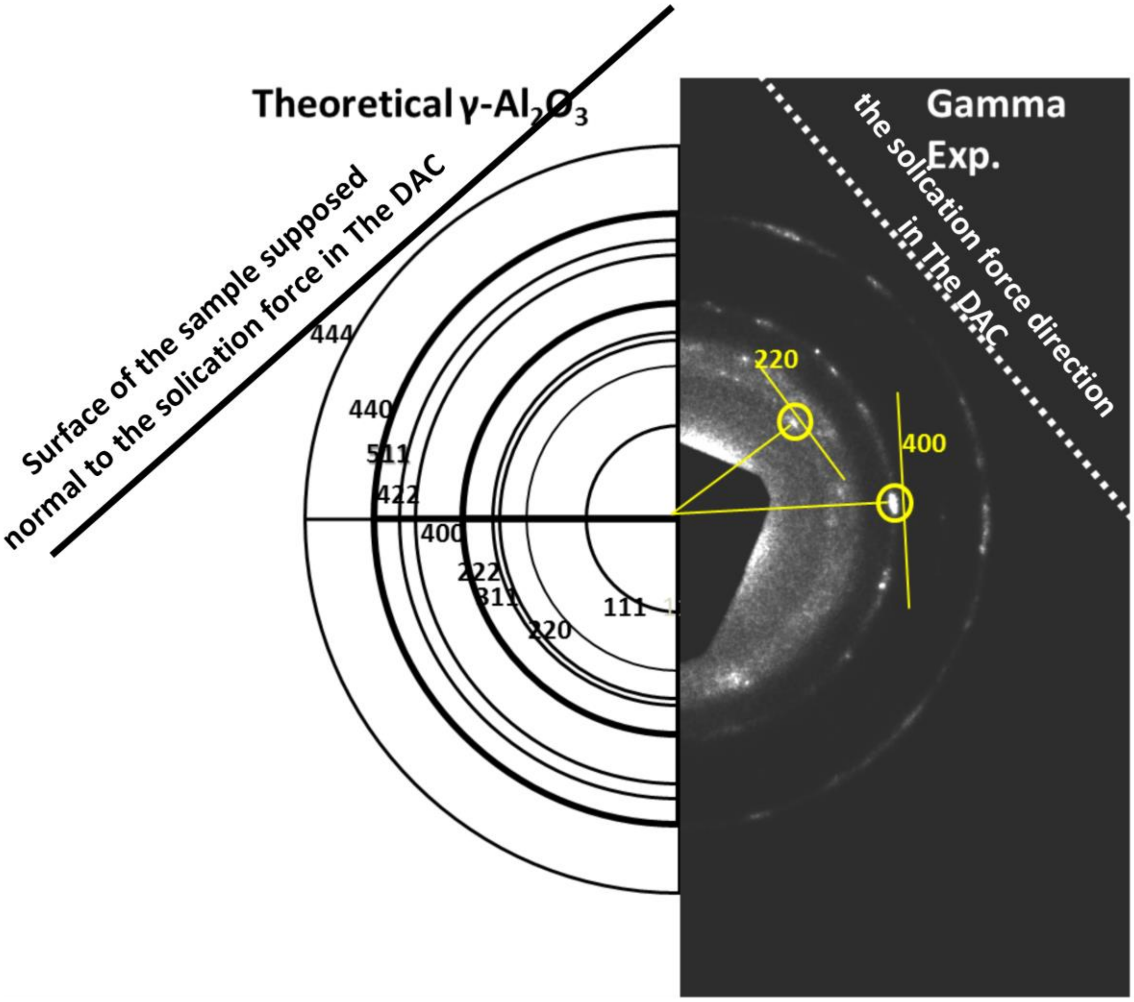

Figure 98: *Theoretical Debye Scherrer pattern of γ- Al2O3 compared with the experimental Debye Scherrer pattern of the sample compacted at 20 GPa.*

Moreover, minor detection of rings corresponding to δ^*-Al_2O_3 and δ-Al_2O_3 can be observed in the Debye-Scherrer pattern. We mention δ-Al_2O_3 because classical diffraction patterns of 5 nanoparticles could be indexed as δ phase. Moreover, a mixed nanoparticle can be indexed with γ- Al_2O_3 in the center of the nanoparticle and δ-Al_2O_3 (or δ*-Al_2O_3) at the surface. This is shown in ***Figure 99***, where the center of the nanoparticle is in the γ phase with {220} planes parallel to the nanoparticle facets. The surface cannot be indexed with the γ phase, and it is hard to decide whether it is δ or δ*.

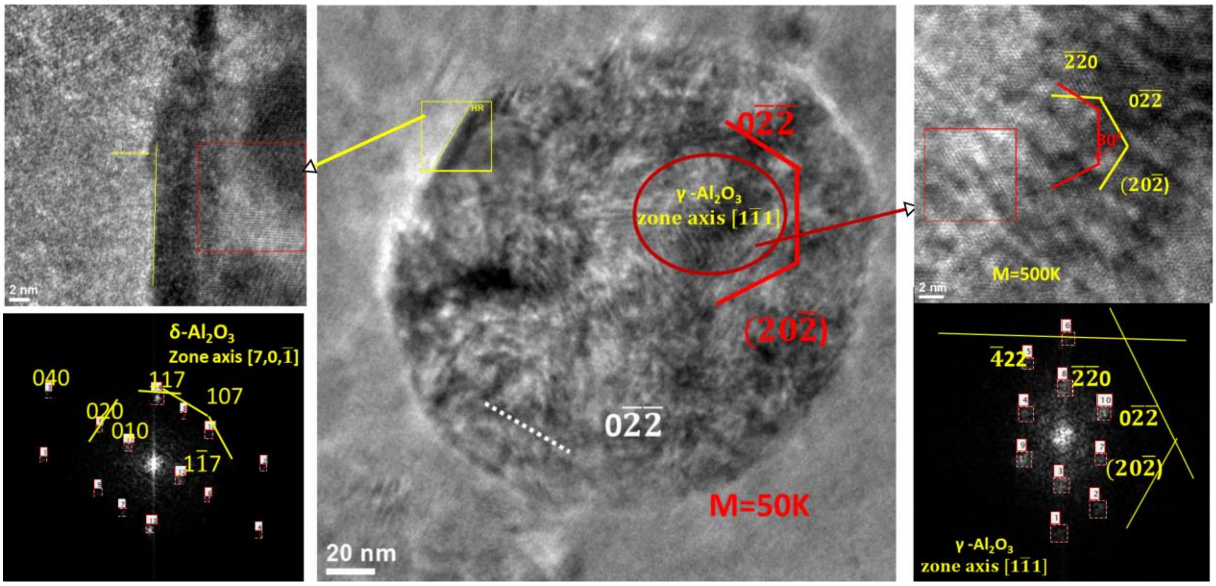

Figure 99: *HRTEM image of deformed nanoparticle. Two zones are studied and corresponding FT indexation reveal the phase* γ*-*Al_2O_3 *near the core of the nanoparticle and the phase* δ^**-*Al_2O_3 *near the surface*

Table 11 summarizes the results obtained from the indexation of classical diffraction patterns of selected nanoparticles in the sample compacted at 20 GPa.

Table 11 *summary on the nanoparticle phases and eventual preferred crystallographic orientation in the sample compacted at 20 GPa.*

	Number of nps	Specific orientation
γ-Al_2O_3	3	3/3: {220}// solicitation axis in DAC
δ^*-Al_2O_3	3	
δ-Al_2O_3	5	3/5: {117} at 20° from the solicitation axis

Figure 100 displays a second Debye Scherrer performed on nanoparticles of the sample compacted at 20 GPa. The theoretical Debye Scherrer pattern of δ^*-Al_2O_3 and γ-$Al_2O_3$are given for comparison. It is clear that the rings that are not compatible with the γ phase are coherent with rings of δ^*-Al_2O_3. In fact, the classical diffraction patterns performed on several nanoparticles reveal that some particles are δ^*-Al_2O_3 and others are δ-Al_2O_3, among γ-Al_2O_3 nanoparticles shown above.

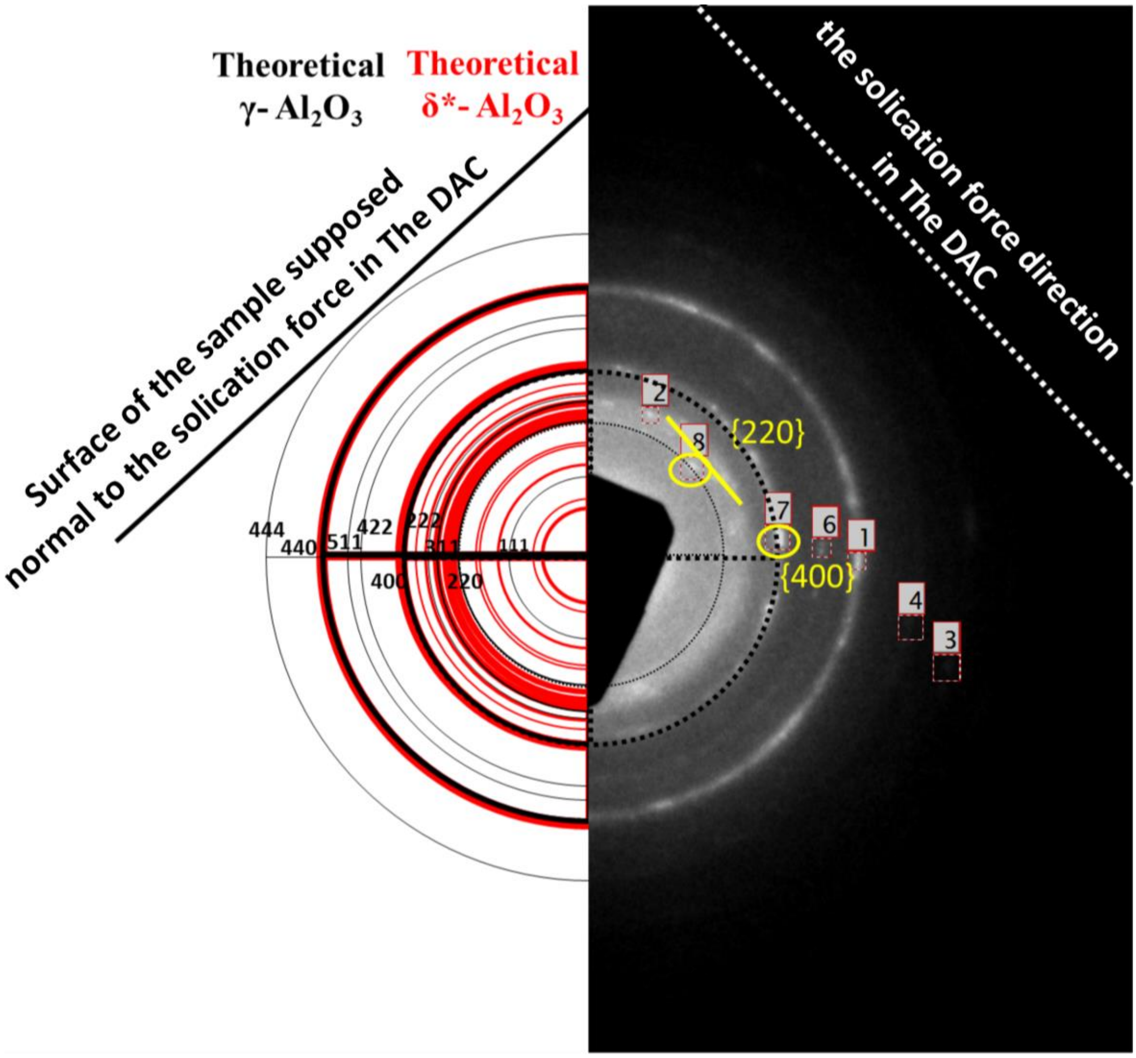

Figure 100 Theoretical Debye Scherrer pattern of γ- Al_2O_3 (black rings) and δ-Al_2O_3 (red rings) compared with the experimental Debye Scherrer pattern of the sample compacted at 20 GPa.*

5.1.3. Conclusion on Texture and Coupling with the behavior of transition Alumina compressed *in situ in* TEM

The texture, observed in transition alumina nanoparticles compacted at 5 GPa and that become more important with increasing pressure in the DAC to 15 and 20 GPa, can be related to thermodynamics and/or mechanical considerations. Unfortunately, the literature is poor on transition alumina studies.

- **Thermodynamics Considerations:**

It was mentioned in the review [*Levin et al. (1998)*] dealing with metastable alumina that: "γ-Al_2O_3 obtained by three processes: thermal oxidation of aluminum containing alloys, by annealing of amorphous anodic Al_2O_3 films, or plasma spraying reproducibly shows preferred crystalline texture with both <100>γ and <110>γ directions preferentially oriented parallel to the surface normal [*Levin (1997)*][*Levin-1998*]". Moreover in this review [*Levin et al. (1998)*] they referred to MD simulations of the surface structure of γ-Al_2O_3 [*S. Blonski (1993)*] where results revealed the following relation between surface energies: $\boldsymbol{\gamma_{\{001\}} < \gamma_{\{111\}} < \gamma_{\{110\}}}$.

These results may explain the {001} preferential orientation but not the {110} observed in the cases cited above or in our case.

However, a more recent work focused on molecular statics and molecular dynamics simulations of surfaces structures of bulk Alumina (α-Al_2O_3) and metastable alumina such as γ-Al_2O_3. The simulations were coupled with characterizations using virtual diffraction methods. [*Coleman. P- et al. (2014)*] showed that at room temperature the relation between surfaces energies of γ-Al_2O_3 planes is the following: $\boldsymbol{\gamma_{\{110\}} < \gamma_{\{111\}} < \gamma_{\{001\}}}$.

This relation may explain a preferential {110} crystallographic texture. Indeed, it is coherent with the {220} crystallographic texture obtained herein with transition alumina compacted in DAC at 5, 15 and 20 GPa. However, Debye Scherrer patterns of nanoparticles compacted at 20 GPa, shown in ***Figure 98***, ***Figure 100***, show a clear preferential crystallographic texture of planes {220} and {400}, i.e. {110} and {100}. However, we believe that the energy supplied to the nanoparticles during compaction in DAC is high enough to explain the observed preferential crystallographic texture by processes other than surface energy considerations. Thus mechanical considerations for this preferential crystallographic texture are also investigated.

- **Mechanical Considerations**

HRTEM and diffraction patterns show a preferential crystallographic orientation of the {220} planes. This texture is observed in three samples of alumina nanoparticles compacted at 5, 15 and 20 GPa. Each time, the {220} planes are parallel to the surface in contact between neighboring deformed nanoparticles. Moreover classical diffraction patterns and Debye Scherrer on large number of nanoparticles compacted at 20 GPa show that the {220} planes are also parallel to the solicitation direction in the DAC.

We would like to mention one more time that within the {220} plane family, when considering one (220) plane there are 2 other planes over 12, which are perpendicular($(2\bar{2}0)$, $(\bar{2}20)$). This indicates that the nanoparticle is deformed along the compression axis <110>. In other words, during the pressure increase from 0 to 5, 15 or 20 GPa, the nanoparticles are free to rotate and accommodate in the configuration that allows deformation of the nanoparticle along the <110> compression axis. Such compression axis appears to be parallel to the direction of the principal force in the sample compacted at 20 GPa. A <110> compression axis allows the activation of the <110> {111} slip system with the highest Schmidt factor. This is compatible with the fact that γ-alumina can be described as a spinel structure as described in **chapter 4**, for which the commonly observed slip system is the <110> {111} [*book-plastic deformation of ceramics-Richard C.Bradt-1995*]. Moreover, HRTEM images were taken on a few nanoparticles containing twins. Twins are usually formed in the dense planes. Indexations of these images show that {111} are the twin planes of γ-alumina (see ***Figure 101***). This also suggests that {111} could be the slip planes of this phase.

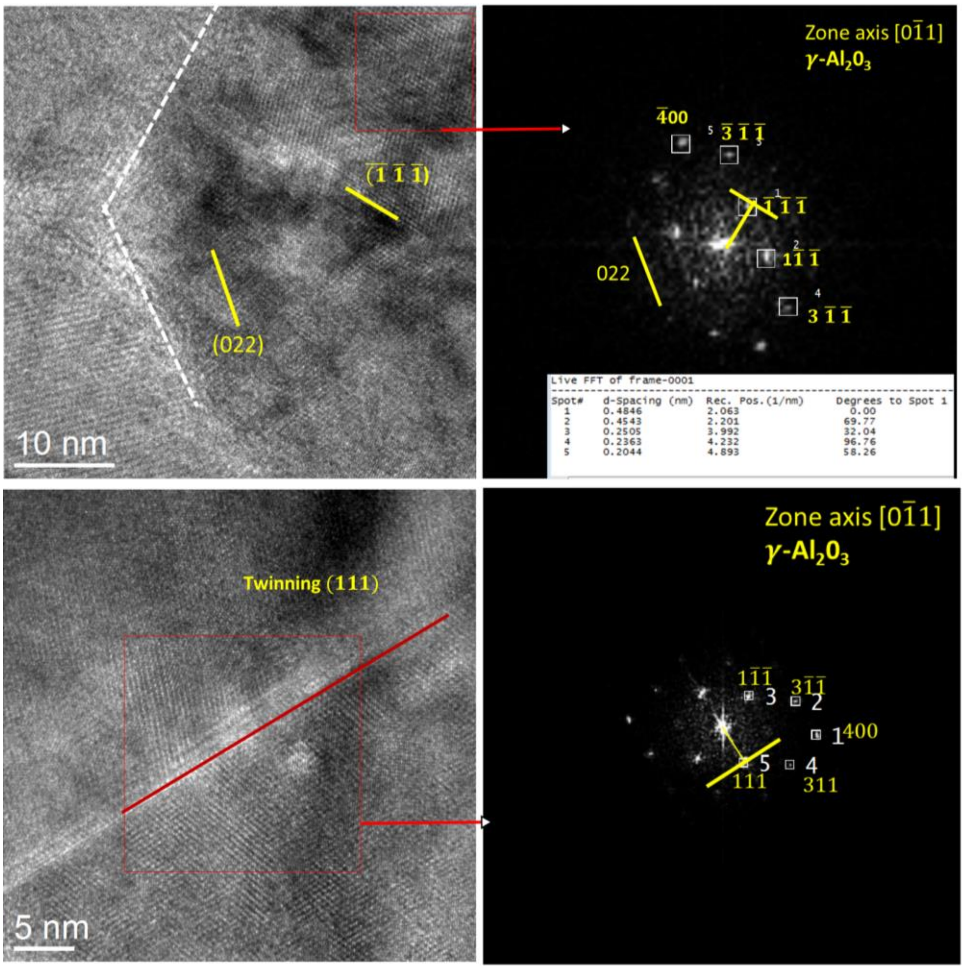

```
Live FFT of frame-0001
--------------------------------------------------------------------------
Spot#    d-Spacing (nm)  Rec. Pos.(1/nm)     Degrees to Spot 1
  1      0.4846          2.063                 0.00
  2      0.4543          2.201                69.77
  3      0.2505          3.992                32.04
  4      0.2363          4.232                96.76
  5      0.2044          4.893                58.26
```

Figure 101: *HRTEM images of nanoparticles showing twins. FT indexations reveal that these twins occurs in {111} planes.*

➔ Coupling with the behavior of isolated nanoparticles compressed *in situ* in TEM

Interestingly, the analysis performed on the nanoparticles compacted in the DAC can bring useful pieces of information on the nanoparticle behavior during the *in situ* TEM nanocompression tests performed by Emilie Calvié during her PhD at MATEIS laboratory. Indeed, similar isolated alumina nanoparticles were tested *in situ* in TEM. The three available tests on these nanoparticles show that during uniaxial compression, slip bands appear during plastic deformation of these nanoparticles (see ***Figure 102***). They are oriented at more or less 35° with respect to the compression axis. This angle represents the angle between {220} and {111} planes in γ-Al_2O_3. By drawing a comparison with the DAC experiments, it can be concluded that the slip bands correspond to the {111} planes and the compression axis to the <220> direction. Thus, if one plane from the family of {220} planes is parallel to the solicitation direction, two others are parallel to the surfaces of the nanoparticle which are in contact with the diamond punch and the sapphire substrate. As a consequence, the nanoparticle is thought to accommodate by rotating from its initial random orientation to a preferential orientation, where a (220) plane becomes parallel to the compression axis, see ***Figure 102***. One must mention that movies acquired on these nanoparticles tests show often a slight rotation of the nanoparticle at the early beginning of the compression test. This orientation then permits the activation of the <110> {111} slip system dominant in a spinel structure.

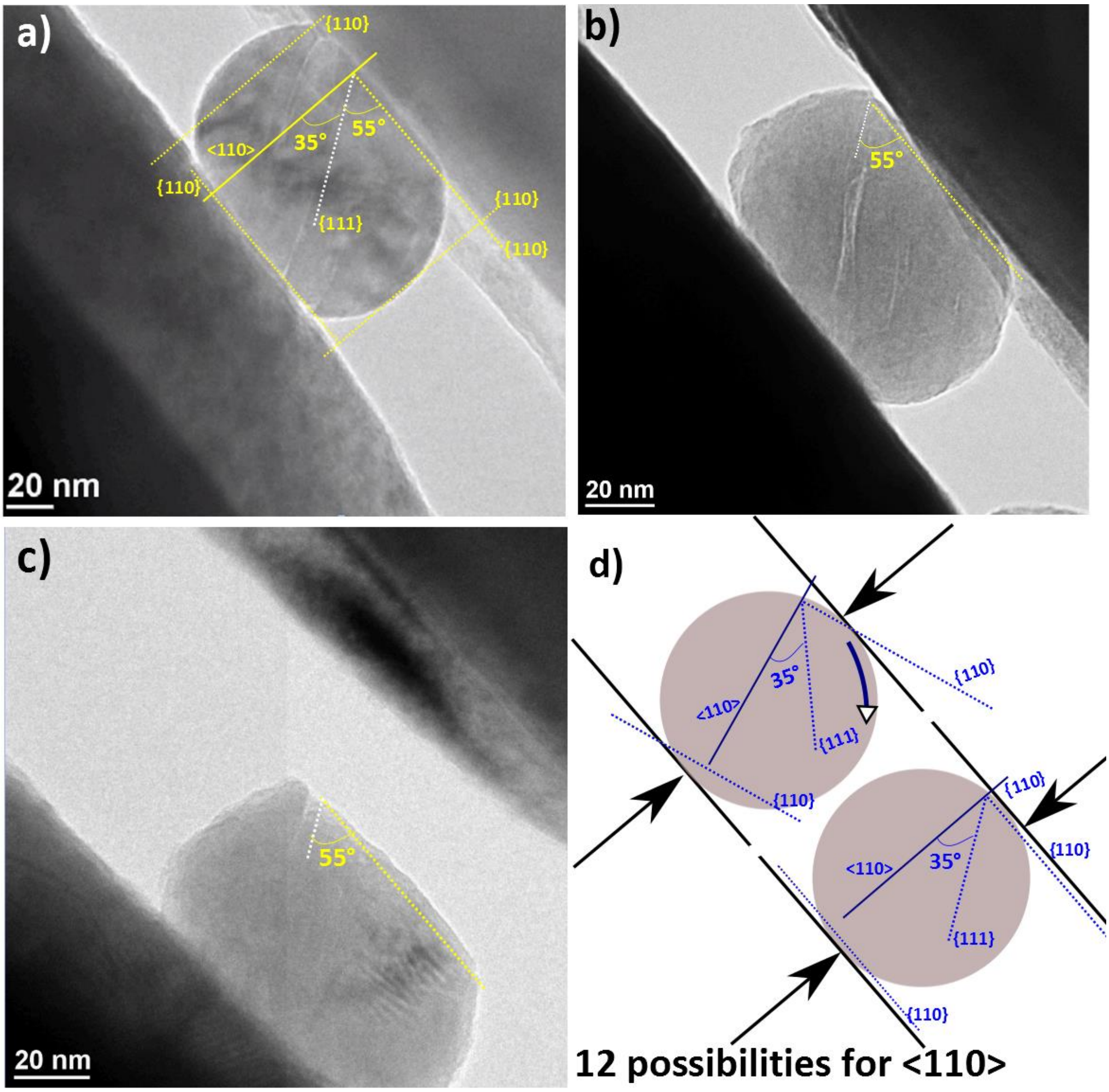

Figure 102:a-b-c) *The three available tests on nanocompression of transition alumina nanoparticles show that during uniaxial compression, slip bands appear during plastic deformation of these nanoparticles oriented more or less 35° with respect to the compression axis.* ***d)*** *Nanoparticles are thought to accommodate by rotating from its initial random orientation to a preferential orientation, where a (220) plane becomes parallel to the compression axis. Thus the latter is along <110>. Slip planes {111} with a highest Schmid factor accommodate the deformation.*

5.2 Phase Transformation

As mentioned before, the initial powder of nanoaprticles compacted in DAC, consists approximately of 70% γ-Al_2O_3 (Face-Centered-Cubic) and 30% δ*-Al_2O_3 (tetragonal).

On the sample compacted at 5GPa, TEM images have been taken on deformed nanoparticles only. These nanoparticles are indexed and identified as γ- Al_2O_3, all with the previously mentioned preferential {220} crystallographic orientation. On the sample compacted at 15 GPa, γ-alumina is detected with the preferential crystallographic orientation, but the δ*-alumina phase (orthorhombic) is also evidenced in deformed nanoparticles. This orthorhombic phase is an intermediate phase between γ-alumina and δ-alumina, as cited in the sequence of phase transformation of metastable alumina polymorphs based on Face-Centered-Cubic packing of oxygen anions (γ, δ, θ…). One must mention here that these transformations between metastable alumina consist in a reordering of aluminium cations sublattice that migrate from tetrahedral sites into vacancies in octahedral sites and settle into the new configuration. These are displacive transformations that do not need a high activation energy. They can occur at low temperatures contrary to the the transformation from a metastable alumina phase to the thermodynamically stable alumina α-phase (rhombohedral - hcp packing of oxygen anions- stable phase of alumina at bulk), for which a high activation energy is needed.

However, no preferential crystallographic orientation is detected in the nanoparticles compacted at 15 GPa and indexed in the δ*-phase. As a consequence, it is difficult to state whether the δ*-phase was present in the initial nanoparticles, or if it results from phase transformation of nanoparticles initially in the γ-phase.

The answer fortunately comes from a few nanoparticles, which contain both phases. An example was given in ***Figure 99***, which centre is in the γ-phase, with a preferential orientation of {220} planes parallel to the surface in contact with the neighbouring nanoparticle. However, in the contact area, the crystallographic phase is found to be δ* or δ. The existence of such nanoparticles strongly suggests that the δ*-phase is created from the γ-phase during compaction at room temperature, with an applied pressure of 15 GPa and 20 GPa (knowing that the local pressure, in the contact area, may be far higher than 15 and/or 20 GPa).

These analyses are reinforced with a study performed on the evolution of the diffraction spectra in three samples: initial powder of, and both samples compacted at 5 and 20 GPa in DAC.

The diffraction patterns of the powder could reveal the fraction of each phase present in the sample. Thus getting diffraction patters in those three samples could reveal the evolution of each fraction and prove if a possible phase transformation occurs with increasing pressures in the DAC.

However, in samples compacted in DAC, we could not acquire XRD diffractogram. This is due to the depth of the hole drilled in the imprint in the steel gasket where transition alumina is compacted in DAC. This depth (~ 60 µm, See ***Figure 103***) hinders the focus of the X-ray beam on the compacted transition alumina only, especially for angles 2θ in the range [44°-48°] where the phases δ* and γ can be identified separately and the proportions between these two phase can be studied. As a consequence, the XRD diffractogram contain a huge background coming from the steel gasket and useful signal was not significant.

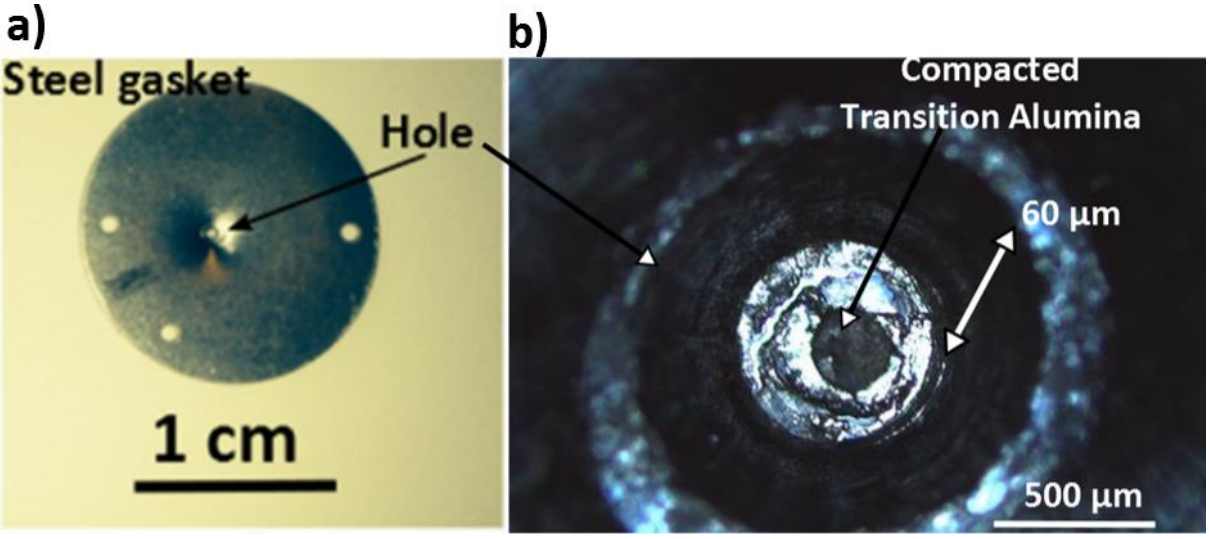

Figure 103: ***a)*** *the steel gasket where the hole is drilled in the imprint present in the middle* ***b)*** *optical microscopy image of the imprint and the hole drilled in the middle where transition alumina powder is compacted. The depth of the imprint is of ~60µm.*

Fortunately, we can quantify the diffraction patterns obtained by electron diffraction in TEM. This is performed on the initial powder and on the thin foils prepared by FIB from compacted transition alumina in DAC (5 and 20 GPa), on which HRTEM observations were taken and presented (see **section 5.1).**

For each sample, Debye Scherrer patterns performed on large number of nanoparticles is transformed into diffraction profiles (*Digital Micrograph® option: Interactive Rotational profile*). These profiles represent the intensities of diffraction rings plotted in function of the inverse of the inter-reticular distance (nm^{-1}).

In order to quantify the presence of γ-Al_2O_3 and δ^*-Al_2O_3, we calculate the theoretical electron diffraction profile. First, it is used to find the inter-reticular distances (d^{-1}) for which the peaks of each phase can be identified separately. Secondly, it is used to investigate the evolution of these peaks in different samples, i.e. in function of the pressure. In other words if we assume that a phase transformation occurs in the sequence γ-Al_2O_3→ δ*-Al_2O_3, one can expect that the intensities of the peaks relative to δ*-Al_2O_3increases. In order to calculate the theoretical electronic diffraction profiles, we used data from JEMS software. The structural parameters of γ-Al_2O_3 and δ*-Al_2O_3 are those mentioned in **chapter 4.**

For each phase, we have calculated the theoretical diffraction intensities for all crystallographic planes which can be detected by electron diffraction, for one unit cell as following:

$$I_e = L * F^2 * D * m \qquad \text{Eq. 4}$$

with:

- $\boldsymbol{I_e}$: Intensity of electronic diffracted beam by an *hkl* plane.
- $\boldsymbol{L}$: Lorentz factor $\propto \frac{1}{\sin 2\theta} \propto \frac{1}{\theta}$, where θ is the Bragg angle for diffraction of a specific plane (*hkl)* of inter-reticular distance d ($2d\sin\theta=\lambda$ → small electronic diffraction angles and thus $2\theta=\lambda d^{-1}$).
- $\boldsymbol{F}$: Structure factor ∝ $\boldsymbol{A}$: Amplitude
- $\boldsymbol{D}$: Debye-Waller factor ≈ $e^{-\beta(\frac{1}{2d})^2}$, $\beta=0.005$ Å^2. It describes the atomic displacement with respect to the equilibrium position due to a thermal effect.
- $\boldsymbol{m}$: multiplicity of plane (number of possible planes for each *hkl* plane)

We show in ***Table 12*** the calculations of the theoretical electron diffraction intensities of *hkl* planes in γ-Al_2O_3. For δ*-Al_2O_3, calculations are shown in **appendix 7.**

Table 12 : *Calculations for theoretical diffraction intensities for (hkl) planes in γ-Al_2O_3*

hkl	***d*** **(nm)**	$\frac{1}{d}$ **(nm-1)**	***A*** **(V|nm|e)**	**θ (mrad)**	**m**	$L \approx \frac{1}{\theta}$	$F^2 = A^2$	$D=e^{-\beta(\frac{1}{2d})^2}$	I_e
111	0,457	2,188183	1,245	2,745	8	0,364298725	1,550025	0,99403269	4,49042046
220	0,2797	3,575259	2,562	4,483	12	0,223064912	6,563844	0,984148875	17,29145577
311	0,238	4,201680	2,054	5,257	24	0,19022256	4,218916	0,978174059	18,84040717
222	0,22837	4,378858	1,876	5,491	8	0,18211619	3,519376	0,976316945	5,006048335
400	0,197	5,076142	6,532	6,34	6	0,157728707	42,667024	0,968304162	39,09904442
422	0,161	6,211180	1,031	7,765	24	0,128783001	1,062961	0,952920835	3,130717889
511	0,152	6,578947	1,461	8,237	24	0,121403424	2,134521	0,94733435	5,891771464
440	0,139	7,19424	6,05	8,967	12	0,111520018	36,6025	0,937351959	45,91425235
444	0,114	8,771929	3,048	10,982	8	0,091058095	9,290304	0,908297382	6,147047022

The intensities are plotted in function of the inter-reticular distances by applying a Gaussian of the form:

$$y = \frac{1}{\sqrt{2\pi\sigma}} * e^{\frac{(x-\mu)}{2\sigma^2}} , \qquad (\sigma = 0.1) \qquad \text{Eq. 5}$$

In this way, the theoretical Debye Scherrer patterns can be converted into theoretical electron diffraction profiles, for one unit cell of γ-Al_2O_3 and δ^*-Al_2O_3. The theoretical Debye-Scherrer pattern and the corresponding profile of γ-Al_2O_3 are displayed in *Figure 104*.

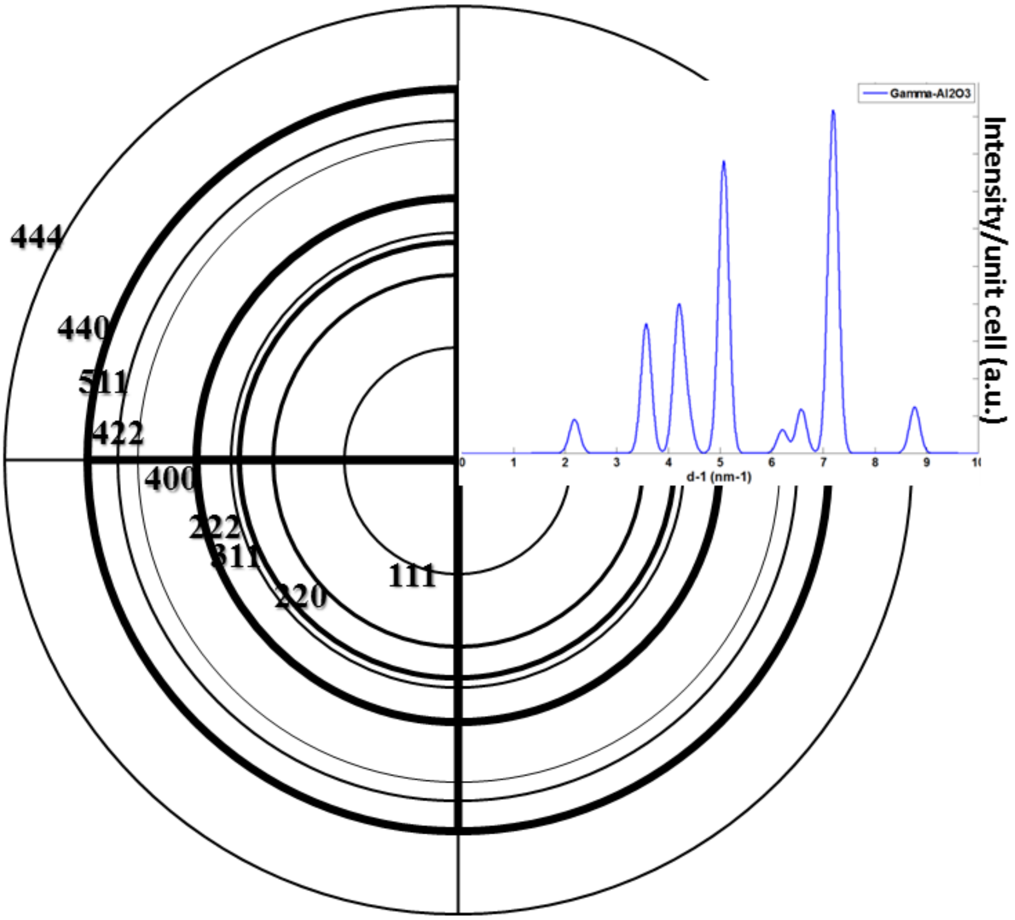

Figure 104 *Theoretical Debye Scherrer pattern related to the theoretical electron diffraction profile of one unit cell of* γ-Al_2O_3.

In order to locate d^{-1} where peaks of γ-Al_2O_3 and δ*-Al_2O_3 can be identified separately, we plot both diffraction profiles of one unit cell of each phase, as in *Figure 105*.

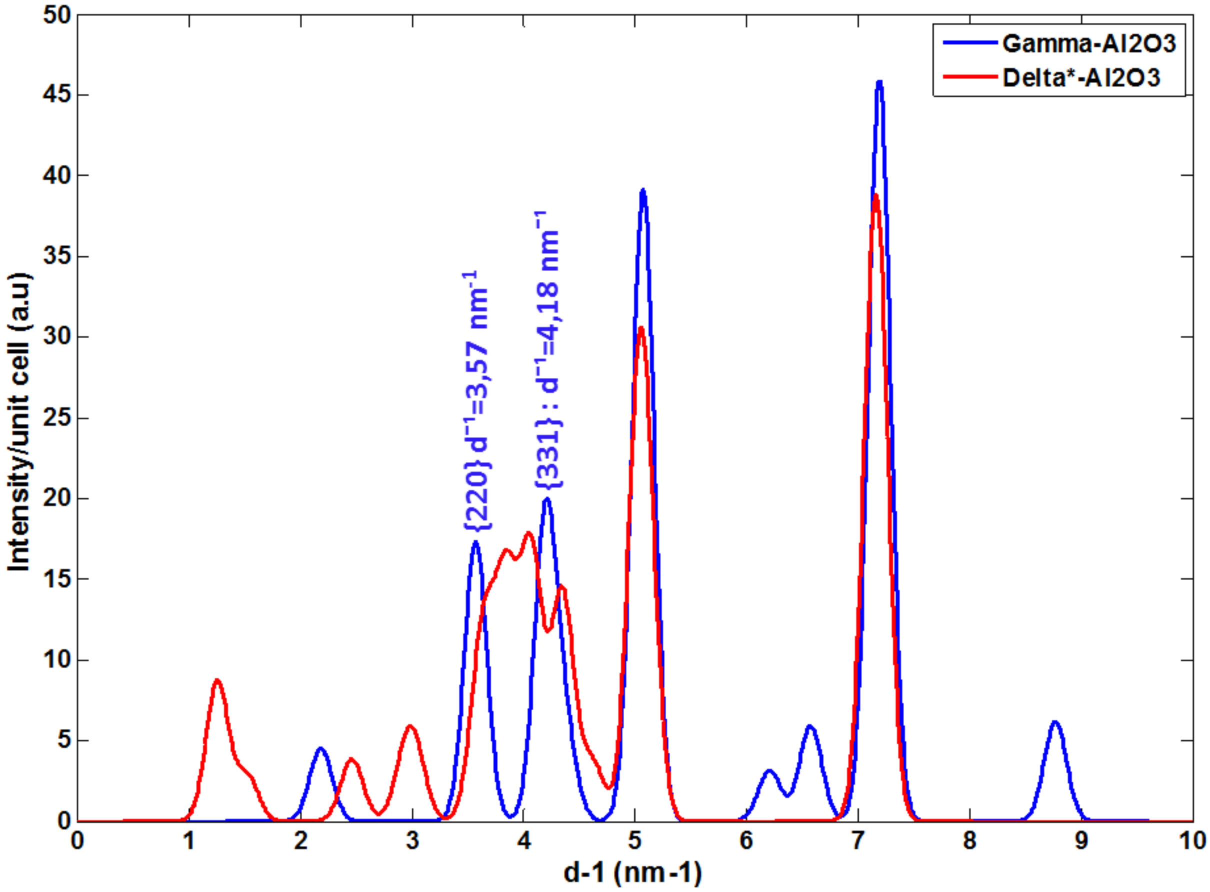

Figure 105 : Theoretical electron diffraction profiles of one unit cell of γ-Al_2O_3 and one unit cell of δ-Al_2O_3.*

It is clear from the theoretical diffraction profiles that many peaks can be used to differentiate γ-Al_2O_3 and δ*-Al_2O_3 phases in the powder electron diffraction. For example, peaks corresponding to large inter-reticular distance (*d*) are interesting. But in experimental Debye Scherrer patterns, these peaks are hidden by the large intensity of the background that becomes very high near the centre of the pattern because of the direct beam. Moreover, for peaks corresponding to small inter-reticular distances, one can see from *Figure 105* that only peaks of γ-Al_2O_3 can be identified separately from those of δ*-Al_2O_3 at d^{-1}=8.72 ;6.57 and 6.17 nm^{-1}. This does not allow an evaluation of the evolution of presence of δ* over γ phase in different samples. Peaks at d^{-1}=3.57 and 4.18 nm^{-1}, respectively corresponding to {220} and {331} planes of the γ phase, are interesting. Indeed, peaks characteristics of the δ* phase can be found between these two peaks relative to the γ phase. One can see that for a powder composed of both phases with similar fractions, the sum of the intensities in the range of d^{-1} [3.57-4.18 nm^{-1}] will result in a large Gaussian peak since the four peaks may be hardly distinguished. On the contrary, a high presence of γ over δ* will clearly show the two peaks higher than those of δ* in this range. Note that for the quantification, one must take into account the unit cell volume of each phase when proportions of phases in a powder are in question. This will be presented later on.

The experimental diffraction profiles obtained on the initial powder (0 GPa) and the samples compacted at 5 and 15 GPa are displayed in ***Figure 106***. Where correction of intensities due to beam stop is applied taking to account its shape (correction of the length of each ring).

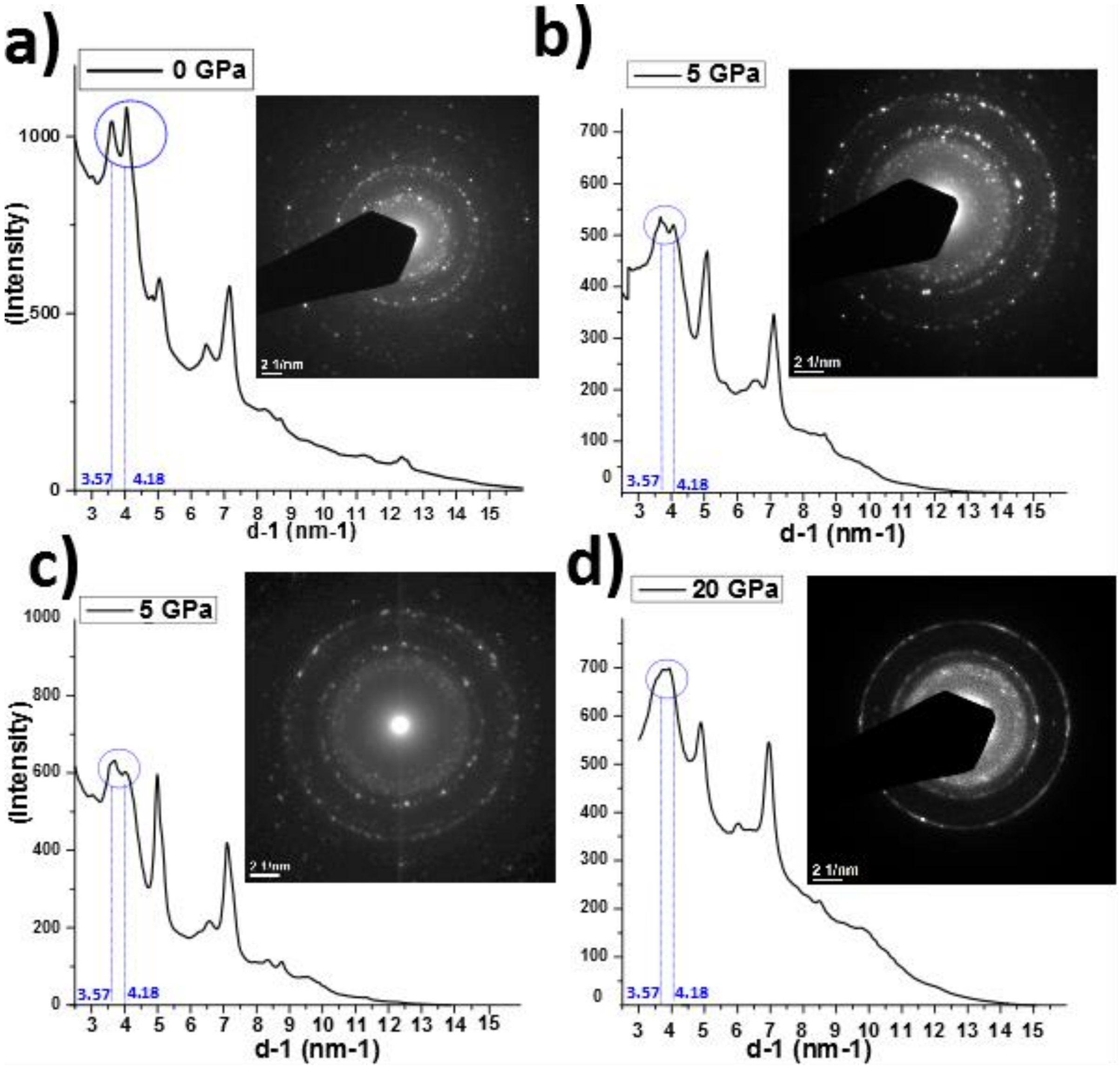

Figure 106: *Experimental diffraction profiles of:* ***a)*** *the initial powder of alumina (0GPa).* ***b)*** *The sample compacted at 5GPa.* ***c)*** *The sample compacted at 5GPa without beam stop.* ***d)*** *The sample compacted at 20 GPa. Note that the intensities in* ***a)-b)*** *and* ***d)*** *are corrected, for* d^{-1} *>2.5* nm^{-1}*, along the beam stop taking into account its shape (correction of the length of each ring).The insets display the Debye Scherrer patterns.*

In the experimental profiles, the background intensity coming from the direct beam is a function of the form: $\boldsymbol{y} = a\boldsymbol{x}^n + b$.

The background intensity becomes very high at large inter-reticular distance, near the pattern center. It is still possible to identify the peaks corresponding to the diffraction of the planes {220} and {311} of the γ-phase in the diffraction profile of the initial powder, see ***Figure 106***-a. The peaks of the δ*-phase in this range of d^{-1} are hardly visible in the experimental profile of the initial powder. ***Figure 106***-b and c display the diffraction profiles of transition alumina nanoparticles compacted at 5 GPa in DAC. one can see that a large Gaussian in the range of d^{-1}[3.57-4.18 nm^{-1}], both peaks characteristic of the γ-phase are less visible in comparison to the initial powder. This may be due to an increase of intensities of peaks of δ*-phase theoretically present between these two peaks of γ and thus making the minima between the peaks of the latter higher. This effect is highly pronounced in the diffraction profile of the sample compacted at 20 GPa, see ***Figure 106***-d. Indeed, the minimum between the peaks relative to the γ-phase at 3.57 and 4.18 nm^{-1} becomes high enough to hinder these two peaks. Once again, we suggest a higher fraction of δ* phase in the sample compacted at 20 GPa.

From a quantitative analysis of the diffraction profiles, it can clearly be concluded that a phase transformation occurs during compaction of transition alumina nanoparticles in DAC, even at 5 GPa. This phase transformation becomes more important when the pressure of compaction in DAC is increased to 20 GPa.

We have tried to quantify the proportion of γ and δ* phases in each sample in order to quantify the effect of pressure of compaction in DAC on the phase transformation. This is performed by calculating the ratio of peak intensities of one phase to the other phase in each sample by following the procedure below:

$$I_{tot} = I_\gamma + I_{\delta*} \qquad \textbf{Eq. 6}$$

- I_{tot}: total intensity
- I_γ: total intensity coming from the γ phase
- $I_{\delta*}$: total intensity coming from the δ∗ phase

Knowing that:

$I_\gamma = I_{\gamma,unit\ cell} * N_{\gamma,cells}$ & $I_{\delta*} = I_{\delta*,unit\ cell} * N_{\delta*,cells}$

with

- $I_{\gamma,unit\ cell}$: intensity of one unit cell of γ phase
- $I_{\delta*,unit\ cell}$: intensity of one unit cell of δ* phase
- $N_{\gamma,cells}$: Number of cells ≈ $\frac{V_\gamma}{V_{\gamma,unit\ cell}}$ & $N_{\delta*,cells}$: Number of cells ≈ $\frac{V_{\delta*}}{V_{\delta*,unit\ cell}}$
- V: volume. $V_{\gamma,unit\ cell}$= 500.4 Å^3 & $V_{\delta*,unit\ cell} = 741.6$ Å^3,

thus $\frac{V_{\gamma,unit\ cell}}{V_{\delta*,unit\ cell}} = 0.675$.

Now, if we call α the fraction of γ phase, then we can write:

$$\frac{V_\gamma}{V_{tot}} = \alpha \rightarrow \frac{(V_{\gamma,unit\ cell}) * (N_{\gamma,cells})}{V_{tot}} = \alpha \quad \rightarrow \quad N_{\gamma,cells} = \alpha * (\frac{V_{tot}}{V_{\gamma,unit\ cell}})$$

$$\& \ \frac{V_{\delta*}}{V_{tot}} = \frac{(V_{\delta*,unit\ cell}) * (N_{\delta*,cells})}{V_{tot}} = (1-\alpha) \rightarrow \quad N_{\delta*,cells} = (1-\alpha) * \frac{V_{tot}}{V_{\delta*,unit\ cell}}$$

Now we can write **Eq. 6** as follow:

$$I_{tot} = \left[I_{\gamma,unit\ cell} * \alpha * \left(\frac{V_{tot}}{V_{\gamma,unit\ cell}}\right)\right] + \left[I_{\delta*,unit\ cell} * (1-\alpha) * \left(\frac{V_{tot}}{V_{\delta*,unit\ cell}}\right)\right] \qquad \textbf{Eq. 7}$$

Simplifying by $V_{\gamma,unit\ cell}$:

$$I_{tot} = [I_{\gamma,unit\ cell} * \alpha * V_{tot}] + [I_{\delta*,unit\ cell} * (1-\alpha) * V_{tot} * 0.675]$$

$$I_{tot} = [I_{\gamma,unit\ cell} * \alpha * V_{tot}] + [I_{\delta*,unit\ cell} * (1-\alpha) * V_{tot} * 0.675] \qquad \textbf{Eq. 8}$$

Theoretically, we could obtain the diffraction profile, if we consider that the total volume is the sum of only one unit cell of γ and one unit cell of δ* ($V_{tot} = 1.2\ nm^3$). We calculated the theoretical diffraction profile with two different values for α, 0.7 and 0.4, to study how the increase of the δ*-phase fraction can affect the form of the profile in the range [3.57-4.17 nm^{-1}]. This is displayed in ***Figure 107***.

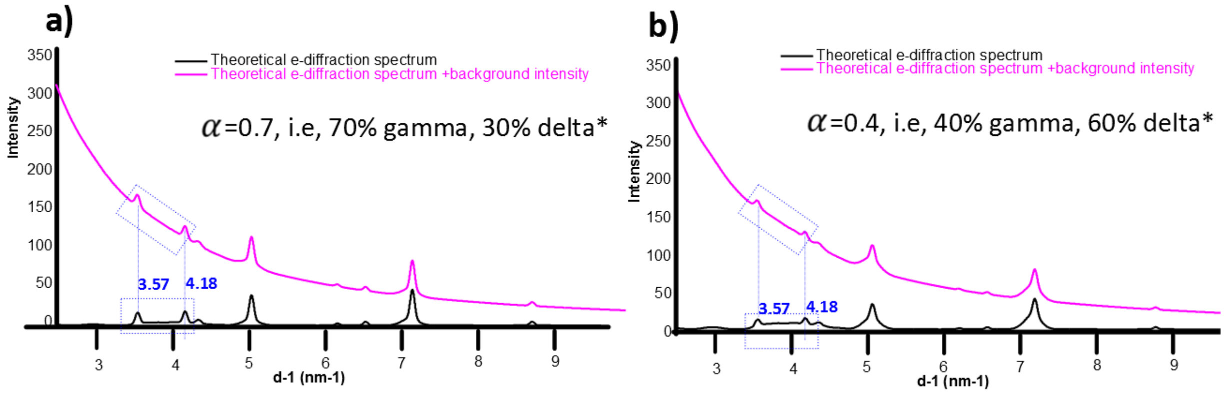

Figure 107: *theoretical diffraction profiles obtained by Eq. 8 for one unit cell of γ and one δ^* in proportions* ***a)*** *of 70% γ and 30% $\delta^*$and* ***b)*** *40% γ and 60% δ^**

Finally, we can conclude by comparing theoretical and experimental profiles that a phase transformation in the sequence γ-Al_2O_3 →δ* Al_2O_3 occurs when the pressure of compaction in the DAC increases from 0 to 5 and then to 20 GPa.

To quantify this transformation, we perform a fit between experimental and theoretical profiles (i.e **Eq. 7**). With

- $A = \alpha * \left(\frac{V_{tot}}{V_{\gamma,unit\ cell}}\right)$
- $B = (1-\alpha) * \left(\frac{V_{tot}}{V_{\delta*,unit\ cell}}\right)$

Then we can write **Eq. 7** as follows:

$$I_{tot} = [I_{\gamma,unit\ cell} * A] + [I_{\delta*,unit\ cell} * B] \qquad \textbf{Eq. 9}$$

$$\rightarrow \alpha = \frac{A * V_{\gamma,unit\ cell}}{V_{tot}} \quad \& \quad (1-\alpha) = \frac{B * V_{\delta*,unit\ cell}}{V_{tot}}$$

$$\rightarrow \frac{(1-\alpha)}{\alpha} = \frac{B}{A}\left(\frac{V_{\delta*,unit\ cell}}{V_{\gamma,unit\ cell}}\right) \rightarrow \frac{1}{\alpha} - 1 = \left(\frac{B}{A} * 1.5\right)$$

$$\rightarrow \alpha = \frac{1}{\left(\frac{B}{A}*1.5\right)+1}$$

→

If A and B are fit constants, thus α can be deduced. We can thus fit the experimental profile with the **Eq. 9**, and extract the value of α and thus evaluate quantitatively the phase transformation in the sequence γ-Al_2O_3 →δ* Al_2O_3.

Figure 108 displays the fit performed on the experimental profile in the range $\mathrm{d}^{-1}[2.5-4.5]\mathrm{nm}^{-1}$, where we suppose that the presence of δ* may affect the general form of the two peaks of γ phase at 3.57 and 4.18 nm^{-1}.

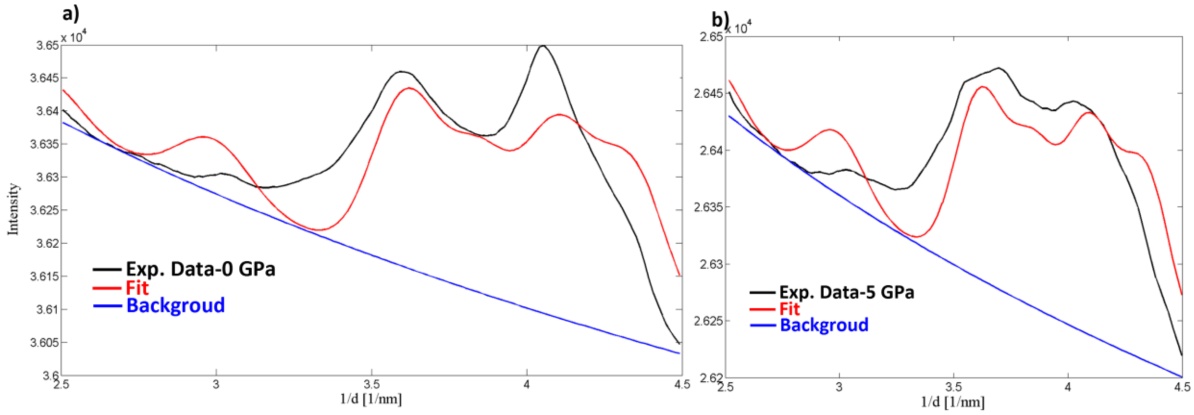

***Figure 108:** Experimental profile fitted with Eq. 9 **a)** initial powder **b)** sample compacted at 5GPa*

In fact the fit of the experimental profile with the theoretical (**Eq. 9**), seems working. (See ***Figure 108***). But results (i.e.α values) obtained by the fit are very low:

- at 0 GPa (initial powder) : $\alpha = 0.23$
- at 5 GPa: $\alpha = 0.19$ and 0.18 (two Debye Scherrer patterns are studied for this sample)
- at 20 GPa : $\alpha = 3.10^{-15}$

However, the values of α seem to continuously decrease when increasing the pressure, which is coherent with previous analysis of the diffraction profiles.

We believe that the values of α obtained by the fit are not so representative, especially because we obtained only 23% of γ-Al_2O_3 in the initial powder. This has to be compared to the XRD results, which showed that the fraction of γ-Al_2O_3 is approximately 70%. We think that the cause may be due to many factors in the TEM patterns that make the proportions obtained by the fit very low.

Nevertheless, the decreasing tendency of α values, shown above, with increasing pressure in the DAC reveals a decrease of the proportion of γ-Al_2O_3 which seems compatible with HRTEM indexations of compacted nanoparticles. Moreover, analysis shown above on the evolution of the peaks general form in the electronic diffraction profiles at d^{-1} [3.57-4.18 nm^{-1}] (see ***Figure 106***) reveal that δ^* Al_2O_3 phase become more present with increasing pressure. With this, we can conclude that a phase transformation following the sequence γ-Al_2O_3 $\rightarrow \delta^*$ Al_2O_3 seems to occur when increasing the pressure in the DAC.

5.3 Conclusion

We could identify the deformation mechanism of transition alumina nanoparticles. A preferential orientation of the {220} planes was observed to be often parallel to the surface in contact between neighbouring nanoparticles. At higher pressures in DAC, this texture is observed to be often parallel to the solicitation direction in the DAC. These observations could be coupled with of the appearance of shear bands in *in situ* TEM compressed nanoparticles. These shear bands are observed in three cases to be at ~35° from the compression axis. The movies of these *in situ* TEM compression tests show that nanoparticles exhibit a slight rotation at early compression. Even in DAC, the nanoparticles are compacted without a pressure transmitting media, and thus are able to freely rotate. This possible rotation in both cases seems to occur to activate the common slip system in a spinel structure, <110> {111}. Indeed, the Schmid factor (0.47) is the highest when the nanoparticle is compressed in <110> direction. Finally, in *in situ* TEM compression of transition alumina nanoparticles, the orientation of the shear bands relative to the compression axisfairly corresponds to the angle between the <110> axis and {111} planes.

Moreover, the analysis of Debye Scherrer patterns on three samples (initial powder, samples compacted at 5 and 20 GPa) reveals a phase transformation of transition alumina in the sequence γ-Al_2O_3 $\rightarrow \delta^*$ Al_2O_3. A procedure was proposed to quantify the fractions of γ and δ^* phases from the diffraction profiles. Although fits results are rather poor, the proportion of γ-Al_2O_3 is found to decrease with increasing pressure. This phase transformation is compatible with the literature where the sequence of transition alumina from γ-Al_2O_3 $\rightarrow$ δ-Al_2O_3, seems to exhibit an intermediate orthorhombic structure, described by δ^*-Al_2O_3.

References

- **Levin,** Igor, et David Brandon. « Metastable Alumina Polymorphs: Crystal Structures and Transition Sequences ». *Journal of the American Ceramic Society* 81, n^o 8 (1 août **1998**): 1995-2012. doi:10.1111/j.1151-2916.1998.tb02581.x.
- **Levin,** I., L. A. Bendersky, D. G. Brandon, et M. Rühle. « Cubic to monoclinic phase transformations in alumina ». *Acta Materialia* 45, n^o 9 (septembre **1997**): 3659-69. doi:10.1016/S1359-6454(97)00040-2.
- **Blonski, S**., et S.H. Garofalini. « Molecular Dynamics Simulations of α-Alumina and γ-Alumina Surfaces ». *Surface Science* 295, n^o 1-2 (septembre **1993**): 263-74. doi:10.1016/0039-6028(93)90202-U.
- **Coleman**, Shawn P., et Douglas E. Spearot. « Atomistic Simulation and Virtual Diffraction Characterization of Stable and Metastable Alumina Surfaces ». *Acta Materialia* 78 (octobre **2014**): 354-68. doi:10.1016/j.actamat.2014.06.061.
- **Bradt,** R. C., C. A. Brookes, et J. L. Routbort. *Plastic Deformation of Ceramics*. Springer Science & Business Media, 2013 (1st edition-**1995**) chapter: the brittle to ductile transition in $MgAl_2O_4$ spinel.

General Conclusion

This PhD was dealing with in situ mechanical tests at the nanoscale, using Transmission Electron Microscopy. The aim was to develop a quantitative observation protocol and to investigate the mechanical properties of ceramics under load in real time. After a review of nanocompression tests, from ex situ to in situ TEM ones, the dissertation was composed of two main parts.

The first part was devoted to MgO nanocubes. We have investigated the mechanical behavior of <100>-oriented and initially dislocation-free MgO nanocubes in the 100 nm size range, using *in situ* TEM nanocompression tests. The results show high strength as well as homogeneous and wide deformation without failure. The analysis of TEM contrast bands observed in the nanocubes at early plastic deformation suggests possible {110} slip. WBDF TEM images for dislocations analysis confirm that these contrast bands are ½<110> {110} dislocations. The results are confirmed by the MD compression simulations, in which the nucleation of ½<110> {110} perfect dislocations is at the onset of the plastic deformation. Schmid factor analysis and considerations based on GSF energy calculations consolidate these results.

After identification of the deformation mechanism, we investigated the effect of the nanocube size on the deformation behavior and the yield strength of single crystal MgO nanocubes under uniaxial compression along the [001]. MgO nanocubes sizes in this study are in the range of [62-450 nm]. A strong size effect is revealed, with a power-law fit exponent $x = 1.3$, which is higher than what was observed in FIB milled single-crystalline micropillars or pristine microparticles of fcc or bcc metals. The smallest MgO nanocube yields at 3.09 GPa which is ~ 60 times higher than the yield stress of bulk single crystal MgO (50 MPa) but only at 1/10 of the theoretical resolved shear strength (15.89 GPa).

Stress-strain curves clearly show a size effect in the plastic regime, where stress drops are large in smaller nanocubes and stress-strain curves become smoother in larger nanocubes. Reinforced with DF and WBDF TEM observations, it was shown that such behavior was correlated to the predominance of dislocation starvation in smaller nanocubes (<200 nm). In larger nanocubes, it seems that dislocation interactions become predominant, which reduces the dislocation nucleation mechanism in order to accommodate further deformation. Finally, it has to be mentioned that the effect of the electron beam has been investigated. A large effect was found on the plastic behavior. The electron beam has been estimated to reduce the yield strength of MgO nanocubes by a factor ~ 2.5. Therefore we believe that the measured yield stresses in all beam-on tests are under-estimated.

In the second part of the dissertation, we investigated the plastic deformation of transition alumina nanoparticles compacted in DAC at 5 GPa, 15 GPa and 20 GPa. Thin foils were prepared by FIB from these compacted transition alumina nanoparticles. A statistical study by HRTEM images of contact zones between neighbor nanoparticles revealed a preferential {110} crystallographic texture often observed parallel to the surface in contact with the neighboring nanoparticle. This crystallographic texture becomes more pronounced with the increase of pressure in DAC. Conventional TEM images revealed that the texture in thin foils (nanoparticles) represent a parallel direction with respect to the uniaxial pressure direction in DAC until ~1µm below the surface. These observations represent useful pieces of information for the identification of the deformation mechanism of similar transition alumina isolated nanoparticles compressed *in situ* in TEM by Emilie Calvié during her PhD at Mateis laboratory. In these tests, shear bands were observed in deformed nanoparticles, oriented at 35° from the compression axis. These observations have been coupled with HRTEM analyses performed on the thin foils prepared from compacted nanoparticles in DAC. We could conclude that rotation of the nanoparticles may occur in both cases (during *in situ* TEM nanocompression tests and in DAC) in order to accommodate the particle along the <110> compression axis, so that the nanoparticle can deform along <110>{111} slip system. These analyses explained both the {110} preferential texture observed in the thin foils and the preferential orientation of shear bands observed in *in situ* TEM nanocompression tests.

Moreover, electron diffraction profiles have been obtained from Debye Scherrer patterns on three samples (initial powder, samples compacted at 5 and 20 GPa in DAC). They revealed the occurrence of a phase transformation in the sequence γ-$Al_2O_3 \rightarrow \delta^*$ Al_2O_3. These analyses were reinforced with a fit of experimental data with theoretical electron diffraction profiles of γ-Al_2O_3 and δ^*-Al_2O_3. The results of the fit were coherent with experimental data analysis and revealed the decrease of γ-Al_2O_3 and the increase of δ^*-Al_2O_3 with increasing pressure in the DAC. Although the proportions of both phases could not be quantified, the results are coherent with the experimental spectra analysis and with HRTEM observations, where more nanoparticles could be indexed as δ^*- Al_2O_3 at high pressures.

Perspectives

- We have investigated the effect of the electron beam on the yield strength of MgO nanocubes. This was performed by blanking the electron beam just during the compression test. However, the MgO nanocubes were exposured to illuminations before the test, during a certain time to acquire an image of the initial state, and position properly the nanocube for a uniaxial nancompression test. It would be interesting to investigate the effect of the electron dose (and dose rate) received by the nanocube on the yield stress and plastic behaviour. It would be also interesting to study other ceramic nano-objects.

After the evaluation of the electron dose effect on the yield stress, it would be intresting also to test the nanocubes *ex situ* by another procedure. For example, it could be possible to:

-indent a susbtrate (Si for example) with a conventional Berkovich tip in order to make a indent pattern, equally separated (few µms)

-deposite MgO nanocubes in the SEM –FIB chamber by using the micro-manipulator. If they are placed between two indents as shown in the sheme (*Figure 109*), it would be easier to locate them under the optical microscope of a conventional nano-indenter outfitted for micro/nano-compression tests.

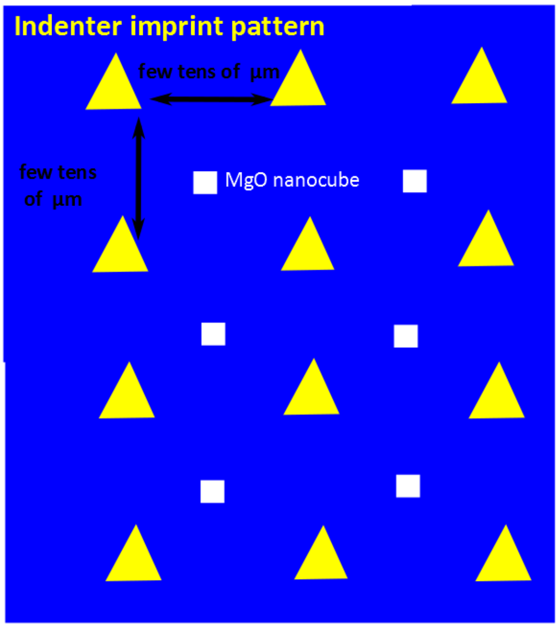

Figure 109: Scheme of imprints pattern of a Brkovich tip. MgO nanocubes may be placed between these imprints using the micro-manipulator in a FIB-SEM chamber

Moreover, it seems that the dislocations are nucleated at the surface of the nano-objects. As a consequence, changing the environment of the nano-objects during compaction might lead to different mechanical behaviours. This could possibly be studied by performing in situ nano-compression tests in an Environmental TEM.

- As far as transition alumina nanoparticles are concerned, the nanoparticles might be studied during compaction using small and wide-angle synchrotron X-ray scattering (SAXS and WAXS) (see Figure 110). This would allow a direct monitoring of crystallographic reorientation of nanoparticles and detect phase transformation under pressure [*Zhongwu Wang et al. (2011)*].

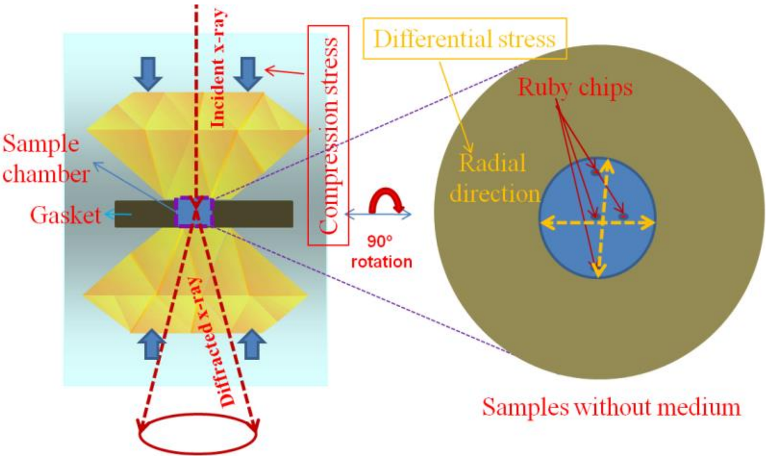

Figure 110: *in situ* SAXS and WAXS during DAC compaction. [*Zhongwu Wang et al. (2011)*].

Finally, compaction of transition alumina nanoparticles should be studied at higher pressures, or with similar pressures but with moderate temperatures. It would be interesting to investigate if the nanoparticles can transform into the α-phase, without any sintering step. Indeed, such a phase transformation at moderate temperature would be of high impact for the synthesis of bulk ceramics, as it would make significant energy savings and might lead to deformable ceramics.

- **Reference:**

Wang, Zhongwu, Constanze Schliehe, Tie Wang, Yasutaka Nagaoka, Y. Charles Cao, William A. Bassett, Huimeng Wu, Hongyou Fan, et Horst Weller. « Deviatoric Stress Driven Formation of Large Single-Crystal PbS Nanosheet from Nanoparticles and in Situ Monitoring of Oriented Attachment ». *Journal of the American Chemical Society* 133, nº 37 (21 septembre **2011**): 14484-87. doi:10.1021/ja204310b.

Appendix

Appendix 1 : δ-Al_2O_3 (Repelin and hosson-1990: XRD)

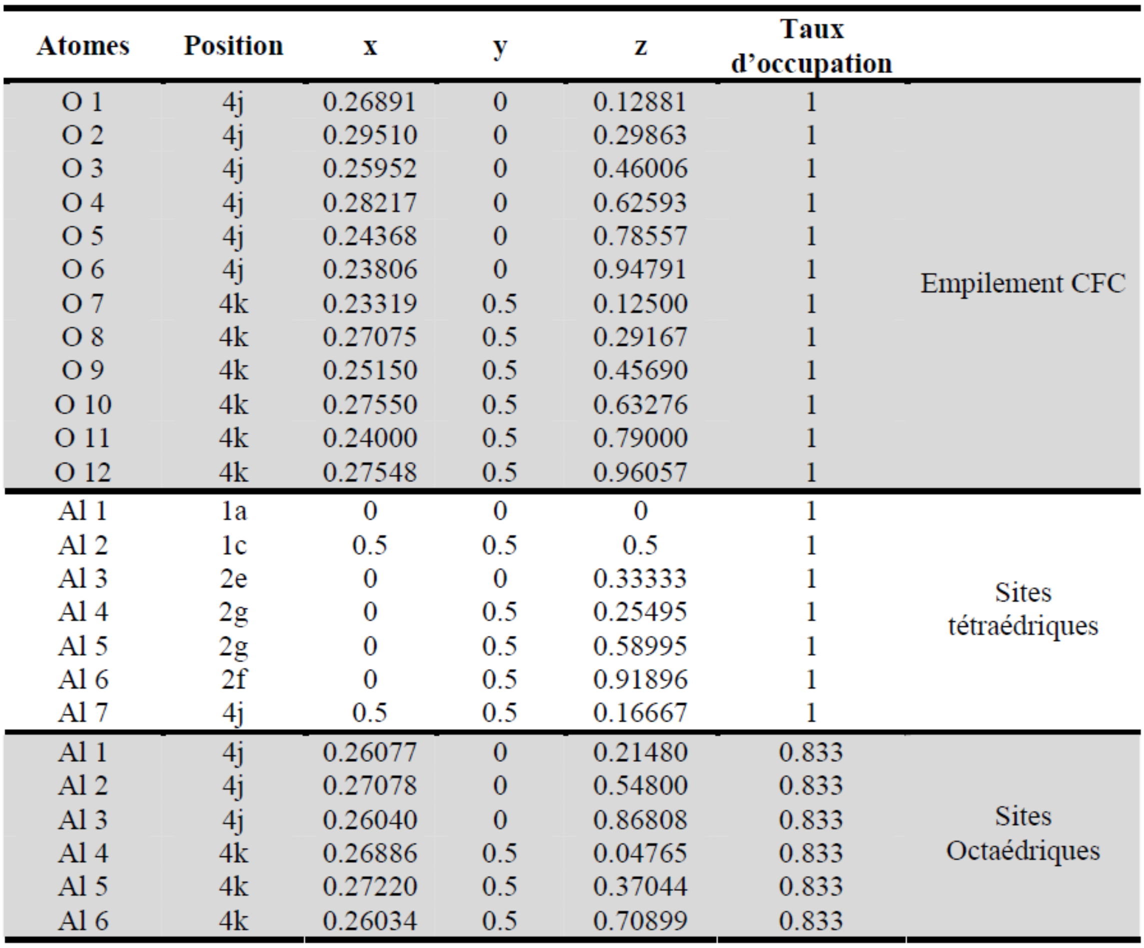

Atomes	Position	x	y	z	Taux d'occupation	
O 1	4j	0.26891	0	0.12881	1	Empilement CFC
O 2	4j	0.29510	0	0.29863	1	
O 3	4j	0.25952	0	0.46006	1	
O 4	4j	0.28217	0	0.62593	1	
O 5	4j	0.24368	0	0.78557	1	
O 6	4j	0.23806	0	0.94791	1	
O 7	4k	0.23319	0.5	0.12500	1	
O 8	4k	0.27075	0.5	0.29167	1	
O 9	4k	0.25150	0.5	0.45690	1	
O 10	4k	0.27550	0.5	0.63276	1	
O 11	4k	0.24000	0.5	0.79000	1	
O 12	4k	0.27548	0.5	0.96057	1	
Al 1	1a	0	0	0	1	Sites tétraédriques
Al 2	1c	0.5	0.5	0.5	1	
Al 3	2e	0	0	0.33333	1	
Al 4	2g	0	0.5	0.25495	1	
Al 5	2g	0	0.5	0.58995	1	
Al 6	2f	0	0.5	0.91896	1	
Al 7	4j	0.5	0.5	0.16667	1	
Al 1	4j	0.26077	0	0.21480	0.833	Sites Octaédriques
Al 2	4j	0.27078	0	0.54800	0.833	
Al 3	4j	0.26040	0	0.86808	0.833	
Al 4	4k	0.26886	0.5	0.04765	0.833	
Al 5	4k	0.27220	0.5	0.37044	0.833	
Al 6	4k	0.26034	0.5	0.70899	0.833	

Appendix 2: File JCPDS γ-Al2O3

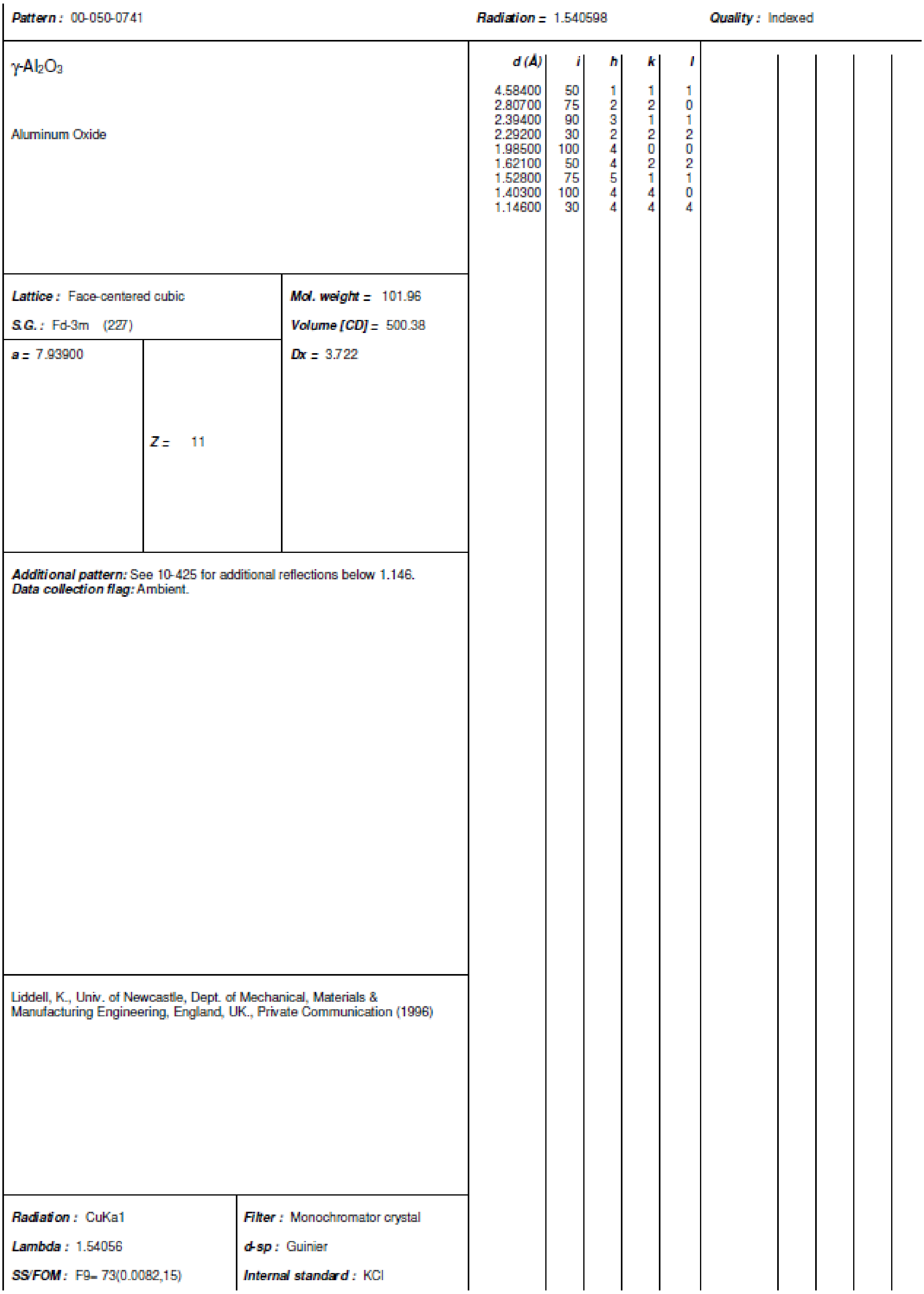

Pattern : 00-050-0741 **Radiation =** 1.540598 **Quality :** Indexed

γ-Al_2O_3

Aluminum Oxide

d (Å)	i	h	k	l
4.58400	50	1	1	1
2.80700	75	2	2	0
2.39400	90	3	1	1
2.29200	30	2	2	2
1.98500	100	4	0	0
1.62100	50	4	2	2
1.52800	75	5	1	1
1.40300	100	4	4	0
1.14600	30	4	4	4

Lattice : Face-centered cubic

S.G. : Fd-3m (227)

a = 7.93900

Z = 11

Mol. weight = 101.96

Volume [CD] = 500.38

Dx = 3.722

Additional pattern: See 10-425 for additional reflections below 1.146.
Data collection flag: Ambient.

Liddell, K., Univ. of Newcastle, Dept. of Mechanical, Materials & Manufacturing Engineering, England, UK., Private Communication (1996)

Radiation : CuKa1

Lambda : 1.54056

SS/FOM : F9= 73(0.0082,15)

Filter : Monochromator crystal

d-sp : Guinier

Internal standard : KCl

Appendix 3: File JCPDS δ*-Al2O3

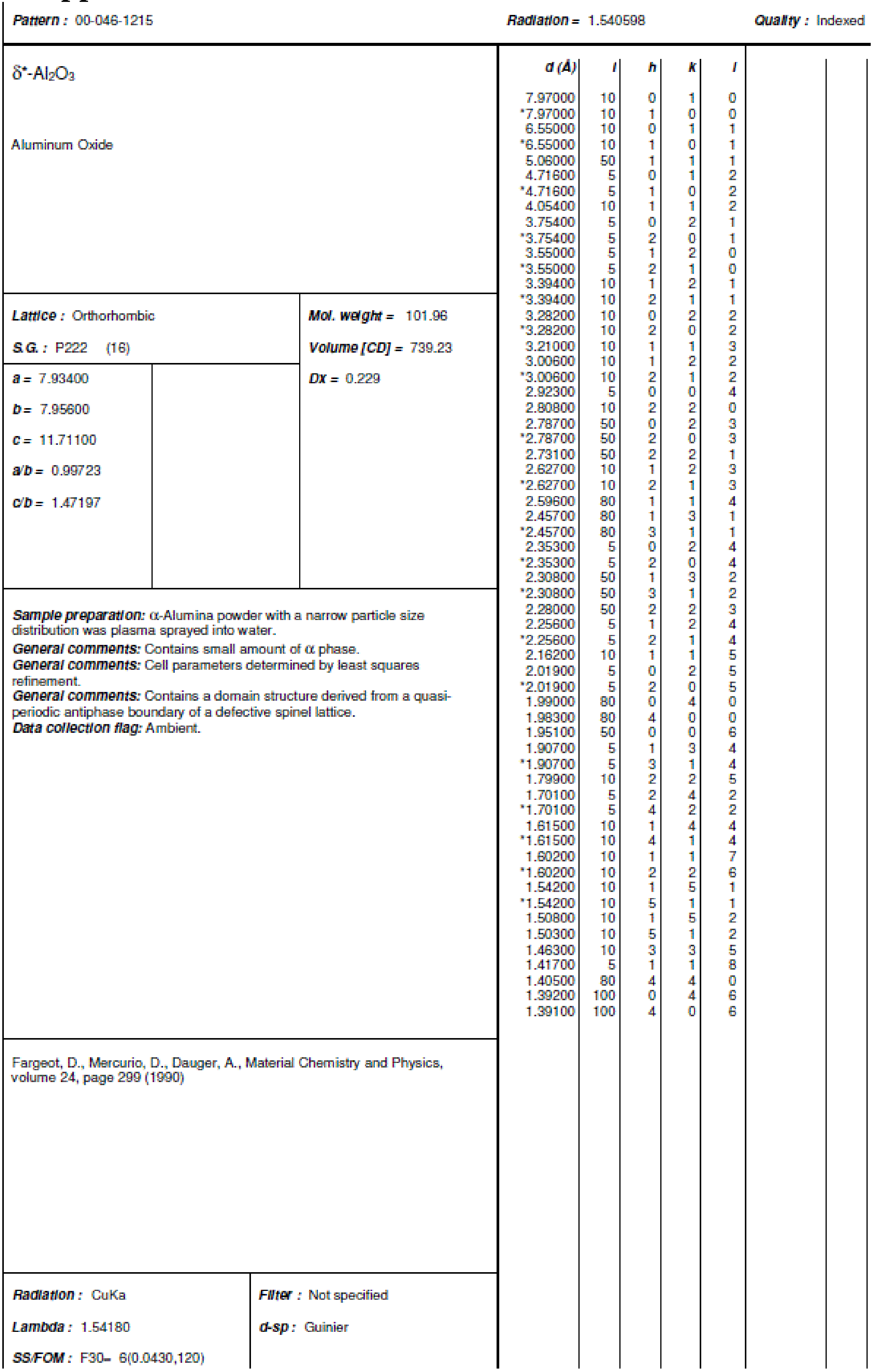

Pattern : 00-046-1215 **Radiation =** 1.540598 **Quality :** Indexed

δ*-Al_2O_3

Aluminum Oxide

Lattice : Orthorhombic

S.G. : P222 (16)

Mol. weight = 101.96

Volume [CD] = 739.23

Dx = 0.229

a = 7.93400

b = 7.95600

c = 11.71100

a/b = 0.99723

c/b = 1.47197

Sample preparation: α-Alumina powder with a narrow particle size distribution was plasma sprayed into water.
General comments: Contains small amount of α phase.
General comments: Cell parameters determined by least squares refinement.
General comments: Contains a domain structure derived from a quasi-periodic antiphase boundary of a defective spinel lattice.
Data collection flag: Ambient.

Fargeot, D., Mercurio, D., Dauger, A., Material Chemistry and Physics, volume 24, page 299 (1990)

Radiation : CuKa

Lambda : 1.54180

SS/FOM : F30= 6(0.0430,120)

Filter : Not specified

d-sp : Guinier

d (Å)	I	h	k	l
7.97000	10	0	1	0
*7.97000	10	1	0	0
6.55000	10	0	1	1
*6.55000	10	1	0	1
5.06000	50	1	1	1
4.71600	5	0	1	2
*4.71600	5	1	0	2
4.05400	10	1	1	2
3.75400	5	0	2	1
*3.75400	5	2	0	1
3.55000	5	1	2	0
*3.55000	5	2	1	0
3.39400	10	1	2	1
*3.39400	10	2	1	1
3.28200	10	0	2	2
*3.28200	10	2	0	2
3.21000	10	1	1	3
3.00600	10	1	2	2
*3.00600	10	2	1	2
2.92300	5	0	0	4
2.80800	10	2	2	0
2.78700	50	0	2	3
*2.78700	50	2	0	3
2.73100	50	2	2	1
2.62700	10	1	2	3
*2.62700	10	2	1	3
2.59600	80	1	1	4
2.45700	80	1	3	1
*2.45700	80	3	1	1
2.35300	5	0	2	4
*2.35300	5	2	0	4
2.30800	50	1	3	2
*2.30800	50	3	1	2
2.28000	50	2	2	3
2.25600	5	1	2	4
*2.25600	5	2	1	4
2.16200	10	1	1	5
2.01900	5	0	2	5
*2.01900	5	2	0	5
1.99000	80	0	4	0
1.98300	80	4	0	0
1.95100	50	0	0	6
1.90700	5	1	3	4
*1.90700	5	3	1	4
1.79900	10	2	2	5
1.70100	5	2	4	2
*1.70100	5	4	2	2
1.61500	10	1	4	4
*1.61500	10	4	1	4
1.60200	10	1	1	7
*1.60200	10	2	2	6
1.54200	10	1	5	1
*1.54200	10	5	1	1
1.50800	10	1	5	2
1.50300	10	5	1	2
1.46300	10	3	3	5
1.41700	5	1	1	8
1.40500	80	4	4	0
1.39200	100	0	4	6
1.39100	100	4	0	6

Appendix 4: File JCPDS δ-Al2O3

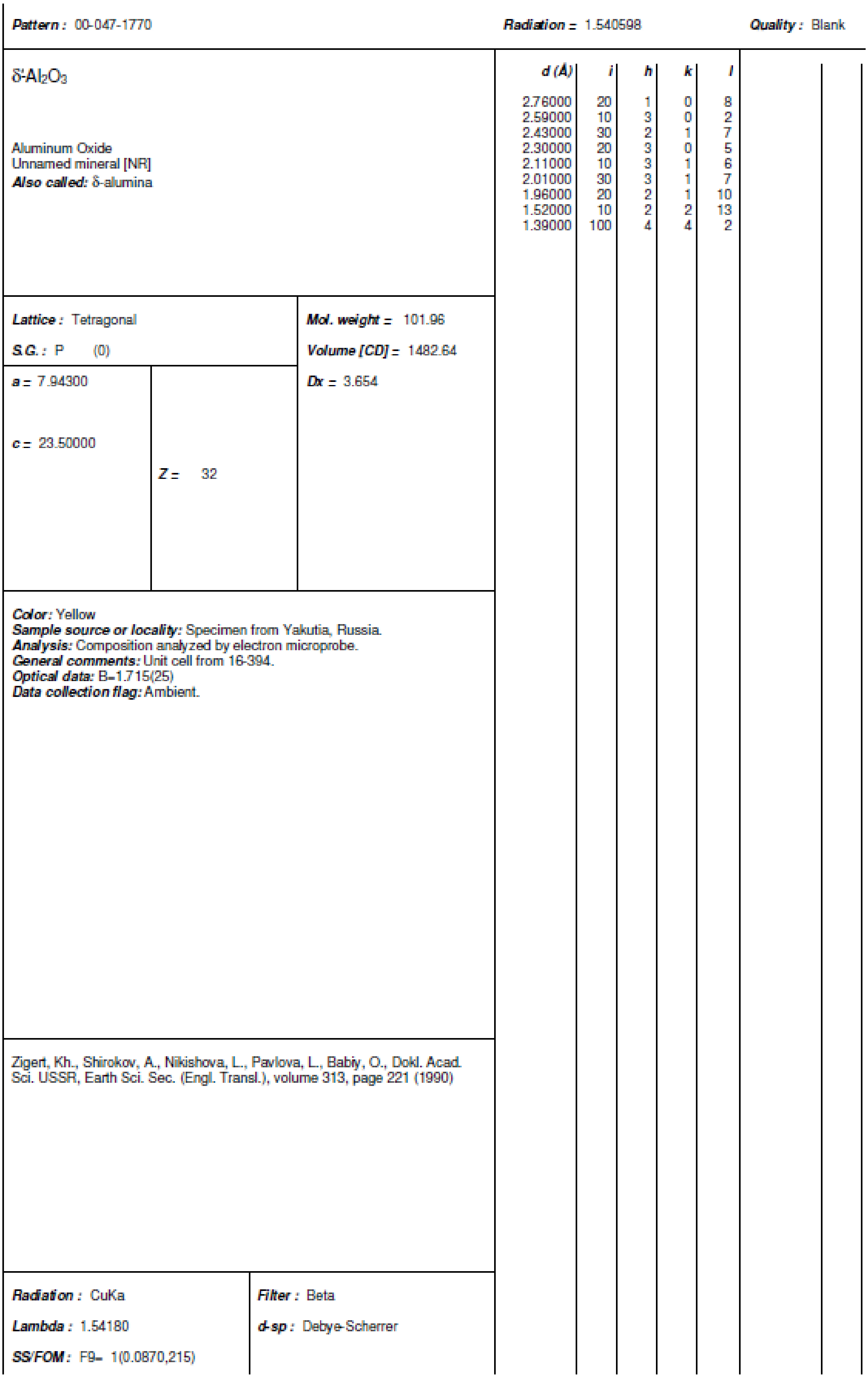

Pattern : 00-047-1770
Radiation = 1.540598
Quality : Blank

δ-Al_2O_3

Aluminum Oxide
Unnamed mineral [NR]
Also called: δ-alumina

d (Å)	i	h	k	l
2.76000	20	1	0	8
2.59000	10	3	0	2
2.43000	30	2	1	7
2.30000	20	3	0	5
2.11000	10	3	1	6
2.01000	30	3	1	7
1.96000	20	2	1	10
1.52000	10	2	2	13
1.39000	100	4	4	2

Lattice : Tetragonal
S.G. : P (0)
a = 7.94300
c = 23.50000
Z = 32
Mol. weight = 101.96
Volume [CD] = 1482.64
Dx = 3.654

Color: Yellow
Sample source or locality: Specimen from Yakutia, Russia.
Analysis: Composition analyzed by electron microprobe.
General comments: Unit cell from 16-394.
Optical data: B=1.715(25)
Data collection flag: Ambient.

Zigert, Kh., Shirokov, A., Nikishova, L., Pavlova, L., Babiy, O., Dokl. Acad. Sci. USSR, Earth Sci. Sec. (Engl. Transl.), volume 313, page 221 (1990)

Radiation : CuKa
Lambda : 1.54180
SS/FOM : F9= 1(0.0870,215)
Filter : Beta
d-sp : Debye-Scherrer

Appendix 5 : Gamma→ Delta*

Gamma→ Delta*

FCC(Fd-3m)

a_γ=7,939 Å

b_γ=7,939 Å

c_γ=7,939 Å

Orthorhombique(P222)

$a_{\delta*}$=7,934 Å

$b_{\delta*}$=7,956 Å

$c_{\delta*}$=11,71 Å

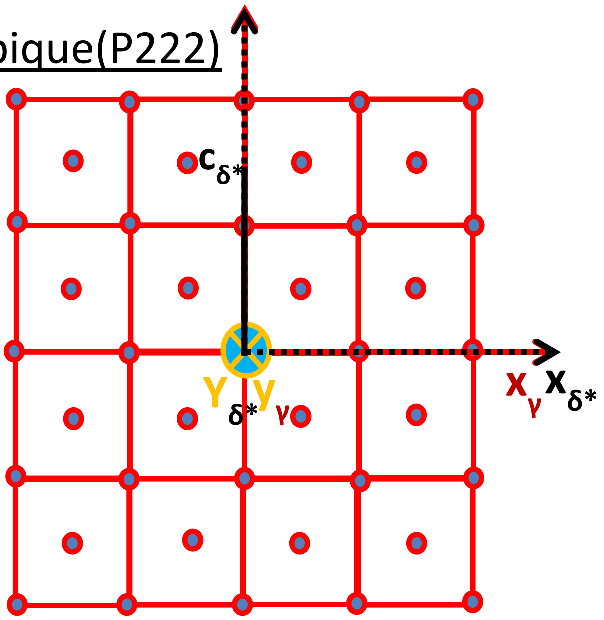

En 2D

$a_\gamma = a_{\delta*}$

$b_\gamma = b_{\delta*}$

$c_\gamma = \frac{c_{\delta*}}{1,5}$

En3D

$a_{\delta*} = a_\gamma + 0 + 0$

$b_{\delta*} = 0 + b_\gamma + 0$

$c_{\delta*} = 0 + 0 + 1,5c_\gamma$

$$\begin{pmatrix} a_{\delta*} \\ b_{\delta*} \\ c_{\delta*} \end{pmatrix} = \begin{pmatrix} 1 & 0 & 0 \\ 0 & 1 & 0 \\ 0 & 0 & 1,5 \end{pmatrix} \begin{pmatrix} a_\gamma \\ b_\gamma \\ c_\gamma \end{pmatrix}$$

$$\begin{pmatrix} h_{\delta*} \\ k_{\delta*} \\ l_{\delta*} \end{pmatrix} = \begin{pmatrix} 1 & 0 & 0 \\ 0 & 1 & 0 \\ 0 & 0 & 1,5 \end{pmatrix} \begin{pmatrix} h_\gamma \\ k_\gamma \\ l_\gamma \end{pmatrix}$$

$h_{\delta*} = h_\gamma$

$k_{\delta*} = k_\gamma$

$l_{\delta*} = \frac{3}{2} l_\gamma$

$h_\gamma = h_{\delta*}$

$k_\gamma = k_{\delta*}$

$l_\gamma = \frac{2}{3} l_{\delta*}$

	Gamma	Delta*
1	220	220
2	2-20	2-20
3	-220	-220
4	-2-20	-2-20
5	022	023
6	0-22	0-23
7	02-2	02-3
8	0-2-2	0-2-3
9	202	203
10	-202	-203
11	20-2	20-3
12	-20-2	-20-3

Appendix 6: Gamma→ Delta*

Gamma→ Delta

FCC	Tetragonal (quadratique)(P-4m2)
a_γ = 7,939 Å	a_δ = 5,599 Å
b_γ = 7,939 Å	b_δ = 5,599 Å
c_γ = 7,939 Å	c_δ = 23,657 Å

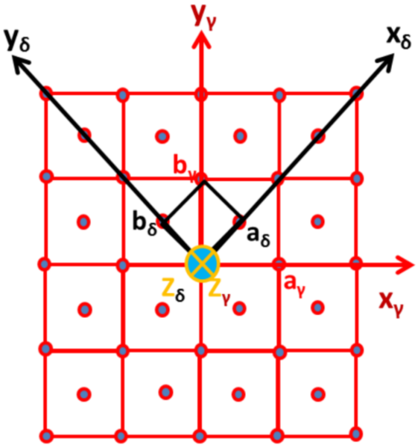

En 2D

$$a_\delta = \frac{a_\gamma}{2} + \frac{b_\gamma}{2}$$

$$b_\delta = \frac{-a_\gamma}{2} + \frac{b_\gamma}{2}$$

$$C_\delta = 3c_\gamma$$

En3D

$$a_\delta = \frac{a_\gamma}{2} + \frac{b_\gamma}{2} + 0$$

$$b_\delta = 0 + b_\gamma + 0$$

$$c_\delta = 0 + 0 + 3\,c_\gamma$$

$$\begin{bmatrix} a_\delta \\ b_\delta \\ c_\delta \end{bmatrix} = \begin{bmatrix} 1/2 & 1/2 & 0 \\ -1/2 & 1/2 & 0 \\ 0 & 0 & 3 \end{bmatrix} \begin{bmatrix} a_\gamma \\ b_\gamma \\ c_\gamma \end{bmatrix}$$

$$\begin{bmatrix} h_\delta \\ k_\delta \\ l_\delta \end{bmatrix} = \begin{bmatrix} 1/2 & 1/2 & 0 \\ -1/2 & 1/2 & 0 \\ 0 & 0 & 3 \end{bmatrix} \begin{bmatrix} h_\gamma \\ k_\gamma \\ l_\gamma \end{bmatrix}$$

(M)

$$(M)^{-1}$$

$$\begin{pmatrix} 1 & -1 & 0 \\ 1 & 1 & 0 \\ 0 & 0 & 1/3 \end{pmatrix}$$

$$h_\delta = \frac{h_\gamma}{2} + \frac{k_\gamma}{2}$$

$$k_\delta = \frac{-h_\gamma}{2} + \frac{k_\gamma}{2}$$

$$l_\delta = 3l_\gamma$$

$$h_\gamma = h_\delta - k_\delta$$

$$k_\gamma = h_\delta + k_\delta$$

$$l_\gamma = \frac{1}{3} l_\delta$$

	Gamma	Delta
1	220	200
2	2-20	0-20
3	-220	020
4	-2-20	-200
5	022	116
6	0-22	-1-16
7	02-2	11-6
8	0-2-2	-1-1-6
9	202	1-16
10	-202	-116
11	20-2	1-1-6
12	-20-2	-11-6

Appendix 7: Calculations for theoretical diffraction intensities for hkl of δ*-Al2O3

hkl	d (nm)	$\frac{1}{d}$ (nm-1)	A (V|nm|e)	θ (mrad)	m	$L \approx \frac{1}{\theta}$	$F^2 = A^2$	$D=e^{-\beta(\frac{1}{2d})^2}$	I_e
010	0,7956	1,256913	1,62056	1,576	2	0,63451776	2,62621471	0,99920908	3,33012387
100	0,7934	1,260398	2,04957	1,581	2	0,63251106	4,20073718	0,99921345	5,30984581
101	0,6561	1,524157	1,15945	1,909	4	0,52383446	1,34432430	0,99946206	2,81529835
112	0,40539	2,466760	1,21704	3,093	8	0,32331070	1,48118636	0,99979459	3,83028029
121	0,34	2,941176	1,22734	3,685	8	0,27137042	1,50636347	0,99985551	3,26978740
022	0,329	3,039513	1,79429	3,811	4	0,26239832	3,21947660	0,99986470	3,37868384
203	0,2782	3,594536	2,10062	4,507	4	0,22187708	4,41260438	0,99990326	3,91584425
221	0,2731	3,661662	2,21291	4,591	8	0,21781746	4,89697066	0,99990677	8,53237054
114	0,2596	3,852080	2,89503	4,83	8	0,20703933	8,38119870	0,99991576	13,8807332
131	0,2459	4,066528	1,65946	5,099	8	0,19611688	2,75380749	0,99992441	4,32021861
311	0,2453	4,076640	2,75516	5,11	8	0,19569471	7,59090662	0,99992478	11,8831087
132	0,2311	4,327131	1,99745	5,426	8	0,18429782	3,98980650	0,99993324	5,88210859
312	0,23	4,347826	1,53008	5,436	8	0,18395879	2,34114480	0,99993387	3,44516556
223	0,228	4,385964	1,90514	5,5	8	0,18181818	3,62955842	0,99993502	5,27901466
115	0,2161	4,625774	1,60328	5,801	8	0,17238407	2,57050675	0,99994158	3,54470829
040	0,1989	5,027652	6,44784	6,305	2	0,15860428	41,5746406	0,99995055	13,1871799
400	0,1983	5,041593	5,53725	6,322	2	0,15817779	30,6611375	0,99995082	9,69934506
006	0,1951	5,123475	5,79774	6,425	2	0,15564202	33,6137891	0,99995238	10,4629380
440	0,1404	7,119971	5,43165	8,928	4	0,11200716	29,5028217	0,99997534	13,2177841
046	0,1393	7,178750	5,45692	9,001	4	0,111098767	29,77797589	0,99997574	13,2328646
406	0,13912	7,188039	5,65001	9,014	4	0,11093854	31,922613	0,999975807	14,1654496

FOLIO ADMINISTRATIF

THESE DE L'UNIVERSITE DE LYON OPEREE AU SEIN DE L'INSA LYON

NOM : ISSA DATE de SOUTENANCE : 19/1/2016
(avec précision du nom de jeune fille, le cas échéant)

Prénoms : Inas

TITRE :
In situ TEM Nanocompression & Mechanical Analysis of Ceramic Nanoparticles

NATURE : Doctorat Numéro d'ordre : 2016LYSEI008

Ecole doctorale : Ecole doctorale Matériaux de Lyon

Spécialité : Science des matériaux

RESUME :

Les matériaux micro- et nanométriques comme les fils, les films minces, les piliers et les particules ont suscité un intérêt considérable ces dernières années dû à leurs surprenantes propriétés mécaniques. Ces systèmes montrent une limite d'élasticité bien supérieure à celle des matériaux massifs et une grande déformation plastique. À l'origine de ce comportement, plusieurs mécanismes potentiels sont proposés comme la nucléation de dislocations en surface, la troncation ou encore l'appauvrissement des sources actives. De plus, la nature même des mécanismes peut devenir dépendante de la taille. La majeure partie des études récentes sur les nano-objets a été dédiée aux métaux cubiques à faces centrées. Ce n'est que dernièrement que davantage de travaux ont visé les métaux cubiques centrés, hexagonaux ou les alliages complexes. Quelques travaux expérimentaux, sur des nanoparticules d'alumine de transition, ont montré que ces céramiques classiques, bien que réputées pour leur caractère fragile sous leur forme massive, présentaient des propriétés mécaniques comparables (notamment en terme de ductilité) à celles des métaux aux petites échelles. Une meilleure appréhension des processus mécaniques, qui agissent aux petites échelles dans ces matériaux, permettrait d'optimiser leur mise en forme et d'adapter leur utilisation.
Dans cette étude, nous proposons d'utiliser la compression in situ dans le MET afin de caractériser les propriétés mécaniques de nanoparticules céramiques dont la taille caractéristique est de l'ordre de quelques dizaines de nanomètres. Nous appliquerons cette méthode à des nanocubes monocristallins de MgO, une céramique modèle dont la plasticité est bien connue dans le matériau massif. Les essais de nanocompression montrent que les nanocubes de MgO se déforment de façon homogène jusqu'à de grandes déformations (>50%) sans fissure apparente. L'analyse des résultats est assistée par des méthodes de corrélation d'images numériques et simulations de type dynamique moléculaire. Le mécanisme de déformation est identifié.
En outre, une étude statistique sur des nanocubes compressés in situ dans le MET montrent l'effet de taille sur la limite élastique des cubes dans une gamme de taille [62 nm-450 nm]. La limite élastique d'un cube de 62 nm est trouvée 60 fois plus grande que celle du MgO monocristallin massif et correspond à 1/10 de la contrainte de cisaillement résolue théorique.
Le faisceau d'électrons a montré dans des études sur des matériaux cristallins et amorphes un effet sur les propriétés élastiques et plastiques étudié de ces matériaux. Ici nous présentons également cet effet du faisceau sur la limite élastique des nanocubes de MgO, cristallins et ioniques.

Dans une deuxième partie de la thèse, nous présentons une étude sur des nanoparticules d'alumine de transition compactée en CED (Cellule à Enclumes en Diamant) à température ambiante, sous plusieurs pressions (5 GPa, 15 GPa et 20 GPa). Des lames minces préparées par FIB ont été étudiées en MET. Des images HRTEM montrent une texture cristallographique qui devient plus importante à des pressions plus élevées. Une orientation cristallographique préférentielle est observée, avec les plans {220} de la phase gamma de l'alumine la plupart du temps parallèles à la surface de contact avec une particule voisine. Ce comportement mécanique est cohérent avec un système de glissement <110>{111}, connu pour les structures spinelles. Une corrélation de ce

comportement avec les tests in situ MET réalisés sur des nanoparticules similaires, par Emilie Calvié lors de sa thèse, est présentée.
Enfin, des clichés de diffraction de type Debye Scherrer sont réalisés sur ces lames minces de nanoparticules d'alumine de transition compactées en CED à différentes pressions. L'analyse quantitative de ces clichés montre une transformation de phase de ces nanoparticules d'alumine de phase gamma en phase delta, de manière croissante avec la pression.

MOTS-CLÉS : *in situ* TEM nanocompression, nanoparticules céramiques, propriétés mécaniques et mécanismes de déformation à l'échelle nanométrique, effet de taille.

Laboratoire (s) de recherche : MATEIS/ LAMCOS

Directeur de thèse: Karine MASENELLI-VARLOT

Président de jury : J. CHEVALIER

Composition du jury :

Rapporteur	M. LEGROS	Professeur, Université Paul Sabatier III Toulouse
Rapporteur	C. TROMAS	Professeur, Université de Poitiers
Examinateur	A. EGGEMAN	Docteur, University of Cambridge
Examinateur	D. MACHON	Maitre de conférences, Université Claude Bernard Lyon 1
Examinateur	J. CHEVALIER	Professeur, INSA de Lyon
Directrice de thèse	K. MASENELLI-VARLOT	Professeur, INSA de Lyon
Co-directeur de thèse	J. RETHORE	Chargé de recherches CNRS, INSA de Lyon
Encadrante de thèse	L. JOLY-POTTUZ	Maitre de conférences, INSA de Lyon